ANNA FERRÉ-MATEU

Detailed stellar population analysis of Early-Typegalaxies with redshift to constrain their evolution

Directores
ALEXANDRE VAZDEKIS
IGNACIO G. DE LA ROSA

A la vida, porque solo hay una

Todos vivimos en el cielo
pero solo algunos levantan
los ojos hacia las estrellas
Oscar Wilde

Mil millones de gracias...

el meollo, por ayudarme en tantos momentos y por seguir confiando en mí... Algún día lo conseguiremos, nuestras "niñas" serán muy importantes. Y gracias también a Jesús, por su inquestionable ayuda con la nueva página web, por el sinfín de charlas tanto personales como científicas. Pero sobretodo, por los magníficos comentarios que han ayudado sustancialmente a mejorar esta tesis y por aceptar ser miembro de mi tribunal junto con Jordi, Ignacio, Evencio y Francesco. Y muchísimas gracias a Reynier y a Sune por ejercer de árbitros externos para la mención europea.

¡Y muchas gracias al grupo de trabajo más molón del IAC! Voy a echar de menos nuestras reuniones de horas, y a cada uno de vosotros. Espero que coincidamos en algún otro lugar. Gracias a la beca de Residente Astrofísico en el IAC y al proyecto coordinado de RAVET (AYA2010-21322-C03-02), ambos del Programa Nacional de Astronomía y Astrofísica del Ministerio Español de Ciencia e Innovación, he disfrutado haciendo ciencia. Sin ese apoyo no hubiera podido asistir a las innumerables conferencias a las que he podido ir ni dedicarme sin preocupaciones a la tarea que se me había encomendado. A los *raveros* Vicent, Susana, Javi, Elena, Cenarro y al nodo de Madrid, por la mejor agua de Valencia, por el torico y por la majestuosidad del Escorial. Gracias a la beca de movilidad para la mención europea del Ministerio Español de Ciencia e Innovación, que me permitió pasar tres inolvidables meses en Oxford. Así que agradezco también desde aquí al Prof. Roger Davies por su supervisión durante ese tiempo y a toda la gente que me adoptó durante esa estancia. Por las tardes de fútbol, por las fiestas en las casas, y por hacerme sentir como en casa, gracias Alessandra, Marc, Quique, Mayte, Marta, Hyun, Billy, Tere, Viddha y Mara.

Pero un trabajo no se disfruta sin una buena compañía. Durante estos años, innumerables personas han ido y venido, cada una regalándome momentos increíbles que me han permitido sobrellevar los momentos más duros de la tesis y de la vida. A la siempre atenta Inma, a la siempre fiestera Esther, a mi gran despistadilla Patri, a mi fashion-alma gemela MJ y a la siempre sonriente Adri... en resumen, a mis rubias preferidas, ¡sin las ladies night esto hubiera sido muy aburrido! Pero también a los *toperos*, a Jairo, a Aarón, a Helena, a Cris, a Nayra, a Miriam y a César. Al grupo de "Rs" de mi año, en especial a mi K y a mi M, ¡chicos, somos la caña! Aunque no cuajara lo de los jueves de Rs, me lo he pasado genial en todos esos miércoles de kebab, esos cumpleaños, y esos asábados. A mis hermanas isleñas, Marta y Paula, habéis sido mi familia aquí, gracias por hacerme sentir como una más. A mis compis de cruzada, Mar y Pau. El tiempo todo lo cura y ahora lo tenemos claro, amigos hasta el final, no sabéis lo mal que me sabe permerme vuestra boda... Mar, mica en mica, els nostres somnis estàn cada vegada més a prop! A la peña del moco surf, habéis

sido los últimos en llegar, pero afrontar cada semana no hubiera sido lo mismo sin las risas, buen rollo, surfing y solete de los fines de semana con las furgonas. Así que espero vuestra visita Silvi, Marta, Sandra, Migue, Richi, Vito, Chino, Lio, Atte, Diana, Cinturita y Co.

Para llegar al punto inicial de la tesis, otras muchas personas han jugado un papel crucial en mis primeros años en la isla. Para empezar, a mis vascos, Txarly, Gupi y Cano, y al único representante isleño durante mucho tiempo, Aarón. El primer año fue, sin lugar a dudas, el mejor. Sin él, ¡quién sabe si me hubiera quedado! Y a las grandes fiestas en el piso de los catalanes, Jordi, Roger, Vic, Macu, Alba, Ari, Fer, Laurita,... y por la mejor época del Cuadrilátero... ¡qué lejos quedan las bombas de gas lacrimógeno en la calle del Blues Bar! Y al Decafé, con Monky, el Tortuga y mi amiga sideral Janire... El Erasmus en Padova consolidó mis ganas de viajar y vivir fuera. Gracias a mi familia italiana, en especial a Maria y a Filipe, pero sin olvidarme de Filippo, Jacopo, Elena y Ale... Mile grazzie, non essiste il mio Erasmus sense la vostra amicizia. A los gallegos, Abrahan e Iria, por vuestra calidez y por acogernos en vuestra casa durante tanto tiempo.

Pero una parte enorme se la lleva toda mi gente de Barcelona, que hace ya años que dejé, pero que sigo llevando conmigo allá donde voy y que sin su apoyo y amistad, jamás lo hubiera logrado. Començant per la colla, que hagués sigut de mi sense les tardes al parc, els berenars a les piscines o les festes majors? En especial a la Maria, he disfrutat cada un dels viatges, cada una de les esquiades, cada una de les festes, i lo que encara ens queda! Al trio là-là-là, Marta y Mire, aquest està sent el nostre any! Una mama, l'altra doctora... Marcet, la próxima ets tú! A les dels casals, perquè no té sentit tornar a la feina després d'uns nadals sense un amic rebaixat, oi Anna, Ari, Bea, Laura, Imma, Quera i Mar? Als de travi, amb vosaltres vaig fer-me adulta, vosaltres em vau ensenyar com disfrutar de la vida i del esquí y sobretot, lo que significa l'amistad. Vosaltres em vau disfressar d'astronauta i a vosaltres us ho dedicaré si arriva el moment. Per els caps d'any, pels llits de 8 persones, per les millors esquiades, per Menorca, per *REC*, per les més guapes del món i pels que esteu formant una legió de mini-travis... Mil millons de gràcies! A les de Ramar, en especial a la Cris. Tú em vas ficar al cap la idea de l'astrofísica i Tenerife. Els camins es van separar, però una part de tú també ho ha aconseguit! I als de la uni, tant als de físiques com als de biotecnologia... quantes hores d'estudi a la biblio però quantes hores de riure al bar també! No hi hauria hagut tesis si no hi hagués hagut carrera primer, així que moltes gràcies també a la Jou, la Jessi, la Sandra, el Sergi, en Jordi, en Dani, en Xuís, la Laia, la Judith, la Jordina, l'Edu i el Jordi. I evidentment, un especial i enorme gràcies a la SonSon. Ja

són molts anys, moltes vivències, molt de riure i molt de plorar. Però ho he aconseguit, i en part, t'ho dec a tú, al teu suport i a la teva amistat. Gràcies xipi-monxi-tronxi!

No m'oblido pas dels més importants, no! A la meva familia, què els hi he de dir que no sàpiguen ja? Mama, saps que el mèrit acadèmic és totalment teu. Papa, tú m'has donat lo que més estimo en el món, l'esquí. Pau, perquè els viatges mai haguéssin sigut igual com a filla única, sempre, sempre, tindràs un lloc allà on visqui, Bro. Meme i tieta Montse, m'heu fet de cosina, tieta, padrina i d'àvia a la vegada. Sense les mones, no hi ha Setmana Santa. A l'avi, a l'àvia, al tiet Joan i als que ja no hi són...per els estius a Altafulla: les becaines a l'eixida, les 100 pessetes de xuxes, els canelons, les hores i hores a la platja, i per estimar-nos com ho vau fer. I a la resta de *family*, per els grans dinars que ja casi mai puc disfrutar. A tots, mil millons de gràcies.

Y como no, finalmente, a Ale. Van ya casi ocho años, ocho años en los que yo he aprendido de ti a vivir y disfrutar un poco más, y tu de mi, espero, a ser un poco más responsable. Pero sobretodo, nos lo hemos pasado genial juntos. Gracias por haberme apoyado, gracias por haberme aguantado el mal humor, gracias por haberme consolado cuando estaba triste y no me salían las cosas, gracias por haberme querido cuando echaba de menos a mi gente. Gracias por las experiencias, gracias por los viajes, gracias por la compañía. Gracias mi amor.

<div style="text-align: right">

Anna Ferré-Mateu
La Laguna, Abril 2013

</div>

Abstract

One of the long-standing questions in modern Astronomy is how galaxies of different families have evolved since they formed. One of these families, the Early-Type Galaxies (ETGs), which is formed by elliptical and lenticulars galaxies, containing most of the luminous matter in the Universe, have been deeply studied for decades. Several scenarios for the formation and evolution of these galaxies have been proposed but, so far, non of them seem to be conclusive. In the Local Universe, ETGs follow very tight relations on their properties, indicative of a slow evolution since their formation. But the early epochs of the Universe are still to be unraveled as they add new unknowns into the equation. For example, massive ETGs at high redshift. It has been recently discovered that they were much more compact in the early Universe (z∼2) than the massive ones we see today. However, the mechanisms regulating this size evolution are not yet clearly understood and the ones proposed do not completely match the predictions from the competing scenarios to explain this evolution.

In this thesis, we aim to shed some light into this puzzling topic by analyzing the stellar populations of massive ETGs over cosmic time from different points of view. For this purpose, we exploit new state-of-the-art analysis tools and methods, such as the full-spectrum-fitting approach combined with a more classical index-index analysis from the spectroscopic absorption features. The novelty of this work is the detailed analysis of the stellar populations, performed on an individual galaxy basis. Altogether, these methods can pose strong constrains on the competing scenarios for the formation and evolution of ETGs.

Most of the mechanisms proposed to explain the size evolution of massive ETGs predict the presence (although scarce) of relic compact massive galaxies in the local Universe. The first part of the thesis presents a full characterization of a unique sample of local compact massive galaxies. We address the question whether they are the descendants of those that we observe in the early Universe. However, our results from a detailed analysis of their kinematics, morphologies

and stellar population properties suggest that local compact massive galaxies are nearly the exact copies of those at high redshift instead of their descendants. The vicinity of these objects place them as the perfect laboratory for the exploration of the mechanisms responsible for the formation of their counterparts at high redshift.

Further constrains on the evolution of massive galaxies are possible from a detailed study of the stellar populations of ETGs in clusters at varying redshift. Such detailed analysis is possible out to z∼ 0.8, i.e. approximately half the age of the Universe, where obtaining spectra with high enough quality is still possible pushing current observing facilities to their limit. We have derived mean ages, metallicities, abundance ratios and SFHs on an individual galaxy basis at such high redshift. The obtained results have been compared to those for their local counterparts in clusters with similar properties to discriminate between different evolutionary paths. Our results point out that a relation between the position within the cluster, the velocity dispersion and the SFH may allow us to understand better the galaxy cluster evolution. We find that the most massive galaxies evolve passively while the lower-mass ones, generally located in the surroundings, experience a more extended star formation history.

However, all these studies are performed under the assumption of a universal Initial Mass Function (IMF). The debate on the possible variations of the IMF for explaining several aspects of ETGs evolution, such as e.g. their chemical enrichment and abundance pattern, uses to peak almost every decade. The most recent contributions point towards a bottom-heavier IMF for more massive galaxies. We present an analysis about the biased results that can be obtained when adopting a standard, universal IMF. We have quantified the impact of varying the IMF slope and shape into various galaxy properties. For this purpose we use two samples: a sample of ETGs with varying masses and a sample of local compact massive galaxies. We find that galaxies are rejuvenated and get more massive as we steepen the slope of a Salpeter-like power-law IMF. However, this trend is milder if we consider a Kroupa-like multi-segmented IMF, where the weight of the very low-mass stars is decreased. In addition, we find that by tuning each IMF slope according to the central velocity dispersion of the galaxy, as recently claimed, their derived SFHs tend to be more similar, although still different. This pattern involves a varying amount of recent residual star formation, for the most massive ones.

Resumen

Una de las cuestiones básicas de la Astronomía moderna es cómo las galaxias de las diferentes familias han evolucionado desde su formación. Una de estas familias, las galaxias de tipos tempranos (ETGs, del inglés Early-Type Galaxy), formadas por galaxias elípticas y lenticulares, que contienen la mayor parte de la materia luminosa del Universo, ha sido profundamente estudiada durante décadas. Se han propuesto varios escenarios de formación y evolución para estas galaxias, pero por el momento, ninguno de ellos es definitivo. En el Universo local, las ETGs siguen unas relaciones muy ajustadas en sus propiedades globales, indicativas de una evolución lenta desde su formación. Pero las épocas más tempranas del Universo aún tienen que ser desentrañadas, y siguen sumando más incógnitas a la ecuación. Una pieza clave de este rompecabezas son las galaxias masivas. Se ha descubierto recientemente que éstas eran mucho más compactas a alto desplazamiento al rojo ($z\sim2$) que las galaxias masivas que vemos hoy en día. No obstante, los mecanismos que regulan dicha evolución de los tamaños no están aún del todo claros, ya que no coinciden con las predicciones de los escenarios que explican su evolución.

En esta tesis se propone esclarecer este tema, analizando las poblaciones estelares de las ETGs masivas a través del tiempo cósmico desde diferentes puntos de vista. Para tal fin, explotamos las nuevas herramientas y métodos de última generación, como el ajuste completo del espectro (*full-spectral-fitting*) combinado con el análisis de los índices espectrales mediante los diagramas índice-índice. La novedad de este trabajo está en el estudio detallado de las poblaciones estelares, llevado a cabo galaxia por galaxia incluso a alto desplazamiento al rojo. Este conjunto de observaciones y métodos utilizados, permite acotar los diferentes escenarios propuestos para la formación y evolución de las ETGs.

La mayoría de los mecanismos propuestos para explicar la evolución de las ETGs masivas predice la presencia (aunque escasa) de fósiles vivos de galaxias

compactas masivas en el Universo local. En la primera parte de la tesis se presenta una caracterización completa de una muestra única de estas galaxias. Queremos responder la pregunta de si son los descendientes de las galaxias masivas a alto desplazamiento al rojo. No obstante, nuestros resultados sugieren que las galaxias compactas masivas locales son prácticamente una copia exacta de las del alto desplazamiento al rojo, en vez de sus descendientes. La proximidad de estos objetos hace que sean un laboratorio ideal para explorar los mecanismos responsables de la formación de sus análogos a alto z.

Otra manera de acotar la evolución de las galaxias masivas es a través del estudio detallado de las poblaciones estelares de ETGs en cúmulos a diferentes desplazamientos al rojo. Un estudio detallado de este calibre solo es posible a z∼ 0.8, es decir, aproximadamente a la mitad de la edad del Universo. Obtener espectros de calidad suficiente a dicho desplazamiento al rojo es posible llevando al límite la capacidad de los telescopios actuales. Con ellos, hemos derivado edades, metalicidades, patrones de abundancia relativa y las historias de formación estelar (SFHs, del inglés Star Formation History) de forma individual. Los resultados se han comparado con los que se obtienen para galaxias análogas en cúmulos cercanos de propiedades similares para discriminar entre los posibles escenarios de evolución. Nuestros resultados indican que la relación entre la posición dentro del cúmulo, la dispersión de velocidades y la SFH puede ayudar a entender mejor la evolución de las galaxias del cúmulo. Encontramos que las galaxias más masivas evolucionan de forma pasiva, mientras que las de menor masa, generalmente localizadas en la perfieria, experimentan una SFH más extendida en el tiempo.

No obstante, estos estudios se hacen bajo la suposición de una Función Inicial de Masas (IMF) universal. El debate acerca de las posibles variaciones de la IMF para explicar varios aspectos de la evolución de las ETGs, como su enriquecimiento químico o su patrón de abundancias, suele reaparecer casi cada década. Las contribuciones más recientes apuntan hacia una IMF de mayor pendiente para las galaxias más masivas. Presentamos un análisis de los sesgos en los resultados que se pueden obtener al adoptar una IMF estándar y universal. Hemos cuantificado el impacto de variar la forma y la pendiente de la IMF sobre varias propiedades de las galaxias. Para tal fin, usamos dos muestras: una con ETGs de varias masas y otra que contiene las galaxias compactas masivas locales. Encontramos que las galaxias rejuvenecen y se vuelven más masivas a medida que aumentamos la pendiente de una IMF tipo Salpeter (una única exponencial). Sin embargo, esta tendencia es más suave si se consideran IMFs tipo Kroupa (una exponencial segmentada), donde el peso de las estrellas de muy baja masa es menor. Además, encontramos que al escoger una pendiente

de la IMF según la dispersión de velocidades de la galaxia, tal y como se ha indicado recientemente, las SFHs que se derivan tienden a asemejarse (aún manteniendo sus diferencias). Dichas SFHs muestran una cantidad variable de formación estelar reciente.

Contents

List of Figures

1

Introduction

Blinding ignorance does mislead us.
O! Wretched mortals,
open your eyes!
Leonardo da Vinci

U nraveling the formation and evolution of galaxies has been for decades and even a century, one of the main goals of astronomers. Phrased in another way, it is the goose that lays the golden eggs of modern astronomy. Galaxy evolution is defined by several independent clocks. The most obvious, the history of *star formation*, when stars are formed. As it proceeds, the material in the galaxies must also evolve its *chemical composition*. Finally, a galaxy evolves *dynamically*, changing the structure of stars in the orbits and creating or destroying other structures as disks, rings, etc.

We must understand how galaxies were discovered to understand the puzzle they have created. Galaxies were not recognized as a distinct type of nebular objects until the early 20th century. By that time, our Galaxy was assumed to be the entire Universe, formed by stars, gas and dust. The extended objects were named nebulae but their nature was not clearly understood. However, the idea that some of those objects, the ones classified as *spiral nebulae*, were in reality larger and independent objects (*island universes*), created a big controversy. This led to the "Great Debate" of 1920 between Harlow Shapley and Herber Curtis to discuss the scale of the Universe. The main points of the debate were the size of our Galaxy and the location of the Sun within it. The problem was that the evidences from both sides were partly wrong and each one disagreed with the other. However, they both made points that changed

completely the understanding of our place in the Universe. Shapley showed that the Milky Way was much larger than previously believed, with the Sun shifted from the center, while Curtis assessed the external nature of the spiral nebulae (for good reviews on the process, see e.g. Shapley & Curtis 1921, Berendzen, Hart & Seeley 1976, Hoskin 1976, Smith 1982, Trimble 1995).

These controversies were conclusively settled when E. Hubble identified Cepheid variable stars in the Andromeda Nebula (which was, in fact, the Andromeda Galaxy), allowing him to measure its distance and to prove that our Universe was composed of many other extended objects or galaxies. He classified the galaxies on the well-known "Tuning Fork Diagram" (1926, 1936). This diagram presented the first evolutionary sequence for galaxies based solely on a morphological classification (Reynolds 1920, Hubble 1926, Hubble 1936). In it, galaxies were separated in two families: early-type galaxies (E), representing the first evolutionary stages, with no signs of substructure, and late-type galaxies on the right side, branched off by the presence/absence of a bar (SB/S). In the junction of these two families, the lenticulars lied. Despite the lack of spiral arms, they do have disks, reason why they were named S0 but were considered as early-type galaxies. For a long time, S0s were only considered as a transition phase, but then they proved to be a family itself (Spitzer & Baade 1951, de Vaucouleurs 1959, Sandage 1961, Sandage, Freeman & Stokes 1970).

The upper panel of Figure 1.1 shows an schematic diagram of Hubble's classification. Afterward, different subscripts were added to classify the galaxy ellipticity, the size of its bulge, the degree of aperture of the arms, the presence of rings, order in the spiral pattern and other features (Holmberg 1958, de Vaucouleurs 1959, van den Bergh 1960a, van den Bergh 1960b). Figure 1.1 middle and lower panels show the evolution of the tuning-fork diagram as the new nomenclatures were adopted. Stunningly the stellar content of galaxies varies systematically along the linear sequence from E to Sm (Sandage, Freeman & Stokes, 1970). This was unexpected because the initial classification was done purely based on the morphological aspects of galaxies.

The idea of the evolution along the Hubble sequence was soon discarded, as some difference must have occurred at the time of the formation of E and S systems to cause such different forms with different populations. Despite these facts, the notation of early/late type remains and the vast majority of the works in the extragalactic field have been performed following this nomenclature. Nonetheless, attempts for a different classification not based on the morphology alone but also on intrinsic properties of the galaxies have been proposed since then (e.g. van den Bergh 1976, Kormendy & Bender 1996, Cappellari et al. 2011, Cappellari 2012, Kormendy & Bender 2012).

Discarded the evolution along the Hubble sequence, which is then the path that galaxies undergo, from their creation to the present days? Is it the same for ellipticals than for spirals? Do they move along the colour-magnitude diagram?
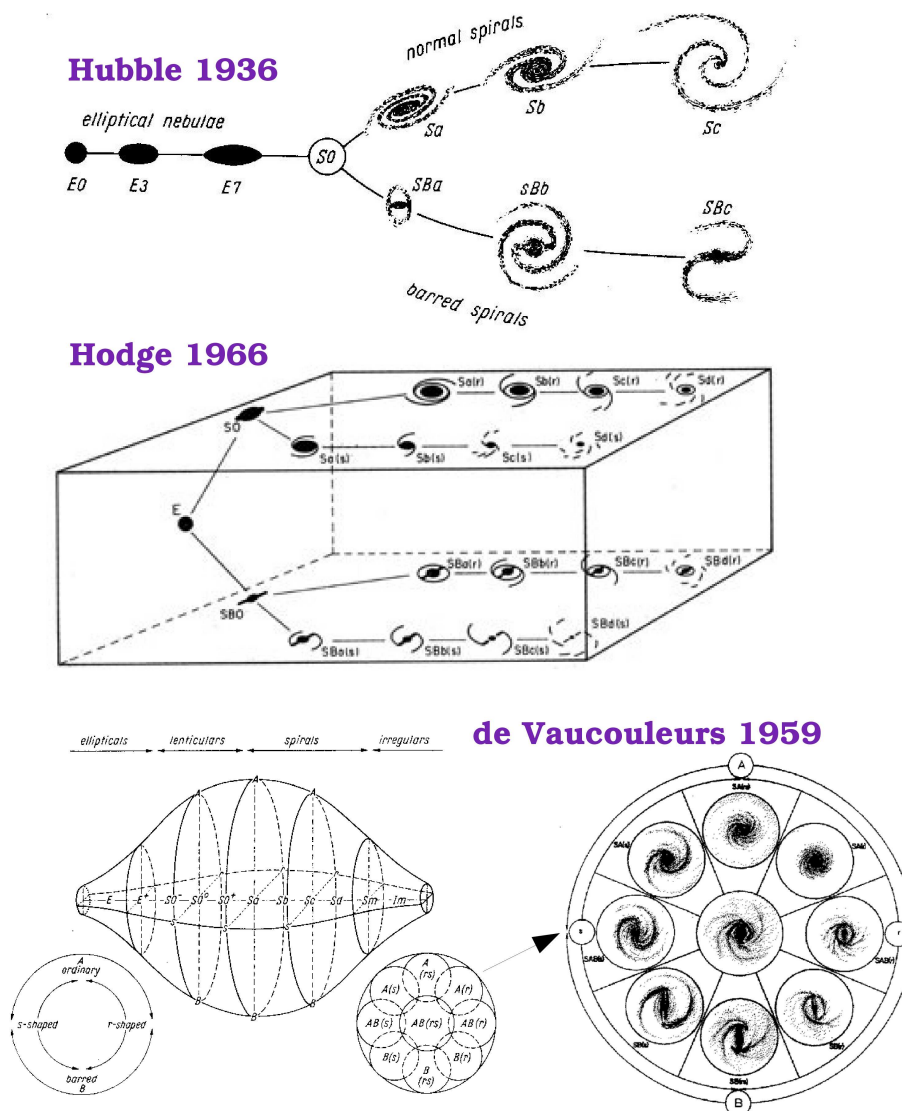
FIGURE 1.1— Different schematic diagrams representing the tuning fork diagram and the new nomenclatures added with time. *Upper panel*: the original tuning fork from the *Realm of the Nebulae* of Hubble (1936). *Middle panel*: a 3D version from Hodges (1966). *Lower panels*: the extended volume classification from the de Vaucouleurs (1959). The righter most panel is a zoomed picture of the cross-section of de left one near the region of the Sb and SBb spirals to show the different transitions (from the *Reference Catalogue of Bright Galaxies* of de Vaucouleurs 1964).

1.1 *Star Wars*: Competing formation and evolution scenarios

Two scenarios have hold for decades the reins of the debate on how galaxies, and in particular, the early-type ones have formed and evolved: the "hierarchical" and the "monolithic" models. Whatever mechanism predicted to explain galaxy evolution has to be supported by observations. In particular, it has to match the observed stellar populations as they are a fossil record of the processes that the galaxy has undergone. In fact, new scenarios have been recently proposed to explain the evolution that the most massive galaxies undergo. This issue will be expanded on Section 1.3, while we focus here on a more historical view.

Monolithic collapse

Within this scenario, galaxies were formed at very earlier epochs in a unique and violent episode of star formation in the protogalactic cloud (Eggen, Lynden-Bell & Sandage 1962, Larson 1974a, Larson 1974b, Larson 1975, van Albada 1982, Carlberg 1984a, Carlberg 1984b, Arimoto & Yoshii 1987, Chiosi & Carraro 2002). The star formation occurs everywhere in the galaxy, with an efficiency that is proportional to the dynamical time of the cloud's collapse, and the gas, enriched by the most massive stars, collapses towards the center of the galaxy.

This scenario predicts old populations that fade and get redder by passively aging through cosmic time. This is supported by the global scaling laws that govern the stellar populations (e.g. the Colour-Magnitude Relation, the Fundamental Plane, described in detail in Section 1.2.1), because it is shown that the structure of early-type galaxies was already settled by the scale of the initial condensing material, with nearly any subsequent change on these properties (e.g. Kodama & Arimoto 1997, Terlevich et al. 1999, Kuntschner 2000, Vazdekis et al. 2001a, Terlevich, Caldwell & Bower 2001, Matteucci 2003). However, this scenario has the disadvantage that it is not conceived within the framework of the current standard cold dark matter cosmological model (ΛCDM, Blumenthal et al. 1984, Davis et al. 1985).

Hierarchical formation

Within this scenario, small-scale objects collapsed first due to gravitational instabilities and merged forming bigger and bigger systems ("bottom-up" formation), the so called dark-matter halos. The gas in these halos then condensed and formed stars, creating the galaxies (e.g. Press & Schechter 1974, Toomre & Toomre 1972, Toomre 1977, White & Negroponte 1982, Primack & Blumenthal 1984, Blumenthal et al. 1984, Frenk et al. 1988, White & Frenk 1991, Kauffmann 1996, Somerville & Primack 1999). Therefore, massive early-type galaxies would be formed by mergers of disks at relatively recent times. This

scenario is favoured by the semi-analytical models (e.g. Cole 1991, Lacey & Cole 1993, Kauffmann, White & Guiderdoni 1993, Navarro, Frenk & White 1997, Kauffmann et al. 1999, Blanton et al. 2000, Cole et al. 2000, De Lucia et al. 2006) within the framework of the current standard ΛCDM cosmological model.

In this scenario, elliptical galaxies are redder (hence older or more metal rich) than spirals because the merging probability is higher at earlier epochs (Kauffmann & Charlot 1998). This implies that the stellar populations depend on the mass and environment (e.g. Bower et al. 1990, Guzman et al. 1992, Rose et al. 1994, Terlevich et al. 1999, Poggianti & van Gorkom 2001). The morphological evolution, known as Butcher-Oemler effect (Butcher & Oemler, 1978), shows that over cosmic time, the amount of spiral galaxies decreases at the same rate that S0 increase, while elliptical are found to be more or less constant in time (e.g. Couch et al. 1994, Dressler et al. 1994 Dressler et al. 1997, Oemler, Dressler & Butcher 1997, Smail et al. 1997, Couch et al. 1998). This could be explained by S0s being formed from the merging of spiral galaxies (e.g. Moore et al. 1996, Lubin, Postman & Oke 1998, Abadi, Moore & Bower 1999, van Dokkum et al. 1999). Moreover, this scenario can explain the possible migration of gas-rich blue cloud galaxies to the red sequence through a rapid evolutionary transition via merging and the subsequent quenching of their star formation (e.g. Faber et al. 2007 and references therein). In addition, the existence of structural features (such as shells, $\sim$20%) and gas in some ellipticals, which are indicatives of a recent interaction, further support this scenario (e.g. Schweizer 1982, Schweizer, Whitmore & Rubin 1983, Kormendy 1984, Barnes 2002, Serra et al. 2006).

However, these semi-analytical results may be in tension with a number of observations. For example, the presence of massive, red and passively evolving galaxies already assembled at high redshifts, the fact that most massive galaxies show mean luminosity-weighted ages larger than less massive ones (e.g. Caldwell, Rose & Concannon 2003, Kauffmann et al. 2003b, Carretero et al. 2004, Yamada et al. 2006), or the fact that less satellites are found than predicted by these models (Klypin et al. 1999, Kaviraj et al. 2009, Jackson et al. 2010, Nierenberg et al. 2011, Man et al. 2012, Newman et al. 2012, Mármol-Queraltó et al. 2012). Nonetheless, several of these observational constraints have been recently incorporated to the the semi-analytical models, which can now successfully reproduce the downsizing effect in star formation (e.g., De Lucia & Helmi 2008).

1.2   *Jurassic Park*: Early-Type Galaxies

Early-Type Galaxies (ETGs from now onwards), which comprise both elliptical and lenticular, contain the majority of the luminous matter in the Universe ($\sim$75 %, Renzini 2006). The classical picture was that present-day ETGs were a rather uniform, isothermal and structureless family, with a smooth intensity distribution. They were all thought to be composed of old stars that formed at high redshift and then aged passively, showing red colours and with little or no dust (e.g. Visvanathan & Sandage 1977, Tinsley 1978, Bower, Lucey & Ellis 1992, Renzini & Ciotti 1993, Ellis et al. 1997, van Dokkum et al. 1998). It was assumed that they were axially symmetric, with an isotropic distribution of velocities and that they increasingly flattened the more rapidly they rotated around their symmetry axis. They span a wide range of absolute luminosities (from $M_v=$ - 24 to $M_v=$ - 9), stellar masses (from $10^8 M_\odot$ to $10^{13} M_\odot$), sizes (from few kpc up to 200 kpc) and central velocity dispersions (from less than $100\,\mathrm{km\,s}^{-1}$ up to more than $400\,\mathrm{km\,s}^{-1}$).

1.2.1   Global Properties

ETGs are ideal laboratories to study the theories of galaxy formation and evolution proposed in Section 1.1 and have the power to constrain their cosmological implications through the analysis of their stellar populations. The principal observables in ETGs are summarized below.

Luminosity profile

This is one of ETGs crucial observable properties that permits to define the galaxy structure. ETGs show a pronounced maximum at the center followed by a rapid an uniform decrease to the outer parts, following a quasi power law. Classically, these profiles were represented by a de Vaucouleurs profile following the r$^{1/4}$ law (de Vaucouleurs, 1948):

$$log(I(r)/I_e) = -3.33[(r/r_e)^{1/4} - 1] \tag{1.1}$$

were I is the surface brightness at a given radius r, and r_e is the effective radius, which contains half of the total luminosity of the galaxy. However, the observed profiles are best fitted if we control their degree of curvature following the Sérsic law (Sérsic 1968, Graham & Colless 1997, Trujillo, Graham & Caon 2001, Trujillo et al. 2002):

$$I(r) = I_0\, exp[(r/r_0)^{1/n}] \tag{1.2}$$

where I_0 is the central surface brightness, and n is the parameter that shapes the profile's curve, also known as the Sérsic index. When $n=4$, this expression is

converted into the classical de Vaucouleurs law, while $n=1$ gives an exponential profile.

In fact, this Sérsic index is a good indicator of the morphology of the object. In the nearby Universe, galaxies with $n <2.5$ are normally disk-like objects while $n >2.5$ is indicative of spheroidals (e.g. Ravindranath et al. 2002, Shen et al. 2003, Barden et al. 2005, McIntosh et al. 2005).

Stellar kinematics

Despite the classical assumption of ETGs being oblate, axisymmetric rotating objects, a dichotomy on the kinematics of ETGs was found on the late 70s, when it became possible to extract the stellar kinematics of the bright galaxies (e.g. Bertola & Capaccioli 1975, Illingworth 1977, Binney 1978).

From one side, some ETGs show little or non rotation and kinematically decoupled components in their centers with boxy isophotes. These are usually the most massive objects, being redder, brighter and more metal-rich. They are generally classified as ellipticals, as they appear nearly round on the sky, renamed as slow-rotators. On the other hand, the other group of ETGs tend to present a well defined rotation pattern, with the rotation axis well aligned with the photometric minor axis and disky isophotes. They are typically less massive, bluer, fainter and usually appear very flat on the sky. For this reason, they are generally classified either as ellipticals or as lenticulars, renamed as fast-rotators (Davies et al. 1983, Binney 1985, Bender 1988, Davies & Birkinshaw 1988, Wagner, Bender & Moellenhoff 1988, Franx, Illingworth & de Zeeuw 1991, Kormendy & Bender 1996).

Nonetheless, recent works making use of larger and well defined samples of local ETGs with the ATLAS^{3D} survey have shown that the majority of ETGs are, in fact, fast rotators (Emsellem et al. 2011).

Scaling relations

The different global properties of ETGs (luminosity, colour, velocity dispersion, surface brightness and effective radius) have shown to strongly correlate.

- A very well known correlation is the *Colour-Magnitude Relation* (CMR), where the luminosity of a galaxy tightly correlates with its colour: redder galaxies are more luminous (e.g. Faber 1972, Faber 1973, Visvanathan & Sandage 1977, Bower, Lucey & Ellis 1992, Colless et al. 1999). This can be translated like more massive galaxies have more metal-rich stars, which is supported by the correlation of the line-strengths with velocity dispersion (e.g. Terlevich et al. 1981, Bender, Burstein & Faber 1993,

Colless et al. 1999). The origin of the CMR can be explained by the galactic winds theory (Arimoto & Yoshii, 1987), where more massive galaxies, with larger potential wells, are able to retain the enriched material from SN explosions, thus are more metal rich.

The CMR has been claimed to favour the monolithic collapse model (e.g. Kodama & Arimoto 1997, Kodama et al. 1998, Vazdekis et al. 2001a, Terlevich, Caldwell & Bower 2001, Yamada et al. 2006). It has been suggested that the tightness of this relation is the result of a conspiracy of age and metallicity, in the sense that there is an age-metallicity anticorrelation implying that more metal rich galaxies are younger (Trager et al. 1998, Ferreras, Charlot & Silk 1999, Trager et al. 2000b).

- When size, luminosity and velocity dispersion of ETGs are compared, they create a plane known as the Fundamental Plane (e.g. Dressler et al. 1987, Djorgovski & Davis 1987, Hudson et al. 2001, Bernardi et al. 2006). Projections of this plane create other relations such as the Faber-Jackson relation (Faber & Jackson, 1976) where more luminous galaxies have the higher velocity dispersions ($L \propto \sigma^4$). The origin of the relation between these three observable is not that surprising if ETGs are in Virial equilibrium, where its velocity dispersion is defined as $\sigma_{vir} \propto (L/2)/R_{vir}^2$ and the virial estimates are linear converted into σ and r_e.

  However, several problems are still to be faced. From one side, the observed FP presents an inclination with respect to the predicted one, known as the tilt of the FP (e.g. Faber et al. 1987, Prugniel & Simien 1996, Pahre, Djorgovski & De Carvalho 2001, Trujillo, Burkert & Bell 2004, Falcón-Barroso et al. 2011b, Cappellari et al. 2012b). From the other side, systematic differences on the zero-point and in the dispersion of the relation are found for galaxies at different environments and different redshifts (e.g. Larson, Tinsley & Caldwell 1980, Guzman et al. 1992, Franx 1995, Jørgensen, Franx & Kjaergaard 1996, Vogt et al. 1996, Ziegler & Bender 1997, van Dokkum et al. 1998, Jørgensen et al. 1999, Treu et al. 1999, Bernardi et al. 2003, van Dokkum & Ellis 2003, Yi et al. 2005, Bernardi et al. 2006, La Barbera et al. 2010b).

- The stellar populations and dynamical properties are connected through the scaling relation Mg-σ, which presents a remarkable small scatter (e.g. Burstein et al. 1988, Guzman et al. 1992, Bender, Burstein & Faber 1993, Jørgensen 1999, Colless et al. 1999, Kuntschner 2000, Trager et al. 2000a, Ziegler et al. 2001). As it is distance-independent, it is useful to constrain the models of formation and to test environmental variations in the FP (i.e. variations on the M/L would be produced solely by the different

star formation histories related with the environment; e.g. Burstein et al. 1988, Bender, Ziegler & Bruzual 1996). In addition, correlations of the α-enhancement with velocity dispersion imply that high σ galaxies were formed in shorter timescales (Sánchez-Blázquez et al. 2003, Carretero et al. 2004, de La Rosa et al. 2011).

1.2.2   Nature *vs* Nurture

It is known that ETGs do not behave the same way in all the environments, but at the same time, it seems that ETGs of different masses residing in the same environment also show different patterns. Then, a key question arises: which is the mechanism that drives galaxy evolution? Do galaxies evolve because of the influence of the environment they reside in (nurture) or is something intrinsic of the galaxy (nature)?

This has been for decades largely debated, studying mainly the differences on the stellar populations between dense (or cluster) and low-density (or field) environments (e.g. Dressler et al. 1997, Oemler, Dressler & Butcher 1997, Dressler 1980, Kauffmann, Charlot & White 1996, Kuntschner & Davies 1998, Couch et al. 1998, Trager et al. 2000a, Caldwell, Rose & Concannon 2003, Treu 2002, van Dokkum & Ellis 2003, Bernardi et al. 2003, Sánchez-Blázquez et al. 2003, Carretero et al. 2004, Denicoló et al. 2005, Thomas et al. 2005, Sánchez-Blázquez et al. 2006a, Gobat et al. 2008, Rettura et al. 2010). It seems that massive ETGs in low-density environments are on average $\sim$2 Gyr younger and slightly more metal rich than their analogues in the high-density environment. Getting into smaller scales, the local density or location within the clusters seems to play an important role too (e.g. Braglia et al. 2009, Demarco et al. 2010, Vulcani et al. 2012).

However, a consensus is not reached in this topic, as some other authors find no environmental differences, claiming that what drives galaxy evolution is the mass of the galaxy (or the morphological type, to some extent; e.g. Bernardi et al. 1998, Treu et al. 1999, Treu et al. 2001, Poggianti & van Gorkom 2001, van der Wel et al. 2004, Blanton et al. 2005a, van der Wel et al. 2005, Ferreras et al. 2006, Poggianti et al. 2006, Disney et al. 2008, Ferreras et al. 2010, Thomas et al. 2010, Vulcani et al. 2010, Harrison et al. 2011). Figure 1.2 summarizes both the impact of the environment and of the mass: the most massive galaxies are formed faster than low-mass ones, while galaxies in high-density regions are formed before those of same mass in low-density environs (Thomas et al., 2005).
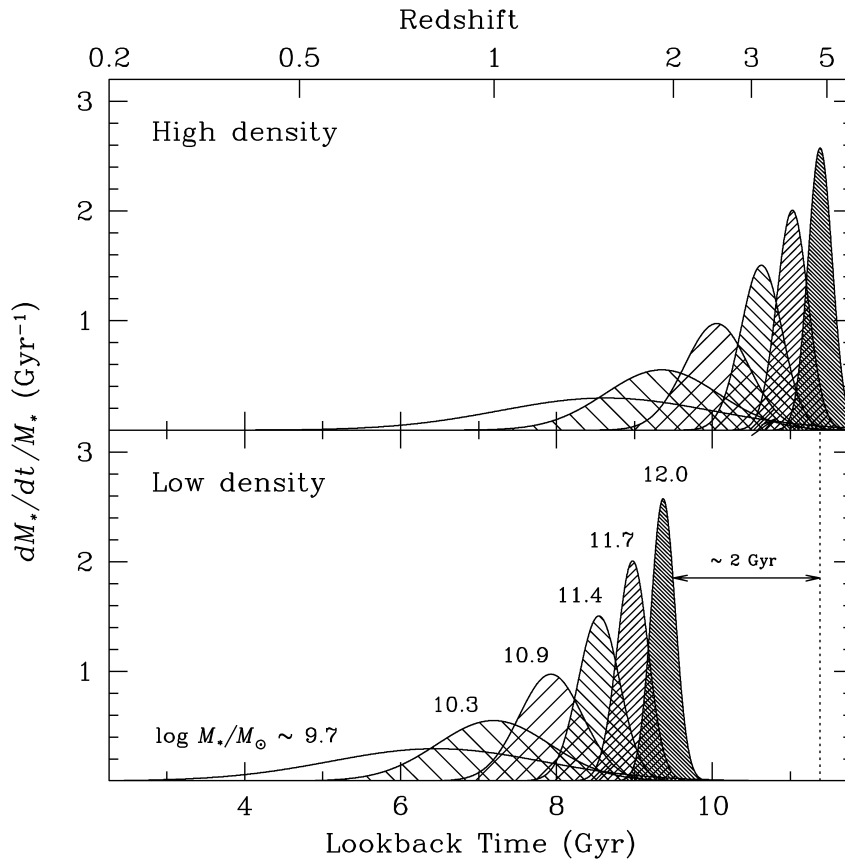
FIGURE 1.2— Star formation histories of ETGs as seen in figure 10 of Thomas et al. (2005). They are presented as a function of their stellar mass and show the dependence in mass and environment. Figure from Thomas et al. (2005).

1.2.3   Clues from the stellar populations

We have seen that the study of the stellar content of a galaxy is a key-piece to understand the puzzle of galaxy formation and evolution, as it traces back all the processes that took place during the galaxy lifetime, allowing to discriminate between different environments. Baade was the first to classify stars into populations back in the 1940 (Baade, 1940). He distinguished between two categories depending on different properties of their most luminous stars. Population I stars are blue, very hot, massive, young and metal rich, therefore with similar properties than the stars in the Galactic plane. On the contrary,

Population II stars are cool, red, giant, very old and metal-poor, like those in the globular clusters of the Milky Way. The Hubble sequence was by that time thought to express a continuous variation in relative importance of these two populations. In this sense, elliptical galaxies were formed only by PopII stars.

As every star has a specific colour associated with its spectral type, colour-magnitude diagrams are a powerful tool to study the galaxy evolution. In fact, a significant bimodality in the colour distribution is seen, where galaxies are clearly separated in a "red-sequence" (with mostly red, non-star forming ellipticals) and a "blue cloud" (mostly star-forming blue spirals). In between, there is the rather unpopulated region, the "green valley", which contains red spirals and blue ellipticals (e.g. Strateva et al. 2001, Bell et al. 2003, Hogg et al. 2003).

But stars can be counted and resolved only in our own Galaxy and in other few from the Local Group. Thus, the general approach is to study the unresolved light coming from the contribution of the different populations from integrated spectra. This can be predicted with the approach of the *population synthesis models*. These models, defined over different wavelength ranges, can be either based on purely theoretical stellar spectra (e.g. Schiavon & Faber 2000, González Delgado et al. 2005, Coelho et al. 2007) or from empirical data of a well-defined sample of stars (e.g. Vazdekis 1999, Bruzual & Charlot 2003, Vazdekis et al. 2003, Maraston 2005, Schiavon 2007, Conroy, Gunn & White 2009, Conroy & Gunn 2010, Vazdekis et al. 2010, Maraston & Strömbäck 2011, Conroy & van Dokkum 2012a). Three large spectral libraries of stars are widely used, which cover a great range of atmospheric parameters: ELODIE (Prugniel & Soubiran 2001), Indo-US (Valdes et al. 2004), and MILES (Sánchez-Blázquez et al. 2006c).

Population synthesis models are also classified in empirical and evolutionary synthesis models. The first, try to match the observed colours in galaxies with the integrated colours of a combination of stars (e.g. Tinsley 1980a, O'Connell 1986). For the second models, a complete evolution of the system until the actual time is predicted (e.g. Tinsley & Gunn 1976, Tinsley 1978, Bruzual 1981, Arimoto & Yoshii 1987, Guiderdoni & Rocca-Volmerange 1987, Worthey 1994, Bressan & Tautvaisiene 1996, Vazdekis et al. 1996, Vazdekis 1999, Bruzual & Charlot 2003, Vazdekis et al. 2010). These models need more initial conditions to be constrained than the empirical ones, such as the initial mass function (IMF), the set of stellar evolutionary isochrones, the stellar spectral library or the star formation rate (SFR), which depend on each model prescriptions.

Although all these models constitute a step forward for the understanding of composite spectra, a few considerations should be taken into account. First, it

is assumed that *all* the stars were formed in a single event, hence with a unique metallicity and age. Thus, if the galaxy was formed from different bursts of star formation, the mean estimates (e.g. age and metallicity) will be biased towards the youngest burst, which dominates in light. Second, the modeling itself is difficult and not completely constrained, as a myriad of aspects related to the evolution of the stars used to create the isochrones are not well understood (e.g. latter stages of stellar evolution), and due to the limited coverage of very metallic and metal-poor stars in the solar neighborhood in the spectral libraries.

In addition, the first works using the population synthesis models showed that a degeneracy on the age and metallicity was present and difficult to overcome with the models alone (O'Connell 1986, Renzini & Buzzoni 1986, Worthey et al. 1994, Arimoto, Sofue & Tsujimoto 1996, Puzia et al. 2002). This degeneracy makes that a change in metallicity by a factor of 2 renders similar variations in the colours and spectral features than a change in the age of a factor of 3 (known as the 3/2 rule; Worthey et al. 1994). This degeneracy can be partially broken by studying certain spectral indices (absorption features on the galaxy spectra) that are sensitive to variations in age or metallicity, known as the index-index diagrams (see section 2.4 for a further description of this topic).

Furthermore, it is is known that some elements such as Mg, N, Na, Si, Ne, S, C and O present in elliptical galaxies are enhanced with respect to Fe (e.g. Spinrad & Taylor 1971, O'Connell 1976, Peterson 1976, Peletier 1989, Worthey, Faber & Gonzalez 1992, Davies, Sadler & Peletier 1993, Worthey et al. 1994, Kuntschner et al. 2001, Thomas, Maraston & Bender 2003). This creates an overabundance or α-enhancement of these elements (although some authors claim that the Fe is the one depressed with respect to the solar values; Vazdekis et al. 1997, Trager et al. 2000b). Models can barely predict these overabundances or their impact on the derived ages and metallicities (e.g. Chaboyer, Sarajedini & Demarque 1992, Salaris, Chieffi & Straniero 1993, Tripicco & Bell 1995, Salaris & Weiss 1998, Tantalo, Chiosi & Bressan 1998, Trager et al. 2000b, Thomas, Maraston & Bender 2003, Korn, Maraston & Thomas 2005, Lee & Worthey 2005). However, these overabundances are useful chemical clocks, as each element is produced at different timescales (e.g. Bender, Ziegler & Bruzual 1996, Worthey 1998, Kuntschner et al. 2002, Sánchez-Blázquez et al. 2003, Carretero et al. 2004, Thomas et al. 2005, Bernardi et al. 2006, Schiavon 2010).

1.3 *The flight of the Phoenix*: The puzzle of massive galaxies

All the properties of ETGs studied in the previous sections present them as a rather uniform, well constrained family. For a long time, they were though to

be "boring" objects, in the sense that they were old, passive evolving objects. However, with the advent of bigger telescopes and by pushing their capabilities to the limits to reach the high redshift Universe, elliptical galaxies are back in the game as they have shown to be much interesting than assumed.

This is the case for the most massive ones ($M_* \geq 10^{11} \, M_\odot$), which turned out to be truly exciting objects and the center of many scientific debates for the past years, as there is not yet a consensus in the community about some of their properties. Recent works have shown that massive galaxies at high redshift were much more compact than their equally massive present-day counterparts, by a factor of ~ 4 at z$\sim$2 (e.g. Daddi et al. 2005, Trujillo et al. 2006, Longhetti et al. 2007, Trujillo et al. 2007, Toft et al. 2007, Zirm et al. 2007, Cimatti et al. 2008, Buitrago et al. 2008, Cassata et al. 2011, McLure et al. 2012, Huertas-Company et al. 2012). On the contrary, these objects suffer a milder evolution of their stellar mass (by a factor of 2 since z$\sim$2; e.g. Cenarro & Trujillo 2009, Cappellari et al. 2009, Newman et al. 2010, Onodera et al. 2010, van Dokkum & Conroy 2010, van de Sande et al. 2011, Toft et al. 2012).

Obviously, the first approach was to assume that these estimates were incorrect, as many systematic effects can contaminate the measurements (see e.g. van Dokkum et al. 2008, Bezanson et al. 2009, Muzzin et al. 2009, Mancini et al. 2010). However, several works have proved their robustness from both ultra-deep images and good dynamical mass estimates (e.g Cenarro & Trujillo 2009, Cappellari et al. 2009, Carrasco, Conselice & Trujillo 2010, Cassata et al. 2010). It is worth to note recent works that claim that this mas-size evolution is in fact, due to a progenitor bias (e.g. Newman et al. 2012, Carollo et al. 2013, Cassata et al. 2013). These authors claim that the growth of the size of the quiescent ETG population is driven by the appearance of larger quiescent ETGs at later epochs.

Apart from this size evolution with cosmic time, a strong morphological evolution has occurred for the most massive galaxies. We see that the most common morphology in high-z massive galaxies are disky-shapes, resembling S0s, while for present-day massive galaxies, the morphology that dominates is the spheroidal (e.g. Buitrago et al. 2008, van der Wel et al. 2008, Oesch et al. 2010, Cameron et al. 2011, van der Wel et al. 2011, Law et al. 2012, Buitrago et al. 2013).

Therefore, it is mandatory to address two key questions for these galaxies: how were the high-z galaxies formed and how have these high-z massive compact galaxies evolved into the present-day massive population. These questions are hard to answer by considering only a hierarchical or a monolithic scenario. In

fact, it is now thought that the formation of these objects occurred first in a fast, monolithic-like phase at $3<z<6$ dominated by a dissipational in-situ star formation fed by cold flows (e.g. Kereš et al. 2005, Dekel et al. 2009, Oser et al. 2010) and/or gas rich mergers (e.g. Ricciardelli et al. 2010, Wuyts et al. 2010, Bournaud et al. 2011). At the end of this phase, massive galaxies are expected to be flatter and with shapes more disky than their lower redshift massive counterparts. After this formation phase, several scenarios are proposed to explain the subsequent evolution:

- *Major mergers*: this scenario was the first one to be suggested (Ciotti & van Albada 2001, Boylan-Kolchin, Ma & Quataert 2006, Naab et al. 2007) but was quickly dismissed by the observations (e.g. Bundy et al. 2009, Bluck et al. 2009, de Ravel et al. 2009, López-Sanjuan et al. 2009, Wild et al. 2009). It was seen that there was not enough major mergers to account for the strong size evolution and at the same time the mild evolution in stellar mass.

- *Puffing up*: this scenario predicts that the size evolution can occur without suffering any merging (e.g. Fan et al. 2008, Damjanov et al. 2009, Fan et al. 2010). In it, the AGN feedback is the responsible for removing huge amounts of cold gas from the central regions, quenching the star formation and puffing-up the galaxy. However, this has to occur in very short timescales ($< 1\,\mathrm{Gyr}$; Ragone-Figueroa & Granato 2011) causing only a few systems to be caught as quiescent and still compact, and it also produces a dichotomy on the ages, which is not seen in observations.

- *Minor mergers*: this scenario is currently the most accepted and tested. It suggests that the size evolution has occurred due to the continuous accretion of minor bodies that locate the accreted material in the periphery of the central galaxy (Khochfar & Silk 2006, Maller et al. 2006, Naab, Khochfar & Burkert 2006, Hopkins et al. 2009b, Naab, Johansson & Ostriker 2009, Conselice, Yang & Bluck 2009, Bluck et al. 2009, Sommer-Larsen & Toft 2010, Oser et al. 2010, Wuyts et al. 2010, López-Sanjuan et al. 2012, Quilis & Trujillo 2012).
  This scenario reproduces well the three main observational evidences: *(i)* the continuous increase in size due to the progressive build up in the external parts (e.g. Bezanson et al. 2009, Hopkins et al. 2009b, van Dokkum & Conroy 2010); *(ii)* the mild velocity dispersion evolution (e.g. Cenarro & Trujillo 2009) and *(iii)* a size growth that is not related with the age of the main galaxy (e.g. Trujillo, Ferreras & de La Rosa 2011).
  However, two observational evidences are difficult to explain within this

scenario. From one side, the lack of satellites surrounding the massive galaxies. An excess of a factor of ~ 2 of satellites compared to observations is found in semi-analytical models (Quilis & Trujillo, 2012). From the other side, the scarce presence of compact massive galaxies in the nearby universe. This latter puzzle is described below in more detail.

1.3.1   Local compact massive galaxies

Do compact massive galaxies exist in the local Universe? If so, are they the true relics of the high redshift massive galaxies? Their existence has been another issue of debate. As minor mergers is a process of stochastic nature, a few ($\sim 10\%$) of the high-z massive galaxies should have survived untouched until the present. This means that, in order to be the relics of the high-z galaxies, these local objects should be old (Hopkins et al., 2009b).
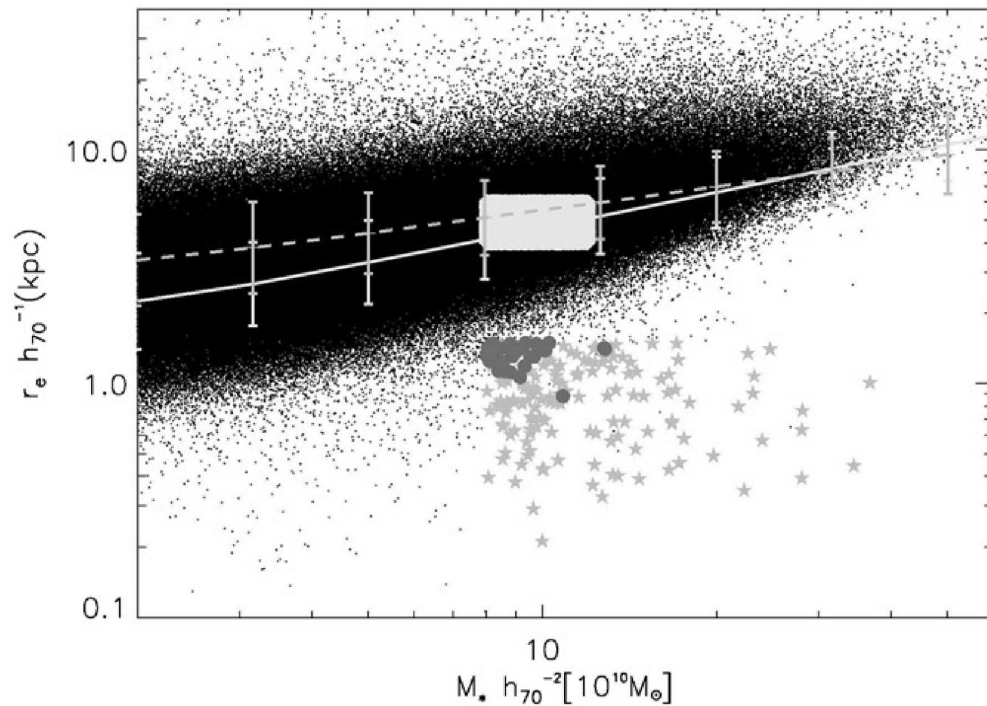
FIGURE 1.3— Stellar mass-size distribution of galaxies from the NYU Value-Added Galaxy Catalog (Blanton et al 2005) in the SDSS DR6 sample. T09 compact galaxies are shown with circles. The stars are sources that were classified as QSOs. Following Shen et al. (2003), overplotted are the mean and dispersion of the distribution of the Sérsic half-light radius of SDSS early-type ($n>2.5$; solid line) and late-type ($n<2.5$; dashed line) galaxies as a function of stellar mass. The gray rectangular area shows the region used to extract the control sample galaxies. Figure from Trujillo et al. (2009)

Indeed, Trujillo et al. (2009) (T09 hereafter) were the first to find a sample of these superdense massive compact galaxies in the SDSS DR6 spectroscopic survey at z<0.2 (see Figure 1.3). Afterward, a significant fraction of compact massive galaxies in the SDSS at z∼0.1 were also found by Taylor et al. (2010), followed by the discovery of massive compact objects in nearby galaxy clusters from the WINGS survey (Fasano et al. 2006, Valentinuzzi et al. 2010). More recently, Poggianti et al. (2013) have studied how their fractions and characteristics change with the environment in the PM2GC sample (Padova Millennium Galaxy and Group Catalogue; Calvi, Poggianti & Vulcani 2011).

The first problem arises from the fact that the numbers in the local universe are very low. Except for Valentinuzzi et al. (2010), with 122 objects (22% of all cluster members), local compact massive galaxies do not reach the predicted values from the theory. The fraction of compact massive galaxies is the ∼0.03% of the SDSS sample up to $z = 0.2$ in T09 (48 objects), ∼1.3% (63 objects) in Taylor et al. (2009) sample, and ∼4% (44 galaxies) in Poggianti et al. (2013). In addition, this variations between field and cluster seem to indicate a strong environmental dependence of the distribution of massive and compact galaxies in the local Universe. It is important to highlight that the above candidates are not seen in common among the different works. This is due to the selection criteria used in each one, which do not coincide. For example, all T09 galaxies are found within a redshift range of 0.1<z<0.2, while the other works are usually limited to z∼0.1. The cuts in stellar mass and galaxy size also vary, therefore, a direct comparison between these works is not straightforward.

A first approach analyzing the modest-quality SDSS spectra for 29 of these objects in T09 showed that they had large velocity dispersions ($\sim 230 \, \mathrm{km \, s^{-1}}$), small effective radii ($\leq 1.5 \, \mathrm{kpc}$) and young stellar populations ($\sim 2 \, \mathrm{Gyr}$) (Trujillo et al. 2009). This last result is in contradiction with the idea that these objects are the relics from the high-z Universe. Unfortunately the modest quality of the SDSS spectra did not allow them to perform a more detailed study of their stellar populations (e.g. gradients, star formation histories). However, these findings are not supported by the works on the other local samples, where older mean ages are found, hence claiming that they could indeed be the descendants of the high-z massive galaxies.

The paucity and the not well understood properties of local compact massive galaxies demonstrate the need to fully characterize these intriguing objects, not only to understand their formation, but also to understand the formation and evolution of their high-z compact analogues, to assess whether these can be the progenitors of massive ellipticals.

1.4   *The Colossus*: Galaxy clusters

The battle of nature *vs* nurture could pose strong constrains on the different scenarios proposed. Hierarchical models of galaxy formation predict that galaxies in the highest density peaks started forming stars and assembling their mass earlier. Equivalently, galaxies in high-density environments will form earlier because the star formation is accelerated (e.g. Baugh, Cole & Frenk 1996, Kauffmann, Charlot & White 1996).

Galaxy cluster are considered high density regions, formed by thousands of galaxies, therefore are the right place to look for ETGs, particularly the challenging massive ones. Galaxy clusters are excellent laboratories to study this family of objects and the physical mechanisms by which a galaxy can transform (either its morphology and its global properties) by analyzing them at different epochs of the Universe. Some of the processes in clusters proposed to drive galaxy evolution, eventually truncating their star-formation and strongly affecting their morphologies are:

- *Galaxy-galaxy interactions*: or galaxy mergers. They are considered rare in the cluster environment due to the large velocity dispersion of the systems, but are efficient in the infalling group environment (e.g. Toomre & Toomre 1972, Toomre 1977, Hausman & Ostriker 1978, White 1978, Barnes & Hernquist 1996, Dressler et al. 1994, Bekki 1999, De Lucia et al. 2006, Hopkins et al. 2008, De Lucia et al. 2010).

- *Gas stripping*: the cold gas can be swept out of the stellar disk of galaxies in dense intra-cluster regions by strong ram-pressure stripping (e.g. Gunn & Gott 1972, Faber & Gallagher 1976). It is supposed to be more effective at the center of massive systems (Brüggen & De Lucia, 2008). However, this process is not included in semi-analytical models because it causes only mild variations on the stellar populations.

- *Strangulation*: this occurs to galaxies that fall onto larger systems, where the cold gas is rapidly consumed as the hot gas halo of the infalling galaxy is removed, moving the galaxy onto the red-sequence (e.g. Larson, Tinsley & Caldwell 1980, Abadi, Moore & Bower 1999, Balogh, Navarro & Morris 2000, Diaferio et al. 2001, Bekki, Couch & Shioya 2002, McCarthy et al. 2008).

- *Harassment*: Repeated fast encounters together with the effects of the global tidal field of the cluster can drive a strong evolution (e.g. Moore et al. 1996, Moore et al. 1999). However, this is not usually included in semi-analytical models because its efficiency is limited to low-luminosity

objects, therefore has only impact on shaping dwarf ellipticals (e.g. Mastropietro et al. 2005, D'Onghia et al. 2009).

- *AGN heating*: it is considered to suppress the cooling flows at the center of massive halos (White & Rees, 1978). However, it is not yet well understood how and when AGN feedback is important (Fontanot et al., 2011).

1.4.1 Evolution over cosmic time

For a long time, the only way to test the formation processes was through observations of the Local Universe. However, with the advent of large-aperture ground-based and modern spatial telescopes, we have reached the era of unraveling the early-epochs of the Universe. Considerable observational efforts have been made to trace the evolution of the global properties of ETGs in galaxy clusters and field over cosmic time. However, not that much is known in detail about their properties beyond z∼1, as very few stellar population works have been conducted there.

The general approach to test the evolution is to assume a redshift of formation (z_f) for the epoch at which ETGs were formed. Then, it is assumed to evolve only through the evolution of its stellar populations and finally it is compared to present-day observations. Therefore, combining the local and the high redshift data is the most powerful tool to constrain the predicted scenarios.

The most relevant properties of ETGs and how they evolve through cosmic time (mainly up to z∼1) are summarized here:

- *The CMR*: it has been assessed that the evolution of colours with redshift is generally slow and that the CMR keeps its slope with redshift, with a recognizable red sequence already established at high-z (e.g. Bower, Lucey & Ellis 1992, Aragon-Salamanca et al. 1993, Stanford, Eisenhardt & Dickinson 1995, Kodama & Arimoto 1997, Ellis et al. 1997, Kodama et al. 1998, Kodama & Bower 2001, van Dokkum & Franx 2001, Blakeslee et al. 2003, Bell et al. 2004, De Lucia et al. 2007, Faber et al. 2007). However, it should be mentioned that this tightness up to high-z could be due to the "progenitor bias" (van Dokkum & Franx, 2001). This warns about the fact that some of the progenitors at z∼1 might not have yet been formed or accreted, therefore this is an artifact from a selection bias.

- *The FP*: the evolution of the FP can be linked to the evolution of the mass-to-light ratio of ETGs and therefore, with the star formation history (e.g.

Franx 1993, van Dokkum & Franx 1996, Kelson et al. 1997, Bender et al. 1998, van Dokkum et al. 1998, Jørgensen 1999, Kelson et al. 2000, Wuyts et al. 2004, Holden et al. 2005). It is seen that the FP does not change at least up to z∼1 (van Dokkum & Stanford, 2003), with a slow evolution of the M/L ratio, which is compatible with the passive evolution of the stellar populations formed at high-z.

- *Index-sigma*: the study of the line strengths with velocity dispersion up to z∼1 indicate that passive evolution is a plausible scenario (e.g. Bender, Ziegler & Bruzual 1996, Ziegler & Bender 1997, Barbaro & Poggianti 1997, Kelson et al. 2001, Jørgensen et al. 2005, Sánchez-Blázquez et al. 2009, Jørgensen & Chiboucas 2013).

- *Morphology*: The fraction of ETGs decreases considerably with increasing redshift, while the fraction of spirals increases correspondingly, as seen in the left panel of Figure 1.3 (e.g. Oemler, Dressler & Butcher 1997, Dressler et al. 1997, Fasano et al. 2000, van Dokkum & Franx 2001, Lubin, Oke & Postman 2002, van der Wel et al. 2011, Buitrago et al. 2013). This implies that a more complex star formation history than a single burst has occurred, going against the monolithic case. Several works have shown that both the size and the morphological evolution are intimately related, as seen in the right panel of Figure 1.3.

- *Size*: We have already shown in Sect. 1.3 that the most massive galaxies in the high-z Universe (z∼2, $M_* \geq 10^{11}\,M_\odot$) were more compact (a factor of ∼4 at z > 1.5) than their equally massive local counterparts (Daddi et al. 2005, Trujillo et al. 2006, Trujillo et al. 2007, Toft et al. 2007, Buitrago et al. 2008, McLure et al. 2012). However, the mass-size relation is already in place since z∼3 (Trujillo et al. 2007, Buitrago et al. 2008), as seen in the upper panel of Figure 1.4.

- *Luminosity function*: this can be translated into number density and it is seen to remain unchanged over time up to z∼1, compatible with passive evolution and a high redshift of formation (e.g. Moustakas et al. 1997, Menanteau et al. 1999, de Propris et al. 1999, Treu et al. 1999, Daddi et al. 2000, McCarthy et al. 2001, Kodama & Bower 2001, Poggianti & van Gorkom 2001, Barrientos & Lilly 2003, Toft, Soucail & Hjorth 2003, De Lucia et al. 2004, Kodama et al. 2004, Rudnick et al. 2008).

- *Mass function*: There is no significant evolution up to z∼0.8. This remains true for the massive end of the stellar mass function up to z ∼ 1.5 (e.g. Pozzetti et al. 2003, Rudnick et al. 2003, Conselice, Blackburne &

Papovich 2005, Drory et al. 2005, Fontana 2005, Bundy et al. 2006, Pérez-González et al. 2008, Mortlock et al. 2011, Conselice et al. 2011). Going up to earlier epochs, differences appear all along the stellar mass range, as can be seen in the lower panel of Figure 1.4.

- *Mass density profiles*: this observable gives an independent M/L and also tests the existence of universal dark matter profiles through galaxy lensing. It has shown the evidence of extended dark matter haloes and a lack of dynamical evolution out to z∼1 (e.g. Treu & Koopmans 2004, Koopmans et al. 2006, Treu et al. 2006, Gavazzi et al. 2007, Bolton et al. 2008, Auger et al. 2010a).

- *Downsizing*: Many of these properties support the idea of the "downsizing" (Cowie et al., 1996), for which the most massive galaxies are the oldest and reddest, while less massive are younger or present an extended star formation history (e.g. Kauffmann et al. 2003b, Kodama et al. 2004, Treu et al. 2005, van der Wel et al. 2005, Bundy et al. 2006, Sánchez-Blázquez et al. 2009). It varies with redshift and with environment (Tanaka et al., 2005) in the sense that star formation is truncated from high-mass systems in high-density environments to low-mass systems in low density regions.
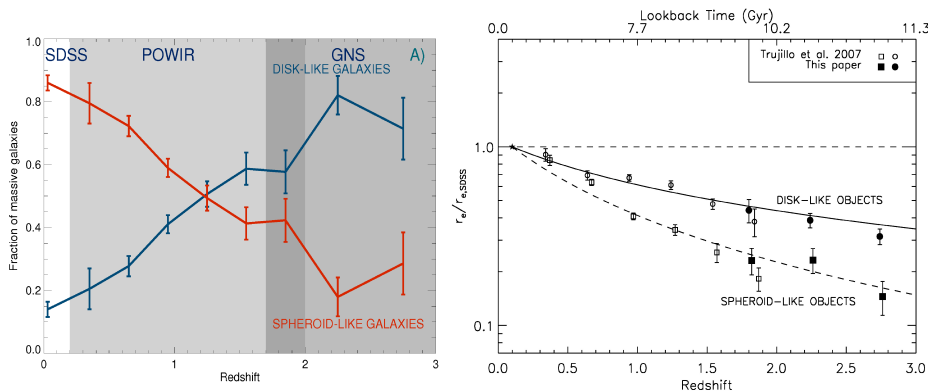
FIGURE 1.4— *Left panel*: Fraction of early and late type galaxies (selected by their Sérsic index) and its evolution with redshift. Figure taken from Buitrago et al. (2011). *Right panel*: Size evolution of massive galaxies over cosmic time. It shows the ratio of the median sizes of galaxies in Trujillo et al. (2007) and Buitrago et al. (2008) sample with respect to the sizes of nearby galaxies in the SDSS local comparison. Figure from Buitrago et al. (2008).
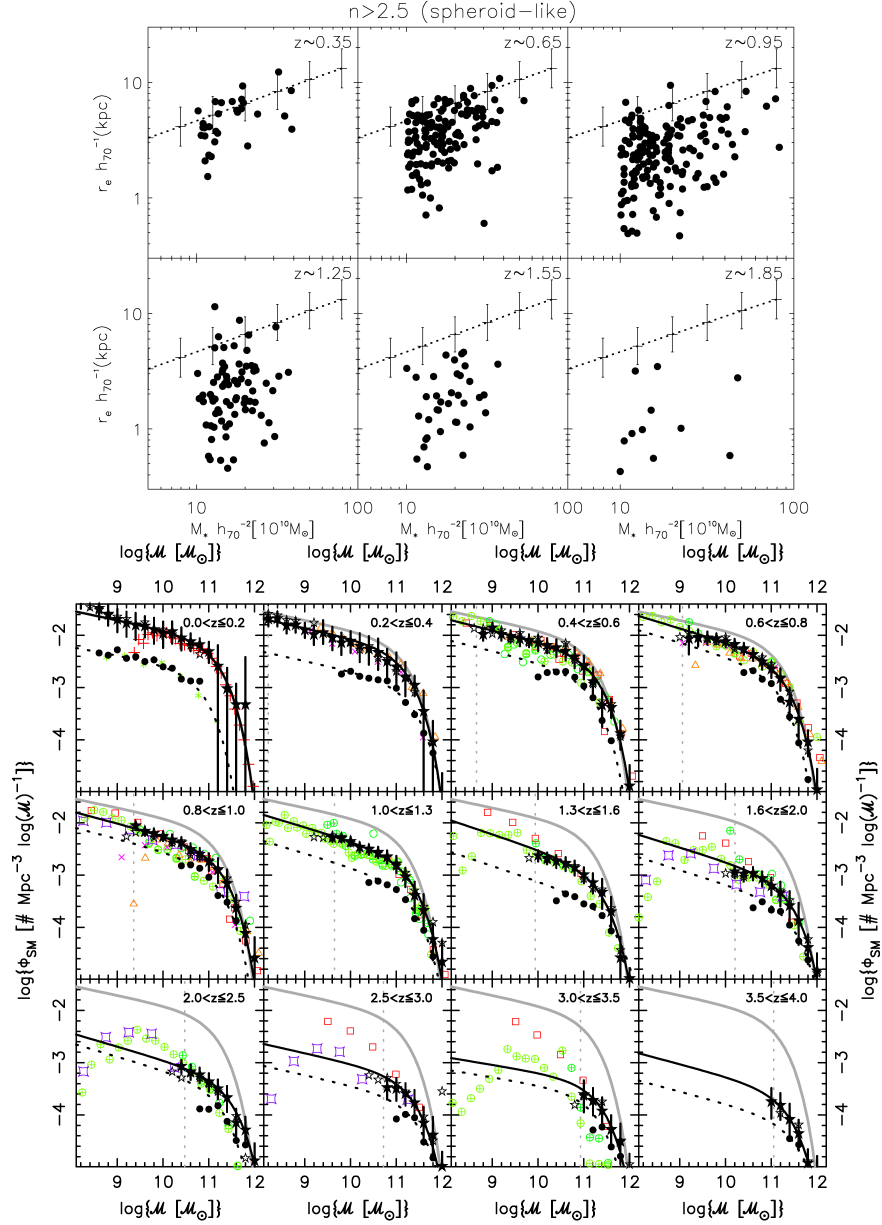
FIGURE 1.5— *Upper panel*: Stellar mass-size distribution of spheroid-like ACS galaxies from Trujillo et al. (2007). Overplotted are the mean and dispersion of the distribution of the Sérsic half-light radius of SDSS ETGs as a function of stellar mass. Figure from Trujillo et al. (2007). *Lower panel*: Stellar mass functions (SMF) up to z=4, divided in 12 redshift intervals. Stars (either filled and open) are the SMF estimations fitted with a Schechter function (solid black line). The local SMF from Cole et al. (2001) is shown with a gray curve. Figure taken from Pérez-González et al. (2008).

1.5 *The NeverEnding Story*: The overall picture

From the evolution in the properties and what has been treated so far, the overall picture for the formation and evolution of ETGs is the following: massive ellipticals in high density regions resemble single-burst old objects, compatible with a formation redshift for the bulk of the stars at earlier epochs ($z_f \sim 3$), therefore, they are already assembled at $z \sim 1$. However, low-mass and low density environment elliptical galaxies are on average $\sim$1-2 Gyr younger, presenting more complex star formation histories. These can be either due to a secondary burst of star formation, known as "frosting" of younger stars, or by a "rejuvenation" of the galaxy due to a more extended star formation history (e.g. Trager et al. 2000a, Kuntschner et al. 2002, Ellis, Abraham & Dickinson 2001, Kaban, Nolan & Raychaudhury 2005, Kaviraj et al. 2005, Thomas et al. 2005, Yi et al. 2005, Ferreras et al. 2006). Regarding to the metal content, as the bulk of star formation took place at high redshift, most cluster metals should have already been produced and disseminated by that time, hence little evolution on the composition of the intracluster medium is expected.

This is all well fitted within the downsizing scenario because this is an implication of a spatial bias in galaxy formation: massive galaxies were formed earlier because they were formed from higher density peaks at high-z, accelerating their star formation, while low-mass galaxies started with a delay because they formed from lower density peaks. Therefore, the mechanism that decides the fate of ETGS seems to be a mixture of environment and mass. However, many observables that do not match the predictions from the competing models prevent us to close this chapter, hence further exploration and digging needs to be performed.

1.6 *Playing God*: Variations on the Initial Mass Function

Stellar population studies can lead to different results for the same data depending on the choice of e.g. the models, the cosmology adopted, the wavelength range, the selection limits, the use of spectroscopy *vs* photometry, etc. For some of them, the user can freely choose, while others are assumed to be universal.

1.6.1 Being universal

This is the case of the Initial Mass Function (IMF), the distribution of stellar masses in a single population of stars at the time of birth. This IMF is an hypothetical property, but the existence of a unique distribution of stars can be tested by observing several systems with the same number of N stars (e.g. Elmegreen 1997, Massey 2003). Then a universal, standard or canonical stellar IMF is assumed for all the stellar populations.

The IMF determines the baryonic content, the chemical enrichment, the kinematic feedback into the ISM and in general, it governs to some extent galaxy formation and evolution. It was first introduced by Salpeter (1955), presenting a power law IMF with the form:

$$\Phi(logm) = dN/dlogm \propto m^{-\Gamma} \tag{1.3}$$

where m is the mass of a star, N the number of stars in the mass range ($logm + dlogm$) and Γ the logarithmic slope of the IMF function. By integrating this function and normalizing it, the number of stars within a logarithmic mass interval is calculated. It can also be derived in linear mass units as:

$$\chi(m) = dN/dm \propto m^{-\alpha} \tag{1.4}$$

were $\alpha = \Gamma + 1$.
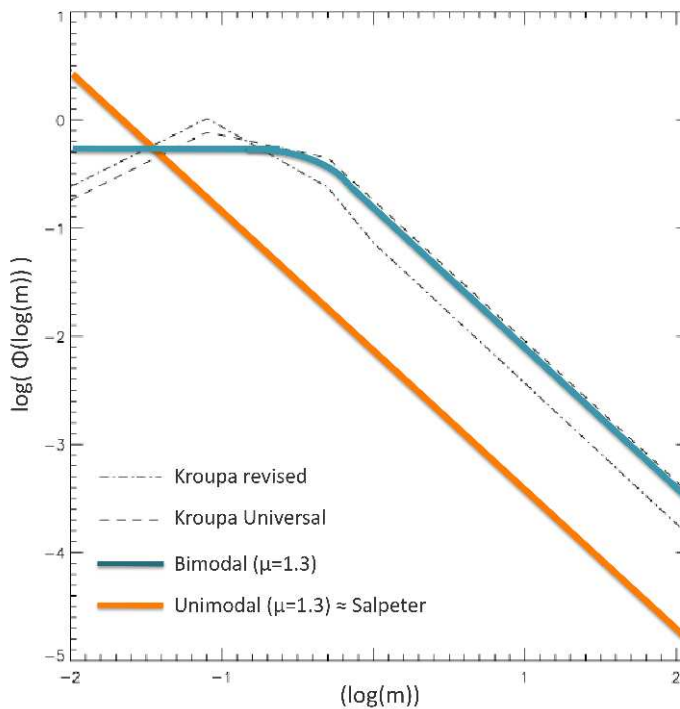
FIGURE 1.6— Schematic view of the canonical IMFs historically considered (Salpeter and Kroupa). The unimodal and bimodal are the nomenclature introduced in Vazdekis et al. (1996) and for both, the slope of the power-law is allowed to vary. Figure taken from Vazdekis et al. (2003).

During the following decades, it was seen that the IMF was not likely to follow a single power-law among all the stellar masses. Various alternative definitions emerged, such as a log-normal form (Miller & Scalo 1979, Scalo 1986), which was later revised by Chabrier (2003), or a multi-segmented power-law (Kroupa, Tout & Gilmore 1993, Kroupa 2001). They all have been regarded as standard IMFs. Therefore, IMFs that follow a single(segmented) power-law are named "Salpeter(Kroupa)-like IMFs" and, when $\Gamma \sim 1.35$ (or $\alpha = 2.35$), it is said that they have a "Salpeter logarithmic slope", as shown in Figure 1.6.

Determining the IMF is not trivial, as various parameters need to be considered to match the observations (Figure 1.7), such as the characteristic mass or the peak *(1)*, the variance *(2)*, and the mass break, mass slope and mass limit for both the high and the low mass regimes *(3, 4, 5, 6, 7, 8)*. In addition, these parameter need to be adequately modeled and be physically consistent.
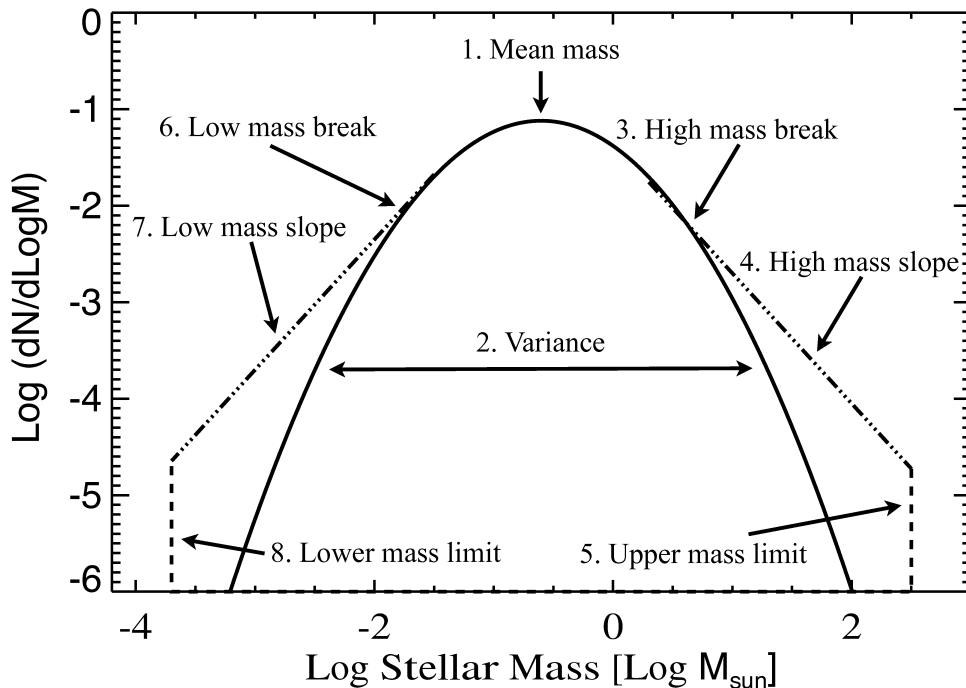
FIGURE 1.7— Summary of the different parameters determining the stellar IMF. All these parameters need to be adequately modeled and be physically consistent in order to reproduce the observations. Figure from Bastian, Covey & Meyer (2010).

The impact of each physical process on shaping the IMF is not yet completely understood (e.g. turbulence and the Core Mass Function (e.g. Padoan, Nordlund & Jones 1997, Padoan & Nordlund 2002, Hennebelle & Chabrier 2008, Hennebelle & Chabrier 2009, Offner, Hansen & Krumholz 2009); accretion (Adams & Fatuzzo 1996, Myers 2008, Myers 2009); triggered star formation (Whitworth et al. 1994, Elmegreen 1995, Bisbas et al. 2011); radiative feedback (Bate 2009b, Offner et al. 2009, Krumholz et al. 2009); fragmentation (Bate 2009a, Kratter et al. 2010, Oey 2011); the central limit theorem (Adams & Fatuzzo, 1996); magnetic fields (Hocuk et al., 2012); hydrodynamics, outflows, filaments).

Despite the different IMFs considered as standard, those IMFs have been assumed to be universal for a long time, this means that we consider the same IMF at all cosmic times, no matter the environment or the mass of the galaxy. This universal assumption was adopted mainly due to the difficulties at obtaining direct constrains. So far, the IMF can only be directly constrained from our own Milky Way by counting individual stars (Salpeter, 1955).

Many works have supported this universality, warning us about the consequences of freely varying it (see e.g. Gilmore 2001, Bastian, Covey & Meyer 2010, Greggio & Renzini 2012, Narayanan & Davé 2012). For example, an IMF with a steeper slope than Salpeter would probably fit better the near-infrared CaII triplet, but it would also produce too red V-K colours and too high M/L (e.g. Cenarro et al. 2003).

1.6.2   Being non-universal

Nonetheless, scenarios with a non-universal IMF have been discussed at length, starting with Schmidt (1963) and followed by Faber & Gallagher (1979), Tinsley (1980b), Worthey, Faber & Gonzalez (1992), Elbaz, Arnaud & Vangioni-Flam (1995), Vazdekis et al. (1996) or Vazdekis et al. (1997), among others. In fact, abundant recent observational evidence from a variety of independent techniques have pointed out that a non-universal IMF might be in fact the real case (Tortora, Romanowsky & Napolitano 2012 and references therein).

From the measurements of spectral features sensitive to the slope of the IMF in massive giant elliptical galaxies (e.g. CaII triplet, the Wing-Ford band and the NaI8200), it has been discovered the existence of a larger population of low-mass stars than predicted by a Kroupa or even a Salpeter IMF (e.g. Vazdekis et al. 2003, Cenarro et al. 2003, Falcón-Barroso et al. 2003, van Dokkum & Conroy 2010, Conroy & van Dokkum 2012a (CvD12 hereafter), Spiniello et al. 2012, van Dokkum & Conroy 2012, Conroy & van Dokkum 2012b). Colours are also highly sensitive to IMF variations, in the sense that redder galaxies have

bottom-heavier IMFs, i.e. steeper slopes (see e.g. Dutton, Mendel & Simard 2012, Pforr, Maraston & Tonini 2012, Ricciardelli et al. 2012, Vazdekis et al. 2012).

In addition, recent works have added strong evidence on the non-universality of the IMF by constraining the dark matter fraction in galaxies with gravitational lensing and dynamical studies. They find an IMF dependence with galaxy mass (e.g: Grillo et al. 2009, Auger et al. 2010b, Napolitano, Romanowsky & Tortora 2010, Treu et al. 2010, Barnabè et al. 2011, Thomas et al. 2011, Cappellari et al. 2012b, Dutton et al. 2012, Sonnenfeld et al. 2012 or Tortora, Romanowsky & Napolitano 2012). Moreover, in Ferreras et al. (2013) a tight correlation between the velocity dispersion of early-type galaxies and the IMF slope is shown, in the sense that higher velocity dispersion galaxies need steeper IMF slopes, while the low mass ones need flatter slopes. Cappellari et al. (2012a) have shown a similar result, where the use of different IMF slopes varies the amount of dark matter and implies a change in the dynamical masses by a factor of three in early-type galaxies.

As the IMF is a parameter that clearly influences most of the stellar population properties, its determination is crucial to understand the formation and evolution of galaxies. Most works in the field of the stellar populations are based on its assumed universality (e.g. Bender, Burstein & Faber 1992, Kuntschner & Davies 1998, Jørgensen 1999, Poggianti et al. 2001, Terlevich, Caldwell & Bower 2001, Blanton et al. 2003, Kauffmann et al. 2003b, Gallazzi et al. 2006). However, a number of still open questions could be addressed by changing the IMF according to the recent claims in this direction, giving some hints about the formation and evolution of the most massive galaxies.

1.7   *Caótica An(n)a*: Objectives in this Thesis

Motivated by the revival of the ETGs, the main objective of this thesis is to shed some light into the puzzling formation and evolution of these objects by analyzing in detail their stellar populations from different points of view.

In particular, we will focus on the most massive ones, which have shown to be very challenging objects. They were much more compact in the early Universe (z∼2) than the present-day massive galaxies. However, which mechanisms regulates this size evolution is not yet clearly understood and the proposed models predict the existence of untouched relics in the nearby Universe. Therefore, we first need to answer the question if the compact massive galaxies found in the nearby Universe are truly their descendants. If we are able to understand them, we may have the clue to unravel the processes governing the formation of the massive galaxies at high-z.

Second, by studying the stellar population properties of massive ETGs in galaxy clusters at different redshifts, we can infer how those have evolved through cosmic time and pose some constrains into the various scenarios of galaxy evolution.

Finally, motivated by the recent evidences pointing towards a variation of the Initial Mass Function (IMF) with galaxy velocity dispersion, we need to quantify the impact that assuming this non-universality would have on the derived galaxy properties.

The word "*detail*" in the title is the key and the novelty of this work. It implies an analysis on a galaxy per galaxy basis even at the highest redshift here considered, in contrast to previous works where the analysis was performed by stacking the spectra of several galaxies. As we focus on the most massive ones, we can observe them up to higher redshifts with enough quality to perform this detailed analysis. Therefore, we use high-quality long-slit spectra (both self-obtained and from archive data) and we apply the different methods and techniques described in Chapter 2. We use the modern approach of the full-spectrum-fitting to derive the star formation history of the galaxies combined with the classical index-index analysis making use of a newly defined system of indices (LIS) and optimized indices (e.g. Hβ_0). Together, these methods pose strong constrains on the competing scenarios for the formation and evolution of ETGs.

The principal objectives of the thesis are:

- *Characterization of the compact massive galaxies in the nearby Universe*
  A full characterization of the main properties of this intriguing family

is conducted and described in Chapter 3. Their morphologies, profiles, kinematics, stellar populations and star formation histories are derived from deep K-band imaging and high quality long-slit spectra.

- *Are the compact massive galaxies in the local Universe the descendants of the high redshift massive galaxies?*
  Once these objects are characterized, we are in the position to compare their properties with those seen at high redshift. This can help to discard formation and evolution scenarios and, at the same time, give hints on the formation of most massive galaxies at earlier epochs.

- *The impact of varying the IMF on the stellar population parameters*
  Recent claims pointing out that the IMF slope should be tuned according to the galaxy velocity dispersion open new means to understand the formation of galaxies. In Chapter 4 we quantify the impact of varying the IMF slope and shape on the derived star formation history of a galaxy and other stellar properties such as stellar mass, mean ages and the timescales for the mass assembly.

- *A detailed study of the stellar populations of ETGs in clusters at intermediate redshift (z∼0.8)*
  With the modern approach of the full-spectrum-fitting and new stellar populations tools for the classic index-index diagrams, we study in Chapter 5 the relation between the stellar properties (velocity dispersion, age, metallicity, abundance ratios, star formation histories) and their location within the cluster, accounting for variations in the IMF.

- *How have galaxy clusters at intermediate redshift evolved to the present day clusters?*
  The relations of the above properties with the galaxy velocity dispersion (scaling relations) are compared with a cluster of similar properties at low-z (Coma), to test different evolutionary scenarios.

The concordance cosmology of $\Omega_m = 0.3$, $\Omega_\Lambda = 0.7$ and $H_0 = 70 \, \mathrm{km \, s^{-1} \, Mpc^{-1}}$ has been used throughout this thesis.

2

Methodology

You have to learn the rules of the game.
And then you need to play
better than anyone else
Albert Einstein

This chapter summarizes the different methods used along the thesis. The reduction process of the long-slit spectroscopic data is described in detail, while the several scientific tools and programs used to study the stellar populations are briefly introduced.

2.1 Spectroscopic data reduction

The work presented in this thesis is mostly based on both newly obtained and archive spectroscopic data. The characterization of the local compact massive galaxies and the study on the effects of varying the IMF have been done with long-slit spectra. The data used in the chapter about clusters of galaxies is, instead, multi-slit archive data. However, the reduction process performed in all of them is very similar.

The reduction has been performed with the reduction package $\text{RED}^{\text{uc}}_{\text{m}}\text{E}$ (Cardiel, 1999) instead of the commonly used `IRAF`. This package is optimized for long-slit spectra and has the advantage that it allows a parallel treatment of the scientific data and the errors propagated through the process. Therefore, it produces an associated error spectrum in each step of the reduction, which is key to properly derive the stellar population parameters. The basic steps in a standard reduction process are here described and summarized in Table 2.1.

program	task
addnf	Adds several images, accounting for shifts in the spatial direction
adnsc	Adds spectra into a single image, creating a new one with the same size than the original
autocos	Automatic rejection of the cosmic rays using several similar frames (for short exposures)
basicred	Determines the bias level in an image by averaging its value on the under/overscan regions. The detector's useful region is divided by the flats, creating at the same time its error frames from the known values of the gain and the readout noise.
calambda	Determines the wavelength as a function of the number pixel of a spectra. It uses the calibration polynomial generated by *fitlin*
cdisc	Corrects from C-distortion an image using the polynomial fits created from *fitcdis*
cleanest	Removes automatically, manually or mixed, the cosmic rays in an image (long exposures)
corrext	Corrects from the interstellar and atmospheric extinction
corrfft	Cross-correlates the problem spectra with a number of reference spectra
fcalspl	Calculates the flux calibration of a spectrum by fitting splines
findarc	Identifies interactively the lines in the reference arcs
findmax	Automatically detects peaks in the spectra
fitcdis	Determines the C-distortion of an image by fitting polynomials to the reference arcs lines
fitlin	Makes the wavelength calibration with the polynomial fitting of the reference arcs lines
fit2dspl	Fits bidimensional splines and polynomial to an image
genimage	Creates an artificial image, allowing to insert parts of other images
rebincw	Calibrates in wavelength an image (using the polynomial fits from *fitlin*) and corrects the C-distortion (using the polynomial created with *fitcdis* and *cdisc*)
resample	Transforms a wavelength calibrated image with given λ_0 and dispersion to another image with different λ_0 and dispersion
sdistor	Determines and corrects the S-distortion of an image
shpol	Determines how an origin change affect to the polynomial coefficients
skysubm	Determines and subtracts an sky image from a sky+object image. It uses polynomial fits to each image column

TABLE 2.1— Summary of the most commonly used programs in the $\mathrm{RED^{uce}_{m}E}$ package for the data reduction and the task they perform

1. **Cosmic rays**: During the exposures, several cosmic rays hit the CCD, which accumulate linearly in time. They can be distinguished because they are sharp-edged, taking up several pixels and with very high counts. Both scientific and calibration frames need to be cleaned from them before treatment. For short exposures, such as the calibration frames, an automatic task that removes them from the comparison of similar images is used (*autocos*). However, for the scientific frames, which are usually taken in longer exposures, a more accurate cleaning is needed (*cleanest*). This can be done by detecting in each frame pixel counts which deviate a certain number of times from the typical count of its surrounding pixels and also by detecting those pixels that are over a given threshold. The central pixel and its affected neighbors are then selected and interpolated, as shown in Figure 2.1.
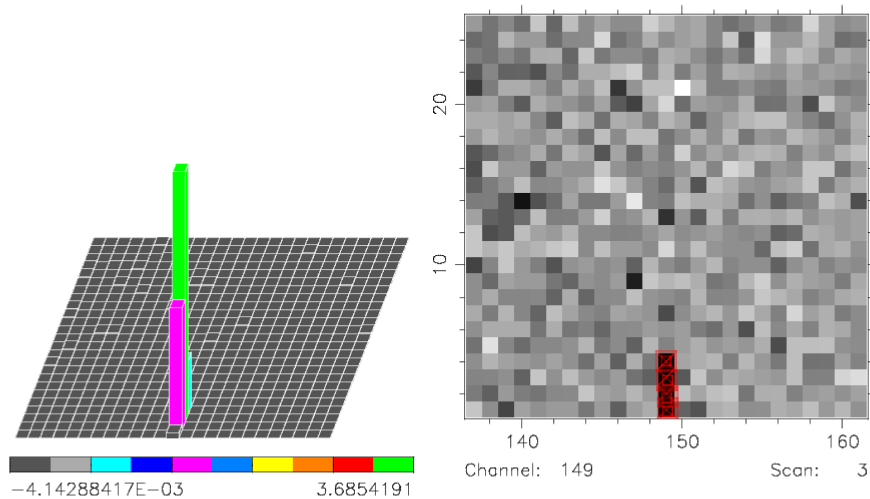
FIGURE 2.1— A cosmic ray is found and selected with the task *cleanest*. The cosmic ray counts are color scaled on the left panel. The right panel is where the user selects those pixel that are affected (marked with red symbols) and then an interpolation in the spatial direction is done.

2. **Bias level subtraction**: It is important to remove any effects that are due to the nature of the detector and the telescope. The bias level is an electronic offset added to the signal from the CCD that makes sure that the Analogue-to-Digital Converter always receives a positive value. This bias level can be quantified from the bias images, which are 0 seconds

exposure frames. These frames include the underscan and overscan, two lateral sections that are not physically part of the CCD but that are added during the readout. Apart from the bias level, bias frames also content the readout noise. Several bias are observed each night, and the bias level and an averaged bias frame are constructed for each night. This image is then subtracted from all the scientific and calibration images.

3. **Flat-fielding**: The sensitivity of a CCD varies from pixel to pixel, so if the data is to be relatively flux calibrated, this variations must be removed. To achieve this correction, exposures of a photometrically flat source must be taken, known as flatfields. They can be both "lamp flats", which correct the high frequency differences pixel to pixel, and the "sky flats", which correct the low frequency variations. A sensitivity map is created from all the flatfield frames, and the scientific data is then divided by it.

4. **C-distortion correction and wavelength calibration**: It is necessary to determine the relation between the pixel and the wavelength scales. However, some small-scale geometric distortions in the spatial direction (C-distortion) and in the spectral direction (S-distortion) can be found. It is very important that, while observing, several arc exposures are taken, particularly between large scientific exposures. We first correct from the C-distortion, creating a correction polynomial that is subtracted from the arcs. With the corrected arcs, we fit a gaussian profile to those lines that are over a certain threshold (to avoid selecting noise). That wavelength is then assigned to the pixel associated to the maximum of the gaussian. The spectra is then converted into a linear wavelength scale by fitting as many arc lines as possible with 3th-5th order polynomials (Figure 2.2), creating a wavelength calibration polynomial. Each polynomial is then applied to its associated scientific frame, to convert it into the wavelength scale.

5. **S-distortion correction**: Before we can proceed with the reduction of the scientific frames, we need to correct from possible tilts and curvatures on the spectral direction, otherwise we could be adding sky on our galaxy spectra. It works iteratively, as illustrated in Figure 2.3, by fitting a polynomial to the maximum of a spatial cross-section (upper panel). This is used to spatially shift each column signal with respect a reference one, rejecting those counts that deviate (middle panel) until we obtain a flat relation (lower panel).
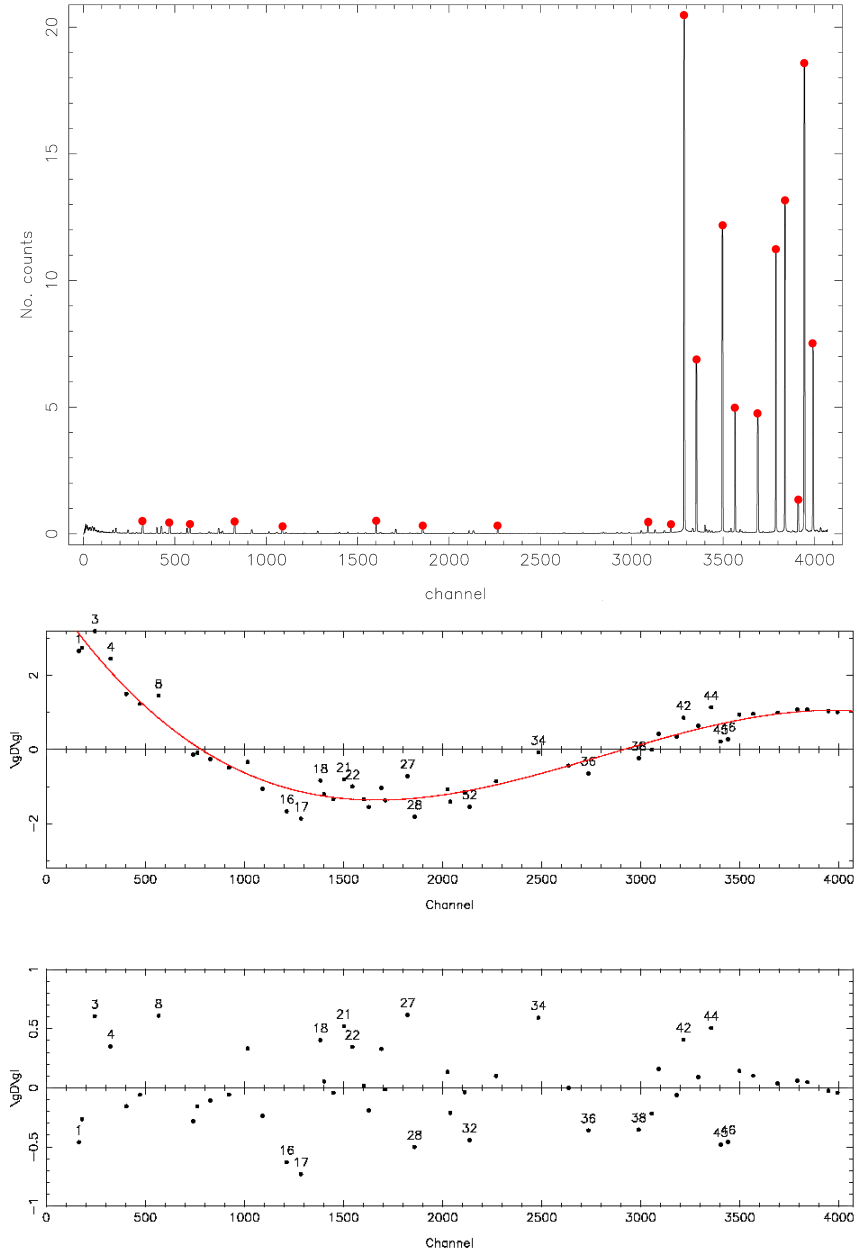
FIGURE 2.2— Some steps to illustrate the wavelength calibration process. The upper panel shows the selected lines above a given threshold that are used to create an initial line list. The lower panel shows the polynomial fit to the lines that have been assigned a wavelength. The polynomial created from this fit is then used to calibrate the scientific frames into a wavelength scale.
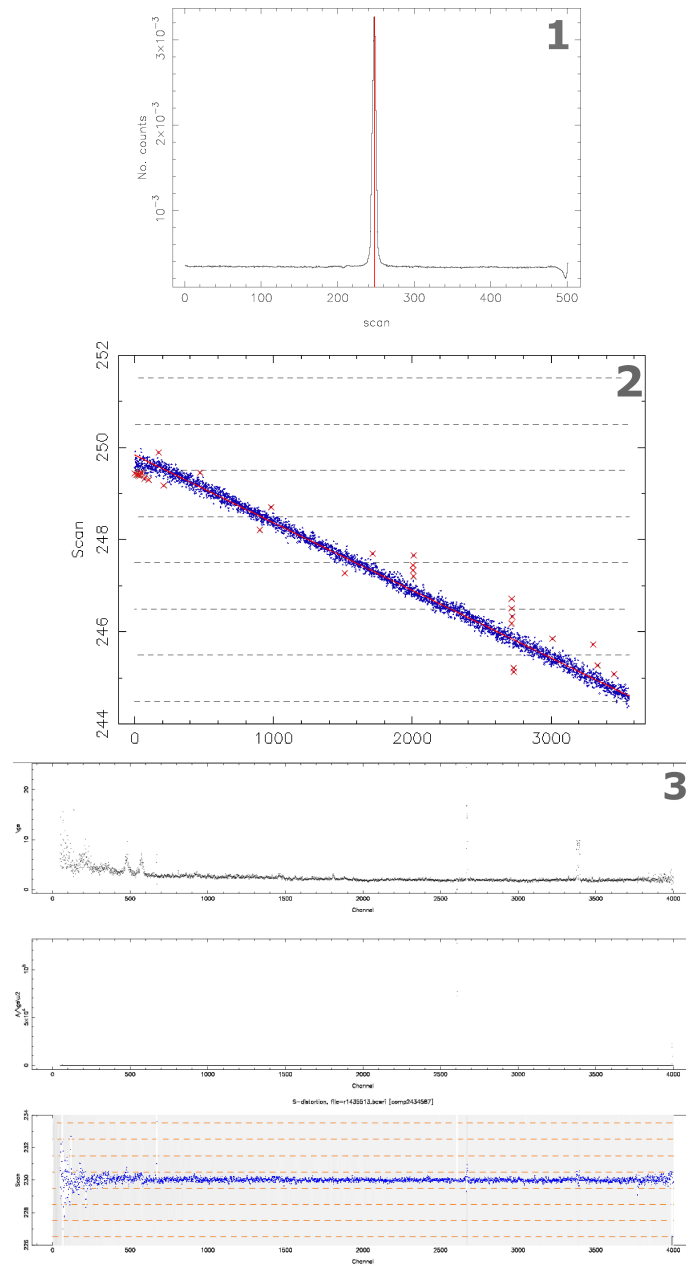
FIGURE 2.3— Illustration of the task that corrects the spectral distortion (*sdistor*). *1)* The upper panel shows the position of the maximum on the spatial cross-section. *2)* This is fitted by a low order polynomial that is corrected by rejecting the scattered points (middle panel). *3)* Iterating this rejecting-fitting process, we finally obtain a flat relation (bottom panel).

6. **Sky subtraction**: The observed spectrum is the sum of the target and the emission from the night sky. Therefore, we need to quantify the contribution from the sky and subtract it from the scientific spectrum. We select two external regions in each side of the galaxy from a spatial cut of the image (*skysubm*, Figure 2.4). We fit those regions with a low-order polynomial, which will create a spectra containing the continuum and the sky emission lines. This image is then directly subtracted from the original galaxy frame, removing the contamination from the sky. This step is repeated in an iterative way until no sky residuals are affecting our spectra. This is a critical step of the reduction process, as cleaning our scientific spectra from residual sky lines is vital, particularly for works at high redshift, where the lines of interest fall in the region of strong sky lines.

Scan
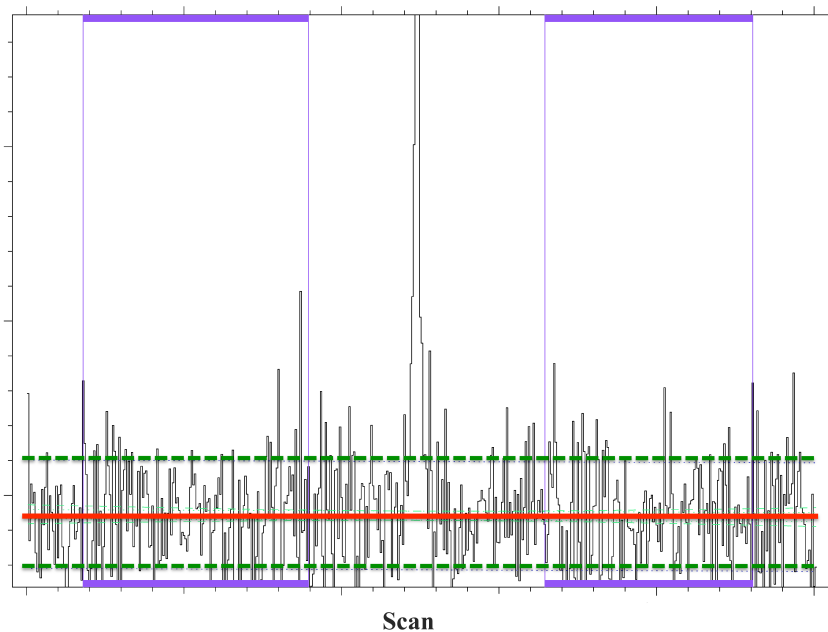
FIGURE 2.4— Illustration of the way the sky regions are selected (purple rectangles). A first order polynomial is fitted within those regions (solid red line) to create an image that contains the sky level and it is subtracted from the scientific frames. This process is repeated iteratively until no emission sky lines are present on the spectral cut. The dashed gray lines mark the 3σ level to compute the errors.
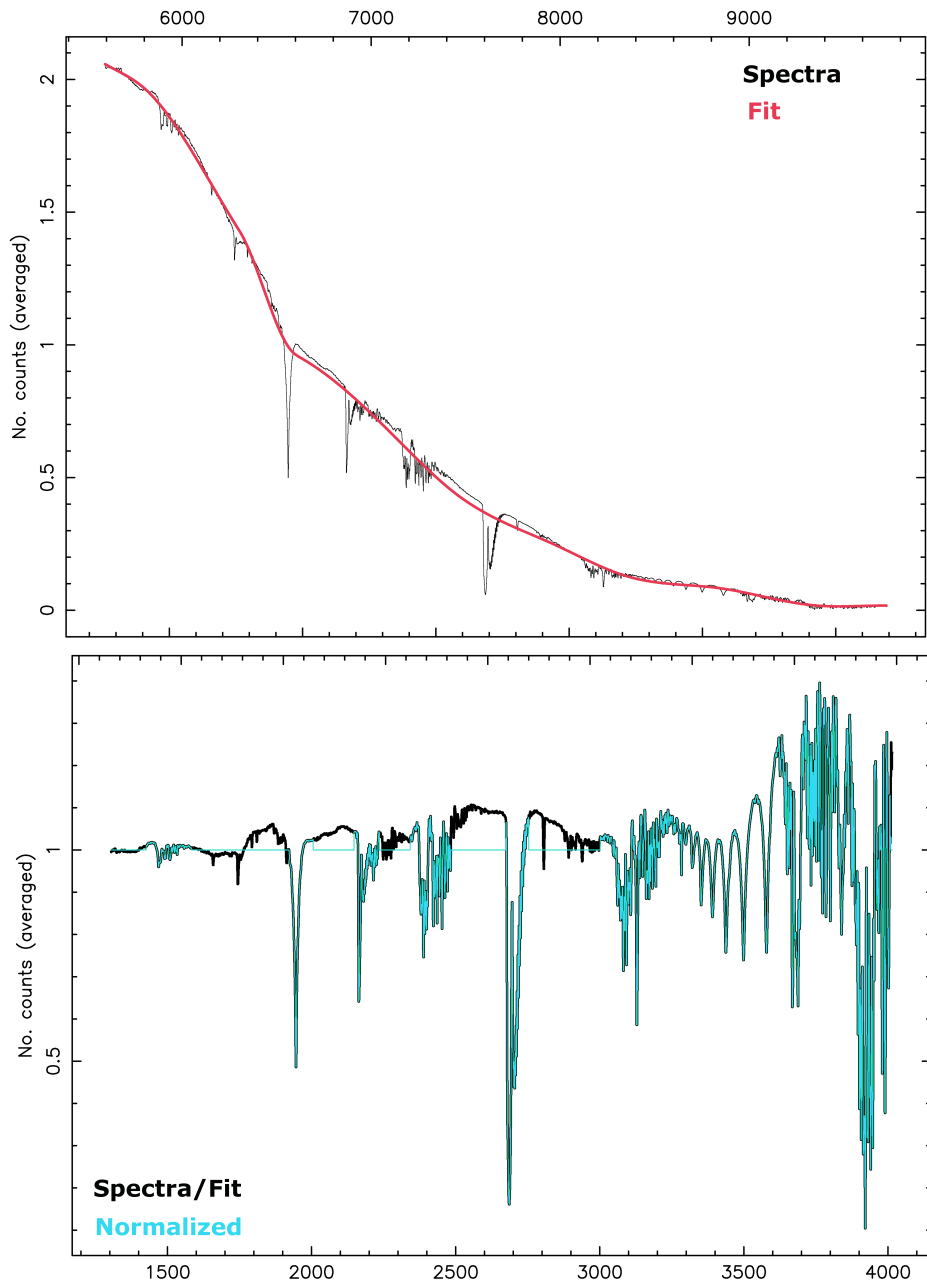
FIGURE 2.5— Illustration of the telluric removal from a star spectra. The upper panel presents the curve fitted with splines (*fit2dspl*) and the lower panel the normalized spectra containing only the telluric lines, which will be subtracted from the scientific frames.

7. **Atmospheric extinction correction**: After the sky is subtracted and the spectral features are clean, the atmospheric extinction correction is performed with an extinction curve, scaling it to the airmass of each frame.

8. **Telluric lines correction**: Apart from the contribution of the sky emission lines, the residuals from the telluric features also need to be removed. The telluric lines are atmospheric absorption lines inherent in the Earth's atmosphere that appear superimposed in the spectrum. With the spectra of some standard stars observed during the campaigns, the star spectra is fitted with splines, creating a telluric curve (upper panel of Figure 2.5). We then subtract it from the original star spectra and normalize it, creating a frame where only the telluric lines are present (lower panel). We finally subtract this frame from our scientific images.

9. **Flux calibration**: A relative flux calibration is needed, as both the indices (in particular the broad ones) and the full-spectrum-fitting approaches are sensitive to the form of the continuum. With the spectrophotometric standard stars observed during the campaigns, which have a well known tabulated spectrum, we create a calibration curve for each star. Averaging all these curves, we create a unique calibration curve, which will be divided to our scientific frames, to relatively flux-calibrate them.

10. **Extracted spectra**: Once flux calibrated, we add all the scientific frames of each object in a single image to increase the resulting S/N. Before the extraction, we first need to bring all the pixels to the central radial velocity (see Sect. 2.3 for a description of the kinematics determination) and then broad all the points to the central velocity dispersion, as Figure 2.6 shows. This creates a "flat" spectra which ensures that we are not artificially broadening any spectra feature, which would imply a mixing of the different kinematics of each population. We finally extract the part of the spectra of interest (in our case, usually the central part), either with annular apertures or with single points.

2.2 Stellar population synthesis models

The study of the integrated light to quantify the stellar content of galaxies demands the use of stellar population synthesis models. The predictions from these models are compared to the galaxy observables to determine the stellar population parameters such as the age or the metallicity. Several stellar population synthesis models exist, following different prescriptions.
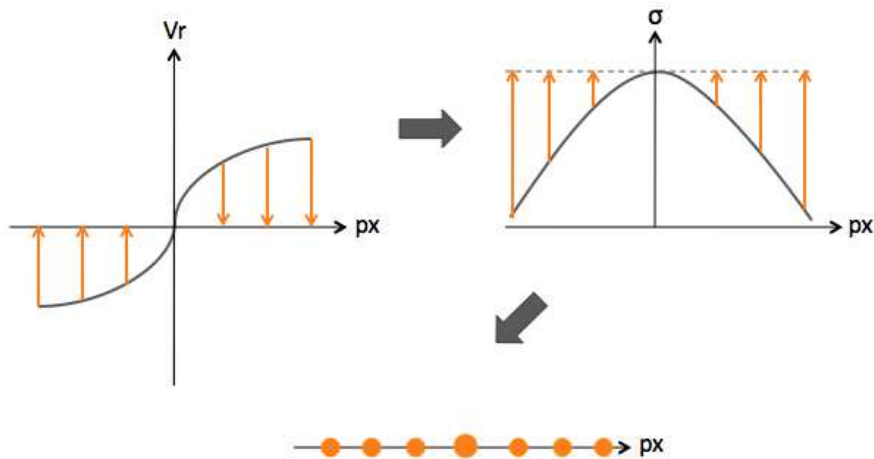
FIGURE 2.6— Schematic example where all the pixels are first brought to zero radial velocity (upper left figure) and then broaden to the central velocity dispersion (upper right figure), to avoid artificially broadening the spectra and thus, mixing the kinematics from different populations. Afterward, the desired region can be extracted from the flat spectra.

All the stellar population analysis in the different sections presented in this thesis employ the Single-Stellar-Population models (SSP) of MILES and MIUS-CAT (Vazdekis et al. 2010, Ricciardelli et al. 2012, Vazdekis et al. 2012). These models use the library of empirical stellar spectra of MILES (Sánchez-Blázquez et al., 2006c). This stellar library comprises around 1000 high-quality stellar spectra, covering a wide range of spectral types, luminosities, metallicities and all the evolutionary phases (Vazdekis et al., 1996). The models are flux-calibrated and have a high resolution (2.51 Å FWHM), which is virtually constant along the entire wavelength range (Falcón-Barroso et al., 2011a). This means that the models predict not only individual indices but also the entire spectral energy distributions as a function of age and metallicity.

The set of MILES SSPs cover the visible range ($\lambda\lambda$ 3500-7500 Å), and have been extended to $\lambda\lambda$ 3465-9469 Å (MIUSCAT)[1]. Both span a wide range of ages (up to 17.8 Gyr) and metallicities (-2.42$\leq$[M/H]$\geq$+0.22). The inclusion of models with ages larger than the adopted age for the Universe is widely used in stellar population studies, due to the uncertainties in the zero point of the models. Moreover, the user can choose the IMF (Initial Mass Function) shape and slope, which allows taking into account the recent claims about the non-universality of the IMF. This allows to tune the models according to the user requirements.

---

[1]http://miles.iac.es/

2.3 Galaxy kinematics

To extract the information about the stellar kinematics we use the code `pPXF` (Penalized Pixel-Fitting; Cappellari & Emsellem 2004). This program is based on a penalized likelihood approach, working directly on the pixel space. Using as templates the library of SSP models of V10, `pPXF` convolves them with a particular LOSVD (line-of-sight velocity distribution) with a Gauss-Hermite expansion, to match the data. This algorithm is able to overcome the typical template mismatch problem, as it constructs an optimal template with a linear combination of large sets of SSPs. Errors on the recovered parameters are derived from 1000 Monte-Carlo simulations.

In addition, we need to take into account possible nebular emission to properly measure the line indices. For a long time it was assumed that ETGs did not contain gas and dust. However, detailed analysis of large samples of ETGs have shown that approximately half of them do have weak emission lines (e.g. Caldwell 1984, Goudfrooij et al. 1994, Sarzi et al. 2006). These lines may contaminate both the absorption feature itself by filling it (e.g: filling in Balmer lines would give a lower value of the index, hence older ages) or the bands where the pseudocontinuum is calculated. Either way, it is crucial in the stellar population analysis to correct this effect. The code `GANDALF` (Sarzi et al., 2006) permits to extract the gas kinematics, responsible for this absorption-line filling. It cleans the spectrum without masking the emission features, which is known to introduce biases. Instead, it treats the emission lines as additional gaussian templates. It fits simultaneously the stellar continuum and the emission lines, while iteratively searches for the best radial velocity and velocity dispersion. Figure 2.7 shows an example of the kinematical information recovery for one galaxy using these two codes.

2.4 Deriving ages and metallicities

2.4.1 Line-strength measurements

For decades, stellar population analysis have been based in the study of the absorption features of the spectrum. Line indices are the measurement of the strength of these absorption features. A line index is defined by a central band that encompasses the line in study plus a blue and a red side bands that determine the pseudocontinuum (e.g. Worthey et al. 1994), as seen in Figure 2.8. There are two types of line indices: the atomic indices, measured in Å (eq. 2.1), and the molecular ones, in magnitudes (eq. 2.2). They are defined as:

$$I(A) = \int_{\lambda_{c_1}}^{\lambda_{c_2}} [1 - S(\lambda)/C(\lambda)] \, d\lambda \qquad (2.1)$$
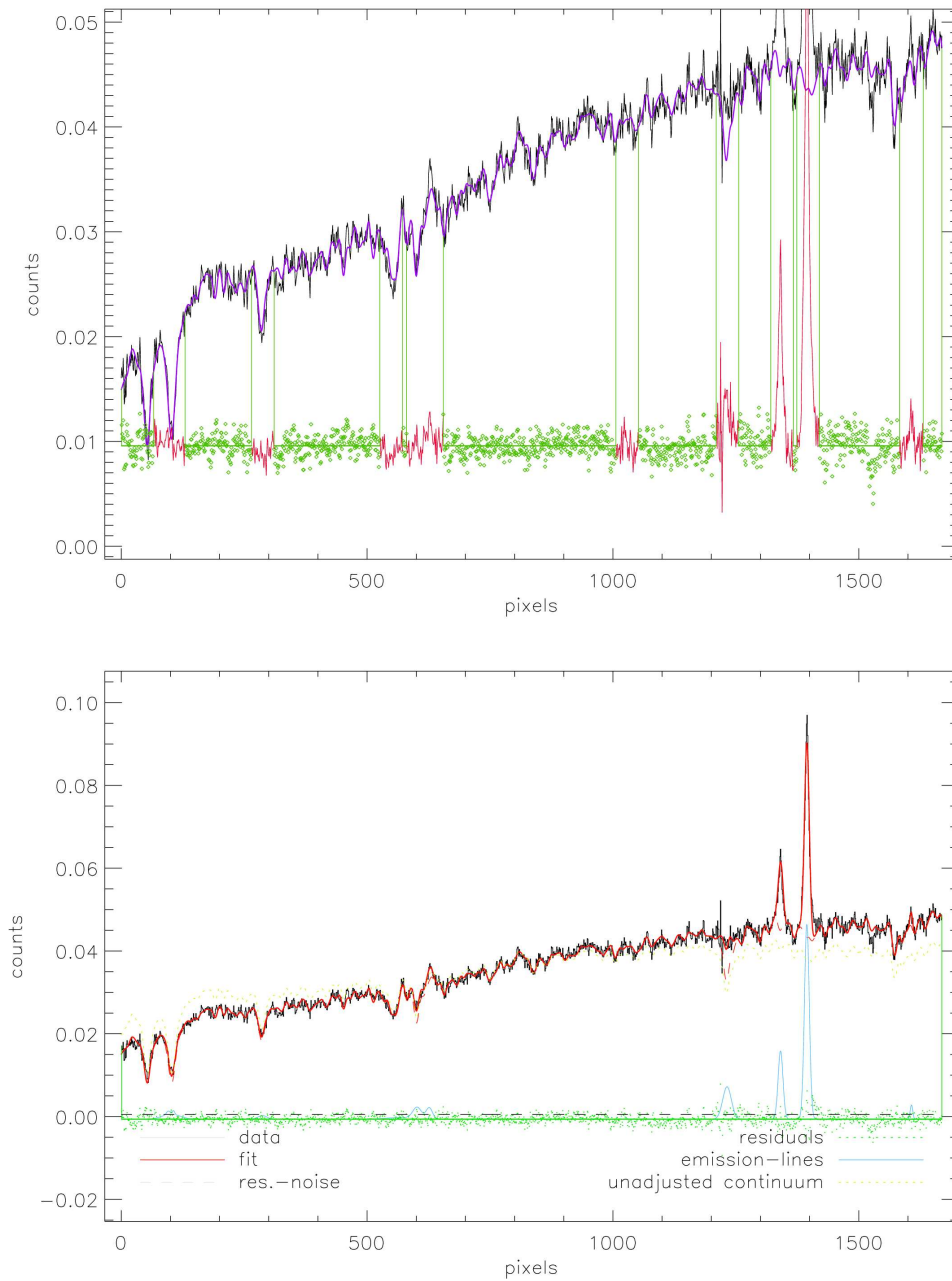
FIGURE 2.7— Example of the process that `pPXF` and `GANDALF` perform together: the upper panel shows the fitting done with the stellar templates to derive the stellar kinematics, while the lower panel shows the position of the emission lines considered to be removed above a given threshold.

$$I(mag) = -2.5 \log \frac{\int_{\lambda_{c_1}}^{\lambda_{c_2}} S(\lambda)/C(\lambda) d\lambda}{\lambda_{c_2} - \lambda_{c_1}} \tag{2.2}$$

where I is the index value, λ_{c_1} and λ_{c_2} are the limits of the central band (in Å), $S(\lambda)$ the flux in the central band and $C(\lambda)$ the flux in the pseudocontinuum of the side bands. Table 2.2 list the definition of the line indices used in this thesis.
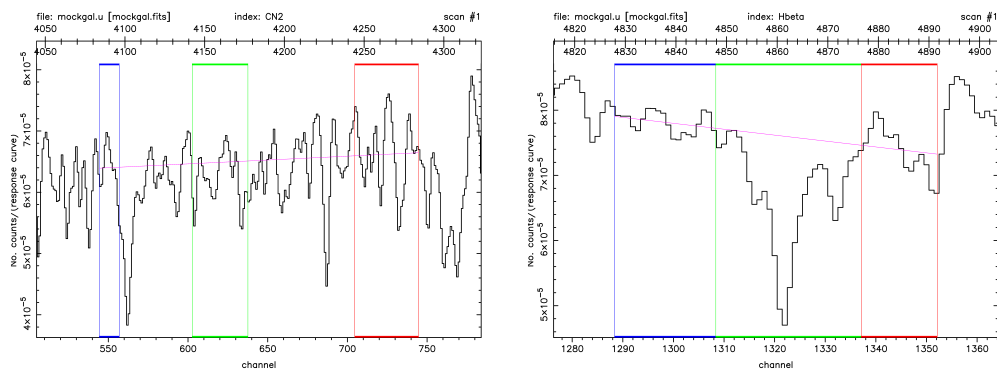
FIGURE 2.8— Example of two index definitions. The left panel shows the molecular band CN_2 and the right one the atomic absorption line Hβ. Although they are measured in different units, the concept of the line index is the same: a central band encompassing the line index (green) plus two side bands (blue and red) that determine the pseudocontinuum.

Line indices are measured with the RED$_{\mathrm{m}}^{\mathrm{uc}}$E task *indexf*. Prior to its measurement, we need to broaden our galaxy spectra (σ_{broad}) to the same resolution as the system of indices used:

$$\sigma_{broad} = \sqrt{\sigma_{sys}^2 - \sigma_{instr}^2 - \sigma_{gal}^2} \tag{2.3}$$

where σ_{sys} is the resolution of the system of indices, σ_{instr} is the spectral resolution of the instrument and σ_{gal} the velocity dispersion measured for the galaxy.

So far, the most extended and used system of line indices is the Lick/IDS (Burstein et al. 1984, Faber et al. 1985, Gorgas et al. 1993, Worthey et al. 1994, Worthey & Ottaviani 1997, Trager et al. 1998). However, using this system presents some disadvantages. The user is limited to a set of defined and previously calibrated set of indices. Furthermore, its resolution is low (~ 9Å), forcing the user to degrade the galaxy spectra and perform a set of transformations,

which at the end can produce the lost of relevant information. However, the most important limitation is related to the age-metallicity degeneracy, which is emphasized for low-resolution indices.

In the recent years, some efforts to overcome these limitations have been done by proposing new alternative indices and with the aid of model SSP SEDs at moderately high spectral resolution, which have to be degraded to match the resolution of the data. The LIS system (Line-Index System; Vazdekis et al. 2010) is characterized for having a constant resolution across the whole wavelength range and a flux-calibrated response curve. Therefore all line-strength measurements, including the Lick indices, are performed on this system, broadening our galaxy data to one of the three resolutions of the LIS system that best resembles the galaxy resolution (5.0 Å, 8.4 Å or 14.0 Å). As the associated error spectrum has been propagated along the reduction process, the measure of the index is delivered with its error. These are computed taking into account several sources of random errors, such as the photonic noise, the errors in the radial velocity estimations and the errors in the flux calibration.

2.4.2 Index-index diagrams

There is a well known problem that astronomers face when trying to determine the stellar population properties of ETGs, particularly for the old ones. This is known as the "age-metallicity degeneracy", for which an old, metal-poor galaxy presents a similar spectrum as a young, metal-rich one (Faber 1972, Rose 1985, Renzini & Buzzoni 1986, Worthey et al. 1994). This is a consequence of the similar dependence of the temperatures of main sequence and giant stars of a given stellar population on age and metallicity. This degeneracy follows the 3/2 law: an increase of the age of a factor of 3 produces the same effects on the colours and in the metallic lines as an increase of metallicity by a factor of 2.

However, it can be partially broken if an index more sensitive to the age is confronted to an index more sensitive to the metallicity (e.g. Gunn, Stryker & Tinsley 1981, Rabin 1982). This creates a bidimensional grid of theoretical predictions, known as the index-index diagrams. Superimposing the index measurements on top of it permits to directly derive the age and the metallicity of the galaxy by interpolating between the model grid. The more orthogonal the grid, the easier it is to interpolate and to retrieve reliable estimates. Several pairs of indices are used, e.g. the Balmer lines, particularly the Hβ and Hβ_O, are good indicators for the age. Confronted with the composite <Fe> or with Mgb (good metallic indicators), they give rather orthogonal grids (Figure 2.9).

We use the program `RMODEL` (Cardiel et al., 2003) to carry this interpolation. We typically use a bivariated polynomial to interpolate both in the age and the

Index	Blue Bandpass λ_i - λ_f	Central bandpass λ_1 - λ_2	Red bandpass λ_i - λ_f	Source
		Atomic		
D4000	3750.000-3950.000	4050.000-4250.000	-	(2)
CaHK	3900.000-3915.000	3915.000-4000.000	4000.000-4020.000	(4)
HδA	4041.600-4079.750	4083.500-4122.250	4128.500-4161.000	(3)
HδF	4057.250-4088.500	4091.000-4112.250	4114.750-4137.250	(3)
Ca4227	4083.875-4096.375	4142.125-4177.125	4244.125-4284.125	(1)
G4300	4266.375-4282.625	4281.375-4316.375	4318.875-4335.125	(1)
HγA	4283.500-4319.750	4319.750-4363.500	4367.250-4419.750	(3)
HγF	4283.500-4319.750	4331.250-4352.250	4354.750-4384.750	(3)
Fe4383	4359.125-4370.375	4369.125-4420.375	4442.875-4455.375	(1)
C$_2$4668	4611.500-4630.250	4634.000-4720.250	4742.750-4756.500	(1)
Hβ	4827.875-4847.875	4847.875-4876.625	4876.625-4891.625	(1)
Hβ_o	4821.175-4838.404	4839.275-4877.097	4897.445-4915.845	(5)
Fe5015	4946.500-4977.750	4977.750-5054.000	5054.000-5065.250	(1)
Mgb	5142.625-5161.375	5160.125-5192.625	5191.375-5206.375	(1)
		Molecular		
CN3883	3760.000-3780.000	3780.000-3900.000	3900.000-3915.000	(4)
CN$_1$	4080.125-4117.625	4142.125-4177.125	4244.125-4284.125	(1)
CN$_2$	4211.000-4219.750	4222.250-4234.750	4241.000-4251.000	(1)
Mg$_1$	4895.125-4957.625	5069.125-5134.125	5301.125-5366.125	(1)
Mg$_2$	4895.125-4957.625	5154.125-5196.625	5301.125-5366.125	(1)

TABLE 2.2— Bandpass definitions for all the indices, both from (1)–the Lick system (Worthey et al., 1994) and defined by other sources: (2)–Bruzual A. & Charlot 1993; (3)–Worthey & Ottaviani 1997; (4)–Davidge & Clark 1994 and (5)–Cervantes & Vazdekis 2009.
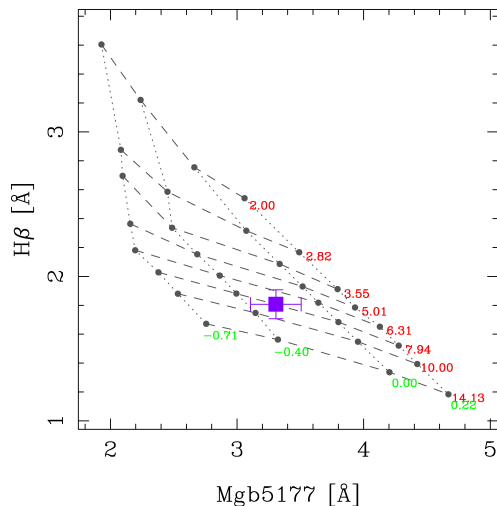
FIGURE 2.9— Example of a typical index-index grid. The model predictions create the grid with age (red labels) and metallicity (green) as labeled in the figure. The purple filled square marks the values of the measured indices for a mock galaxy. It is seen that the orthogonality of the grid permits to interpolate within the model predictions.

metallicity direction. Because models reach only [M/H]$= +0.22$, we only allow extrapolating up to [M/H]$= +0.5$, although we consider the latter as highly uncertain estimations.

It is important to highlight that ages and metallicities derived from different pairs of indices give different estimates for the same galaxy. This effect is associated to the fact that some elements, such as Mg, C or N are overabundant with respect to Fe (O'Connell 1976, Peletier 1989, Worthey 1998, Faber et al. 1999, Vazdekis et al. 2001b, Thomas, Maraston & Korn 2004), known as the relative abundances problem. For this reason, composite indices, such as [MgFe], [MgFe]', [MgFe50] (González 1993, Thomas, Maraston & Bender 2003, Kuntschner et al. 2006), are used to derive the total metallicity of the galaxy, as [MgFe]' is, for example, α/Fe independent.

Nonetheless, we have to remember that this method is based on single-burst populations. A galaxy spectra is the integrated light coming from the contribution of the different populations in the galaxy, gas and dust. Therefore, if galaxies have experienced more than a single episode of star formation, the younger components strongly dominate the light, giving younger ages that do no not reflect the real age of the bulk of the stars.

2.5 Full-spectrum-fitting

To unravel the true history of the formation and evolution of galaxies, we need to look at the imprints on the galaxy spectra. To use all the information encoded into this fossil record and not only the weighted mean values, the modern approach of the full-spectrum-fitting was developed. The idea is that the comparison between model predictions and observations is done pixel-by-pixel with a linear combination of SSPs from the synthesis models.

Several spectral synthesis methods have been developed in less than a decade, like `MOPED` (Multiple Optimized Parameter Estimation and Data compression; Heavens, Jimenez & Lahav 2000, Panter, Heavens & Jimenez 2004), `STARLIGHT` (from the SEAGal collaboration, Cid Fernandes et al. 2005), `STECKMAP` (STEllar Content and Kinematics via Maximum A Posteriori; Ocvirk et al. 2006a, Ocvirk et al. 2006b); `VESPA` (VErsatile SPectral Analysis, Tojeiro et al. 2007) or ULySS (University of Lyon Spectroscopic analysis Software; Koleva et al. 2009). Other programms, which are not devoted to the spectral synthesis themselves, also perform a similar approach, such as the previously mentioned `pPXF`.

Throughout this work we have based our studies on the code `STARLIGHT`. We have selected this code as it provides robust results on the derived SFH if parametrized by different populations (namely *young*, *intermediate* and *old*) (see Cid Fernandes et al. 2005 for a detailed description of this method and its capabilities). The user has to select the models, the wavelength range, the normalization wavelength and the features to be masked in the spectra (e.g. emission lines, bad pixels, etc). We show in Appendix B that in general, the impact that the selected setup has on the derived results is small although not negligible in the case of the wavelength range (Cid Fernandes & González Delgado, 2010). Nevertheless, we have tested the robustness of our results by comparing the derived SFHs from the codes `ULySS` and `STECKMAP`.

2.5.1 `STARLIGHT`

This program of spectral synthesis creates a combination of SSPs that best resemble the observed galaxy spectrum and that minimizes the χ^2. The code models the extinction as due to foreground dust and different reddening-laws can be selected to correct from Galactic extinction. Then, it finds the fraction x_j that a given jth SSP contributes to the total flux of the galaxy (normalized to a certain wavelength, λ_0), creating a full synthetic spectrum M_λ:

$$M_\lambda = M_{\lambda_0}(\sum_{j=1}^{N_\star} x_j \, b_{j,\lambda} \, r_\lambda) \otimes G(v_\star, \sigma_\star) \qquad (2.4)$$

where M_{λ_0} is the synthetic flux at the normalization wavelength, $b_{j,\lambda}$ is the spectrum of the jth SSP normalized at λ_0, $r_\lambda = 10^{-0.4(A_\lambda - A_{\lambda_0})}$ is the reddening term and G is the gaussian distribution centered at velocity $v_\star$ and with dispersion $\sigma_\star$ that models the line-of-sight stellar motions.

We can derive the contribution in mass directly from the mass-to-light ratio of each SSP (γ_j). From these combinations, we can derive stellar masses, the star formation episodes, the stellar kinematics and both mean luminosity/mass-weighted ages and metallicities as:

$$\langle t_\star \rangle_L = \sum_{j=1}^{N_\star} x_j \, t_j \tag{2.5}$$

$$\langle t_\star \rangle_M = \sum_{j=1}^{N_\star} \gamma_j \, t_j \tag{2.6}$$

$$\langle Z_\star \rangle_L = \sum_{j=1}^{N_\star} x_j Z_j \tag{2.7}$$

$$\langle Z_\star \rangle_M = \sum_{j=1}^{N_\star} \gamma_j Z_j \tag{2.8}$$

We show in Figure 2.10 an example to illustrate this method. It shows the fit performed with STARLIGHT and the information about the mean age and the SFH recovered for a simulated galaxy spectrum.
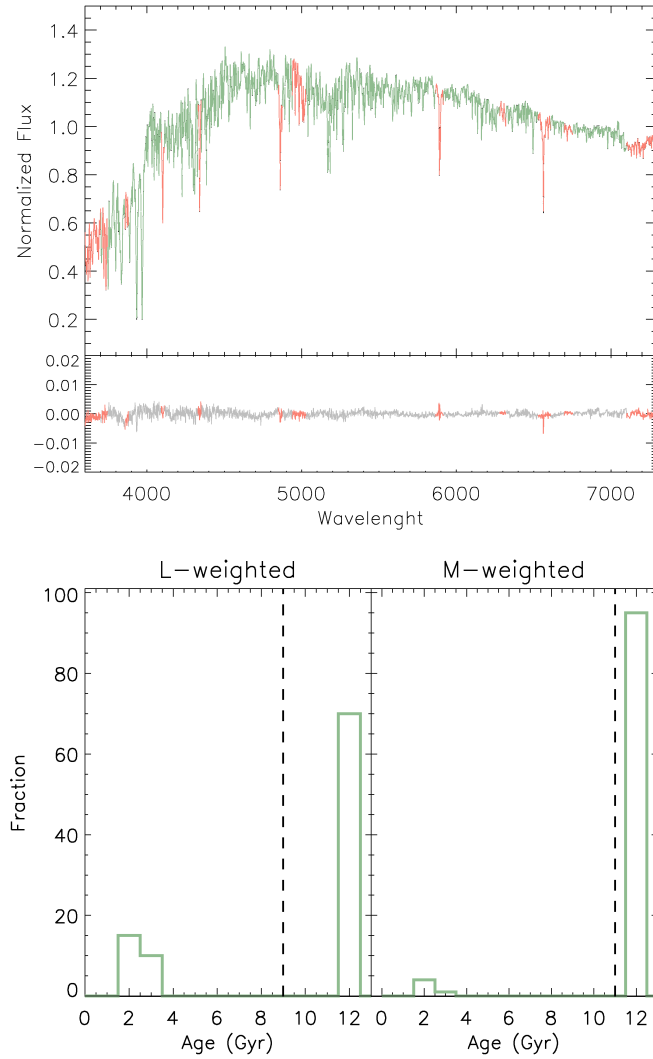
FIGURE 2.10— Example of the fit and outputs of **STARLIGHT** for a mock galaxy. The upper panel shows the observed spectra (black), the synthetic spectra that is a linear combination of the SSPs from the base model (green), the residuals of the fit (gray) and the masked regions (red). The lower panels show the derived SFH for this galaxy, both light- and mass-weighted. The vertical dashed lines show the mean age derived in each case. It is clear that the luminosity-weighted estimate renders younger values, which should be similar to those found from the indices (see Appendix A for a test about this issue).

3

Compact massive galaxies in the nearby Universe

*Adapt yourself to the things
among which your lot has been cast
and love sincerely the fellow creatures
in whom destiny has ordained that you shall live.*

Marcus Aurelius

The recent findings about the strong size evolution of massive galaxies, where the ones at high redshift are much more compact than present-day ones, have opened strong debates about the possible mechanisms for such evolution. Some of them predict the presence of compact massive galaxies in the nearby Universe, thought to be their relics. A rather small fraction of these superdense massive galaxies has been found at low redshift, and now it is crucial to determine *if they are the descendants of the high redshift massive galaxies or not.*

To address this issue, we first need to characterize this new family of scarce objects. This chapter presents a full description of the properties of these galaxies, from newly observed data, both with spectroscopy and imaging. We want to determine their principal characteristics such as their morphologies, kinematics and stellar populations.

However, our analysis shows that local compact massive galaxies are nearly the exact copies of the high redshift galaxies, which might provide a closer look to the nature of these high redshift (z $\sim$ 2.0) massive counterparts.

This chapter is based on the paper *Young ages and other intriguing properties of massive compact galaxies in the local Universe.* Ferré-Mateu, A., Vazdekis, A., Trujillo, I., Sánchez-Blázquez, P., Ricciardelli, E. and de la Rosa, I.G. 2012, MNRAS, 423, 632; and on the letter *Ultra-deep sub-kiloparsec view of nearby massive compact galaxies.* Trujillo, I., Carrasco, E.R and Ferré-Mateu,A. 2012, ApJ, 751, 45.

3.1   Data and Observations

We have studied a subsample of 9 local compact massive galaxies to characterize this new intriguing family of objects. They were chosen from the collection of nearby compact massive galaxies compiled by Trujillo et al. (2009) (T09 from now onwards). The original sample contains 48 compact massive galaxies taken from the New York University Value-Added Galaxy Catalog from the SDSS Data Release 6 (NYU GC, Blanton et al. 2005b, Blanton & Roweis 2007, B07 hereafter). Those were selected to have $M_* > 9.2 \times 10^{10} M_\odot$ and effective radius $R_e < 1.5\,$kpc at $0 < z < 0.2$, adopting a Chabrier IMF. Note that the stellar mass, size and redshift were the only parameters considered for the sample selection in T09 and that no further cut based on morphology, colour or star formation rate was applied to select them.

The galaxies in our subsample were chosen to cover a range in stellar masses, magnitudes and redshifts, so their inferred properties could be extended to the majority of the nearby massive compact objects. Note that the time allocated for the observations limited the number of galaxies. The subsample of galaxies and their main properties from the NYU Value-Added Galaxy Catalog are listed in Table 3.1.

This section describes the observations carried out for this study. From now on, we will refer as the spectroscopic sample to those galaxies for which new long-slit data was obtained (7 galaxies), while the imaging sample refers to those with new deep near-IR images (4 galaxies). Two compact massive galaxies are found in common in both samples, as quoted on last column of Table 3.1.

3.1.1   Deep imaging with NIRI

The high spatial resolution imaging presented in this part of the work was obtained with the Gemini-North telescope using the Near-Infrared Imager and Spectrometer (NIRI) with the ALTAIR/LGS (Laser Guide Star) adaptive optics systems. ALTAIR requires a relatively bright star ($\lesssim 18$ mag in R-band) in the proximity of the target object (within $17''$) to obtain a good Strehl correction. The Strehl ratio is a measure of the optical quality of a telescope, defined as the

ID NYU	SDSS Name	R.A. (J200)	Decl. (J200)	M_* ($10^{10}M_\odot$)	R_e (kpc)	z	Obs. mode
54829	SDSS J153019.45-002918.6	232.57104	-0.4885095	8.39	1.12	0.085	spec.
265845	SDSS J120032.46+032554.1	180.13528	3.4317179	8.01	1.31	0.143	imag.
321479	SDSS J212052.74+110713.1	320.21978	11.120310	10.10	1.38	0.128	spec., imag.
415405	SDSS J103050.53+625859.8	157.71053	62.983350	8.61	1.42	0.167	imag.
685469	SDSS J222140.32+135914.2	335.41803	13.987279	9.03	1.38	0.149	spec.
796740	SDSS J144736.37+432945.7	221.90155	43.496021	9.76	1.47	0.182	spec.
890167	SDSS J153934.07+441752.2	234.89197	44.297863	8.79	1.11	0.143	spec., imag.
896687	SDSS J143547.19+543528.7	218.94667	54.591381	9.23	1.43	0.130	spec.
2434587	SDSS J111659.35+170917.3	169.24737	17.154811	8.37	1.25	0.172	spec.

TABLE 3.1— This table shows the main properties of the galaxies explored in this study, originally selected from the NYU Value-Added Galaxy Catalog. The last column specifies the mode the galaxy was observed: *spec.* for the long-slit spectroscopy and *imag.* for the deep imaging.

ratio of the observed peak intensity at the detection plane from a point source if compared to the theoretical maximum peak intensity of a perfect imaging system working at the diffraction limit.

The imaging sample is composed of four nearby compact massive galaxies, which were observed during the first semester of 2010, in queue mode, using the K (2.2 μm) filter and NIRI f/14 camera, which provides a field of view of $51\farcs1 \times 51\farcs1$ with a pixel scale of $0\farcs0488$.

In addition, standard stars for photometric calibration were observed before or after our galaxies. The standard stars were used to determine the photometric zero points and monitor the image quality of the observations. Throughout the standard stars and the field stars presented in our observations, we determined the effective FWHM of the observations. From standard stars, the effective FWHM varied between $0\farcs11$ and $0\farcs13$ (note that the photometric standard stars have always the maximum Strehl corrections because they are used as AO tip/tilt star). From field stars, the effective FWHM was between $0\farcs16$ and $0\farcs24$ varying with the stellar magnitude, and the location of the star relative to the galaxy of interest.

The data were processed following the standard procedures for near-infrared imaging using the NIRI/Gemini IRAF package v1.10. Normalized flat field images were constructed from flat images observed with the Gemini Calibration unit (GCAL) with the shutter closed (lamps off) and shutter open (lamps on). Dark images observed at the end of each night and flat field images (lamp off) were used to construct a bad pixel mask with bad and hot pixels. The sky images were constructed from the raw science images by identifying objects in each frame, masking them out, and averaging the remaining good pixel (the images were observed with a $3'' \times 3''$ mosaic pattern). The raw science images were then processed by subtracting the sky on a frame-by-frame basis and divided by the normalized flat field images. Finally, the processed images were registered to a common pixel position and median combined. The final images have a field of view of $39\farcs5 \times 39\farcs5$.

Photometric calibrations were derived using the UKIRT Mauna Kea Observatories JHKL'M Standard Stars FS 132 (s860-d), FS 152 (p460-e) and P272-D (Leggett et al., 2006) and the P064-D faint standard star (Persson et al., 1998). Given that only one standard star was observed for each galaxy (before or after), we have used an average value for the extinction of $k_K = 0.052 \pm 0.028$ from Leggett et al. (2006).

Table 3.2 lists all the observational parameters for our NIRI observations. Since we use an average value for the extinction coefficient, the estimated error

ID NYU	Observing Date (UT)	Total t$_{exp}$ (sec)	Airmass	Zero Point (AB mag)	K mag (AB mag)
265845	2010 Feb 28	3540	1.406	24.86	16.63
321479	2010 Jun 5	1620	1.106	24.85	16.06
415405	2010 May 4	3660	1.281(a)	24.91(b)	16.04
	2010 Jun 4				
890167	2010 May 22	3780	1.230	24.90	16.24

TABLE 3.2— Description of the data in the imaging sample from NIRI. Column (1): galaxy NYU Value-Added Catalog name; column (2) Date of observation in UT; column (3): the total exposure time; column (4): effective airmass; column (5): Derived zero point in the AB system; column (6): K-band galaxy magnitude. (a) Average airmass from two nights; (b) Average Zero Point for two nights: night 1–24.90 mag, night 2–24.91 mag

in the photometric calibration will be driven by the uncertainty in the correct value of the extinction coefficient for the night of observation. Hence, we estimated the error by summing in quadrature the median error of the aperture photometry, the error of the standard catalog and the median error of the extinction coefficient. The error varied between 0.03 mag and 0.05 mag, depending on the star. For each galaxy, the adopted zero point is listed in column (5). The values were transformed from the Vega system to the AB system using the relation $K_{AB} - K_{Vega} = 1.91$ mag.

3.1.2 High-quality long-slit spectra with ISIS

The spectroscopic sample is formed by seven massive compact galaxies. High quality long-slit spectra were obtained for them at the 4.2m William Herschel Telescope during 4 nights (22-23 July 2009 (run A) and 3-4 June 2010 (run B)). The blue arm of the ISIS spectrograph with the grating 600B was used, which gave a wavelength coverage $\lambda\lambda$ 3800-5300 Å at resolution 1.74 Å for the first run (slit-width of 1") and 2.64 Å for the second one (slit-width of 1.5"), with a typical seeing of $0.7''$. The setup on the second run was changed to improve the quality of the spectra by slightly opening the slit.

Several exposures of 30 minutes were taken for each galaxy depending mainly on their redshift (Table 3.3), with the slit positioned along the major axis. Several spectrophotometric standards and stars from the MILES library (Sánchez-Blázquez et al., 2006c) were observed for a relative flux calibration. A standard data reduction was performed with $\text{RED}^{\text{uc}}_{\text{m}}\text{E}$, as described in Chapter 1 (bias subtraction, flat-fielding, cosmic-ray removal, C- and S-distortion correction, wavelength calibration, sky subtraction and flux calibration).

ID NYU	Observing Date (UT)	Exposures	Total t_{exp} (s)	S/N (Å^{-1})
54829	2010 Jun 04	3	5400	41
321479*	2009 Jul 22	4	7200	62
685469	2010 Jun 04	5	9000	70
796740	2009 Jul 21	3	7200	26
	2009 Jul 22	1		
890167*	2010 Jun 03	6	12600	32
	2010 Jun 04	1		
896687	2009 Jul 22	4	7200	50
2434587	2010 Jun 03	4	12600	46
	2010 Jun 04	3		

TABLE 3.3— Description of the data in the spectroscopic sample from ISIS. Column (1): galaxy NYU Value-Added Catalog name, the asterisk marks those galaxies in common in both samples; column (2) Date of observation in UT; column (3): the number of exposures in each run; column (4): total exposure time; column (5): Signal-to-noise per Ångström.

3.2   Characterizing the local compact massive galaxies

This section describes in detail the main characteristics of local compact massive galaxies. The morphologies are derived for both samples, the profiles only for those in the imaging sample, and the kinematics and the stellar populations only for those in the spectroscopic sample.

3.2.1   Morphologies

The morphological parameters of the local compact massive galaxies were derived for both subsamples. For the galaxies in the spectroscopic sample, for which no deep imaging is available, their morphologies were obtained from their lower resolution SDSS images.

For this means, we have used the 2-D fitting code `GALFIT` (Peng et al. 2002, Peng et al. 2010). This code makes a convolution of the Sérsic model (Sérsic, 1968) with the PSF of the image, determining the best fit when comparing the convolved model with the galaxy surface brightness distribution that minimizes the χ^2 of the fit.

The Sérsic index n is a measure of the shape of the surface brightness profile, which gives an idea of the morphology of the object. In the nearby Universe, galaxies with $n < 2.5$ are normally disk-like objects while $n > 2.5$ are indicative of spheroidals (Ravindranath et al., 2002). The effective radius was scaled to a

physical scale in kiloparsecs relative to their redshift and then circularized with the following equation:

$$R_e = r_e \sqrt{b/a},$$ (3.1)

where R_e is the circularized effective radius and r_e and b/a the effective radius along the semi-major axis and the axial ratio derived from `GALFIT`.

In this work, only single Sérsic models were fitted, avoiding those regions of the galaxies more severely affected by the PSF (Point Spread Function). This means that only those points beyond the FHWM of the PSF were taken. To see if the results were affected by this particular radial range of exploration, the fitting was repeated for the imaging sample taking only the points outside 2 times the FWHM. The estimates remained very well constrained with changes in the effective radius below 15% and for the Sérsic index less than 11%. This robustness is due to the extreme depth of the K-band images.

ID NYU	source	R_e(arcsec)	R_e(kpc)	Sérsic index	b/a
54829	1	0.69	1.12	4.60	0.90
265845	2	0.53	1.33	3.55	0.32
321479	2	0.59	1.35	2.66	0.28
	1	0.52	1.20	5.80	0.51
415405	2	0.45	1.23	2.20	0.36
685469	1	0.57	1.48	3.03	0.45
796740	1	0.41	1.24	2.40	0.35
890167	2	0.38	0.95	2.18	0.47
	1	0.33	0.83	3.72	0.63
896687	1	0.61	1.63	5.44	0.95
2434587	1	0.39	1.13	5.45	0.40

TABLE 3.4— Morphological parameters of the compact massive galaxies from both samples. Column (1): Image source used, 1–SDSS, 2–deep imaging; columns (2) circularized effective radius in arcsec and (3) in kiloparsecs; column (4): Sérsic index; column (5): axial ratio for the galaxy.
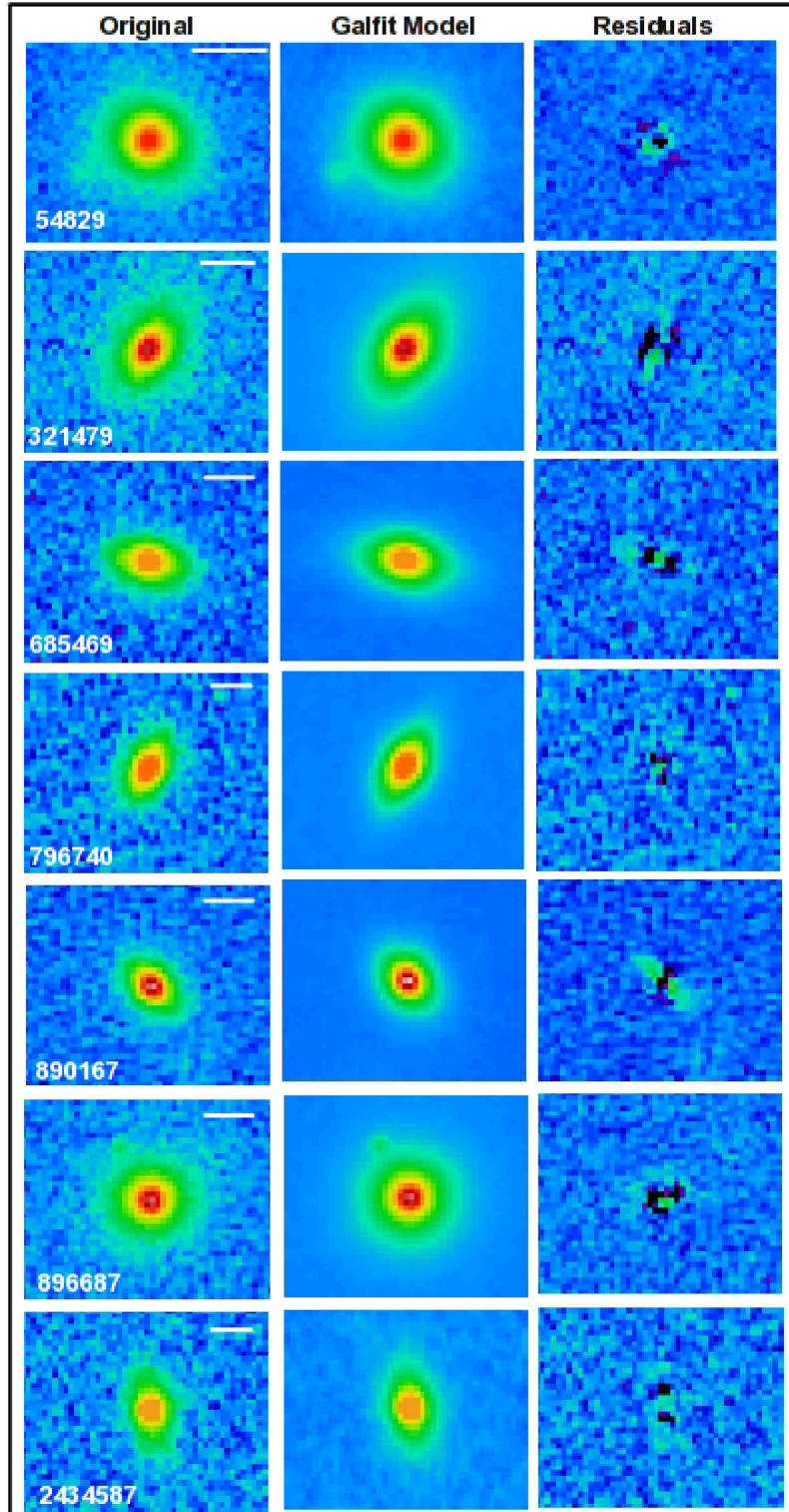
FIGURE 3.1— Thumbnails for each compact massive galaxy from the spectroscopic sample showing: the galaxy image from SDSS (first panel), the fitted model with GALFIT (second panel) and the residuals from the fit (third panel). The white line on the upper right corner of all the first panels is the equivalent size of 10 kpc at the redshift of the object.
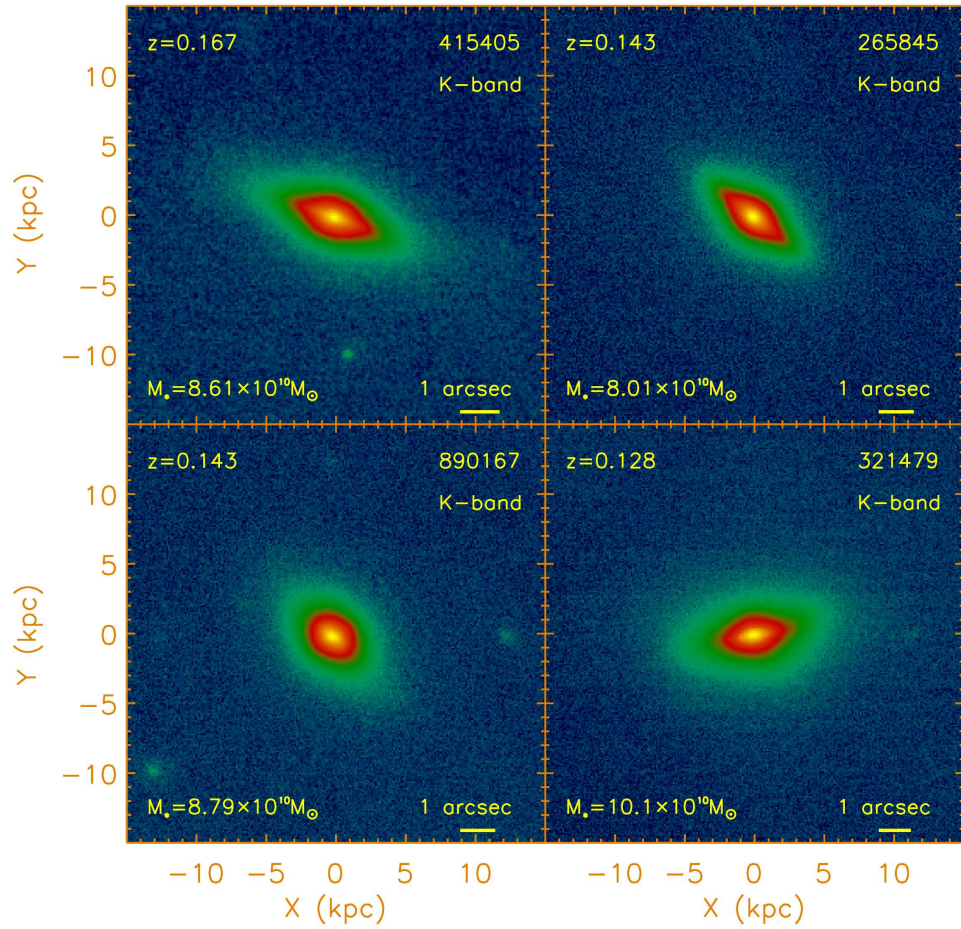
FIGURE 3.2— K-band Gemini high resolution (FWHM∼0.2 arcsec) imaging of the four nearby massive compact galaxies in the imaging sample. Listed on each figure is the galaxy NYU GC name, its stellar mass and its spectroscopic redshift. The solid line indicates 1 arcsec angular size.

However, they also show that some galaxies like NYU321479 and NYU890167 have a more distorted morphology, but still are compatible with being S0 galaxies with a lower inclination (see also Valentinuzzi et al. 2010). In all cases the residuals from the best fit (lowest $\widetilde{\chi^2}$) were visually inspected, to check their quality.

With the low resolution (~ 1") and depth of the SDSS data we were not able to trace any evidence of merging activity, although some residuals were found in the centers. However, Table 3.4 shows the excellent agreement in the derived sizes between the deeper and higher resolution data and the SDSS images, with differences accounting by less than 7%. This is an indirect proof that there is not any hidden component in these massive nearby compact galaxies that may be altering the size of the objects.

The main novelty that the present deep data allows is to explore the shape of these galaxies. In fact, the Sérsic indices and the axial ratios are the values that vary the most between the two samples. In general, these objects are well fitted with moderately low Sérsic indices values ($2<n<4$). The absence of large Sérsic indices is again against the idea that there is a missing faint component surrounding these objects.

3.2.2 K-band surface brightness profiles

In Figure 3.3 we show the circular aperture K-band surface brightness profiles for the 4 compact galaxies in the imaging sample. Although our galaxies have a clear elongation, circular apertures are used to allow a direct comparison with the circular averaged profiles of "normal-sized" galaxies as we will show later. To create our profiles we followed the same technique explained in Pohlen & Trujillo (2006). Briefly, we obtain first the surface brightness profile of the galaxy up to large distances. Then we estimate the sky contribution in those regions outside the galaxy where the profile is flat and we remove (add) this value from (to) the images. Afterward, we calculate again the surface brightness profiles of these galaxies.

For most of our galaxies we can explore their surface brightness profiles down to ~ 27 mag/arcsec^2. This implies probing around 12 magnitudes from the peak of their surface brightness distribution down to their last observed points. This extraordinary depth allow us to investigate whether there is any evidence for any extra hidden (halo-like) component which was not observed in previous shallower images due to its faintness.
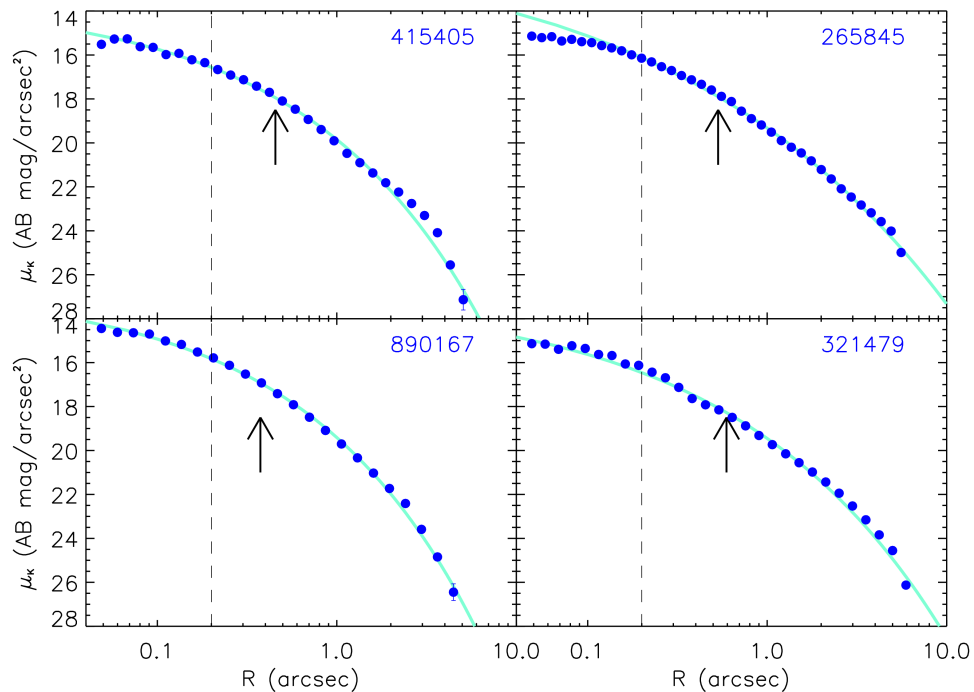
FIGURE 3.3— K-band surface brightness profiles of our sample of nearby massive compact galaxies (blue points). The soft blue lines are the best Sérsic fit to the data. The vertical line shows a FWHM PSF of 0.2 arcsec (the typical resolution of our images). The depth and high resolution of our images allow us to explore the profiles of our sample around 12 magnitudes in range, reaching many (~8) times the effective radii of these objects. The arrows indicate the position of the effective radii of our galaxies.

3.2.3   Stellar mass density profiles

In order to understand the building of the massive galaxies it is worth comparing the stellar mass density profiles of the compact population against the mass distribution of galaxies of a similar mass but with normal sizes. We have transformed our observed K-band surface brightness profiles into stellar mass density profiles using the total stellar masses measured in Blanton et al. (2005b), listed in Table 3.1. We have assumed that the stellar mass to light ratio is constant along the radial distance of the galaxy. The outcome of this exercise is presented in Figure 3.4.

To build the stellar mass density profiles of the "normal-sized" galaxies used as a reference, we took the structural parameters (Sérsic index n, effective radius r_e and stellar mass $M_\star$) of all the galaxies in the NYU catalogue

with $0.8 < M_\star < 1.2 \times 10^{11} M_\odot$ and $0.1 < z < 0.2$. These NYU structural parameters were retrieved from profiles obtained using circular apertures. To facilitate the comparison with our profiles, we divided the NYU galaxies into two different categories: disk-like ($n < 2.5$) and spheroid-like ($n > 2.5$). We find that the average disk-like massive galaxy within the NYU sample at those redshifts has $M_\star = 0.95 \times 10^{11} M_\odot$, $n=2$ and $r_e = 5.7$ kpc. On the other hand, the average spheroid-like object has $M_\star = 0.98 \times 10^{11} M_\odot$, $n=4$ and $r_e = 4.7$ kpc.

Once we obtained these average galaxy profiles, the representative regions of each galaxy category were build using all the galaxies in the NYU sample within the above stellar mass range and redshift interval whose central stellar mass densities were within the 68% of the distribution centered around the mean value.
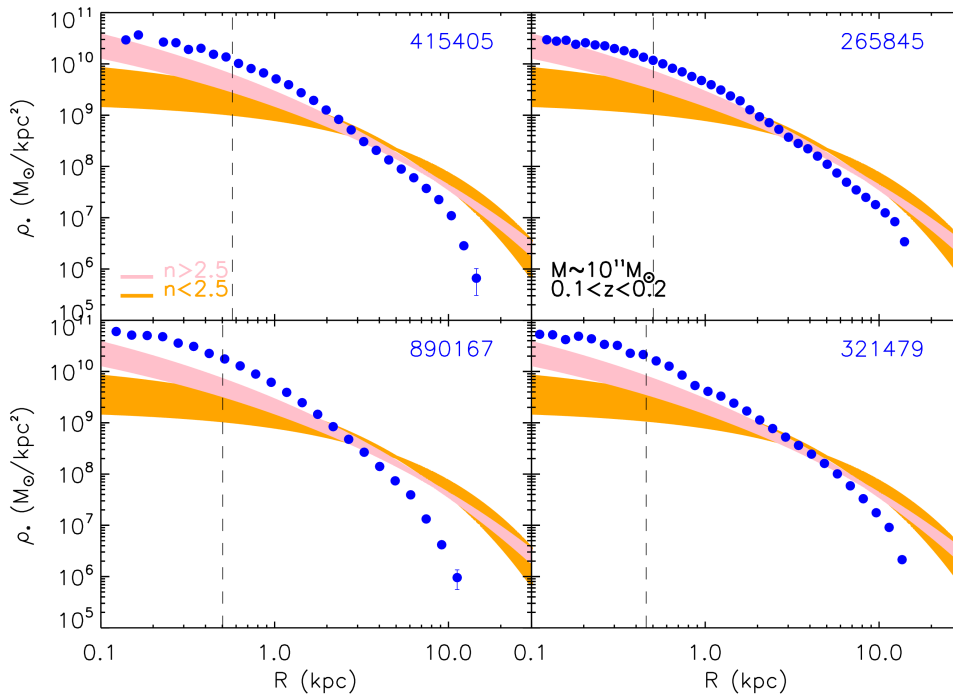
FIGURE 3.4— Stellar surface mass density profiles of our sample of nearby massive compact galaxies (blue points). The observed profiles of the compact massive galaxies are compared with SDSS DR7 stellar mass density profiles of $M_\star \sim 10^{11} M_\odot$ and $0.1 < z < 0.2$ disk-like galaxies (Sérsic index $n < 2.5$; orange region) and with spheroid-like (Sérsic index $n > 2.5$; pink region) galaxies. The vertical line shows the equivalent size in kpc of a FWHM PSF of 0.2 arcsec. The depth and high resolution of our images allow us to explore the profiles of our sample galaxies from 0.1 to 20 kpc.

From the comparison of the stellar mass density profiles of the compact galaxies with those of "normal-sized" objects (Fig. 3.4) it is straightforward to conclude that the compact galaxies do not resemble neither of the two categories. Although visually the elongation of the compact galaxies would suggest that these objects are more like disks, the shape of these profiles are closer to those considered as spheroids in the local universe.

It is easy to see that there is an excess of mass at the center of the compact galaxies and a lack of stars (starting mainly around 3 kpc) in the outer regions. The deep profiles that we present here undoubtedly show that nearby massive compact galaxies do not have an extended outer component and, consequently, are genuinely compact.

An interesting exercise that can be conducted is to estimate the amount of stellar mass within the inner region (R<3 kpc) of the compact galaxies and compare this to the "normal-sized" objects. In the case of the compact galaxies we find that the stellar mass fraction inside 3 kpc ranges from 0.72 up to 0.89. In the case of "normal-sized" objects these fractions are significantly lower: 0.27 for disk-like objects and 0.38 in the case of spheroids. This implies that there is $\sim$2 times more stellar mass inside 3 kpc in the case of the compact massive galaxies than in objects of the same stellar mass but normal size. This difference in stellar mass implies that one would expect a much larger central velocity dispersion in the case of compact galaxies compared to normal galaxies with equivalent stellar mass. A crude estimation (following the virial theorem expectation) suggests that this increase should be of the order of $\sqrt{2}$ as there is a factor of 2 more stellar mass in the central regions.

Are these expectations in agreement with observations? In T09 they found that the average central velocity dispersion of $10^{11}M_{\odot}$ galaxies according to SDSS was 180 km/s. Our massive compact galaxies have an average $\sigma \sim$220 km/s. This is 1.25 larger than the value found in normal galaxies of the same stellar mass and fits quite well with the virial $\sqrt{2}$ expectation. This is another indirect proof of the larger stellar mass densities that massive compact galaxies have in their centers.

3.2.4   Stellar Kinematics

For the kinematical study we used the code `pPxF` with the SSP model templates from V10. To measure the radial velocities we binned the data from the spectroscopic sample in the radial direction to ensure a minimum S/N(Å)=10. In contrast, we binned to achieve S/N(Å) $\sim$ 20 for the velocity dispersion determination. This means that we summed at least two pixels for each bin, to take

into account the effect of the seeing. In those cases where the outermost radii did not reach the required S/N we omitted those points for the analysis.
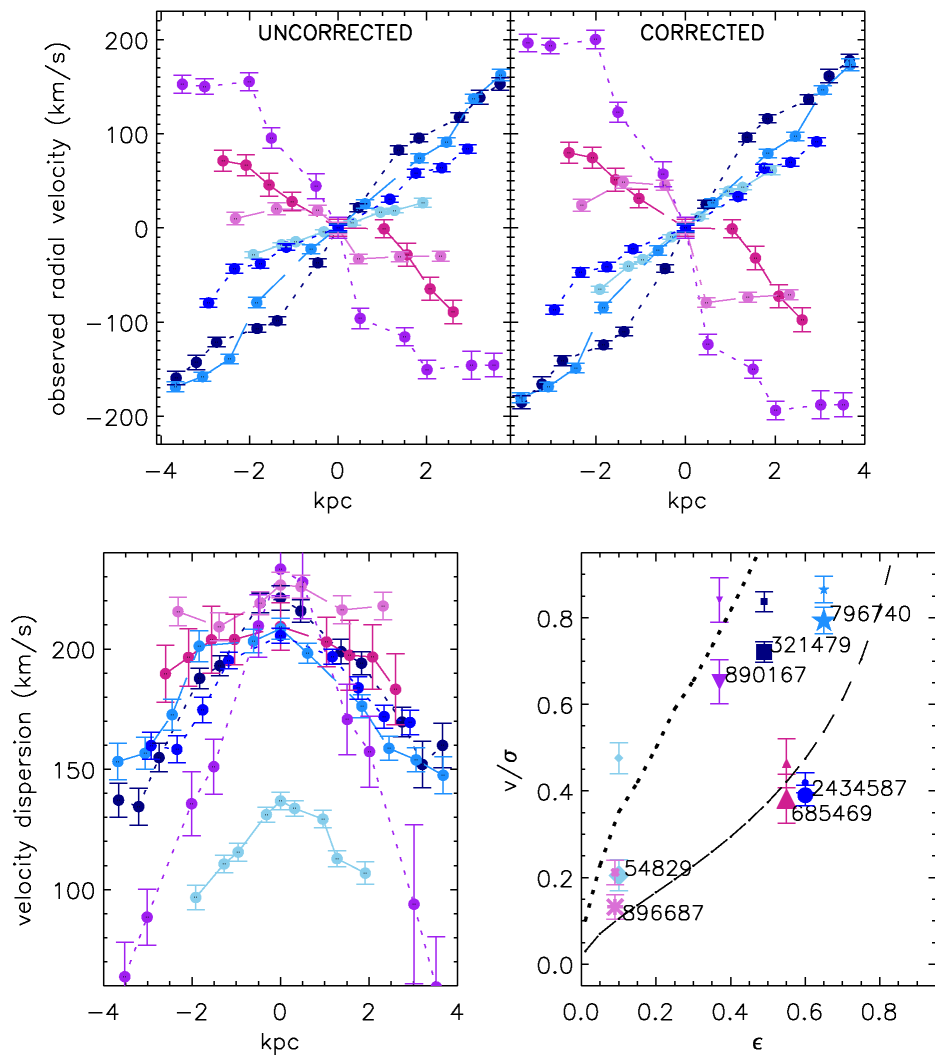
FIGURE 3.5— Radial velocities derived with pPxF: first panel shows the observed radial velocities, while in the second one, radial velocities corrected from inclination effects are plotted. *c)* Velocity dispersions from pPxF; *d)* The anisotropy diagram (V/σ, ε). Big/small symbols correspond to the objects without/with correcting from inclination effects, in case they should be corrected. The dotted black line corresponds to the location of models for oblate edge-on isotropic ($\delta = 0$) galaxies, the dashed one to the linear relation $\delta = 0.7\varepsilon_{intr}$ from Cappellari et al. (2007).

We find that five of our galaxies are rapidly rotating (see Figure 3.5a). The galaxies 890167, 321479 and 796740 show both the largest radial velocities and higher velocity dispersions (σ), whereas for the remaining four galaxies we cannot find a significant rotation. It is worth noticing that except for 890167 and 896687, we can not determine if we have reached the flat part of the rotation curve and, therefore, consider $V_r = V_{max}$. In these cases, we have considered $V_r = V_{high}$. Not reaching this V_{max} prevented us to conclude whether these objects are also supported by rotation.

Considering that our galaxies could have a significant disk component due to their low axial ratio, we explore how would radial velocities be if corrected for inclination effects. The radial velocity is corrected with $v_{r,i} = v_r/sin\,i$ where $cos\,i = b/a$ defines the inclination angle i. Nevertheless, we do not have enough information to select which galaxies are face- or- edge on. Therefore, the applied correction gives us an upper limit to the rotation in case a disk exists. As shown in Figure 3.5b, the maximum velocities derived from the corrected curves, are larger than those derived from the uncorrected ones. Overall, we find high radial velocities (V_r as high as $200\,\mathrm{km\,s^{-1}}$) and high velocity dispersions ($\sim 200\,\mathrm{km\,s^{-1}}$) for most of our galaxies. The high velocity dispersions are in good agreement with the values found in T09 and in Valentinuzzi et al. (2010) for a sample of massive, similarly sized, compact galaxies in local clusters ($z \sim 0.05$).

A dichotomy for the elliptical family has been suggested: from one side, the most massive galaxies, which are slow rotators, metal-rich, with a flat central luminosity profile, showing evidence of triaxiality; and from the other side, the less massive ones, being fast rotators, metal-poor, with a clumpy luminosity profiles, maybe containing disks and being axisymmetric (e.g., Davies et al. 1983, Bender 1988, Kormendy & Bender 1996). However, it has been recently shown that most ETGs in the local Universe are fast rotators if parametrized by their λ_R (Emsellem et al., 2011). They claim that this parameter, which is derived from the first two stellar velocity moments, is much better to classify ETGs.

However, the anisotropy diagram (Binney 2005, Cappellari et al. 2007, and references therein) is still a powerful tool to discriminate between fast and slow rotators. This diagram relates the ratio between the ordered and random motion (V/σ) to the galaxy observed flattening (ε). Figure 3.5d shows the position of our objects in the anisotropy diagram. The observed V/σ value is obtained from the central velocity dispersion (equivalent to approximately $1\,\mathrm{R}_e$) and V_{max} (or V_{high} for those where V_{max} was not reached, representing a lower limit). The two lines in Fig. 3.5d correspond to models for edge-on oblate gala-

xies with different anisotropies: the upper dotted line corresponds to isotropic models $\delta = 0$, the lower dashed one to the linear relation $\delta = 0.7\varepsilon_{intrinsic}$, which approximately traces the lower envelope described by the location of the observed fast-rotating galaxies on the (V/σ) diagram (see Cappellari et al. 2007 for a full discussion of these relations). Although we do not calculate V/σ in the exact same way, fast rotators would lie to the left of the dashed line. As it can be seen, the majority of the massive compact galaxies, without correcting them from inclination effects (big symbols), are fast rotators, except galaxies 685469 and 2434587 that fall in the slow rotators regime. However, if an inclination correction is applied, the latter galaxies practically reach the separating line. As the V_{max} was not reached for some of them, their position should be considered a lower limit, indicating that all our galaxies seem to be fast rotators.

3.2.5 Stellar Population Analysis

Central Properties

We performed a stellar population analysis of the galaxies with high-quality spectra using the V10 models and the newly-defined LIS-8.4Å system of indices introduced in that paper. As described in Section 2.4.1, this means that the models have a constant resolution (FWHM=8.4Å) across the whole wavelength range. We use as age indicator the newly-defined metallicity-insensitive index Hβ_o (Cervantes & Vazdekis, 2009). This index, combined with a metallicity sensitive index, as Mgb or Fe4383, gives a very orthogonal model grid, given its reduced sensitivity to metallicity when compared to the classical Hβ Lick index. The stellar population parameters were derived with `RMODEL` selecting typically the bivariated fits, although a careful visual inspection was also carried out to check the results.

For the central stellar population analysis we summed up the spectra within $\sim 1\,R_e$. Before summation, the galaxy spectra were corrected pixel by pixel for the radial velocity and then all pixels were broadened to the central velocity dispersion. For all galaxies, we corrected from emission line effects using `GANDALF` (Sarzi et al., 2006) with the V10 model templates, although we only found nebular emission in one galaxy, 685469.

Figure 3.6 shows the index Hβ_o *vs* the combined metallic indicator [MgFe50], that is insensitive to α-enhancement (Kuntschner et al., 2006). Our compact galaxies present young mean SSP-equivalent ages ($\lesssim 2\,$Gyr).
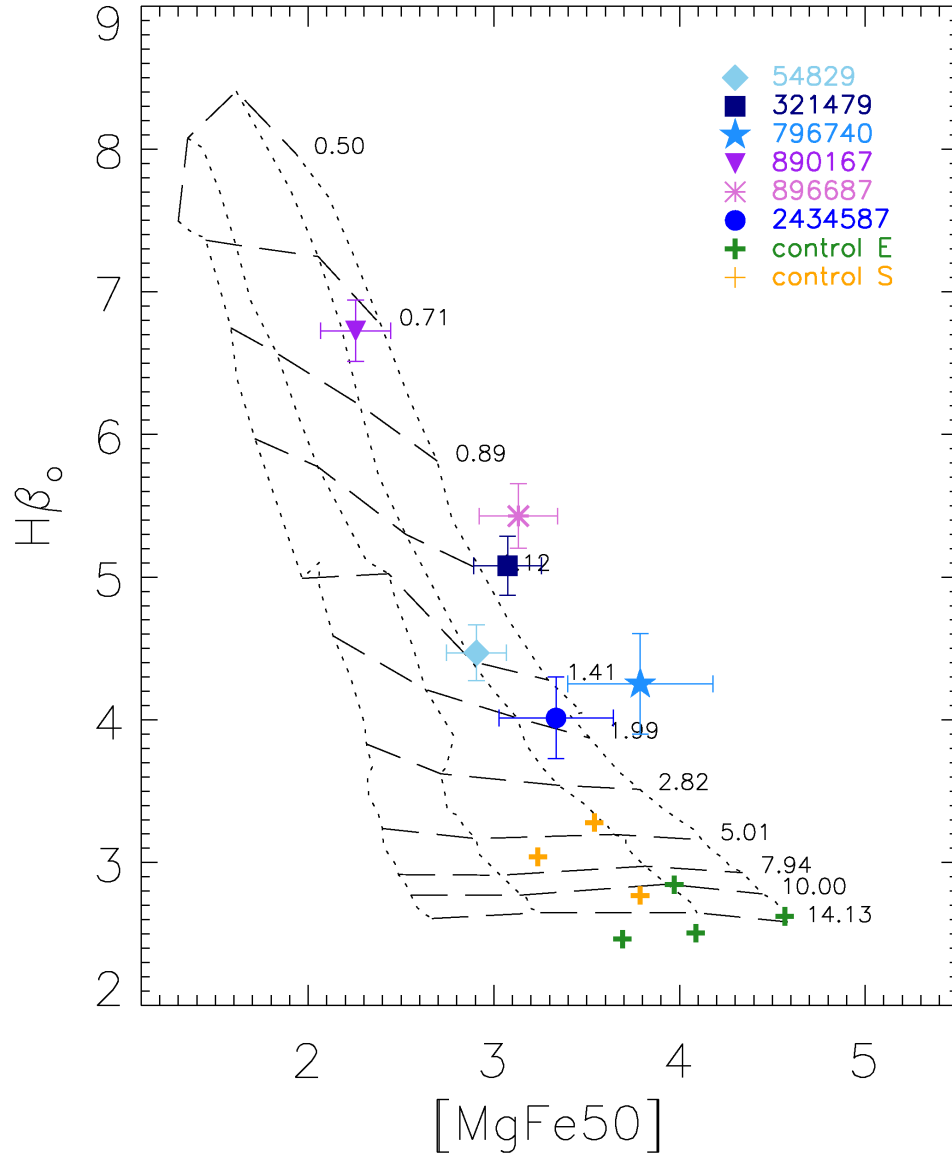
FIGURE 3.6— The age-sensitive indicator Hβ_o is plotted *vs* the composite index [MgFe50], which is a good proxy for the total metallicity. All indices are in the LIS-8.4$\mathring{A}$ flux-calibrated system and the SSP model grids of V10 are plotted. Age (in Gyr) increases from top to bottom as indicated in the labels, and metallicity from left to right ([Z/H]= -0.71, -0.40, 0.00, +0.22). Symbols are like in Fig. 3.5 and green crosses correspond to the control ellipticals from Sánchez-Blázquez et al. (2006a), that have velocity dispersions similar to those from our objects. Also overplotted as yellow crosses, the control spirals with similar velocity dispersions from the Sauron Project (Falcón-Barroso et al., 2011b).

These results are in good agreement with the analysis performed in T09 but in disagreement with Valentinuzzi et al. (2010), who found old stellar populations for their local compact massive galaxies. Galaxy 685469 is not shown in these figures because its age and metallicity were derived from the full spectrum fitting with ULySS. This galaxy was affected by strong emission lines that, even corrected with GANDALF, make the $H\beta_o$ and Fe5015 features unreliable. This galaxy is very different from the rest, being the oldest one with $2.65\,$Gyr and with a total metallicity $[Z/H]= -0.55$. For comparison, we have overplotted some control ellipticals with similar velocity dispersions from Sánchez-Blázquez et al. (2006a) (NGC2329, NGC3379, NGC4621 and NGC5812; green crosses) and some spirals observed for the SAURON project in Falcón-Barroso et al. (2011b) (NGC4235, NGC5689 and NGC6501; yellow crosses). Both control samples are in the region of the grid corresponding to old ages. Thus, our objects are much younger than both ellipticals and spirals of the local universe.

This result is also shown in Figure 3.7, where we present the inferred ages and total metallicities from our index-index plots. Our compact galaxies (purple) show much younger SSP-equivalent ages and higher total metallicities than the elliptical (green) and spiral (yellow) control samples.
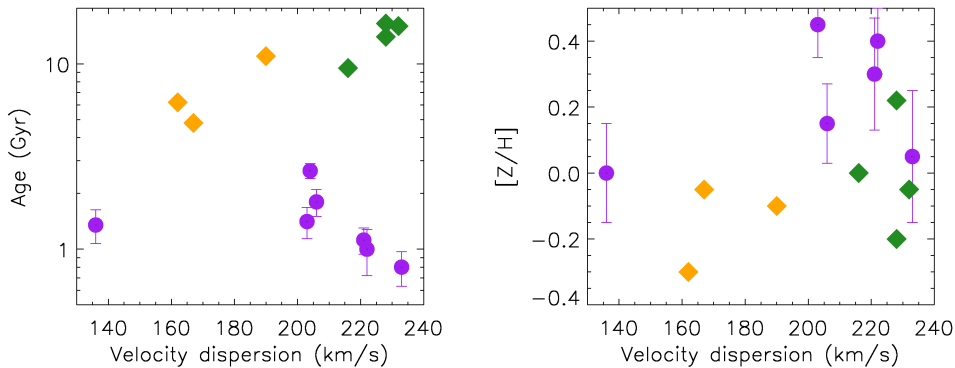
FIGURE 3.7— Derived stellar population parameters plotted *vs* the velocity dispersion for our compact galaxies (purple circles). Control ellipticals (green diamonds) and control spirals (yellow diamonds) are also shown. Note that for a given velocity dispersion, our compact objects do not show similar ages as their local large-sized counterparts, either elliptical or spiral galaxies. Moreover, their total metallicities are systematically richer.

For the metallicity inferred from the different index-index grids, we find in overall values above solar for our compact galaxies, though there is a scatter in the metallicity inferred from the panels in Figure 3.8. The metallicity values derived from the different elements can be used to estimate, on a relative scale,

the abundance ratio pattern of these objects. Note that the values obtained this way ($[Z_x/Z_{Fe}]$) are a good proxy for the abundance ratios (Yamada et al. 2006, V10).

The CN was only measured for four out of the seven galaxies due to the limited spectral coverage. For these four galaxies, we find that $[Z_{CN}/Z_{Fe}] \leq 0$, which is at odds with the typical $[CN/Fe] \geq 0$ found in giant ellipticals of the same mass (see Fig. 3.8). Note, however, that the [CN/Fe] shows a dependence on the environment (Sánchez-Blázquez et al. 2003, Carretero et al. 2004), with lower CN_2 for denser environments, but our objects do not belong to any known cluster or group. The $[Z_{Ca}/Z_{Fe}]$ is also underabundant for most of our galaxies. This result is the same that the one found in Vazdekis et al. (1997) and Cenarro et al. (2004) for massive ellipticals. This behavior is not yet clear, as the Ca, which is an α-element, is supposed to track Mg. For the $[Z_C/Z_{Fe}]$ and $[Z_{Mg}/Z_{Fe}]$, the behavior is more complex. Visual inspection suggests that, discarding the three youngest objects that fall in the fully-degenerated part of the grid, the other galaxies do not show a significant departure from scaled-solar rate. However, the degeneracy of the models in this age regime prevents us to quantitatively determine the abundance ratio for these elements.

We can conclude that the abundance ratio estimates for our compact objects, do not resemble those seen in ellipticals of similar velocity dispersion, except for the [Ca/Fe] abundance ratio.

Gradients

Taking advantage of the spatial information provided by our high-quality long-slit spectra we also carried out a similar analysis to study possible gradients in the stellar population parameters. The previous analysis was done using a central aperture, but we have extracted two other annular apertures or radii reaching, in a couple of cases, $3\,R_e$ and $4\,R_e$. Table 3.6 specifies the radial coverage of each aperture, which will be used throughout the paper (r0 for the central aperture, r1 for the first annular aperture, and r2 for the outermost aperture).

Overall, we do not find any strong age or metallicity gradient, as shown in Figure 3.9. There is a trend suggesting the centers to be slightly younger, but these differences in age are really small ($\leq 0.5\,$Gyr). There is also a small trend of the centers to have slightly higher metallicity, but these changes are within the errors. However, gradients in the abundance trends are difficult to interpret because the grids are too degenerated for such low ages, as stated in the previous section.
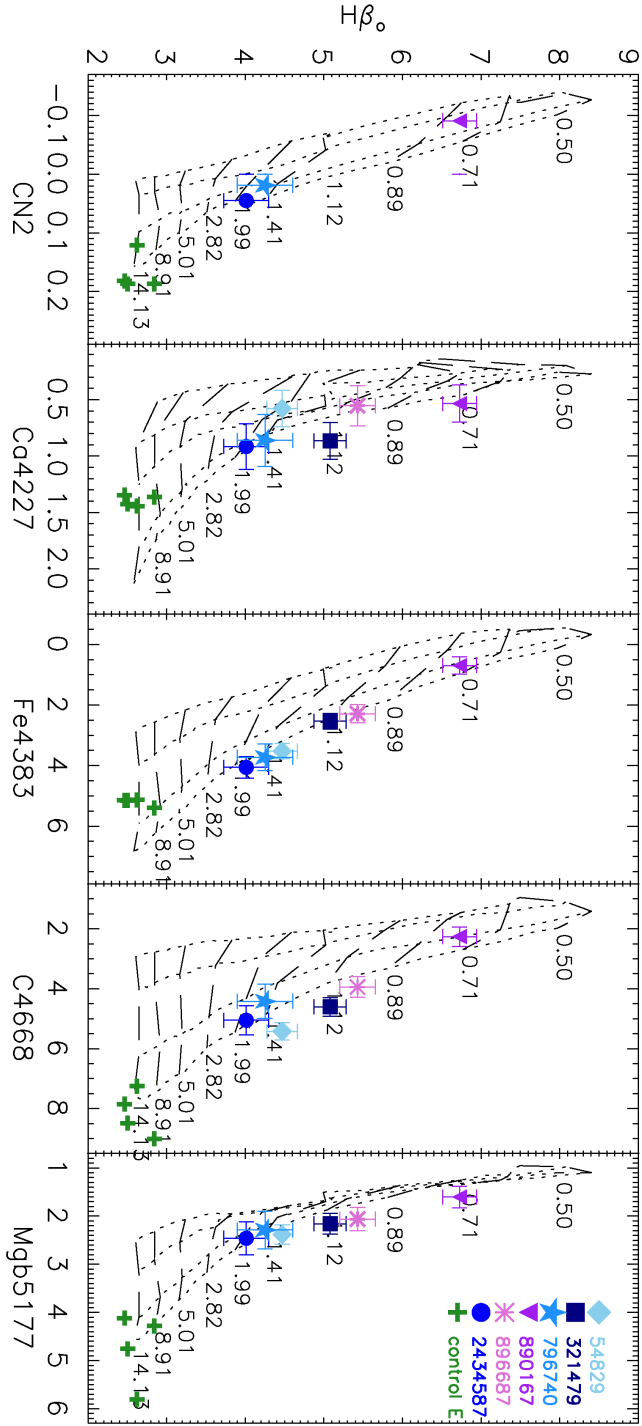
FIGURE 3.8— The age-sensitive indicator Hβ_o is plotted against various metallicity indices in the LIS8.4Å flux-calibrated system. The SSP model grids of V10 are plotted. Age (in Gyr) increases from top to bottom as indicated in the labels, and metallicity from left to right ([Z/H]=-0.71, -0.40, 0.00, +0.22, except for the Ca4227 grid, where we also plot the models with [Z/H]= -1.01). Symbols correspond to Figures 3.5 and 3.6.

ID NYU	age(Gyr)	[Z/H]	age(Gyr)	[Z/H]	age(Gyr)	[Z/H]	age(Gyr)	[Z/H]
	[MgFe50]-Hβ_o		Fe4383-Hβ_o		Mgb-Hβ_o		C4668-Hβ_o	
54829	$1.35^{+0.28}_{-0.05}$	$0.00^{+0.18}_{-0.30}$	$1.33^{+0.10}_{-0.16}$	$0.30^{+0.08}_{-0.07}$	$1.30^{+0.05}_{-0.04}$	$0.35^{+0.05}_{-0.05}$	$1.30^{+0.06}_{-0.13}$	$0.40^{+0.10}_{-0.10}$
321479	$1.12^{+0.08}_{-0.06}$	$0.30^{+0.15}_{-0.21}$	$1.12^{+0.30}_{-0.12}$	$0.22^{+0.16}_{-0.15}$	$1.05^{+0.08}_{-0.05}$	$0.50^{+0.07}_{-0.07}$	$1.11^{+0.08}_{-0.06}$	$0.35^{+0.10}_{-0.10}$
796740	$1.41^{+0.17}_{-0.04}$	$0.45^{+0.12}_{-0.11}$	$1.40^{+0.28}_{-0.08}$	$0.30^{+0.18}_{-0.20}$	$1.48^{+0.21}_{-0.18}$	$0.20^{+0.05}_{-0.05}$	$1.50^{+0.27}_{-0.21}$	$0.10^{+0.10}_{-0.10}$
890167	$0.83^{+0.07}_{-0.03}$	$0.05^{+0.00}_{-0.20}$	$0.80^{+0.08}_{-0.05}$	$0.00^{+0.20}_{-0.21}$	-	-	$0.80^{+0.08}_{-0.10}$	$0.00^{+0.12}_{-0.25}$
896687	$1.05^{+0.08}_{-0.06}$	$0.40^{+0.10}_{-0.13}$	$0.98^{+0.08}_{-0.06}$	$0.25^{+0.10}_{-0.20}$	$0.90^{+0.07}_{-0.04}$	$0.50^{+0.04}_{-0.04}$	$0.99^{+0.05}_{-0.10}$	$0.30^{+0.08}_{-0.08}$
2434587	$1.80^{+0.36}_{-0.25}$	$0.15^{+0.10}_{-0.12}$	$1.75^{+0.40}_{-0.19}$	$0.30^{+0.14}_{-0.11}$	$1.84^{+0.35}_{-0.25}$	$0.15^{+0.07}_{-0.07}$	$1.78^{+0.32}_{-0.18}$	$0.20^{+0.05}_{-0.05}$

TABLE 3.5 — Ages and metallicities derived from the different index-index grids of Figure 3.6. Errors were estimated with 1000 Monte-Carlo simulations using the errors on the indices and deriving 1σ error contours in the age-metallicity space.

ID NYU	r0 (kpc)	r1 (kpc)	r2 (kpc)
54829	0.0 - 0.9	0.9 - 1.4	1.4 - 2.0
321479	0.0 - 1.1	1.1 - 1.9	1.9 - 2.7
685469	0.0 - 1.0	1.0 - 1.8	1.8 - 2.5
796740	0.0 - 1.5	1.5 - 2.5	2.5 - 3.4
890167	0.0 - 1.8	1.8 - 3.0	3.0 - 4.3
896687	0.0 - 1.1	1.1 - 1.8	1.8 - 2.5
2434587	0.0 - 1.2	1.2 - 1.6	1.6 - 2.8

TABLE 3.6— Radial coverage of each aperture. The notation will we followed through all the paper: r0 for the central aperture, r1 for the first annular radius, and r2 for the second and outermost aperture.
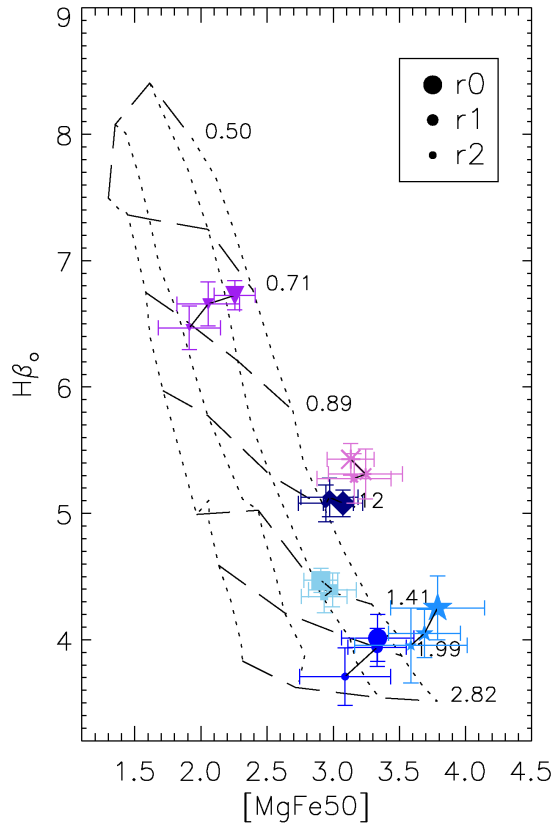
FIGURE 3.9— The age-sensitive indicator $H\beta_o$ is plotted against the mean metallicity indicator [MgFe50] for the seven compact galaxies. We show the model grid corresponding to the age range covered by our galaxies. Age (in Gyr) increases from top to bottom as indicated in the labels, and metallicity from left to right ([Z/H]= -0.71, -0.40, 0.00, +0.22). Symbols are like in previous figures with size indicating the different apertures: decreasing size for increasing aperture.

Star Formation Histories

Here we investigate whether the young mean SSP-equivalent ages obtained for these compact galaxies are due to the contribution of recent starbursts that mask an old embedded population, which is dominant in mass, or, alternatively, whether they are genuinely young objects. For this purpose we apply the full spectrum-fitting approach to estimate their Star Formation Histories (SFHs), with the code STARLIGHT (Cid Fernandes et al., 2005), with the V10 SSP SED library.

We have defined two bins for the ages in the SFHs: "young" for lower than the SSP-equivalent age ($\lesssim 2\,\mathrm{Gyr}$) and "old" for $\geq 5\,\mathrm{Gyr}$. We have selected these two bins as the majority of the galaxies do not present populations in between. Table 3.7 (Figure 3.10 for illustration and Appendix A for the rest of derived SFHs) shows the percentages derived from the SFHs. The uncertainties on the L- and M-weighted "young" parameters were estimated with 2283 pairs of repeated SDSS ETG observations. For all these duplicate spectra, we measured the parameter with STARLIGHT, using the same set-up and set of model templates as for the primary spectra. A linear relation is found between the Δyoung and the average S/N of each pair. The S/N of the observed spectra are fed into the previous relation to estimate the rms value of the "young" parameters presented on Table 3.7.
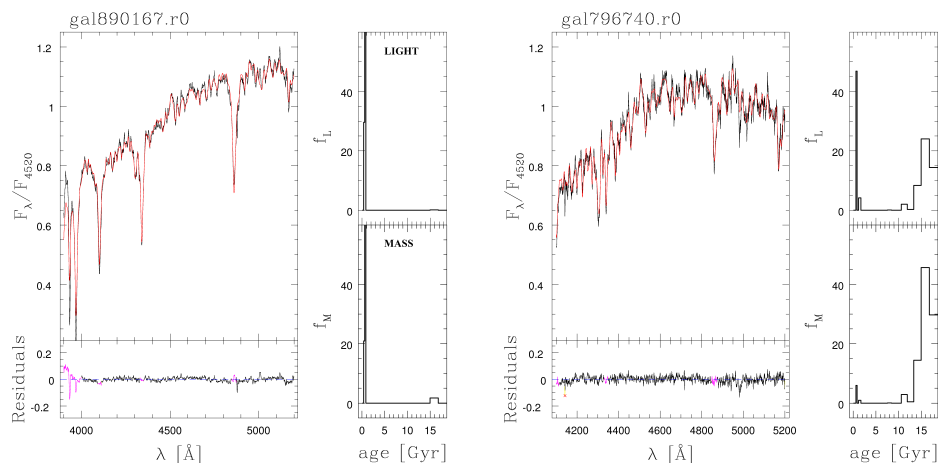
FIGURE 3.10— Results from STARLIGHT for the central apertures of galaxies 2434587 and 54829. On the upper-left hand, the galaxy spectra (black) is fitted with the models from V10 (red), bottom-left panel shows the fitting residuals. The recovered Star Formation History are also shown, in light (upper-right panel) and in mass (down-right panel) for each galaxy. All our objects show recent bursts, some of them leading to a big contribution from the young stellar populations. The rest of galaxies SFHs can be found in Appendix A.

ID NYU	Aperture	%young$_L$	%young$_M$
54829	r0	71± 20	28± 21
	r1	72± 19	36± 19
	r2	73± 19	34± 19
321479	r0	70± 18	17± 18
	r1	68± 17	16± 17
	r2	68± 17	16± 17
685469	r0	82± 19	65± 19
	r1	88± 19	68± 19
	r2	89± 19	66± 19
796740	r0	51± 19	07± 19
	r1	52± 18	07± 19
	r2	59± 15	11± 16
890167	r0	99± 14	97± 15
	r1	98± 10	88± 11
	r2	97± 9	75± 10
896687	r0	60± 18	12± 18
	r1	55± 15	10± 16
	r2	55± 14	10± 15
2434587	r0	60± 20	22± 20
	r1	62± 19	23± 19
	r2	68± 18	35± 19

TABLE 3.7— Fractions of young ($\lesssim 2\,\mathrm{Gyr}$) stellar populations retrieved from the SFHs of the galaxies using the STARLIGHT full-spectral-fitting code. First, the luminosity-weighted fractions, second the mass-weighted ones. For each galaxy, the first line corresponds to the central aperture, the second to the second aperture and the third to the outermost radius considered for this study.

We can separate our objects in two families: (1) those galaxies containing mainly old stellar populations (with a young contribution lower than 25% in mass); (2) those with a large fraction of young stars (contributing with more than 25% in mass). This last result is surprising, as we would not expect these massive galaxies to form nearly half (and even more) of their mass in recent bursts.

The lack of strong gradients derived from the line-strength analysis is confirmed, as fractions remain unchanged through the different apertures. This result also implies that the starburst takes place along the whole structure of the galaxy.

Apart from `STARLIGHT`, we repeated the analysis with two other codes, `ULySS` (Koleva et al., 2009) and `STECKMAP` (Ocvirk et al. 2006a, Ocvirk et al. 2006b), all with the V10 SSP SED library. The analysis was repeated by different coauthors independently to double check the possible bias introduced by the selection parameters, the use of different wavelength spectral regions, etc. We find that the three codes provide very consistent results.

In order to trust the recovered SFHs and check the reliability of the results we have also performed a couple of tests, described in Appendix A. The first test constrains the SFH derived with the full-spectrum fittings techniques in terms of the derived fractions. Following the results, we find that all our galaxies show fractions compatibles with their mean SSP-equivalent age (see Fig. A2). The second test checks the robustness of the results, as it compares the mean age and metallicity from the galaxy and the one inferred when measuring the line-strengths of the fitted model (Fig. A3). We are able to recover the same age and metallicity, although the latter with an error of -0.10 dex.

3.2.6 Mass Estimates

Finally, we have revised the mass estimates for these objects, as the mass was one of the selection criteria of the original sample. We have estimated the stellar and dynamical masses following different approaches.

Stellar masses

As mentioned before, our galaxies were originally selected from the NYU VAGC (B07) with a mean stellar mass for the seven galaxies in the spectroscopic sample of $M^*_{B07} \sim 9.2 \times 10^{10}\,M_\odot$. However, the catalog from the SDSS/DR7/MPA[1] (hereafter MPA), gives systematically lower masses, with a mean stellar mass of $M^*_{MPA} \sim 8.3 \times 10^{10}\,M_\odot$, as seen in Table 3.8. The mass estimates of these two analysis were obtained by fitting the broad-band SDSS (u,g,r,i,z) photometry, with the models of Bruzual & Charlot (2003) (BC03, hereafter) and a Chabrier IMF (Initial Mass Function). However, in B07 they added the near-IR photometric bands of 2MASS (J, H, K_s).

Following the approach of Kauffmann et al. (2003a) based on the spectral fitting, instead of the photometry, we used the SSP model SEDs of V10 with a Kroupa Universal IMF. For this purpose we use the M/L corresponding to the SED model that best fits the galaxy spectra, which provides a mean luminosity-weighted age and metallicity. The stellar mass was inferred by calculating the M/L in the SDSS r-band, adopting the `GALFIT` magnitude as luminosity

---

[1](http://www.mpa-garching.mpg.de/SDSS/DR7/)

estimate, after correcting for galactic extinction. The stellar masses computed in this way take into account the mass of the luminous stars and the remnants which, for the ages we are considering ($\sim 2\,\mathrm{Gyr}$), is of the order of 0.6 times the initial mass of gas converted into stars. The mean stellar mass calculated this way is $\mathrm{M^*}_{SSP} \sim 4.3 \times 10^{10}\,M_\odot$.

In a different approach, we consider instead of an equivalent-SSP stellar population, the spectra resulting from integrating the contribution of different SSPs, with different M/L, according to the SFH derived with `STARLIGHT`, leading to a mean $\mathrm{M^*}_{SFH} \sim 1.5 \times 10^{11}\,M_\odot$. For comparison, we carried a similar approach with the SDSS fiber spectra, but with a longer wavelength-range, using the mass-weighted SFHs solution from `STARLIGHT`, obtaining a mean stellar mass of $\mathrm{M^*}_{SDSS} \sim 1.3 \times 10^{11}\,M_\odot$.

From the above estimates it is clear that the stellar mass determination is not straightforward. It has long been reported that the methodology, the models, the selection of the IMF and other parameters, strongly affect these determinations (see e.g.: Bell & de Jong 2001, Kauffmann et al. 2003a, Swindle et al. 2011 and Cappellari 2012). For example, in B07 the author give a mean mass of $\mathrm{M^*}_{B07} \sim 9.21 \times 10^{10}\,M_\odot$ employing a Chabrier IMF. This is translated into a mean mass of $\mathrm{M^*}_{B07} \sim 1.0 \times 10^{11}\,M_\odot$ if employing a Kroupa IMF, more similar to our $\mathrm{M^*}_{SFH}$ (see also Chapter 4 for more about the IMF impact).

Masses derived with SFHs are systematically larger than the equivalent-SSP measurements. Since in the SSP-method, the ages are luminosity weighted, the final values are strongly biased to the youngest stellar component present in the galaxy and, therefore, the M/L ratios are also biased towards lower values, as their stellar masses. The SFH derived from full-spectrum fitting instead, reveals an important presence in terms of mass fractions of old stellar populations, whose M/L is considerably higher than those of the SSP corresponding to the luminosity-weighted age, giving larger values the those derived with a SSP.

Indeed, the objects with the largest contribution from old stellar populations (321479, 796740 and 896687 and 2434587) show the largest differences (by a factor 4). Instead, the three galaxies with the highest fraction of young stellar population show a more modest difference between the two estimates (by a factor of 2). Moreover, we have calculated the M/L inferred by a single SSP and by the SFH on our control elliptical galaxies. As their luminosity and mass-weighted ages are similarly old, we should not find a relevant difference in the M/L, as we do.

ID NYU	M*$_{SSP}$	M*$_{SFH}$	M*$_{SDSS}$	M*$_{B07}$	M*$_{MPA}$
			[$\times (10^{10} M_\odot)$]		
Model	V10	V10	V10	BC03	BC03
IMF	Kroupa	Kroupa	Kroupa	Chabrier	Chabrier
type	spectra	spectra	spectra	phot	phot
range(nm)	[380-530]	[380-530]	[360-735]	SDSS+2MASS	SDSS
54829	4.06	9.61	8.22	8.39	7.09
321479	5.01	20.30	16.16	10.10	8.19
685469	4.67	5.45	11.10	9.03	7.29
796740	4.45	23.05	13.72	9.76	7.65
890167	2.05	3.21	13.92	8.79	12.49
896687	5.11	23.12	11.18	9.23	7.39
2434587	4.31	14.42	10.63	8.37	6.77
MEAN	4.27	14.89	12.78	9.21	8.29

TABLE 3.8— Stellar mass estimates. M*$_{SSP}$ is the SSP-equivalent mass and M*$_{SFH}$ is the one computed with the mix of SSPs from the SFHs (see sect. 4.3), for both our spectra (M*$_{SFH}$) and the SDSS one (M*$_{SDSS}$). M*$_{B07}$ and M*$_{MPA}$ are the values from B07 and MPA catalogs.

Dynamical masses

The dynamical mass is considered to be a good proxy for the total mass of a galaxy. The estimate comes from the Scalar Virial Theorem (Binney & Tremaine 2008, and references therein). As our objects show both velocity dispersion and rotation motions (the latter to a lesser extent), we should account for both contributions (Epinat et al., 2009): $M_{dyn} = M_\theta + M_{vir}$. These contributions are shown in Table 3.9.

The rotationally supported term is the one contributing less for our galaxies:

$$M_\theta = [V^2 R]/G, \tag{3.2}$$

where V is the velocity at radius R and G the universal gravitational constant. We choose V=V_{max} for those galaxies for which we reached the maximal velocity rotation, while we take V=V_{high} for the rest, considering the highest radial velocity obtained. The three galaxies showing the highest radial velocities (from Sect. 3.2) are the ones showing the largest contributions from this term.

Following the approach from Bertin, Ciotti & Del Principe (2002), the virial mass is:

$$M_{vir,n} = [K(n)\sigma^2 R_e]/G, \tag{3.3}$$

where

$$K(n) \simeq \frac{73.32}{10.465 + (n - 0.95)^2} + 0.954, \tag{3.4}$$

where n is the Sérsic index, R_e the circularized effective radius in kpc and σ the velocity dispersion in $\mathrm{km\,s}^{-1}$. This $K(n)$ factor takes into account the geometry of the mass distribution and velocity projection along the line of sight. Under the assumption of homology, Cappellari et al. (2006) determined that the best-fitting virial relation with dynamical models was using $K(n) = 5$.

A mean $\mathrm{M}_{dyn(nohom)} = 6.89 \times 10^{10}\,M_\odot$ and $\mathrm{M}_{dyn(hom)} = 7.65 \times 10^{10}\,M_\odot$ are obtained, both lower than the mean stellar masses. The mass estimates for the galaxy 54829 are not taken into account to compute mean masses, as it is the only one having a much lower σ (that contributes quadratically on the equation), which would strongly bias the mean values to lower masses. For consistency, we neither use this galaxy for the stellar mean masses.

What is wrong with the mass?

Figure 3.11 shows different stellar masses *versus* the dynamical ones. Filled symbols refer to the homology virial mass, open symbols to the non-homology one. The dashed line corresponds to the 1:1 relation.

ID NYU	M_v	$\mathrm{M}_{v,n}$	M_θ	$\mathrm{M}_{dyn(h)}$	$\mathrm{M}_{dyn(noh)}$
			$[\times (10^{10} M_\odot)]$		
54829	2.56	1.91	0.04	2.60	1.95
321479	6.81	3.52	1.78	8.59	5.30
685469	7.23	8.54	0.38	7.61	8.92
796740	6.05	8.06	2.32	8.37	10.38
890167	5.11	5.11	2.10	7.21	7.21
896687	8.13	5.44	0.02	8.15	5.46
2434587	5.52	3.69	0.43	5.95	4.12
MEAN	6.47	5.72	1.17	7.65	6.89

TABLE 3.9— Dynamical mass estimates. The virial masses are $\mathrm{M}_{v,n}$ and M_v, the first accounting for the non-homology. The rotation contribution is stated as M_θ and $\mathrm{M}_{dyn(h)}$ and $\mathrm{M}_{dyn(noh)}$ are the total dynamical masses again accounting for the homology/non-homology (Cappellari et al. 2006). All mean mass values were computed without the galaxy 54829, due to its low velocity dispersion in comparison to the other galaxies.
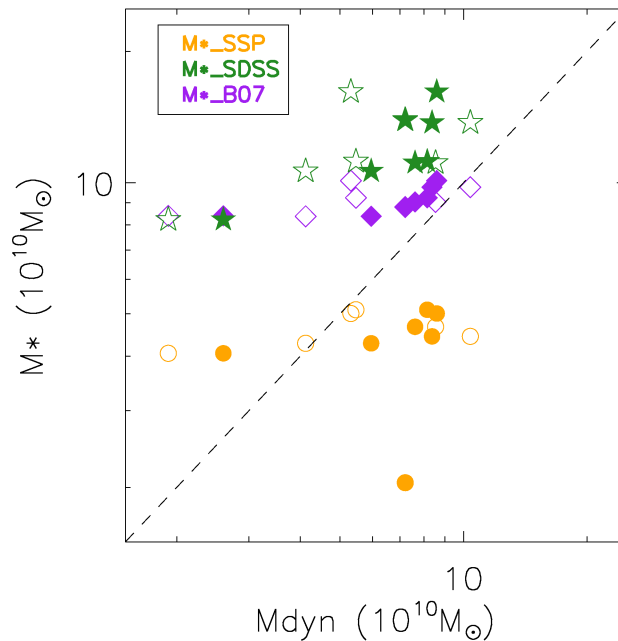
FIGURE 3.11— Dynamical mass *vs* stellar mass computed with different approaches. Filled/open symbols state for the homology/non-homology. Yellow circles are the M^*_{SSP}, violet diamonds are M^*_{B07} and green stars are M^*_{SDSS}. The dashed line is the 1:1 relation. Mainly all the stellar masses, except for the M^*_{SSP}, are similar or bigger than the dynamical mass.

The first noticeable result is the difference in the stellar mass depending on the methodology adopted, as stated above. The lowest stellar masses are obtained with the SSP approach (M^*_{SSP}, yellow circles), and they increase when using the SFHs derived for the galaxy (M^*_{SDSS}, green stars). In between, we have the stellar masses from the photometric fitting in B07 (violet diamonds).

The most intriguing point is that the derived stellar masses are larger, on average, than the dynamical masses (except for the M^*_{SSP}). This should be the contrary, with dynamical masses being larger than stellar masses (Cappellari et al. 2006, van der Wel et al. 2006, van de Sande et al. 2011). Stellar masses (which do not take into account the dark matter fraction) being larger is unphysical and the first idea is to assume that mass estimates are wrong.

However, Figure 3.12 shows the inconsistent but real presence of galaxies whose stellar masses exceed the dynamical ones for SDSS galaxies. This was previously noted by e.g. Drory, Bender & Hopp (2004), where they showed

that this occurs particularly at lower masses, and also in the recent work of Martinez-Manso et al. (2011) for four compact and massive early-type galaxies at z$\sim$1. The figure presents the M$_{star}$ *vs* M$_{dyn}$ for 40,000 ETGs from the SPIDER sample (La Barbera et al. 2010a, LB10 hereafter). Stellar masses were taken from the MPA catalog, which used a photometric SED fitting with the Bruzual & Charlot (2003) models using a Chabrier IMF. However, it is worth noticing that if the stellar masses were derived from the full spectrum-fitting as above, the obtained values would be systematically higher, leading to more galaxies to lie above the 1:1 relation.
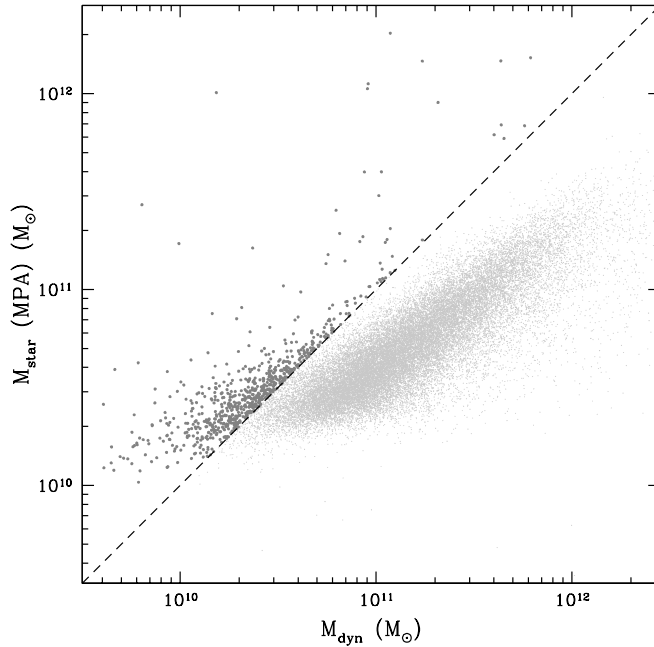
FIGURE 3.12— Dynamical *vs* stellar masses for 40,000 SDSS-DR7 ETGs from the SPIDER project (LB10). Here we want to emphasize that some galaxies do show dynamical masses lower than their stellar mass (highlighted), a contradiction to the well established relation of M$_{star}$ $\leq$ M$_{dyn}$.

Where does the problem come from? Are the stellar masses wrong or are the dynamical ones? Or both?

On one hand, regarding to the stellar mass, the discrepancies may be related to the large contribution of young stellar populations, as discussed above. The SSP-equivalent stellar masses are in much better agreement with the dynamical

masses, as the two are mainly dominated by the young stellar components and the comparison is consistent (dynamical masses are mainly determined by the velocity dispersion of the galaxy, which might be biased by the young populations that dominate the light). Instead, the SFH-based stellar masses are in worse agreement and larger than the dynamical masses, as the old stellar components present in the derived SFH lead to an inconsistent comparison. Moreover, the recent paper of Cappellari (2012) has shown that variations of the IMF with the mass of the galaxy should be taken into account, being this another source in the discrepancy.

On the other hand, if we consider that the problem is on the dynamical mass, we have to draw special attention to the sizes of our objects. As stated in Stockton, Shih & Larson (2010), it could be that we are using a definition for the dynamical mass that was initially calibrated for normally-sized objects, while our galaxies are extremely compact. Should we double our galaxy sizes, we would obtain higher dynamical masses and we would be closer to the 1:1 relation. In addition, we may be also underestimating the derived velocity dispersions due to the beam smearing, as we are here affected by our small PSF, such as galaxies at high-z. This effect results in non-Gaussian profiles that will introduce a bias on the derived kinematics (both underestimating the radial velocities and the velocity dispersion; see Teuben 2002 and Davies et al. 2011 for a further analysis of this effect). If this was the case, our objects would be even more rare in terms of their large radial velocities. However, this is unlikely to cause the increase on the velocity dispersion necessary to match the data (by more than $100 \mathrm{km \, s^{-1}}$).

At this point, it is not clear which mass is most likely to be the one driving the discrepancies. Determining the stellar masses taking into account the IMF employed and obtaining accurate dynamical models to properly derive the kinematics for this objects could help to discriminate between these two parameters.

3.3 Discussion

3.3.1 Can massive compact galaxies be transformed into the core of giant ellipticals?

A popular idea is that massive compact galaxies at high-z will end being the central part of present day most massive objects (e.g. Bezanson et al. 2009, Hopkins et al. 2009a). This scenario is supported by many indirect observational evidences. For example, the progressive growth of the wings of the profiles of the massive galaxies with time (van Dokkum & Conroy, 2010) and the larger

velocity dispersion of the massive galaxies at high-z compared to equally massive objects we see today ($\sim$1.5 times larger; e.g. Cenarro & Trujillo 2009, Cappellari et al. 2009, Onodera et al. 2010, Newman et al. 2010, van de Sande et al. 2011). The similar number density between $10^{11}M_\odot$ massive compact galaxies at high-z and today $\sim$2 times more massive objects also supports this scenario ($\sim$2$\times$10^{-4} Mpc^{-3}; van Dokkum et al. 2010, Cassata et al. 2011, Buitrago et al. 2013), as the expected mass growth by a factor of $\sim$2 of the massive galaxies with time expected theoretically and reproduced by observations (Naab, Johansson & Ostriker 2009, Sommer-Larsen & Toft 2010, Feldmann et al. 2010, Trujillo, Ferreras & de La Rosa 2011, Oser et al. 2012). In this sense, it is natural to compare the stellar mass density profiles for our compact massive galaxies with those of normal-sized objects in the local universe but with twice stellar masses.

The unprecedented resolution of our profiles allow us to see whether there is any change at sub-kpc level in the structure of these objects. In particular, we are interested on estimating how the growing processes that could eventually bring the compact galaxies into the core of more massive objects affect their inner regions. Moreover, we would like to quantify which number of stars should migrate during such transformation towards the outskirts of these objects.

Left panel of Figure 3.13 shows the comparison between the stellar mass density profiles of our nearby compact massive galaxies against objects with normal sizes but 2 times more massive. The nearby massive compact galaxies are clearly more dense at the center than the objects they will potentially be transformed in the future. That implies that the transformation from one class to another should imply a significant migration of the stars from the center of the compact galaxies towards their outer regions. The stellar mass density of both normal-sized and compact galaxies are similar at R=1.7 kpc. We can consequently estimate which is the excess of stellar mass of the compact galaxies compared to the other objects within this radius. We find that compact galaxies have $\sim$3$\times$10$^{10}M_\odot$ more mass than a disk-like normal size galaxy and $\sim$2$\times$10$^{10}M_\odot$ more mass than a spheroid object within 1.7 kpc. This means that such amount of stellar mass should be relocated outwards of 1.7 kpc after the evolution of the compact galaxy into a larger size object.

This enormous evolution of the inner region of the compact galaxies is expected in a minor merging scenario (see e.g. fig. 3 of Oser et al. 2012). Both compact massive galaxies and the larger objects have the same amount of stellar mass within $\sim$5 kpc ($\sim$8$\times$10$^{10}M_\odot$). This suggests that the processes responsible for the growth of the galaxies locate most of the new assembled stars beyond that radius ($\sim$10$^{11}M_\odot$).
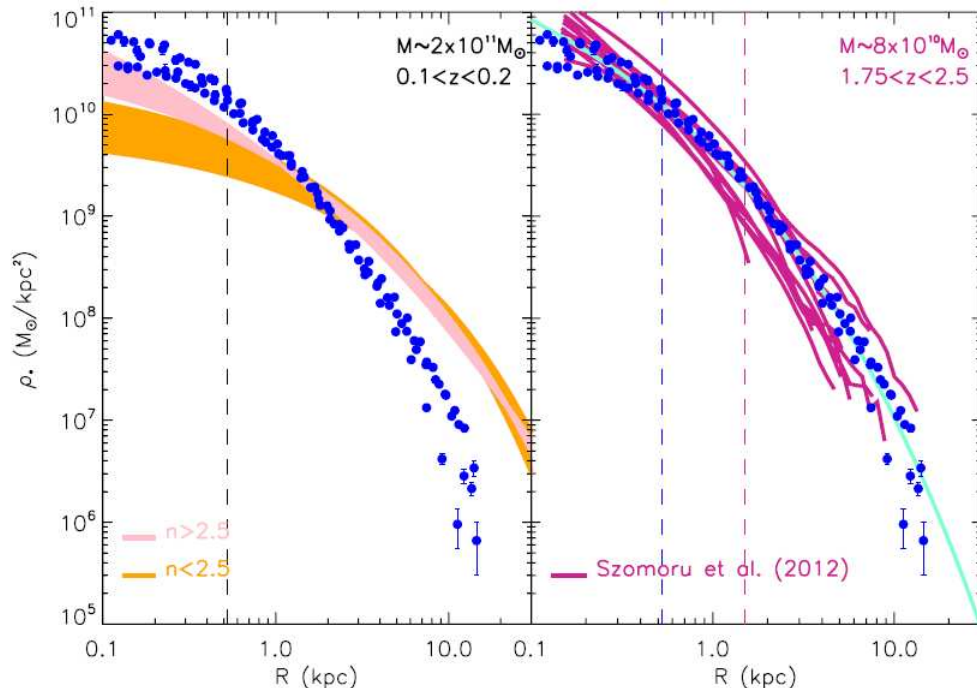
FIGURE 3.13— Stellar surface mass density profiles of our sample of nearby massive compact galaxies (blue points). *Left Panel*: The observed profiles of the compact massive galaxies are compared with the stellar mass density profiles of SDSS DR7 $M_\star \sim 2 \times 10^{11} M$ and $0.1 < z < 0.2$ disk-like galaxies (Sérsic index $n < 2.5$; orange region) and with spheroid-like (Sérsic index $n > 2.5$; pink region) galaxies. The vertical line shows the equivalent size in kpc of a FWHM PSF of 0.2 arcsec at $z = 0.15$. *Right Panel*: The nearby massive compact galaxies profiles are compared with profiles of $z \sim 2$ massive compact galaxies (violet lines) of the same stellar mass (Szomoru, Franx & van Dokkum 2012). The agreement is remarkable. The dashed vertical blue line shows the equivalent size in kpc of a FWHM PSF of 0.2 arcsec at z=0.15 (our Gemini PSF) and the red vertical line the equivalent size in kpc of a FWHM PSF of 0.18 arcsec at z=1.9 (HST WFC3 PSF).

At present it is still unclear which exact mechanism is ultimately responsible for the growth of the massive compact galaxies. The most favoured scenario is the minor dry merging scenario (e.g. Khochfar & Silk 2006, Maller et al. 2006, Hopkins et al. 2009a, Naab, Johansson & Ostriker 2009, but see Nipoti et al. 2012 for a critical vision) but there has been also some support to the puffing-up model. In this last picture (Fan et al. 2008; 2010), galaxy growth is connected to the removal of gas as a result of AGN activity or stellar activity (Damjanov et al., 2009). Based on recent simulations the growth associated to this process should be very fast ($\sim$20-30 Myr; Ragone-Figueroa & Granato 2011). This would imply that objects with stellar populations older than $\sim$1 Gyr should

already have normal sizes. In which scheme better fit the properties of our nearby massive compact galaxies?

Our nearby massive compact galaxies are young but their stellar populations are older than 1 Gyr. This seems hard to reconcile with the puffing up model. On the other hand, some of our objects seem to be accreting minor satellites as they have distorted morphologies. Not having spectroscopic redshifts for the rest of the galaxies in our fields, we are unable to quantify the presence of satellites around our galaxies (see e.g. Newman et al. 2012, Mármol-Queraltó et al. 2012). So far, the data obtained for the nearby compact galaxies seem to support more the minor merging scenario than the puffing up model.

3.3.2   Distant and nearby massive compact galaxies

An interesting aspect that we can address with our data is whether our stellar mass density profiles resemble those of equally massive compact galaxies at z∼2. Contrary to what we find in the local universe, compact massive galaxies were very common at those redshifts. Consequently, if we prove that our nearby massive compact objects are similar in structure to their high-z counterparts, this would favor the idea that these objects share a similar formation origin.

So far, not only the size, stellar mass and velocity dispersion of the nearby compact galaxies are the same than their equivalent high-z objects but also their ages (with a mean stellar age of ∼1-2 Gyr). This age is equivalent to the age of the compact objects found at high-z (e.g. Kriek et al. 2009).

The question that we address here is whether the distribution of the stars in the nearby compact massive galaxies also follow a similar shape to the ones found at high-z. This is shown in the right panel of Fig 3.12. The objects that we have used to compare with our compact galaxies are the massive compact galaxies from the sample of Szomoru, Franx & van Dokkum (2012) at z∼2. This is a collection of 12 galaxies observed with the HST WFC3 as part of the CANDELS GOODS-South (Koekemoer et al. 2011, Grogin et al. 2012). The high-z objects have a median stellar mass of $8.3 \times 10^{10} M_\odot$ (Kroupa IMF) and a median size of 0.84 kpc. The high-z profiles presented in Szomoru et al. (2012) are deconvolved so we can have a better idea of how the profiles at high-z look in their inner (R<1 kpc) regions. We can see that the agreement between the nearby and high-z compact galaxies is excellent.

It was evident from the images in Fig. 3.1 and 3.2 that our galaxies were elongated. Is there any evidence about a similar elongated shape for the compact massive galaxies at high-z? van der Wel et al. (2011) and Buitrago et al.

(2013) have addressed this issue and find that this is the case. Most of high-z massive galaxies at high-z have elongated shapes too.

3.3.3   Local compact massive galaxies: a new family of objects

We find that local compact massive galaxies represent a peculiar type of objects, not only from the detailed analysis of their morphologies, profiles and stellar kinematics, but also according to their stellar populations.

Although local compact galaxies show velocity dispersions and Sérsic indices similar to those in local normally-sized massive ellipticals, they show important rotation curves and seem to be rotationally supported. Moreover, unlike ellipticals of similar mass, our compact galaxy sample shows young SSP-equivalent ages ($\leq 2\,\text{Gyr}$), higher metallicities and their abundance patterns also differ. Their stellar surface mass density profiles also show that they are much denser in the centers than massive ellipticals.

Despite the fact that our galaxies display disky morphologies and strong rotation curves, they differ from S0s and spiral galaxies in their Sérsic indices and their velocity dispersions (the latter showing lower values for both) and present denser mass density profiles in their centers. Moreover, our objects are younger than spirals of similar mass.

For completeness, we compare our objects with dwarf ellipticals, although their masses are much lower than the ones measured in our sample. Many dwarf galaxies show young mean luminosity-weighted ages, which can be similar to those inferred for our galaxy sample, but in general they have lower metallicities. Kinematically, our galaxies are rotating as dwarf ellipticals, but the latter have lower Sérsic indices and lower velocity dispersions.

Our objects present optical spectra resembling 'E+A' galaxies (Dressler & Gunn 1983, Couch & Sharples 1987). E+A objects are considered post-starburst galaxies due to the presence of strong Balmer absorption lines, indicative of a young population ($<1\,\text{Gyr}$) and an absence of major emission lines ([OII] or Hα) indicating the cessation of star formation. It is commonly accepted that E+A represent the transition phase from a disky, rotationally supported system to a spheroid, pressure supported one (Yang et al. 2004, Zabludoff et al. 1996, Pracy et al. 2009), showing a widespread range of properties (ages, metallicities, velocity dispersions, sizes).

Because of their optical spectra and their SFHs, our objects are post-startburst galaxies. However, it is worth noticing that none of our galaxies, which we selected from the SDSS database, was previously identified as E+A (e.g., see the catalogs of Blake et al. 2004, Goto 2005, Goto 2007). The different

catalogs take different limiting values on the equivalent width of the lines that determine the family, reason why our objects may not be found in them.

May it be, that we are in fact seeing an intermediate stage on the thought transformation from spirals to ellipticals via E+As? We have found a new class of objects, unique and rare in the nearby Universe.

Furthermore, based on the derived SFHs, we can divide our objects in two groups. The first one is composed by those compact massive galaxies with large fractions of old stellar populations. These objects could be considered the relics of the high-z universe, although their SSP-ages are still too young, due to the non-negligible fraction of young components. In the second group, we include those galaxies with a huge fraction in mass of young stellar populations, analogous to the high-z massive galaxies. This group is the most intriguing. How is it possible to form half of the mass of a massive galaxy so recently ($\leq 2\,\mathrm{Gyr}$)? Whatever mechanism responsible for this, demands huge quantities of gas to create this amount of stars in such a short time. Is this mechanism analogous to that forming the massive galaxies at high-z (cooling flows or the merger of two "gas rich" spirals, e.g. Ricciardelli et al. 2010)?

The absence of clear stellar gradients along the nearby compact galaxies suggests that the mechanism triggering the starburst in these objects is likely a global one. This could indicate that the structure of the nearby compact massive galaxies has been assembled during this major event, being the old stellar populations the stars associated to the merging units and the young component a product of the gas collapse into stars.

3.4 Conclusions

We have presented the main properties of 9 of the 29 bonafide scarce compact massive galaxies identified by T09 in the nearby Universe ($z \leq 0.2$). The main aim of this work was to characterize these objects in order to understand better their formation and evolution and to assess their relationship with the massive galaxies at high redshift.

We measure large radial velocities (up to $200\,\mathrm{km\,s^{-1}}$) and high velocity dispersions (~ 200 $\mathrm{km\,s^{-1}}$) for these objects. We have shown unequivocally that these objects are genuinely compact ($\mathrm{R}_e \sim 1.3\,\mathrm{kpc}$) with no evidence of an extended faint component altering their size estimate. These nearby massive compact galaxies have an elongated shape resembling S0 objects ($b/a \lesssim 0.6$). Their stellar mass density profiles are significantly more dense in their inner

regions than any galaxy with similar stellar mass and normal size in the local Universe.

From an analysis of their stellar populations, we derive young mean SSP-equivalent ages (2 Gyr) and metallicities solar or slightly higher, showing an abundance pattern that does not differ from a scaled-solar rate. The full-spectrum-fitting derived SFHs reveal that these objects contain an old embedded population but that they all experienced recent bursts of star formation during the last 2 Gyr. The latter contribute strongly to the total light ($\gtrsim 50\%$) and, in some galaxies, surprisingly even to the total mass ($\gtrsim 30\%$).

Nearby massive compact galaxies share a large number of properties with massive compact galaxies in the distant universe: same stellar masses, sizes, shapes, velocity dispersions and the mean age of their stellar populations. They seem more their analogues than their descendants.

Comparing the properties of our sample with those massive but normally-sized galaxies in the local Universe, we find that they deviate from various relations expected at low redshift. Although their optical spectra resembles those of the E+A galaxies, none was found in previous catalogs. Therefore, we can not classify them into any of these families, hence they constitute a completely new family of rare objects.

Although we have fully characterized them, we still need to understand their formation and assess the issue of why these local massive galaxies were born with such a compact structure and large contributions of young stellar populations. Moreover, the discrepancies related to the stellar masses need to be addressed.

The local compact galaxies analyzed in this work seem to be unique and scarce in the nearby Universe and, because of their relative vicinity, they are a perfect laboratory to explore with unprecedented detail the formation mechanisms of massive galaxies at high-z, particularly those involving huge amount of gas leading to the enormous formation of stars we have measured.

4

Towards a non-universal Initial Mass Function

In a time of universal deceit
telling the truth is a revolutionary act
George Orwell

Recent results indicate that the IMF does not seem to be universal and that should be tuned according to the galaxy velocity dispersion. Within this assumption, more massive galaxies demand steeper IMF slopes. This offers the possibility to solve some of the long-standing problems in the stellar population field, but it also shows the need to quantify the impact that varying this IMF has onto different properties.

In this chapter we present how some *stellar population properties vary when adopting a non-universal IMF slope and shape*, such as the Star Formation Histories (SFHs), the mass assembly timescales, the stellar mass and the mean age. We show that using a universal IMF may lead to surprising results, such as the questionable existence of early-type galaxies with virtually no contributions of old stellar populations, while selecting it according to the galaxy velocity dispersion seems to give more constrained results.

The majority of this chapter is based on the paper: *The impact of a non-universal Initial Mass Function on the star formation histories of Early-Type Galaxies.* Ferré-Mateu, A., Vazdekis, and de la Rosa, I.G. 2013, MNRAS, in press (*arXiv:1301.7066*).

4.1   The Data

Spectra from two different ETG samples were used for the present study. The main sample, with high-quality long-slit spectra make the bulk of the work, while a second sample with fiber spectra from the SDSS (*Sloan Digital Sky Survey*) is mainly used for statistical purposes.

The first sample, with S/N$\geq 40\,\text{Å}^{-1}$, was constructed with spectra from Sánchez-Blázquez et al. (2006a) (PSB06a), Yamada et al. (2006) (Y06) and the local compact massive galaxies of Chapter 3 (AFM12). A complete description of the data, their quality and reduction process can be found in the source papers, while we present here the relevant information related to this work.

The first two references contain ETGs covering a range of masses ($\sigma = [50\text{-}300]\,\text{km\,s}^{-1}$), while the third one includes the massive compact galaxies studied in Chapter 3. All these galaxies allow us to cover an ample range of properties, like masses, luminosities, sizes and stellar populations. Therefore, this sample is ideal to detect the effects of IMF variations. In particular, the Y06 sample covers the colour-magnitude diagram of the Virgo Cluster. At the very high mass regime ($\sigma \sim 300\,\text{km\,s}^{-1}$) we find galaxies from PSB06a and Y06 that would need the steepest IMF so far considered. The local compact massive galaxies from Chapter 3 were selected because they have revealed unusually large fractions of young components on their derived SFHs. The massive ellipticals were selected to have similar velocity dispersions to the compact galaxies, albeit larger radii, to compare their mass estimates ($\sigma = 200\,\text{km\,s}^{-1}$). Finally, the low-mass ellipticals are useful probes to study the SFH differences, as a fraction of them show young ages, comparable with those in massive compacts. Table 4.1 lists all the galaxies in the high-quality spectra sample with their main properties. Despite their different origins, they were all treated and analyzed in a similar way.

The ETGs sample from the SPIDER project, with SDSS spectra of 40,000 objects (La Barbera et al. 2010a, LB10 hereafter), was used to obtain stacked spectra of high signal-to-noise presented in Ferreras et al. (2013) (F13 from now onwards), that will allow us to study the mass assembly of ETGs with different velocity dispersions. It was also used to find the rather extreme, but illustrative, cases presented in Section 4.4 and as the benchmark for sanity checks performed to test the robustness of the results in Appendix B.

4.2   Galaxy properties with varying IMF

A study on the quantitative impact of varying the IMF shape and slope on the stellar population properties is presented in this section.

Galaxy ID	Source	environment	type	z	$\sigma(\mathrm{km\,s^{-1}})$
NYU 54829	AFM12	Field	MC	0.085	137
NYU 321479	AFM12	Field	MC	0.128	221
NYU 685469	AFM12	Field	MC	0.149	204
NYU 796740	AFM12	Field	MC	0.182	203
NYU 890167	AFM12	Field	MC	0.143	233
NYU 896687	AFM12	Field	MC	0.130	223
NYU 2434587	AFM12	Field	MC	0.172	206
NGC 4365	Y06	Virgo	HME	0.0041	265
NGC 4472	Y06	Virgo	HME	0.0033	300
NGC 2329	PSB06	Coma	ME	0.0192	225
NGC 4473	Y06	Virgo	ME	0.0074	193
NGC 4621	PSB06	Virgo	ME	0.0013	230
NGC 4697	Y06	Virgo	ME	0.0041	180
NGC 5812	PSB06	Field	ME	0.0065	215
NGC 4239	Y06	Virgo	LME	0.0031	63
NGC 4339	Y06	Virgo	LME	0.0043	114
NGC 4387	Y06	Virgo	LME	0.0015	98
NGC 4458	Y06	Virgo	LME	0.0210	105
NGC 4464	Y06	Virgo	LME	0.0041	135
NGC 4467	Y06	Virgo	LME	0.0047	69
NGC 4489	Y06	Virgo	LME	0.0032	52
NGC 4551	Y06	Virgo	LME	0.0039	105

TABLE 4.1— Main galaxy properties: (1) galaxy ID; (2) publication source: PSB06 (Sánchez-Blázquez et al., 2006a), Y06 (Yamada et al., 2006) and AFM12 (Chapter 3); (3) environment of the galaxy; (4) galaxy type: MC (Massive Compact), HME (High Mass Elliptical), ME (Massive Elliptical) or LME (Low-Mass Elliptical); (5) redshift; and (6) central velocity dispersion. Values are taken from the publication source or from the LEDA database (http://leda.univ-lyon1.fr/) when not available.

A first consideration should be done regarding the shape of the IMF assumed for the models. Historically, two alternative IMFs have been considered: a single-power law over all stellar masses, characterized by its logarithmic slope μ (Salpeter, 1955) and a multi-segmented IMF (Kroupa, 2001). These two IMFs will be regarded as standard through this work. For our illustrative purposes, the other popular choice, the log-normal IMF (Chabrier, 2003) is very similar to that of Kroupa and will not be considered here.

4.2.1 Mass-to-light ratios

We can study the dependence of the mass-to-light ratio (M/L) with the IMF using stellar population synthesis models. We have selected three representative ages (1, 2 and 10 Gyr) and three metallicities ([Z/H]$= -0.40$, 0.00 and 0.22) from the extended MILES single-burst models (MIUSCAT; Vazdekis et al. 2012, V12 hereafter). We have selected six different IMF slopes: $\mu = [0.3, 0.8, 1.0, 1.3, 1.8$ and 2.3] both for a single- and segmented-power law (unimodal and bimodal following the notation of Vazdekis et al. (1996), see Fig. 1.6 in Sect. 1.6.1). As a reference, $\mu = 1.3$ corresponds to a Salpeter IMF slope with a unimodal shape. Instead, a bimodal IMF with the same slope resembles closely to a Kroupa IMF.

Figure 4.1 shows the dependence of the M/L with the slope of the IMF for stellar populations of different ages with both shapes. It can be seen that the M/L from the stellar population models presents a minimum. For the M/L calculation both the alive stars contributing to the light and the stellar remnants are taken into account. Whereas the steepest IMFs emphasize the contribution of long-lived low-mass stars, the flatter IMFs favour the number of remnants resulting from short-lived massive stars. Note that if the stellar remnants were not included, the resulting M/L would not show a minimum when varying the IMF slope (see the predictions shown in the MILES webpage[1]). The location of this minimum depends on the age of the SSP: younger ages reach their minimum at flatter slopes. In the unimodal case, the minimum is found at $\mu \sim 0.8$ for young populations, whereas it is located at $\mu \sim 1.0$ for the old ones. In the bimodal case the minimum is seen at $\mu \sim 1.0$ (1.3) for the young (old) populations.

It is worth noticing the strong variation of the M/L with IMF slope. For the unimodal shape, the M/L value increases strongly for both the flattest and steepest IMFs. For the bimodal IMF, a significantly milder variation is seen, particularly for the oldest stellar populations (see F13). The choice of one shape

---

[1]http://miles.iac.es/

over the other will be affecting in a different way the derived stellar population properties, such as the M/L. A trend with the broad band filters is also seen. At a fixed IMF slope, lower M/L values are obtained for redder filters.
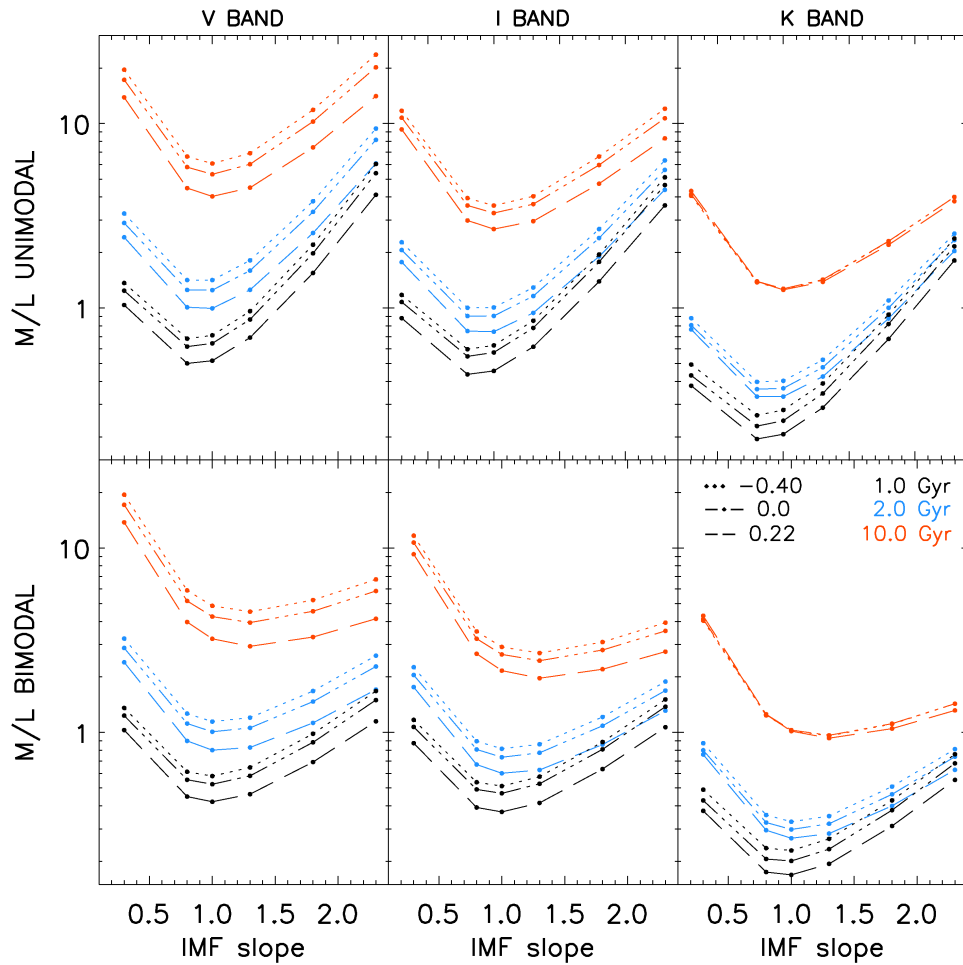
FIGURE 4.1— The M/L ratio in several broad-band filters is plotted against the IMF slope for models of 1 Gyr (black), 2 Gyr (blue) and 10 Gyr (red) and for different metallicities ([Z/H]= −0.40, dotted line; [Z/H]= 0.00, dashed-dotted line and [Z/H]= 0.22, dashed line). Upper rows correspond to models with a unimodal IMF and lower ones to models with a bimodal IMF. A minimum on the M/L is seen around $\mu \sim 0.8$-1.0 (unimodal) or $\mu \sim 1.0$-1.3 (bimodal), depending on the SSP age.

4.2.2 Star Formation Histories

To obtain the SFHs of our high-quality galaxy sample we apply the full-spectrum-fitting approach. We use the code `STARLIGHT` with the MIUSCAT SSP SEDs. The SFH is derived for each galaxy using different base models with all the IMF slopes selected above, both for the unimodal and the bimodal cases.

The high quality of our spectra allows us to perform an accurate fitting. We are aware that our results may be biased due to the relatively short spectral range of the spectra ($\lambda\lambda$ 3800-5300 Å). Although this range encompasses most of the commonly used absorption line features, the reported IMF-sensitive indices are located at redder wavelengths. However, the blue part of the spectrum also shows some sensitivity to the IMF, as shown in figure 9 of Vazdekis et al. (2012). To check the robustness of our results, we have performed various tests to take into account different sources that might change our results (see Appendix B). We first masked different features in the spectra, finding that the variations on the mean derived ages are negligible (smaller than 2%). We also compared the results from selecting a short *versus* a longer spectral range, which may account for variations in the derived luminosity(mass)-weighted ages of the order of a 8% (12%). Finally, due to the sensitivity of some colours to the IMF variations (see e.g. Ricciardelli et al. 2012), we have compared the synthetic colours obtained from our derived SFHs to those from the SDSS broadband photometry, finding good agreement between both. Note that the latter extend to the UV and the IR, i.e. sampling the different populations in the galaxy. These tests confirm the robustness of the results and trends obtained in this work. From now on, all the SFHs presented here are derived using the spectral range of our high quality long-slit sample.

Figures 4.2 to 4.4 show the SFHs of our sample of galaxies, colour-coded by galaxy family: the very massive galaxy in black, the massive ellipticals in green, the massive compacts in purple and the low-mass galaxies in orange. The panels show the derived SFHs with base models where the IMF slope steepens from left to right. In the upper rows we show the results for the unimodal case and in the lower, the ones for the bimodal case. The dashed vertical line shows the mean mass-weighted age for each varying slope, while the solid line is the mean value derived from the standard $\mu = 1.3$ slope.

Some interesting conclusions are drawn from these figures. First, we see noticeable differences in the derived SFHs for these types of galaxies: while massive ellipticals are mainly old, both in light and mass, massive compacts show an unusually large fraction of young stellar populations (≤ 2 Gyr), both light- and mass-weighted (as explained in more detailed in Sect. 3.2.5).
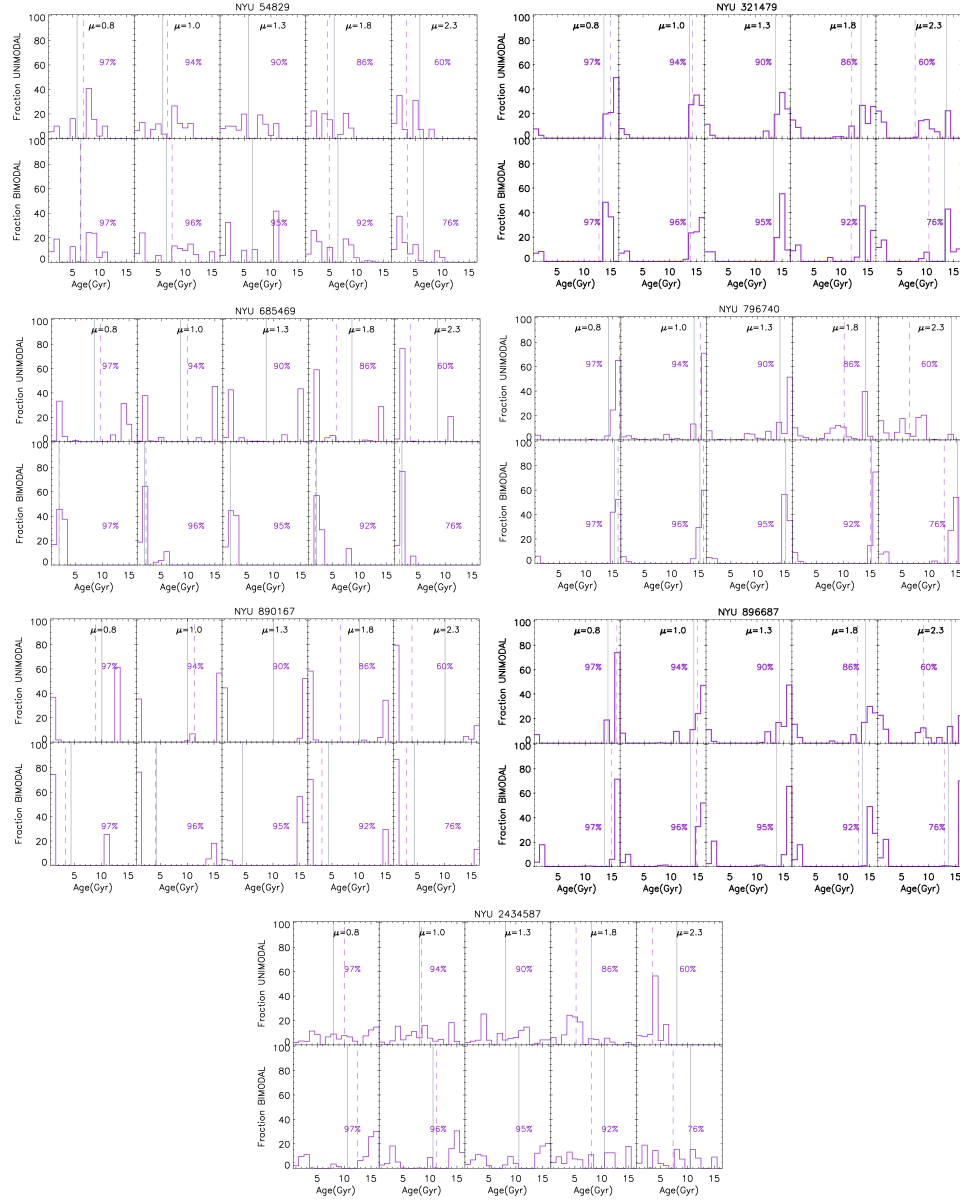
FIGURE 4.2— Star Formation Histories for the massive nearby compact galaxies (purple). From left to right, the mass-weighted SFHs derived with increasing IMF slope (μ), as indicated on top of each panel, in the upper row for the unimodal, and in the lower one for the bimodal case. The dashed vertical line corresponds to the mean mass-weighted age derived for the galaxy with each slope, while the solid line represents the mean value derived from the standard $\mu = 1.3$ slope. The fraction of mass-weighted old populations (>5 Gyr) is quoted in each panel. Note the trend of a decreasing old stellar population contribution when steepening the IMF slope, more remarkably for the massive compacts and the low-mass galaxies (Fig. 4.4).
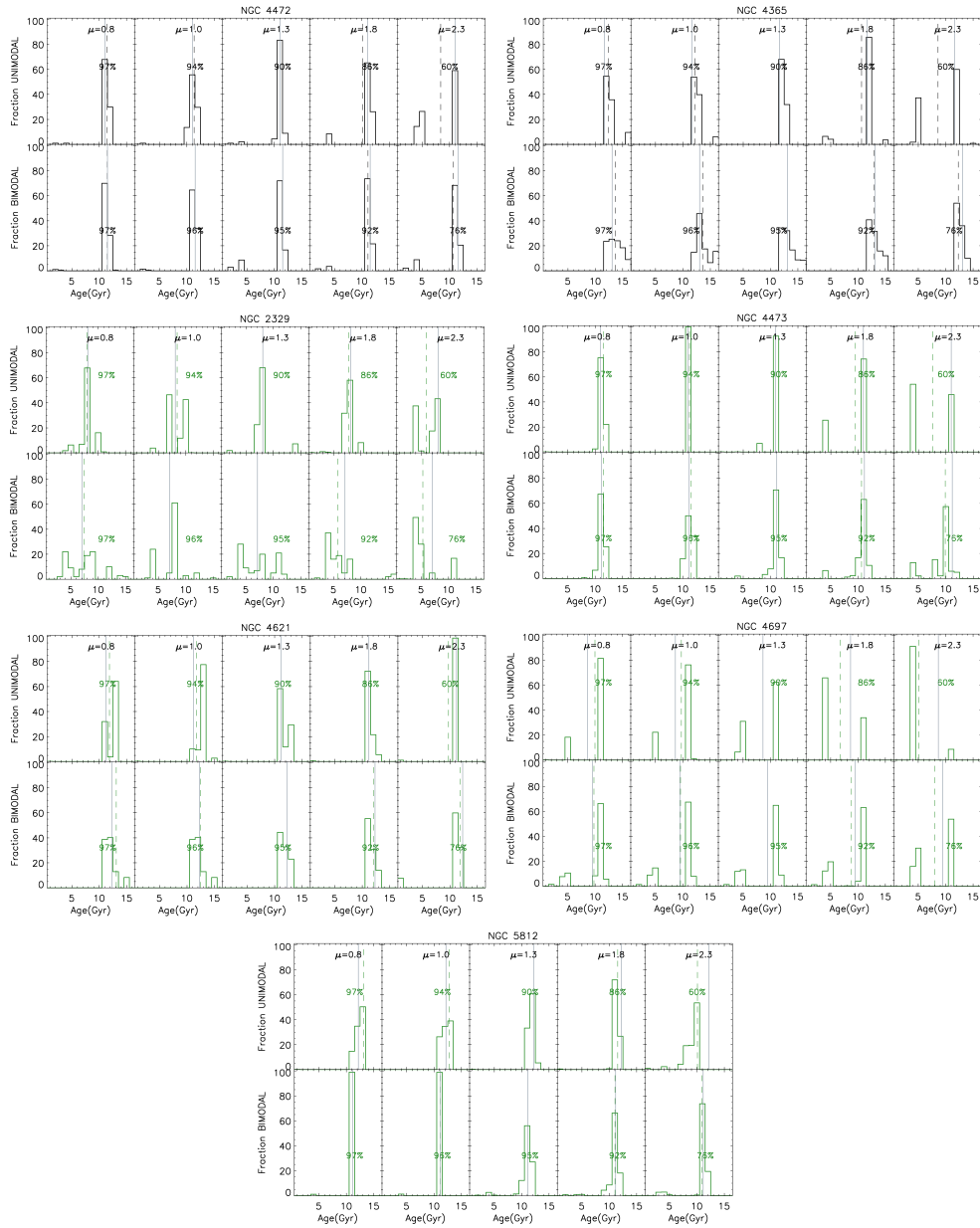
FIGURE 4.3— As in previous figure but for the high-mass (black) and massive (green) galaxies.
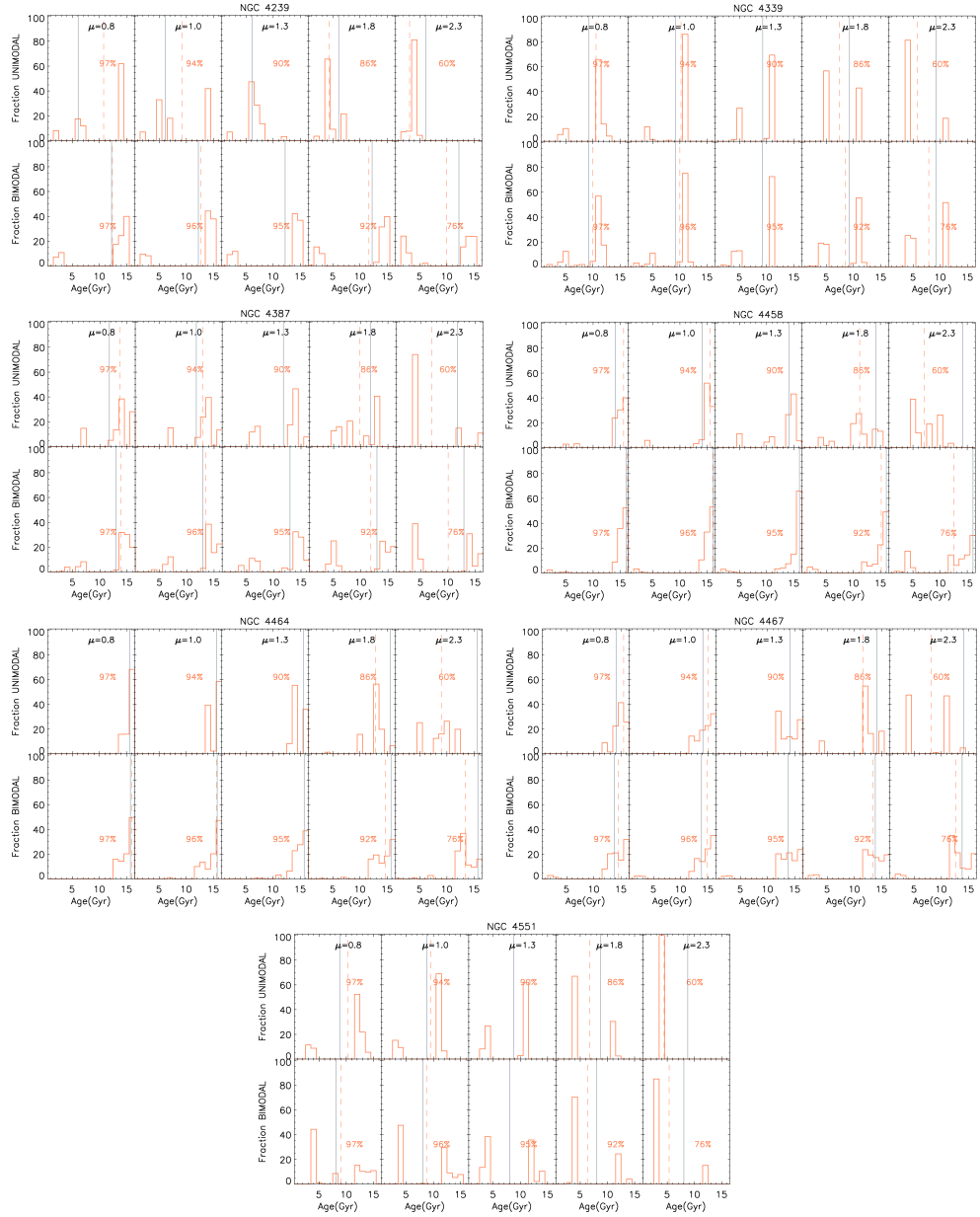
FIGURE 4.4— As in previous figure but for the low-mass galaxies (orange)

Second, we see a general trend of decreasing the fraction of old stellar populations with increasing IMF slope (as in the upper panel of Figure 4.5), emphasized for the unimodal case. For various massive galaxies an intermediate-age stellar population ($\sim 5\,\mathrm{Gyr}$) emerges when adopting an IMF steeper than Salpeter, leading to a more complex SFH. The impact is significantly milder for the bimodal case. Note however, that according to F13 the best fits to the various IMF-sensitive features for the most massive galaxies require an IMF slope around ~ 2 and ~ 3 for the unimodal and bimodal shape, respectively.

This rejuvenating effect implies a decrease in the mean age of the galaxy, as shown in the lower panel of Fig. 4.5, where the derived mean mass-weighted ages are shown with respect to the IMF slope. It is seen that in the unimodal case, the derived ages might decrease by a factor of as much as 3 from $\mu = 0.8$ to $\mu = 2.3$, while for the bimodal case is 1.5.
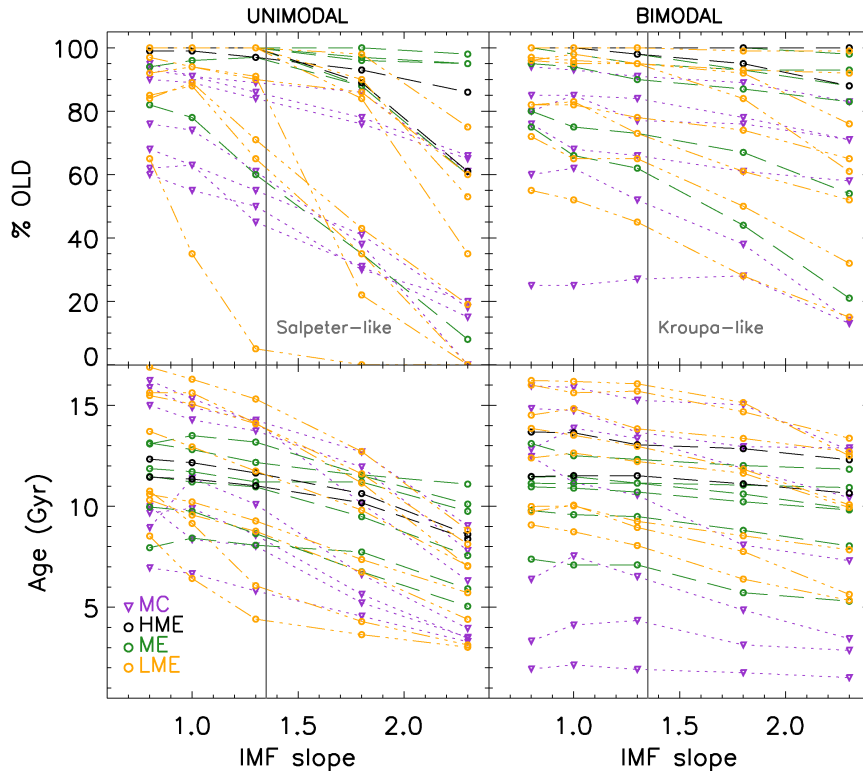
FIGURE 4.5— Fraction of old populations ($>5\,\mathrm{Gyr}$) and mean ages derived from the mass-weighted SFHs using different IMF slopes. Symbols are colour coded as: high massive galaxies in black, massive ellipticals in green, the massive compacts in purple and the low-mass ellipticals in orange. The vertical solid gray line indicates the position of the standard slope for both IMF shapes ($\mu = 1.3$).

Recent results have claimed that more massive galaxies demand steeper IMF slopes than Salpeter (e.g. Cappellari et al. 2012a, van Dokkum & Conroy 2012, Conroy & van Dokkum 2012a), including a systematic correlation with the IMF slope and the velocity dispersion (μ-σ) found by F13. These works pose an upper limit for the steepest slope at $\mu \sim 2$ for a single power-law IMF shape. Therefore, for our illustrative purpose, we will only discuss the unimodal case in this part of the work. From now onwards, we will use the notation $\mu(\sigma)$ to refer to the slope of the IMF according to the galaxy velocity dispersion and μ-σ for the relation from F13. Which SFHs will be derived for our objects following this μ-σ relation? We find that most massive galaxies, for which we adopt $\mu(\sigma) \sim 2$, are typically very old. However, for most cases, a non-negligible fraction of relatively younger stellar components appears (up to 10%). This also applies to massive galaxies, for which a Salpeter or slightly steeper IMF is demanded. In contrast, the contribution from old stellar populations increases for the low-mass ETGs with flatter slopes than Salpeter ($\mu \sim 0.8$-1.0). Table 4.2 summarizes the mass-weighted properties derived from the SFHs obtained when adopting the $\mu(\sigma)$ for each galaxy. The other derived quantities for both the two IMF shapes adopted can be found in Table B1 and B2 in Appendix B.

In summary, our results suggest that the SFHs of ETGs of all masses tend to converge to a common pattern when the prescribed IMF slopes, according to the galaxy velocity dispersion, are used. This pattern involves a varying amount of recent residual star formation. The SFHs of ETGs have always been a challenge in modern astronomy, as they represent a direct way to constrain competing galaxy formation models. Though it is well established that the bulk of the stars in ETGs formed at high redshift (z$\sim$2), a small "frosting" of young stars forms on top of it at more recent epochs (e.g: Trager et al. 2000a). Observations in the UV are particularly useful to trace these recent bursts, as the rest-frame UV is mostly sensitive to stars less than ~ 1 Gyr old (e.g: Ellis, Abraham & Dickinson 2001, Kaban, Nolan & Raychaudhury 2005, Kaviraj et al. 2005, Ferreras et al. 2006). All these works show that there is indeed this residual star formation, which evolves with redshift (Fukugita et al. 2004, Kaviraj et al. 2008). It can be up to $\sim 10\%$ in the local Universe (e.g Kaviraj et al. 2007, Nolan, Raychaudhury & Kabán 2007), in agreement with our results.

Nonetheless, the SFHs of the compact massive galaxies do not change substantially if the IMF is varied with this μ-σ relation because their $\mu(\sigma)$ coincides in most of the cases with the standard estimate. This also applies when adopting a more conservative bimodal IMF shape. Although we expand this issue in Section 4.5, these galaxies reinforce their unique nature here.

4.2.3   Stellar Masses

Stellar masses are computed from the mass-to-light relation corresponding to the SSP mixtures that match best the galaxy spectra, as obtained from the full-spectrum-fitting technique applied here. For our massive compact galaxies, we use the stellar masses derived in Section 3.2.6. Following the same approach to the one described in that section, we adopted the M/L values in the V band as luminosity estimate for the rest of elliptical galaxies in the study. We used the values tabulated for the total magnitude, corrected in the same band, from LEDA (http://leda.univ-lyon1.fr/).

Figure 4.6 shows the dependence of the derived stellar mass with the IMF slope. This is the observable with the largest sensitivity to the assumed IMF shape and slope. It is seen that for the unimodal IMF the stellar mass grows up by a factor of 3 from the standard value $\mu = 1.3$ to the steepest case $\mu = 2.3$, with the smallest stellar mass obtained at $\mu \sim 1.0$. For the bimodal IMF shape the impact is significantly milder. It shows a smaller increase of the factor of 1.5, emphasized for the massive galaxies. This trend of increasing mass with a steepening of the IMF slope is analog to the results found in Cappellari et al. (2012a) for the dynamical masses. This finding provides further support for the need of using the appropriate IMF, in order to avoid galaxy misclassifications due to wrong stellar masses.
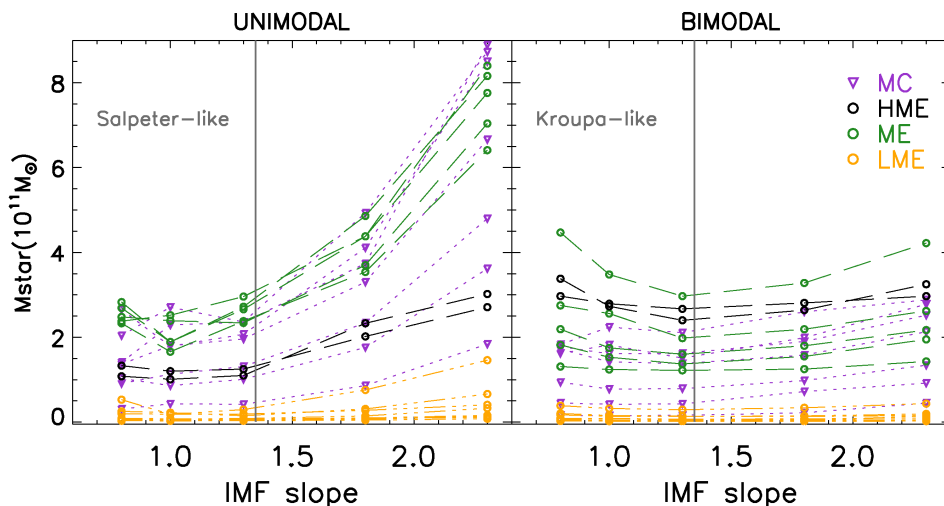
FIGURE 4.6— Stellar masses obtained from the derived M/L ratios with different IMF slopes. Note the large difference between unimodal and bimodal shapes, in particular for the steepest slopes. The stellar masses increase by a factor of 4 in the unimodal case, while it only accounts by a factor of 1.5 in the bimodal one.

GALAXY ID	$\mu(\sigma)$		Age (Gyr)		%old		M_{star} $(\times 10^{11} M_\odot)$	
	un	bi	un	bi	un	bi	un	bi
NYU 54829	0.8 (0.8)	0.8 (0.8)	6.9	6.3	68	60	0.91	0.94
NYU 321479	1.3 (1.5)	2.3 (2.2)	13.7	10.4	84	71	2.35	2.52
NYU 685469	1.3 (1.4)	1.8 (1.9)	8.5	1.9	50	0	1.01	0.72
NYU 796740	1.3 (1.4)	1.8 (1.9)	15.3	15.0	89	89	2.36	2.60
NYU 890167	1.8 (1.7)	2.3 (2.3)	6.6	2.8	41	13	0.86	0.45
NYU 896687	1.8 (1.6)	2.3 (2.3)	12.6	12.9	78	71	4.11	2.78
NYU 2434587	1.3 (1.4)	1.8 (1.9)	8.0	8.1	61	61	1.96	1.58
NGC 4365	1.8 (1.9)	2.8 (2.7)	10.6	12.3	89	100	2.02	3.25
NGC 4472	2.3 (2.2)	3.0 (3.1)	8.4	10.6	86	88	3.02	2.97
NGC 2329	1.8 (1.6)	2.3 (2.2)	7.7	5.9	88	21	4.38	1.95
NGC 4473	1.3 (1.2)	1.8 (1.7)	10.9	10.6	100	93	2.38	3.28
NGC 4621	1.8 (1.6)	2.3 (2.3)	11.2	11.8	96	98	4.38	1.43
NGC 4697	1.0 (1.1)	1.3 (1.5)	9.7	9.4	78	74	1.94	2.65
NGC 5812	1.3 (1.5)	1.8 (2.0)	12.8	11.1	100	95	1.89	1.98
NGC 4239	0.8 (0.8)	0.8 (0.8)	10.7	12.4	92	82	0.07	0.05
NGC 4339	0.8 (0.8)	0.8 (0.8)	10.6	9.9	84	82	0.53	0.38
NGC 4387	0.8 (0.8)	0.8 (0.8)	13.7	13.8	100	96	0.03	0.03
NGC 4458	0.8 (0.8)	0.8 (0.8)	15.6	16.2	97	97	0.07	0.06
NGC 4464	0.8 (0.8)	0.8 (0.8)	16.3	16.0	100	100	0.19	0.20
NGC 4467	0.8 (0.8)	0.8 (0.8)	15.5	14.5	100	96	0.06	0.04
NGC 4489	0.8 (0.8)	0.8 (0.8)	8.5	9.7	65	72	0.09	0.09
NGC 4551	0.8 (0.8)	0.8 (0.8)	10.3	9.1	85	55	0.25	0.17

TABLE 4.2— Stellar population parameters estimated from the derived SFHs using the prescribed IMF slope, according the the galaxy velocity dispersion, $\mu(\sigma)$: (1) galaxy ID; (2-3) The selected $\mu(\sigma)$ for each galaxy, both for the unimodal and the bimodal IMF. We consider the closest slope in our model (0.8, 1.0, 1.3, 1.8 or 2.3) compared to the value obtained following F13 equation (quoted within the parenthesis). Note that all the low-mass galaxies have $\mu(\sigma)=0.8$, because F13 equation is valid for galaxies with $\sigma >150$ km s^{-1}; (4-5) Mean mass-weighted ages; (6-7) Fraction of old stellar populations (>5 Gyr); (8-9) Stellar mass derived from the SSP mixture resulting from the derived SFH.

4.3   NGC 4489: baby galaxy or non-standard IMF?

We have seen in Section 4.3.2 that by tuning the IMF slope related to the velocity dispersion of the galaxy, according to recent evidences in this direction, we tend to derive more similar SFHs among galaxies of different masses. However, such a choice does not change drastically the results one would infer from adopting a standard-universal IMF (e.g. Salpeter or Kroupa). We find that the most massive galaxies are nevertheless old, despite IMF-modulated young population contributions. Nevertheless, in this section we show that there are galaxies for which the use of a standard IMF would lead to surprising results.

Here we focus on the low-mass elliptical NGC 4489. This galaxy has been previously reported to have a young mean luminosity-weighted age from line-strength studies ($\sim$3-5 Gyr; e.g: Gorgas et al. 1997, Terlevich & Forbes 2002, Caldwell, Rose & Concannon 2003, Tantalo & Chiosi 2004, Y06). However, this does not necessarily imply that the galaxy is composed of genuinely young stellar populations, as the old component can be masked by the luminosity of a tiny fraction of young stars on top of it. The mass-weighted SFH reveals the composition of NGC 4489, as presented in the upper panel of Figure 4.7. It shows, like in Figures 4.2-4.4, the derived SFH with different IMF slopes. From the Salpeter panel (unimodal $\mu = 1.3$) one would infer that NGC 4489 is a genuinely young object with almost no contribution from stellar populations older than 5 Gyr (less than 5%), i.e. a "*baby elliptical galaxy*". However, considering a slightly flatter IMF slope as claimed for an elliptical galaxy of such small velocity dispersion (e.g. Cappellari et al. 2012a, F13), an old component appears, which contributes $\sim$65% to the total mass. This result is in much better agreement with those obtained in Section 4.2.2.

Do other galaxies like NGC 4489 exist in the Local Universe that can be considered as *baby elliptical galaxies* assuming a standard IMF slope? Out of the SDSS-based LB10 sample, we selected those galaxies with a mean mass-weighted age younger than $\leq$ 5 Gyr (Salpeter IMF). Only 11 *baby elliptical galaxies* were found, with a similar behavior to NGC 4489, as shown in the lower panel of Figure 4.8. Once again, the apparent extreme youth of these galaxies results from the inadequate use of a standard-universal IMF.

4.4   Shifting the mass assembly by varying the IMF

To study the timescales along which the mass of the galaxy is assembled, we use the stacked spectra from La Barbera et al. 2013 (submitted) and F13. These are 18 high quality spectra, with S/N ranging from 100 up to 800 along the whole SDSS spectral range, comprising velocity dispersions of [100-320]km s^{-1}.
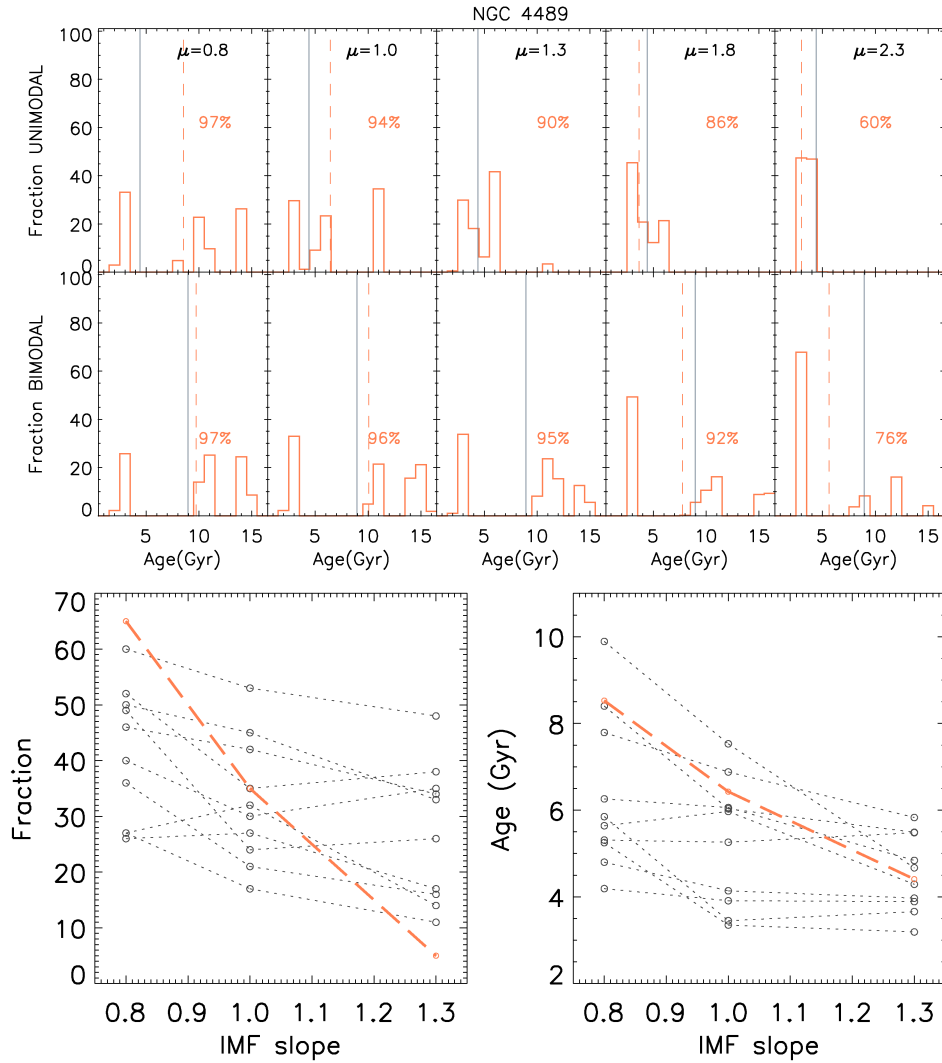
FIGURE 4.7— *Upper panel*: Derived SFHs for NGC 4489 for increasing IMF slopes, as quoted within each panel as in Figure 4.2. Note that for a standard Salpeter IMF (third panel) this object is genuinely young, while a slight flattening gives a SFH with a large contribution of old stellar populations. *Lower panel*: Fraction of old stellar populations (> 5 Gyr) and mean age (in Gyr) estimated from the derived SFH using the unimodal IMF of varying slope for a subsample of 11 *baby elliptical galaxies* from LB10. The Virgo galaxy NGC 4489, with a high-quality spectrum, is highlighted in orange. As for NGC 4489, these *baby elliptical galaxies* always show an almost genuinely young stellar population when a Salpeter IMF is adopted.

We have derived the SFHs for each stacked spectra employing models for both standard IMFs (Kroupa and Salpeter) and for the IMF according to the galaxy velocity dispersion. This $\mu(\sigma)$ was selected according to the work that is presented in La Barbera et al. (2013).

Figure 4.8 shows the time (in Gyr) where the galaxy has assembled the 50, 75 and 90 % of its mass. We find that most massive galaxies assemble their mass in shorter timescales than the less massive ones. However, we generally see a delay when employing the $\mu(\sigma)$. The differences in the time of assembly between a standard IMF and the $\mu(\sigma)$ are presented in Figure 4.9. It is seen that the unimodal IMF presents a clear trend with velocity dispersion for all the fractions. We find that the use of a standard Salpeter IMF slope delays (accelerates) the mass assembly for the massive (low mass) galaxies. In contrast, the bimodal shape variations are practically constant (except for the lowest mass galaxies). However, as we go to larger fractions, we recover the trend with velocity dispersion. In fact, the assembly of the 90% of the mass is where the strongest differences in time are found for the most massive ones, reaching even a 4-5 Gyr delay. This implies that in general, the use of an IMF tuned according to the galaxy velocity dispersion gives a more extended SFH for the most massive galaxies, in agreement with our previous findings.

4.5 A solution for the masses of compact massive galaxies?

As shown in the previous sections, tuning the IMF slope according to the velocity dispersion of the galaxy seems to present more consistent SFHs. However, be have seen that the SFHs of our compact massive galaxies do not depart significantly from the standard estimate when using this $\mu(\sigma)$. Yet, we can study if these variations, although small, can solve or at least alleviate the discrepancies between the stellar and the dynamical masses found in Section 3.2.6.

Figure 4.10 shows the derived M_{star} values for each galaxy when varying the IMF slope for the unimodal case with fixed M_{dyn} under the homology assumption. We have tested whether the non-homology assumption would change the results, but we do not find major differences on the general trends, with a deviation on the relation of ∼0.5% (see Appendix B.2). The figure shows that massive ellipticals (green points) show a better agreement with Salpeter-like IMFs. At the other end of the mass range, low-mass ellipticals give a better agreement for flatter IMF slopes, although a higher dispersion in the points is seen for this regime.
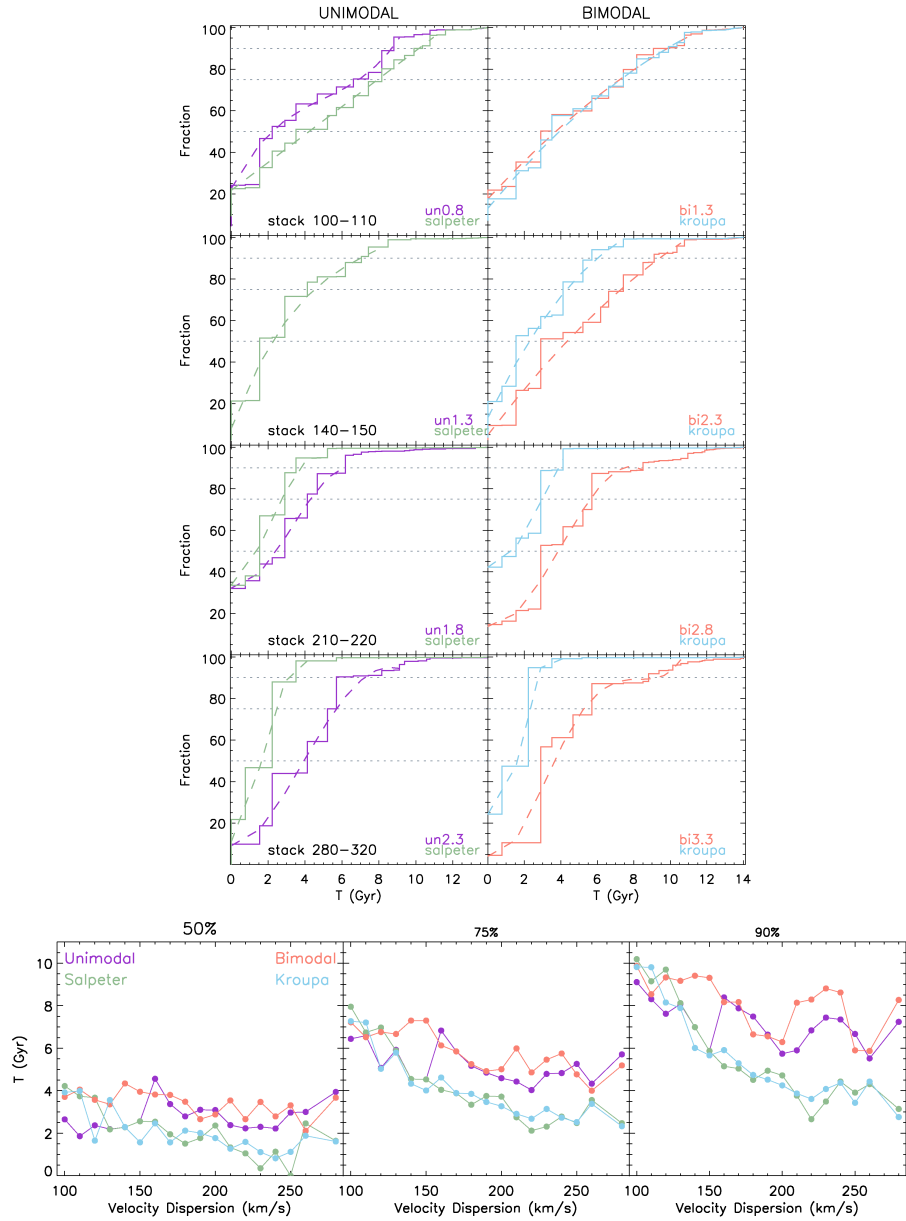
FIGURE 4.8— *Upper figure*: Cumulative mass for some of the stacked spectra to illustrate the differences on the mass assembly. Curves are fitted with polynomials of the lowest order possible (dashed line) and the dotted gray lines mark the position when the 50, 70 and 90% of the mass has been assembled. *Lower figure*: Time at which the the 50, 75 and 90% of the galaxy mass is assembled employing different IMF slopes, to show the delay when non-standard IMFs are used.
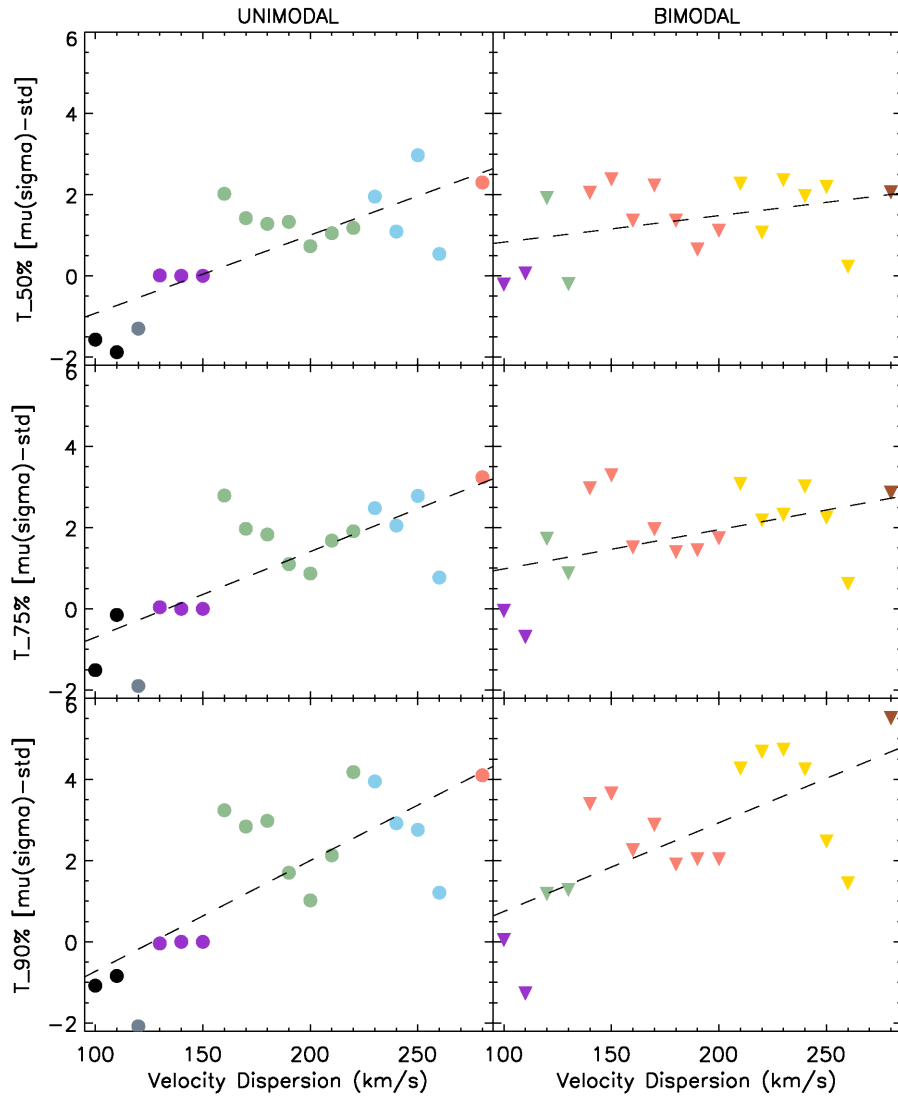
FIGURE 4.9— Differences on the assembly time from using a standard IMF instead of a universal one. Points are color-coded by the $\mu(\sigma)$ assumed: $\mu=0.8$ (black), $\mu=1.0$(gray), $\mu=1.3$(purple), $\mu=1.8$(green), $\mu=2.0$(blue), $\mu=2.3$(orange), $\mu=2.8$(yellow) and $\mu=3.3$(brown). A clear correlation with galaxy velocity dispersion is seen for the unimodal case among all the panels, while it is only emphasized at T_90% for the bimodal case.

On the contrary, massive compacts (purple symbols) are far above the 1:1 relation (dashed line) for all IMF slopes. Slightly lower stellar masses are obtained if an IMF slope is selected in the range of 0.8 - 1.0, as such values minimize the M/L. However, this stellar mass decrease is not sufficient to match the dynamical estimate. Using an IMF slope according to the $\mu - \sigma$ relation, a Salpeter IMF for this type of galaxies should be employed (the stellar mass derived with the Salpeter IMF is highlighted for each galaxy with a filled symbol). However, this assumption neither alleviates the problem.

Since we have pushed all the M_{star} parameters to the limits (e.g. IMF variations, models, methodologies, wavelength coverage) the only remaining explanation to solve the discrepancy could be an underestimation of the dynamical mass for massive compact objects.
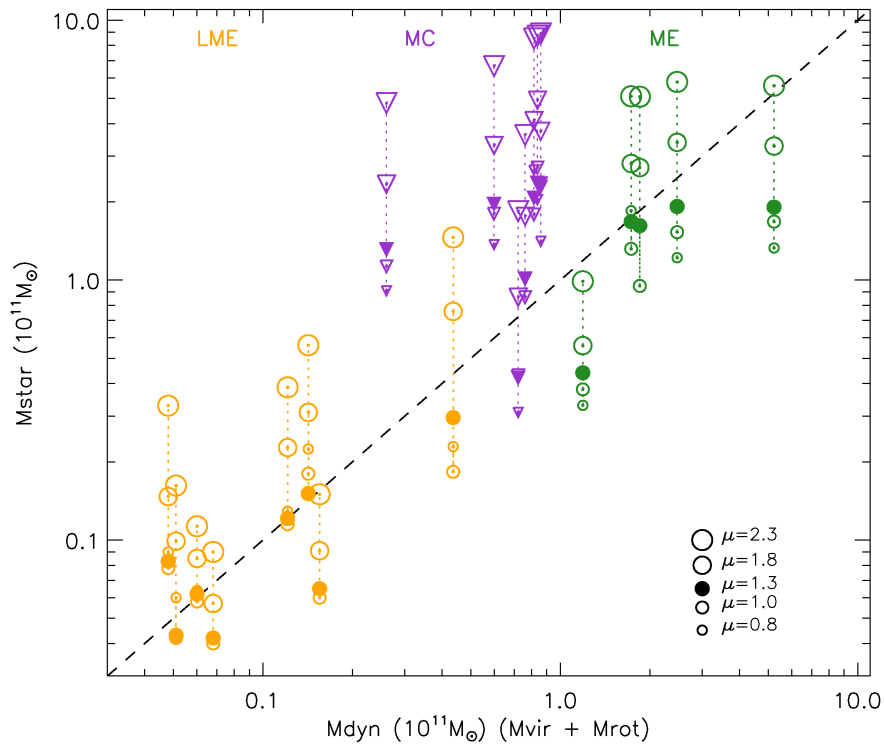
FIGURE 4.10— Dynamical *vs* stellar masses obtained from the SFHs using different IMF slopes. Massive compacts are plotted in purple triangles, massive ellipticals in green circles and low-mass ellipticals in orange circles. Filled symbols correspond to the stellar mass estimate with a Salpeter IMF for each galaxy. Symbol size increases with increasing IMF slope. Dynamical masses were estimated under the homology assumption.

4.6 Conclusions

We have gone one steep further on the discussion about the universality of the IMF. Although in this work we do not attempt to constrain the IMF, we explore and quantify the impact of varying its slope and shape on various galaxy properties (M/L, SFHs, M_{star}, mean ages and mass assembly timescales). We find that the choice of the IMF shape (unimodal *vs* bimodal) results in different stellar population parameter estimates, in particular for the steepest slopes. The unimodal (bimodal) IMF shape shows stronger (milder) deviations on the derived properties with respect to a standard IMF. The quantitative impacts of these variations are summarized as follows:

- We find a minimum on the M/L for an IMF slope that depends slightly on the age of the SSP: $\mu = 0.8$ for young SSPs, increasing towards $\mu = 1.0$ for the oldest stellar populations in the unimodal case. For the bimodal one this minimum is located at $\mu = 1.0$. This implies that at $\mu \sim 0.8$-1.0, the stellar mass derived from the SFHs will be minimized.

- In the unimodal case, the use of steeper IMF slopes increases the derived stellar masses by a factor of 4 (from $\mu = 0.8$ to $\mu = 2.3$), while the increase is by a factor of 1.5 in the bimodal one. This is the most sensitive parameter to the IMF variations.

- IMF slopes steeper than Salpeter tend to produce SFHs with smaller contributions of old populations. This effect decreases the mean age of the galaxy, both in mass and light. This effect is observed for both IMF shapes analyzed here, although in the unimodal case the decreases are more drastic, by a factor of up to 3 (from $\mu = 0.8$ to $\mu = 2.3$). It shows milder versions, up to 1.5, for the bimodal case.

- The use of a non-standard IMF delays (accelerates) the mass assembly of massive (low mass) galaxies. It can delay up to 4 Gyr the assembly of the 90% of the mass for the most massive ones. In fact, a relation between the galaxy velocity dispersion with the differences on the mass assembly timescales is seen, particularly for the unimodal case.

We see that the choice of an IMF slope according to the velocity dispersion of the galaxy, as recently pointed out, seems to provide more constrained results. While standard IMFs produce SFHs that rather depend on the mass (or age) of the galaxy, the use of the μ-σ relation produces comparable SFHs for the whole ETG family.

The most massive ellipticals, for which we adopt slopes steeper than Salpeter, present a small, but not negligible contribution of relatively younger stellar populations. Within this scenario, massive galaxies would no longer be completely dead and passively evolving old objects, supporting recent claims in this direction. Adopting flatter IMF slopes for the low-mass galaxies will render more similar, but still different, SFHs to the massive ones. However, the SFHs derived for our compact massive galaxies, which show unprecedented large contributions of young stellar populations, do not change significantly if the IMF slope is varied.

We also find galaxies with apparently no contribution from old stellar populations using a Salpeter IMF (*baby elliptical galaxies*). However, the use of flatter slopes, implied by their low velocity dispersion uncover a conspicuous old population for these not so "baby" galaxies.

These results point out that a variation of the IMF slope might solve, or at least alleviate, some of the problems encountered when analyzing galaxies of varied masses. Contrary to earlier warnings against the use of non standard IMFs, the present study provides new caveats on the assumption of a universal IMF, such as the questionable existence of early-type galaxies with virtually no contributions of old stellar populations, or the misclassified non-massive galaxies due to mass underestimation. Moreover, the more complex SFHs and the delays on the mass assembly timescales found for most massive galaxies when using steeper IMFs open new means to explain their formation and evolution.

5

Stellar populations of ETGs at high redshift

*Who controls the past
controls the future.
Who controls the present
controls the past.*
George Orwell

An approach to discriminate between the competing formation and evolution scenarios has been to study the differences between high density environments (such as clusters) and low density ones (field). Galaxy clusters are an excellent laboratory to study large amounts of ETGs in a same place at a same time. Moreover, we can study the influence that the local environment has on the stellar populations of the galaxies within the cluster. The tight correlations that ETGs in clusters follow for their global properties are indicative of an evolution with redshift from earlier epochs.

Thus, it is crucial to study these properties and correlations at high redshift to constrain the epoch of formation and the scenario more compatible with it. In addition, going back to earlier epochs presents several advantages in the study of the stellar populations. As the stellar populations become younger, its integrated spectrum varies more regularly, with small changes in the age. We also avoid the oldest stellar populations, i.e. the ones with ages older than the age of the Universe at that epoch, therefore we are avoiding those with the strongest age-metallicity degeneracies.

However, studying how the stellar populations are for galaxies in high red-shift clusters is challenging, as the obtaintion of data with enough S/N to accurately measure relevant absorption lines is difficult and time-consuming. So far, most of the works in this field have been performed by stacking the available spectra to achieve the required quality, only up to moderately-high redshifts (z~1; e.g. Kelson et al. 2001, Barr et al. 2005, Schiavon et al. 2006, Tran et al. 2007, Kelson et al. 2006, Sánchez-Blázquez et al. 2009). Only the high-quality data from the *Gemini/HST Galaxy Cluster Project* (Jørgensen et al. 2005, J05 hereafter) permits a detailed stellar population analysis of high-z clusters on an individual galaxy basis, a powerful tool to assess galaxy evolution.

In this chapter, we present a revised analysis of the stellar populations of RX J0152.7-1357, a rich galaxy cluster at moderately-high redshift (z = 0.83). The major novelty of this work is that we perform the study based on *each galaxy individually*, with the new set of state-of-the-art tools described in Chapter 2. With them, we are able to characterize for the first time, the ages, metallicities, abundance patterns and SFHs of each galaxy individually. In addition, we can analyze how these properties are located within the cluster, to disentangle any relation with the local environment. Finally, we compare the relations found for ETGs at high redshift with those of a cluster of similar properties at low redshift (Coma) to constrain different evolutionary scenarios. This detailed treatment of the stellar populations has permitted us to find a relation between the galaxy velocity dispersion, the type of SFH and the location of the galaxy within the cluster.

5.1   RX J0152.7-1357

The galaxies analyzed in this chapter belong to RX J0152.7-1357, a luminous X-ray galaxy cluster at z = 0.83. It has been the target of many observing programs such as the *ROSAT Deep Cluster Survey*, the *Wide Angle ROSAT Pointed Survey* (Ebeling et al., 2000), the *Bright Serendipitous High-redshift Archival Cluster survey* (Nichol et al., 1999), the *BeppoSAX* (Della Ceca et al., 2004), the *XMM-Newton* and *Chandra* (Jones et al. 2004, Maughan et al. 2003). In the optical range, it has been observed for the *ACS Intermediate Redshift Cluster Survey* (Blakeslee et al., 2006), obtaining a 5' mosaic of deep imaging (Figure 5.1), which permitted to classify morphologically the members of this cluster (Postman et al., 2005). Moreover, RX J0152.7-1357 is one of the nineteen cluster observed in the *Gemini/HST Galaxy Cluster Project* (J05), which is devoted to study galaxy evolution until approximately half the age of the Universe.

Previous X-ray studies of RX J0152.7-1357 have shown that this is a com-

plex cluster in a merging state, with a total mass similar to Coma (Maughan et al., 2003). Two big subclumps, the northern at z= 0.830 (N-SubCl) and the southern at z= 0.845 (S-SubCl) form the main structure, although a third small eastern group at z= 0.845 (E-group) and a diffuse group of galaxies off to the west at z= 0.866 are also part of the cluster (Demarco et al. 2005, Girardi et al. 2005). A dynamical analysis is presented in Girardi et al. (2005), showing that RX J0152.7-1357 is not yet dynamically relaxed, with velocity gradients and substructure. The northern subclump is a more evolved system, confirmed by its higher lensing mass (Jee et al., 2005).

Details about RX J0152.7-1357 structure, colours and physical properties can be found in Blakeslee et al. (2006). Patel et al. (2009) analyzed its red-sequence galaxies and Homeier et al. (2005) focused on the study of its few star forming ones, in order to describe their transformation to the red sequence. Moreover, it has been used in several studies to address the evolution of cluster properties with redshift, such as the role of mass and environment (di Serego Alighieri, Lanzoni & Jørgensen, 2006), the evolution on the K-band luminosity function (Ellis & Jones, 2004), the morphology-density relation (Postman et al., 2005), and the evolution of the Fundamental Plane (Holden et al. 2005, Jørgensen et al. 2006, Chiboucas et al. 2009 and Jørgensen & Chiboucas 2013).

Most of the work presented here is compared to the one published by J05, which we use as a reference. In the latter, the authors discussed possible evolutionary scenarios by comparing the averaged stellar population properties from RX J0152.7-1357 with a sample of galaxies in clusters of the local Universe, including an analysis of the Fundamental Plane. However, their approach was more focused on the general trends for the cluster than looking at the properties of each galaxy individually. The advent of new tools and new approaches for the stellar population analysis is one of the main reasons to revise this cluster. RX J0152.7-1357 needs to be fully characterized, as it is considered as a reference cluster at intermediately-high redshift, like Coma is in the local Universe.

5.2   Data and Reduction

This part of the thesis is completely based on archive data, and we refer to J05 for a full description of the observations and target selection. Nevertheless, we summarize here the relevant information for the analysis.
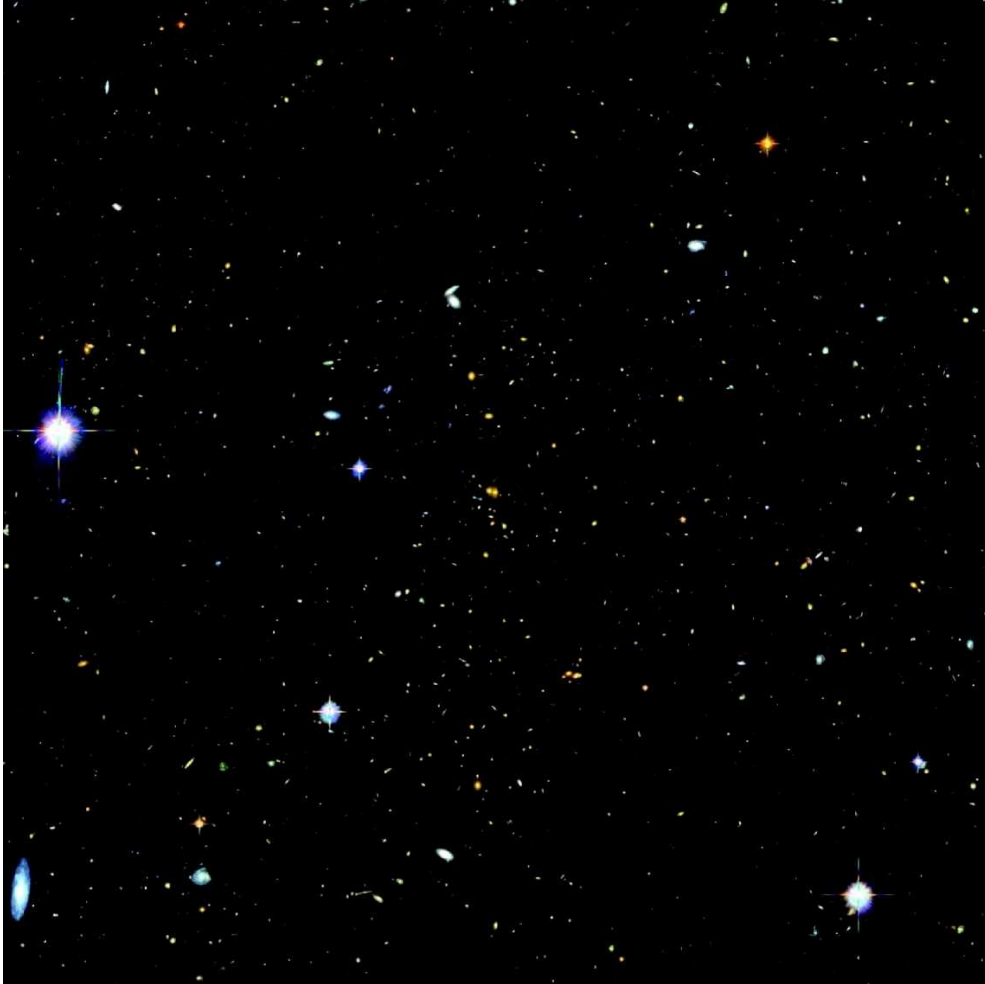
FIGURE 5.1— *ACS/WFC* F625W/F775W/F850LP colour-composite image showing 5' of the RX J0152.7-1357 mosaic field. Figure from Blakeslee et al. (2006).

The spectroscopic data for this cluster were obtained with GMOS-N at Gemini in semester 2002B (program GN-2002B-Q-29). A single mask was employed, with slits of 1" width and the R400 grating. This configuration provided an instrumental resolution of $\sigma = 116 \, \mathrm{km \, s^{-1}}$ at $4300 \, \text{Å}$ (at cluster rest frame). 25 individual exposures of the mask resulted in a total observing time of 21.7 hours. This delivered 41 high S/N galaxy spectra, covering an approximated wavelength rest-frame range of $\lambda\lambda \, 3200\text{-}5200 \, \text{Å}$ (depending on the redshift of the targets). 29 of these 41 spectra were ETGs cluster members. Moreover, two blue stars were included in the mask to remove the telluric absorption lines and

to flux-calibrate the spectra on a relative scale.

Although these data were already reduced by J05, we performed our own reduction with $\mathrm{RED}^{\mathrm{uc}}_{\mathrm{m}}\mathrm{E}$. We briefly describe here the main differences in the reduction process between both works (following Section 2.1). We carried out the data reduction step by step on each single frame, without making use of the pipeline. Therefore, we are in position to follow the critical steps in the process with high precision. Note that J05 used 6th-order polynomials to fit the dispersion function on the wavelength calibration, while we used more restrictive 2nd-order polynomials. We were also more restrictive with the polynomial used for the sky subtraction. We always used linear fits to the regions selected as sky. 2nd-order polynomials were only used when the first clearly failed at removing the lines, which occurred only for a few frames. However, the sky residuals of the reddest part of the spectra were impossible to remove (see Figure 5.5). Before adding all the frames corresponding to each galaxy, we extracted a 1.15" aperture, to match J05 data for comparison purposes. Our sample contains 24 ETGs out of the initial 29. Although the data had a moderately-high S/N for spectra at such redshifts, we discarded a few galaxies as their S/N were not high enough to perform this analysis.

In Section 5.4, we compare the scaling relations of the high-z cluster with those in a local cluster. We have chosen Coma for this comparison as both clusters have similar masses, luminosities and densities, hence both are considered as high-density, rich clusters. The spectra for Coma are those of Sánchez-Blázquez et al. (2006a) (PSB06a, hereafter). We have analyzed them using the same methods as for the galaxies of RX J0152.7-1357, to be consistent in the comparison analysis. Appendix C.3 summarizes the relevant results for Coma. For a more extended description, the reader is referred to PSB06a.

5.3   Galaxy Stellar Kinematics

We extracted the stellar kinematics for our ETGs using `pPxF` with the template models from V10. Our measured velocity dispersions are in general in good agreement with the ones of J05. However, for some galaxies we tend to recover larger velocity dispersions, as seen in Table 5.1. These differences could be attributed to a different choice of spectral regions for the fit. We fitted the region $\lambda\lambda$ 4100-4900 Å, avoiding the D4000-break, which broadens the spectra.

Our spectra reach 5200 Å, but we cannot rely on this reddest region as strong sky residuals are present. `GANDALF` was used to clean the spectra from emission lines. However, only three galaxies showed emission-line features in [OII] and [OIII], marked with an asterisk on Table 5.1. They will not be used

for safety in the stellar population analysis based on the measurements of the indices but they will be considered in the full-spectrum-fitting approach, as it allows for masking the emission lines.

ID	z	subclump	S/N	$\sigma(km\,s^{-1})$	$\sigma_{J05}(km\,s^{-1})$
338	0.8193	N-SubCl	14.32	122.1± 17.3	121.3
346	0.8367	N-SubCl	16.63	217.4± 18.1	151.0
422	0.8342	N-SubCl	17.73	103.5± 11.2	108.6
523	0.8206	N-SubCl	25.25	277.2± 12.4	239.3
566*	0.8369	N-SubCl	17.63	170.9± 13.6	162.5
627	0.8324	N-SubCl	13.79	194.4± 11.2	193.1
766	0.8346	N-SubCl	17.44	262.1± 11.8	244.9
776	0.8325	N-SubCl	20.56	160.7± 13.2	119.9
813	0.8351	N-SubCl	23.41	233.5± 20.1	218.2
908	0.8393	N-SubCl	23.12	250.6± 16.5	183.6
1027	0.8357	N-SubCl	14.44	236.2± 12.4	207.4
1085	0.8325	N-SubCl	22.91	252.2± 13.3	244.3
1110	0.8322	N-SubCl	16.84	220.4± 11.3	200.9
1159*	0.8357	N-SubCl	18.71	175.7± 9.9	150.3
1210	0.8372	N-SubCl	13.54	165.2± 23.6	127.6
1299*	0.8374	S-SubCl	15.17	200.2± 26.6	143.5
1458	0.8324	S-SubCl	12.18	173.9± 10.1	144.2
1507	0.8289	S-SubCl	10.76	206.3± 24.6	217.7
1567	0.8291	S-SubCl	14.38	211.1± 15.0	307.6
1590	0.8317	S-SubCl	17.76	199.7± 19.6	96.8
1614	0.8433	E-group	19.66	247.3± 9.0	222.8
1682	0.8463	E-group	20.89	227.7± 8.2	185.3
1811	0.8351	N-SubCl	13.83	154.4± 26.6	57.8
1935	0.8252	S-SubCl	18.38	207.1± 10.4	159.9

TABLE 5.1— Main properties of the galaxies selected from the J05 mask. (1)ID; (2)redshift; (3)subclump membership–N-SubCl (North Subclump)–S-SubCl (south subclump)–E-group (east group), see figure 5 from Girardi et al. (2005). (4) S/N per Å for the fitted range. (5) velocity dispersion from this work obtained with PPxF; (6)velocity dispersion from table 12 in J05. Asterisks mark the galaxies with emission-lines.

Figure 5.2 shows the position of the 24 ETGs within the cluster. Their measured velocity dispersions are colour-coded: grayish for galaxies with $\sigma <$ $150\,km\,s^{-1}$, yellow for $150 < \sigma \leq 200\,km\,s^{-1}$, green for $200 < \sigma \leq 250\,km\,s^{-1}$ and purple for galaxies with $\sigma > 250\,km\,s^{-1}$. The majority of the galaxies present velocity dispersions in the range 150-$250\,km\,s^{-1}$. We can see that gala-

xies populate the different regions of the cluster grouped by velocity dispersion. The center of the N-SubCl contains the galaxies with the highest velocity dispersions ($\sim 260\,\mathrm{km\,s^{-1}}$). The center of the S-SubCl is mainly populated by slightly lower, though still massive, galaxies ($\sim 230\,\mathrm{km\,s^{-1}}$), like the small E-group. On the contrary, it is clear that the outskirts of the subclumps are mainly populated by galaxies with the lowest masses ($\sigma \leq 200\,\mathrm{km\,s^{-1}}$).
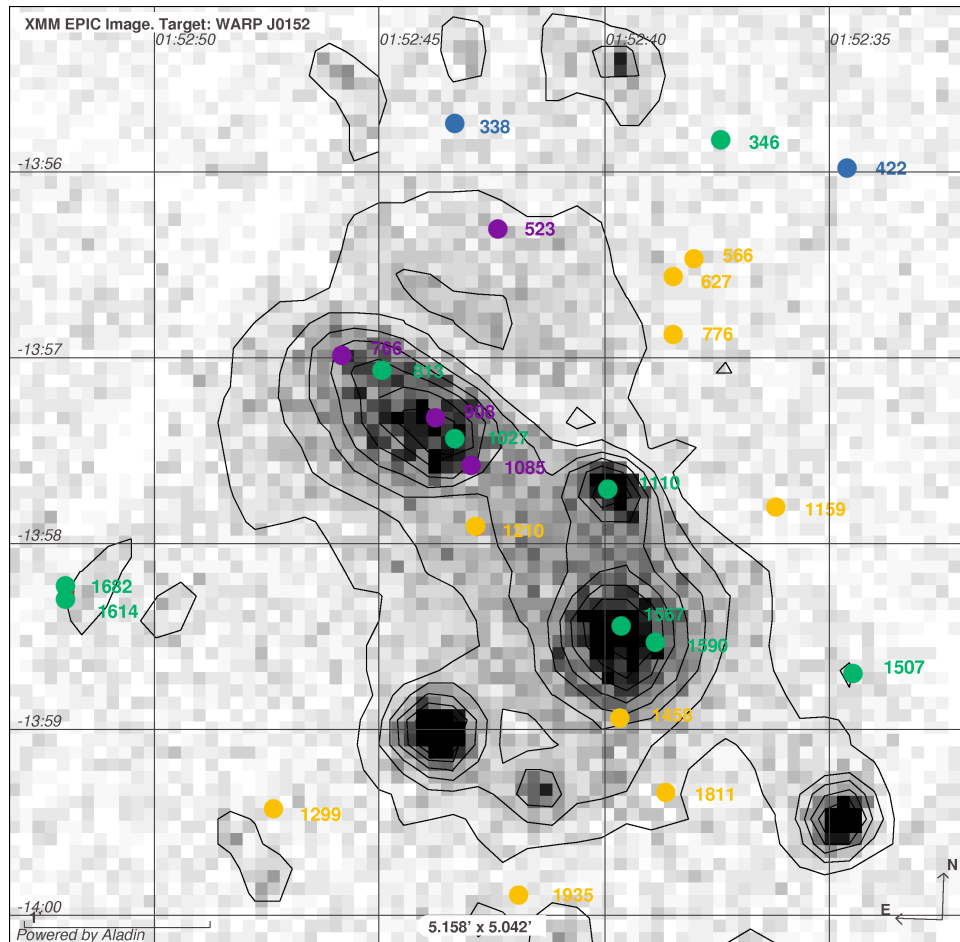
FIGURE 5.2— XMM-Newton image with the contours of the X-ray data superposed, created with `ALADIN`. The image covers approximately 5'×5'. ETG members considered in this study are colour-coded by their velocity dispersion: grayish for $\sigma < 150\,\mathrm{km\,s^{-1}}$, yellow for $150 < \sigma \leq 200\,\mathrm{km\,s^{-1}}$, green for $200 < \sigma \leq 250\,\mathrm{km\,s^{-1}}$ and purple for galaxies with $\sigma > 250\,\mathrm{km\,s^{-1}}$.

5.4   Stellar populations at z∼0.8

5.4.1   Ages, metallicities and abundance ratios

Following the general line of the thesis, we first study the stellar populations from the classical point of view of the index-index diagrams. The usable spectral range selected, discarding the regions with strong sky residuals, was $\lambda\lambda\,3600$-$4800\,\text{Å}$ (rest frame). This encompasses most of the commonly used indices for the stellar population analysis (CN3883, D4000, CaHK, HδA, HδF, CN1, CN2, Ca4227, G4300, HγA, HγF, Fe4383, Ca4558 and C$_2$4668). The new models of V10, which start at 3540Å, are appropriate for studying the bluest indices. Note that no such models were available when J05 published their analysis. However, as we were limited to $4800\,\text{Å}$, we could not safely measure the commonly used age-indicator Hβ, the metallicity-indicator Mgb or the composite total metallicity-indicator [MgFe]. Instead, we used HγF as age indicator and CN2, Fe4383 and C$_2$4668 as the best metallic indices (e.g. Thomas, Maraston & Bender 2003, Thomas, Maraston & Korn 2004, Sánchez-Blázquez et al. 2009). We also measured the CN3883 for the CN abundances, as CN2 in massive galaxies might not be fitted with scaled-solar stellar population models, as these features are observed to be stronger than predicted by those models (Sánchez-Blázquez et al. 2003, Carretero et al. 2004). Moreover, there was a telluric line in the spectral range covered by the CN2 index definition that was difficult to remove. We used the V10 models with the LIS-8.4Å system to derive the stellar populations of the galaxies in RX J0152.7-1357. The complete list of our galaxies and their line-strength measurements can be found on Appendix C.1, together with comparisons of our measurements with those from J05.

We will further characterize the cluster members by deriving their ages, metallicities and abundance ratios, when possible. In contrast, J05 focused on comparing the high-z cluster galaxies with a local sample. Figure 5.3 shows the measured indices with the model grids for our best age indicator (HγF) *vs* several metallic indices. Galaxies are shown in different colours depending on their σ, as in Fig. 5.2.

They are also coded by increasing size (for increasing σ) and membership to the subclumps (circles for the N-SubCl, diamonds for the S-SubCl and squares for the E-group). Some of the galaxies lie outside the grid, thus their ages and metallicities are difficult to extrapolate with RMODEL. We remind here that we do not consider extrapolated metallicities above 0.5 dex (therefore no value is given in Table 5.2). We find that galaxies have, on average, $\sim 3.5\,\text{Gyr}$, slightly younger than the ones stated in J05 (5 Gyr) but in better agreement with the value obtained on the basis of the colours (Blakeslee et al., 2006). It is worth noticing that the derived stellar population parameters might be slightly

different depending on the pair of indices in use. For example, we can see
that in general, the CN2 and the $C_2 4668$ tend to give higher metallicities than
Fe4383. This is because the model grids obtained with $H_\gamma F$ are not orthogonal
and because the galaxies show a non-solar abundance pattern. It is also seen
that the Fe4383 grid presents many galaxies lying outside the grid on the left
side. This occurs because Fe4383 tends to give older ages than the other indices
(see Figures C2 and C3 in the Appendix).
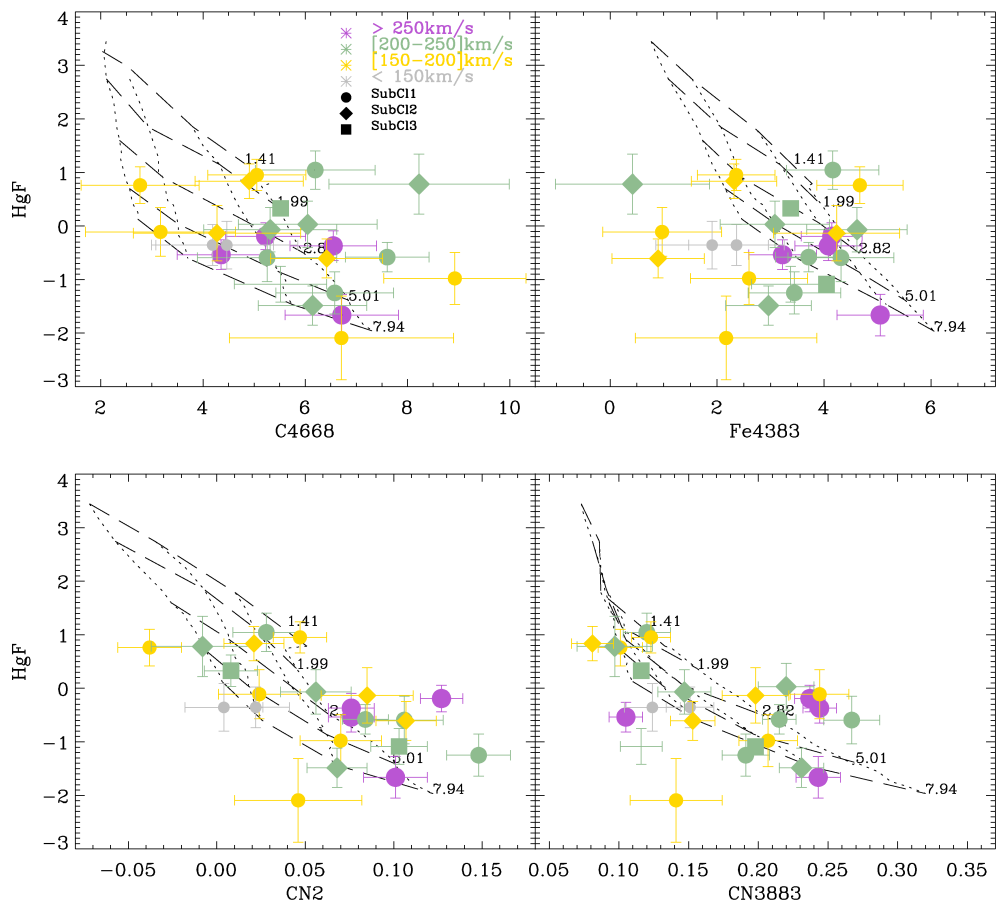
FIGURE 5.3— The age-sensitive indicator $H\gamma F$ is plotted *vs* several metallic-sensitive indices,
all measured in the LIS-8.4Å flux-calibrated system. The SSP model grids of V10 are plotted,
with age (in Gyr) increasing from top to bottom as indicated in the labels, and metallicity
from left to right ([Z/H]= -0.71, -0.40, 0.00, +0.22). Galaxies are colour-coded by the velocity
dispersion as in the previous figure. The membership on the different substructures is shown
by the different symbols: circles for the N-SubCl, diamonds for the S-SubCl and squares for
the E-group.

ID	age(Gyr) $C_2$4668-HγF	[M/H]	age(Gyr) Fe4383-HγF	[M/H]	age(Gyr) CN2-HγF	[M/H]	[C/Fe] from $C_2$4668	[CN/Fe] from CN2
338	$4.73^{+7.23}_{-2.01}$	$-0.203^{+0.41}_{-0.61}$	-	-	$10.07^{+10.15}_{-6.81}$	$-0.716^{+1.12}_{-2.25}$	-	-
346	-	-	-	-	$1.87^{+0.54}_{-0.63}$	$0.006^{+0.53}_{-0.84}$	-	-
422	$5.21^{+5.84}_{-1.98}$	$-0.230^{+0.23}_{-0.54}$	-	-	$7.10^{+6.58}_{-4.01}$	$-0.416^{+0.55}_{-1.23}$	-	-
523	$2.94^{+1.10}_{-0.59}$	$0.005^{+0.12}_{-0.25}$	$3.01^{+2.65}_{-1.01}$	$0.003^{+0.33}_{-0.45}$	-	-	$0.002^{+0.35}_{-0.51}$	-
627	$6.85^{+3.25}_{-2.61}$	$-0.579^{+0.65}_{-1.95}$	-	-	$5.16^{+4.41}_{-4.03}$	$-0.351^{+0.85}_{-1.12}$	-	-
766	$7.04^{+3.06}_{-2.27}$	$0.144^{+0.16}_{-0.32}$	-	-	$6.99^{+2.57}_{-1.69}$	$0.148^{+0.09}_{-0.11}$	$0.284^{+0.50}_{-0.62}$	$0.288^{+0.48}_{-0.54}$
776	$1.56^{+1.55}_{-0.81}$	$0.243^{+0.15}_{-0.34}$	$2.92^{+1.95}_{-1.01}$	$-0.45^{+0.56}_{-1.54}$	$1.86^{+1.62}_{-0.66}$	$0.300^{+0.39}_{-0.36}$	$0.693^{+0.58}_{-1.56}$	$0.750^{+0.68}_{-1.58}$
813	-	-	$6.79^{+6.15}_{-3.06}$	$-0.31^{+0.34}_{-0.92}$	$2.45^{+0.22}_{-0.96}$	$0.351^{+0.21}_{-0.24}$	$0.661^{+0.40}_{-0.95}$	$0.767^{+0.77}_{-1.58}$
908	$5.34^{+3.88}_{-1.80}$	$-0.200^{+0.22}_{-0.68}$	$8.83^{+8.48}_{-4.19}$	$-0.51^{+0.74}_{-1.31}$	$2.51^{+1.31}_{-0.25}$	$0.257^{+0.21}_{-0.28}$	$0.310^{+0.77}_{-0.77}$	-
1027	$3.80^{+6.62}_{-1.08}$	$-0.005^{+0.33}_{-0.43}$	$4.02^{+3.94}_{-1.52}$	$-0.007^{+0.59}_{-0.71}$	-	-	$0.002^{+0.83}_{-0.68}$	-
1085	$2.36^{+0.67}_{-0.12}$	$0.469^{+0.26}_{-0.29}$	$3.72^{+3.47}_{-1.21}$	$-0.11^{+0.44}_{-0.51}$	$3.07^{+1.52}_{-0.56}$	$0.478^{+0.03}_{-0.52}$	$0.579^{+0.51}_{-0.59}$	$0.588^{+0.44}_{-0.73}$
1110	$4.67^{+5.52}_{-3.65}$	$0.172^{+0.36}_{-0.52}$	-	-	-	-	-	-
1210	-	-	-	-	$4.89^{+3.47}_{-3.22}$	$0.006^{+0.09}_{-0.23}$	-	-
1458	$3.85^{+6.72}_{-2.60}$	$-0.181^{+0.35}_{-1.01}$	$2.75^{+2.33}_{-2.09}$	$0.110^{+0.30}_{-1.41}$	-	-	$-0.291^{+0.46}_{-1.76}$	-
1507	-	-	-	-	-	-	-	-
1567	$1.92^{+1.54}_{-1.13}$	$0.347^{+0.31}_{-0.52}$	$5.07^{+3.94}_{-3.82}$	$-0.422^{+0.41}_{-1.32}$	-	-	$0.767^{+0.51}_{-1.42}$	-
1590	$2.72^{+1.41}_{-0.43}$	$0.309^{+0.28}_{-0.35}$	-	-	-	-	-	-
1614	-	-	$9.68^{+6.87}_{-3.38}$	$-0.310^{+0.32}_{-1.02}$	$3.43^{+1.65}_{-0.64}$	$0.387^{+0.23}_{-0.35}$	-	$0.697^{+0.39}_{-1.08}$
1682	$1.98^{+0.89}_{-0.71}$	$0.240^{+0.21}_{-0.36}$	$2.62^{+2.06}_{-0.65}$	$-0.200^{+0.15}_{-0.67}$	$4.80^{+5.06}_{-3.47}$	$-0.530^{+0.78}_{-1.43}$	$0.440^{+0.26}_{-0.76}$	$-0.330^{+0.79}_{-1.58}$
1811	-	-	-	-	-	-	-	-
1935	$6.84^{+5.45}_{-1.02}$	$0.073^{+0.06}_{-0.23}$	-	-	$8.40^{+5.91}_{-3.23}$	$-0.060^{+0.18}_{-0.36}$	-	-

TABLE 5.2— Ages and metallicities derived from different index-index grids (columns 2-7). Errors were estimated with 1000 Monte-Carlo simulations with **RMODEL** using the errors on the indices and deriving 1σ error contours in the age-metallicity space. Columns 8 and 9 are the abundance ratios inferred from the index-index grids.

A trend between the age and the metallicity when deriving them from any pair of indices has been previously reported, where younger galaxies seem to be more metal rich (e.g. Trager et al. 1998, Jørgensen 1999, Ferreras, Charlot & Silk 1999, Terlevich & Forbes 2002, PSB06a). Figure 5.4 shows the ages *vs* the metallicities inferred from the different HγF-metallic index grids. Although the error bars are large, we can recover this slight trend. This effect is largely due to the non-orthogonality of the model grids employed to infer these parameters. This can be also understood if galaxies have undergone different episodes of star formation, where the newly formed stars come from a previously enriched gas from the first episodes. Then, the younger ages would be biased by the more extended SFHs. We will be in the position to address this issue in next section, where we determine the SFHs of these galaxies.
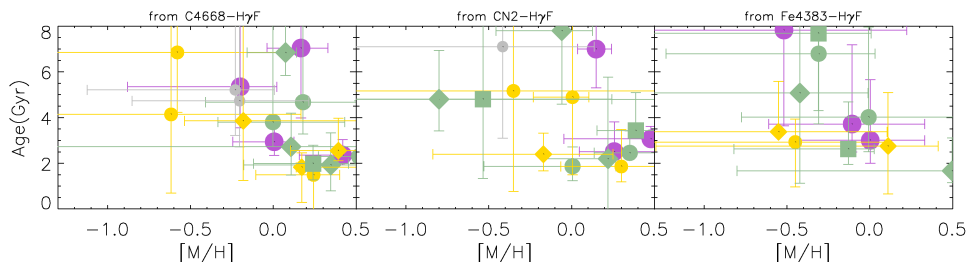
FIGURE 5.4— Age-metallicity relations for the galaxies in the cluster, obtained from the different index-index pairs. Colors, symbols and sizes are like in Figure 5.3. Note that not all galaxies are represented here as we only plot the values that were safely extrapolated. Though the large errors in mainly all metallicity estimates, a slight trend for the youngest galaxies to be more metal rich is seen, particularly from the $C_2 4668$-H_γ pair.

It is known that non-solar abundance ratios exist (e.g Peletier 1989, Faber et al. 1999, Worthey & Jowett 2003, Thomas et al. 2005). Because elements are produced in the stars on different timescales, they encode crucial information about the SFH of the galaxy (e.g. Peletier 1989, Worthey, Faber & Gonzalez 1992, Vazdekis et al. 2001a, Carretero et al. 2004, PSB06a). The difference between the metallicity from a metallic-index X with respect to the metallicity derived from a Fe-sensitive index such as the Fe4383, $[Z_x/Z_{Fe}]$, is a good proxy for these abundance ratios (Carretero et al. 2004, Yamada et al. 2006, V10, LaBarbera et al. (2013)). We have derived them only when all three estimates were reliable (age, Z_x and Z_{Fe}), which occurs only for a few galaxies (around 8 galaxies for each pattern, see Table 5.2). With such a limited sample, we are not able to discuss the abundance patterns here. However, we will fully discuss them in Section 5.3.3, where a new combined method is described.

5.4.2   Star Formation Histories

It is well known that spectra at high-z do not usually have enough S/N and the sky subtraction is difficult, so any feature that remains in the spectra from the reduction process can give misleading line strength values. Therefore, we employ a full-spectrum-fitting approach, which is less sensitive to the sky effects, as these affected regions can be masked. Nonetheless, the outputs from this approach need always to be combined with the information from the analysis of the indices.

For this analysis, we used STARLIGHT with a set of SSP SED models from V10. The age of the Universe at the redshift of the cluster, with the adopted cosmology, is $\sim$7 Gyr. For this reason, we limited our models to ages below the lookback time of the cluster. Considering errors associated to age errors, we limited the base models for RX J0152.7-1357 to 8 Gyr. Removing approximately half the age of the Universe has the advantage of avoiding the models that are heavily affected by the age-metallicity degeneracy. The highest metallicity value is imposed by the models that fed the code. Therefore, for those galaxies for which the code gives [Z/H]$=0.22$, this metallicity should be considered as a lower limit (marked with a $\diamond$ in Table 5.5). This implies that these galaxies could be, in fact younger and more metal rich than stated.

Recent works have highlighted the role of the IMF, reporting a dependence with galaxy mass or velocity dispersion, in the sense that more massive galaxies demand steeper IMF slopes (e.g. Cenarro et al. 2003, Falcón-Barroso et al. 2003, Cappellari 2012, Conroy & van Dokkum 2012a, Spiniello et al. 2012, van Dokkum & Conroy 2012, Ferreras et al. 2013). Moreover, in Chapter 4 we have quantified the impact that such variations have on the derived SFHs from the full-spectrum-fitting approach. For these reasons, we will use in this section the IMF slope that corresponds to the galaxy velocity dispersion according to Ferreras et al. (2013). Similarly to what we did in Chapter 4, we choose for each galaxy the slope closer to $\mu= [0.8, 1.0, 1.3, 1.8]$, specified in Table 5.3.

Figures 5.5 and 5.6 show the 24 ETGs spectra (with the new reduction here performed) together with the mixture of SSPs from the V10 models that best fitted the spectra from the full-spectrum-fitting approach (left panels). The adopted IMF slope, which depends on σ is indicated for each galaxy. The right panels show the derived SFH for all the galaxies in RX J0152.7-1357. Three different SFHs are clearly distinguishable: *(i)* a single episode of star formation with old age ($\sim$ 6-7 Gyr, Pop_O hereafter); *(ii)* a single episode of star formation with intermediate age ($\sim$ 2-4 Gyr; Pop_M); *(iii)* an extended star formation history or a non-negligible contribution from a recent burst of SFH on top of
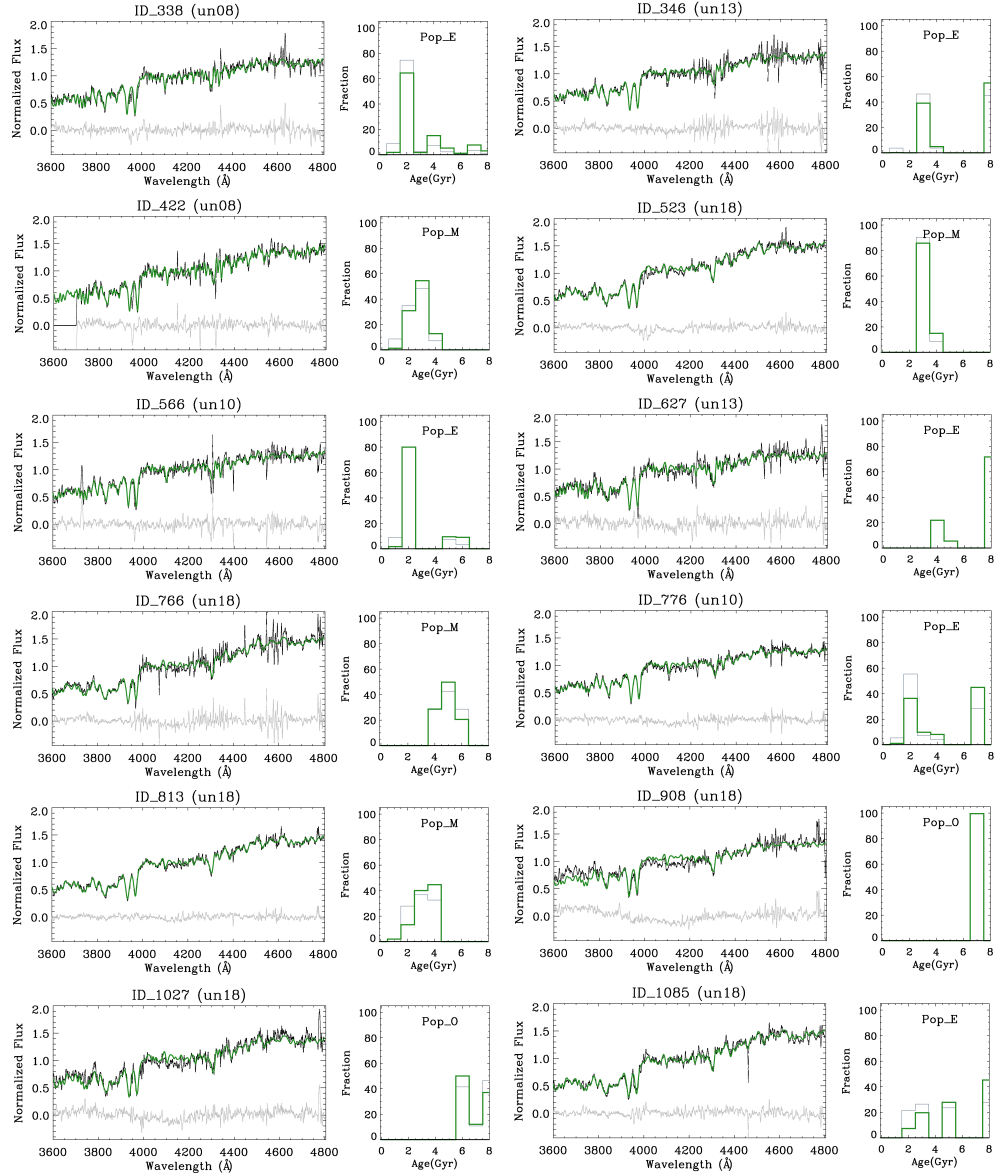
FIGURE 5.5— The RX J0152.7-1357 cluster galaxy spectra for this study are plotted, to-gether with the best fit from STARLIGHT and their residuals (left panels). The IMF slope adopted is stated on top of each panel. We plot in green the histograms corresponding to the mass-weighted SFHs whereas in gray we plot the luminosity-weighted SFHs (right panels). The different types of SFHs, classified according to the age of the dominant burst, are stated on each panel.
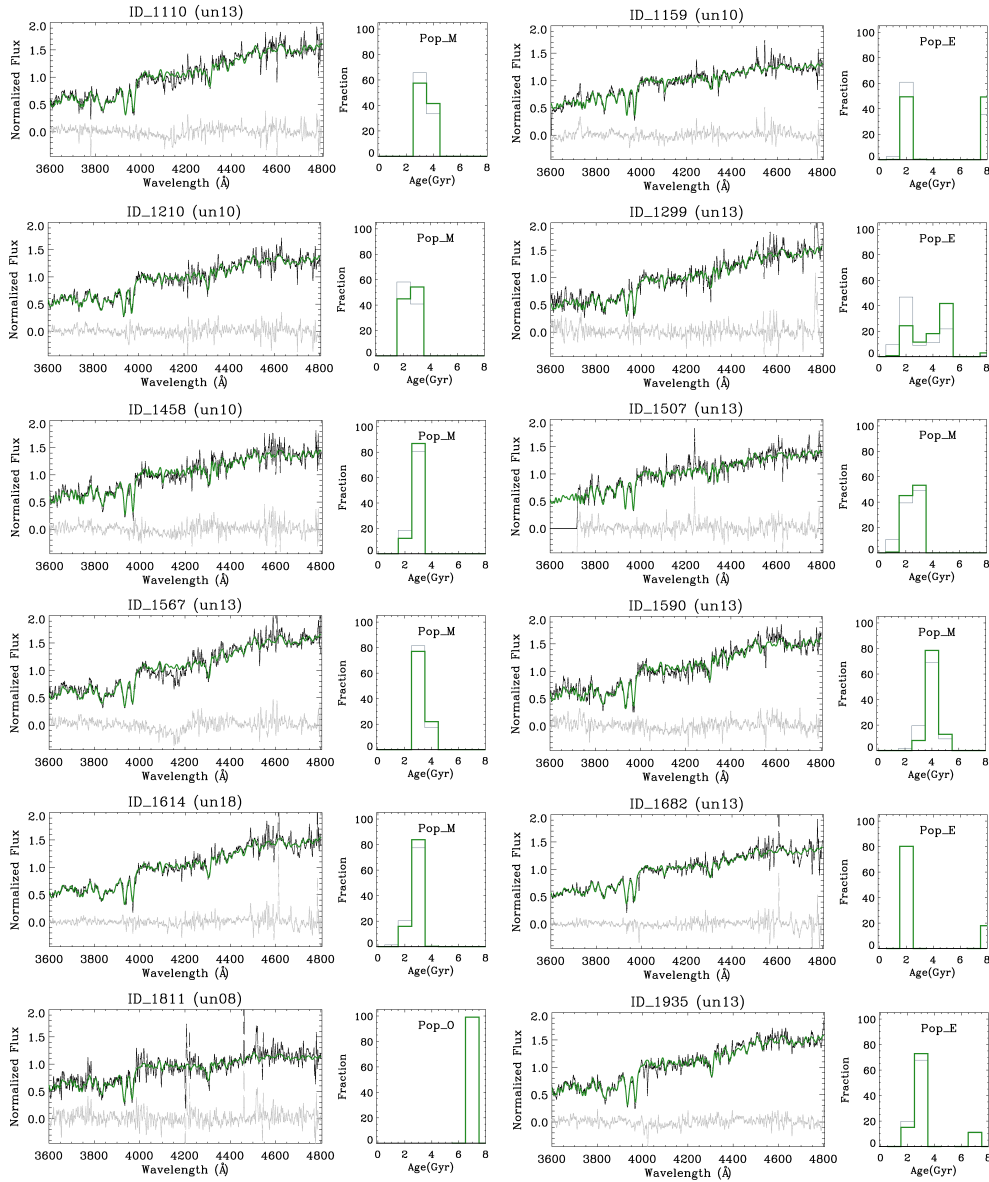
FIGURE 5.6— Continuation of Figure 5.5

ID	IMF slope	L_age (Gyr)	L_met	M_age (Gyr)	M_met	SFH_type
338	08	2.147±0.365	0.1413±0.0803	2.900±0.494	0.1292±0.0803	Pop_E
346	13	4.776±0.725	-0.0442±0.0743	5.429±0.824	-0.0835±0.0743	Pop_E
422	08	2.177±0.328	0.1656±0.0740	2.462±0.372	0.1976±0.0740	Pop_E
523	18	3.705±0.307	0.1558±0.0520	3.642±0.302	0.1620±0.0520	Pop_M
566	10	2.068±0.297	0.1289±0.0717	2.413±0.347	0.1246±0.0717	Pop_E
627	13	6.737±1.176	-0.1164±0.0817	6.804±1.188	-0.1255±0.0817	Pop_E
766	18	5.615±0.816	0.0785±0.0722	5.375±0.781	0.1193±0.0722	Pop_M
776	10	3.543±0.426	0.0581±0.0641	4.733±0.570	-0.0161±0.0641	Pop_E
813$^\diamond$	18	2.971±0.290	0.1942±0.0568	3.328±0.325	0.2200±0.0568	Pop_M
908	18	7.940±0.793	-0.5786±0.0575	7.940±0.793	-0.5554±0.0575	Pop_O
1027	18	6.983±1.183	0.0017±0.0800	7.003±1.186	0.0606±0.0800	Pop_O
1085$^\diamond$	18	4.704±0.478	0.1984±0.0580	5.89±0.598	0.2200±0.0580	Pop_E
1110$^\diamond$	13	3.190±0.479	0.1984±0.0738	3.28±0.493	0.2200±0.0738	Pop_M
1159	10	3.803±0.514	-0.0024±0.0689	4.717±0.638	-0.0852±0.0689	Pop_E
1210	10	2.778±0.490	-0.1981±0.0823	2.952±0.521	-0.1987±0.0823	Pop_E
1299	13	2.664±0.435	0.1706±0.0781	3.752±0.614	0.1967±0.0781	Pop_E
1458$^\diamond$	10	2.116±0.396	0.1984±0.0858	2.157±0.404	0.2200±0.0858	Pop_M
1507	13	1.750±0.348	0.1740±0.0895	1.933±0.384	0.1800±0.0895	Pop_M
1567	13	3.247±0.551	-0.1981±0.0802	3.318±0.564	-0.1982±0.0802	Pop_M
1590$^\diamond$	13	3.240±0.463	0.1921±0.0714	3.565±0.509	0.2200±0.071	Pop_M
1614	18	3.041±0.388	0.1852±0.0665	3.091±0.394	0.1939±0.0665	Pop_M
1682	13	3.095±0.364	0.1178±0.0633	3.123±0.368	0.1158±0.0633	Pop_E
1811	08	7.939±1.701	0.1350±0.0945	7.940±1.701	0.1800±0.0945	Pop_O
1935	13	3.437±0.474	0.1520±0.0698	3.461±0.477	0.1546±0.0698	Pop_E

TABLE 5.3— Mean ages and total metallicities derived from the full-spectrum fitting code STARLIGHT. The type of SFH is specified with Pop_O (old burst), Pop_M (intermediate-age burst) or Pop_E (extended or residual SFH). Galaxies labeled with $^\diamond$ are those that saturate on metallicity.

an old/intermediate burst (Pop E). Table 5.5 lists the mean light- and mass-weighted ages and total metallicities derived from this approach as well as the SFH type for each galaxy.

Figure 5.7 shows the relation between the mean age and the mean metallicity as in Figure 5.4 but with the values from the full-spectrum-fitting approach. Galaxies are now colour-coded by the parametrization of Pop O, Pop M and Pop E. The slight trend where younger galaxies show higher metallicities is emphasized. It is worth to note that the younger and more metal rich galaxies are in fact the ones with Pop E, i.e. showing a more extended SFH. This supports the idea that this age-metallicity relation is due to a secondary burst of star formation that forms stars from a previously enriched material.
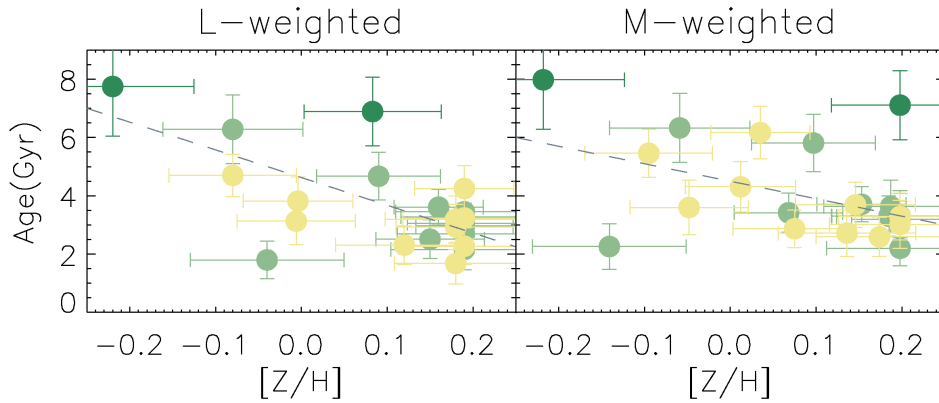
FIGURE 5.7— Age-metallicity relation for the galaxies in the cluster, obtained from the full-spectrum-fitting approach. Galaxies are colour-coded in a green scale depending their SFH type: dark green for Pop O, green for Pop M and pale green for Pop E.

5.4.3 Combined method

We have seen that the various index-index diagrams of Fig. 5.3 do not provide rather orthogonal model grids and therefore it happens that galaxies fall outside the diagrams. Moreover, even though some of the grids are virtually more orthogonal, galaxies with non-solar abundance patterns also fall outside the grids. As the spectral coverage do not allow us to work with more powerful indices such as Hβ_o or [MgFe], we present here a new approach where we remove to a great extent the dependence on age.

This new "combined method" merges the luminosity-weighted age derived from the full-spectrum-fitting (on the y-axis) with the model predictions for the metallicity indicators (on the x-axis). This leads to nearly orthogonal grids, where most of the galaxies fall inside, as seen in Figure 5.8.
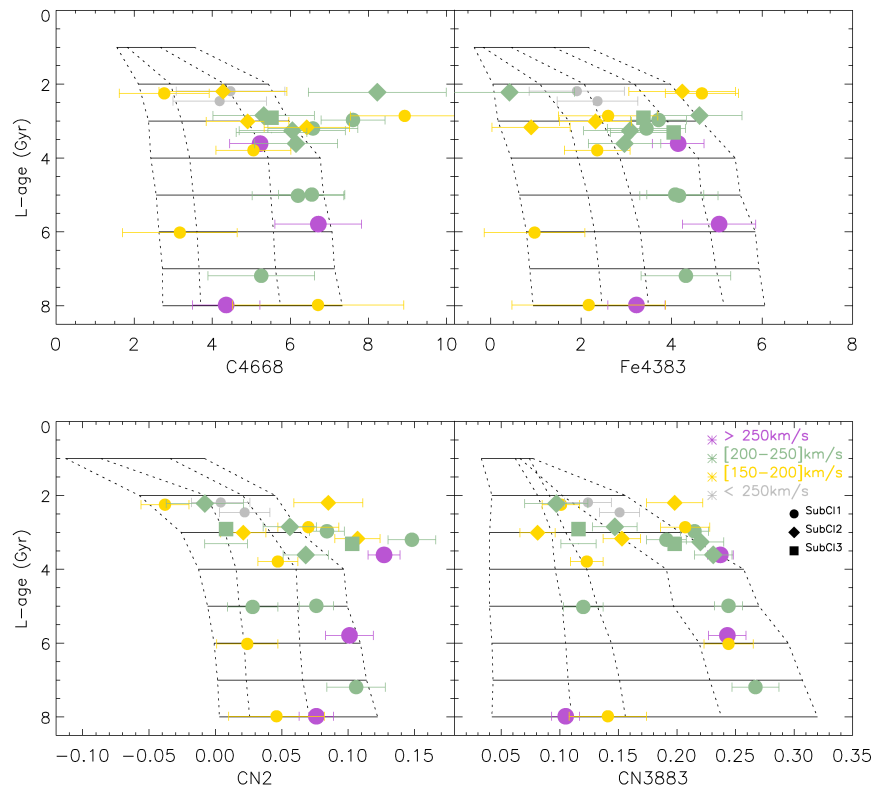
FIGURE 5.8— Diagnostic diagrams where the derived mean luminosity-weighted ages from the full-spectrum-fitting are plotted against various metallicity indicators. Note that the resulting model grids are virtually orthogonal, which permits to extrapolate the metallicities and derive abundance patterns. Colors, symbols and sizes are as in Figures 5.3 and 5.4

We can now derive metallicities and abundance ratios for nearly all the galaxies, listed in Table 5.4. The robustness of this method was tested by comparing the estimates obtained from the index-index diagrams for those few galaxies in which it was possible with those from this approach (Appendix C.2). In addition, we can now determine the abundance patterns in detail.

ID	[M/H] C$_2$4668-L_age	[M/H] Fe4383-L_age	[M/H] CN2-L_age	[M/H] CN3883-L_age	[C/Fe] from C$_2$4668	[CN/Fe] from CN2	[CN/Fe] from CN3883
338	$0.00^{+0.30}_{-0.38}$	$-0.45^{+0.35}_{-0.35}$	$-0.35^{+0.35}_{-0.25}$	$0.10^{+0.05}_{-0.20}$	$0.45^{+0.46}_{-0.51}$	$0.10^{+0.49}_{-0.43}$	$0.55^{+0.35}_{-0.40}$
346	$0.10^{+0.20}_{-0.20}$	$-0.15^{+0.25}_{-0.20}$	$-0.35^{+0.20}_{-0.20}$	$0.55^{+0.17}_{-0.10}$	$0.25^{+0.32}_{-0.28}$	$-0.20^{+0.32}_{-0.25}$	$-0.40^{+0.30}_{-0.20}$
422	$-0.10^{+0.28}_{-0.30}$	$-0.40^{+0.31}_{-0.25}$	$0.10^{+0.10}_{-0.05}$	$0.30^{+0.41}_{-0.25}$	$0.30^{+0.39}_{-0.36}$	-	$0.51^{+0.35}_{-0.27}$
523	$0.00^{+0.18}_{-0.15}$	$0.00^{+0.15}_{-0.20}$	-	$0.22^{+0.17}_{-0.17}$	$0.00^{+0.23}_{-0.25}$	-	$0.22^{+0.22}_{-0.26}$
627	$-0.35^{+0.35}_{-0.45}$	$-1.30^{+0.55}_{-0.70}$	$-0.40^{+0.25}_{-0.28}$	$0.10^{+0.10}_{-0.17}$	$0.75^{+0.65}_{-0.83}$	$0.90^{+0.60}_{-0.75}$	$0.31^{+0.70}_{-0.55}$
766	$0.18^{+0.22}_{-0.18}$	$0.05^{+0.20}_{-0.05}$	$0.20^{+0.10}_{-0.05}$	$0.10^{+0.08}_{-0.05}$	$0.13^{+0.29}_{-0.26}$	$0.15^{+0.22}_{-0.29}$	$0.05^{+0.21}_{-0.20}$
776	$-0.10^{+0.26}_{-0.14}$	$-0.55^{+0.25}_{-0.20}$	$-0.10^{+0.10}_{-0.10}$	$-0.40^{+0.10}_{-0.15}$	$0.45^{+0.36}_{-0.24}$	$0.45^{+0.29}_{-0.20}$	$0.15^{+0.26}_{-0.25}$
813	-	$0.00^{+0.15}_{-0.20}$	$0.40^{+0.10}_{-0.10}$	$0.30^{+0.05}_{-0.08}$	$0.40^{+0.18}_{-0.22}$	$0.40^{+0.17}_{-0.21}$	$0.30^{+0.25}_{-0.15}$
908	$-0.30^{+0.20}_{-0.15}$	$-0.45^{+0.30}_{-0.15}$	$0.02^{+0.08}_{-0.07}$	$-0.75^{+0.15}_{-0.05}$	$0.15^{+0.25}_{-0.33}$	$-0.30^{+0.43}_{-0.30}$	$-0.30^{+0.21}_{-0.30}$
1027	$-0.10^{+0.28}_{-0.25}$	$-0.20^{+0.25}_{-0.25}$	$0.18^{+0.12}_{-0.03}$	$0.10^{+0.08}_{-0.05}$	$0.10^{+0.37}_{-0.35}$	$0.38^{+0.27}_{-0.25}$	$0.30^{+0.26}_{-0.25}$
1085	$0.15^{+0.17}_{-0.10}$	$-0.15^{+0.15}_{-0.15}$	$0.10^{+0.08}_{-0.10}$	$0.18^{+0.04}_{-0.06}$	$0.30^{+0.22}_{-0.18}$	$0.25^{+0.17}_{-0.18}$	$0.33^{+0.15}_{-0.16}$
1110	$0.30^{+0.20}_{-0.25}$	$-0.15^{+0.25}_{-0.25}$	-	$0.18^{+0.08}_{-0.10}$	$0.45^{+0.32}_{-0.35}$	-	$0.33^{+0.26}_{-0.25}$
1299	-	$-0.40^{+0.20}_{-1.20}$	$0.30^{+0.10}_{-0.20}$	$0.30^{+0.10}_{-0.10}$	$-0.22^{+0.42}_{-0.35}$	$0.70^{+0.29}_{-0.29}$	$0.70^{+0.29}_{-0.24}$
1458	$0.00^{+0.30}_{-0.50}$	$0.22^{+0.20}_{-0.20}$	-	-	-	-	-
1507	-	$-1.20^{+0.30}_{-1.20}$	$-0.40^{+0.40}_{-0.25}$	$-0.30^{+0.35}_{-0.60}$	$0.50^{+0.42}_{-0.42}$	$0.80^{+0.44}_{-1.22}$	$0.90^{+0.40}_{-1.34}$
1567	$0.20^{+0.30}_{-0.30}$	$-0.30^{+0.30}_{-0.30}$	-	$0.22^{+0.08}_{-0.04}$	-	-	$0.55^{+0.31}_{-0.30}$
1590	$0.30^{+0.20}_{-0.20}$	$-1.00^{+0.30}_{-0.40}$	-	$0.00^{+0.02}_{-0.10}$	$1.30^{+0.36}_{-0.44}$	-	$1.00^{+0.31}_{-0.41}$
1614	-	$0.00^{+0.20}_{-0.20}$	-	$0.18^{+0.02}_{-0.08}$	-	-	$0.18^{+0.20}_{-0.21}$
1682	$0.12^{+0.18}_{-0.22}$	$-0.10^{+0.20}_{-0.20}$	$-0.40^{+0.20}_{-0.10}$	$-0.35^{+0.20}_{-0.10}$	$0.22^{+0.26}_{-0.29}$	$-0.30^{+0.28}_{-0.22}$	$-0.25^{+0.28}_{-0.22}$
1811	$0.15^{+0.55}_{-0.45}$	$-0.80^{+0.45}_{-0.70}$	$-0.20^{+0.25}_{-0.35}$	$-0.50^{+0.20}_{-0.20}$	$0.95^{+0.71}_{-0.83}$	$0.60^{+0.51}_{-0.78}$	$0.30^{+0.20}_{-0.72}$
1935	$0.20^{+0.30}_{-0.20}$	$-0.35^{+0.20}_{-0.25}$	$0.10^{+0.12}_{-0.10}$	$0.22^{+0.03}_{-0.04}$	$0.55^{+0.32}_{-0.36}$	$0.45^{+0.23}_{-0.26}$	$0.57^{+0.20}_{-0.25}$

TABLE 5.4— Metallicities obtained with the combined age$_{SFH}$-index method, using different metallic indices (Columns 2-5) and their abundance ratios (columns 6-8).

As the abundance patterns are known to depend on the velocity dispersion (e.g. Carretero et al. 2004), by averaging the galaxies with $150 < \sigma \leq 250\,\mathrm{km\,s^{-1}}$ we find that the [C/Fe] is $\sim 0.37\,\mathrm{dex}$. Slightly lower values are obtained for the [CN/Fe] ratio, from both metallic indices CN3883 and CN2 ($\sim 0.30\,\mathrm{dex}$).

We stress that this method should be taken as a proxy for the abundance ratios, as it is subject to the ages derived with the full-spectrum-fitting approach. Note that the ages derived from the full-spectrum-fitting approach may differ from those derived from the various index-index diagrams (e.g. Vazdekis et al. 2001a, Mendel, Proctor & Forbes 2007).

5.4.4 Distribution of the stellar populations within the cluster

The distribution of the stellar population properties within the cluster is studied to find any possible relation with the local environment. By these means, the top-left panel of Figure 5.9 shows that our galaxies present in general ages of ~ 3-$4\,\mathrm{Gyr}$. The center of the N-SubCl contains the galaxies with the oldest ages (~ 5-$7\,\mathrm{Gyr}$). The small range in metallicities derived for our galaxies (top-right panel), only shows that except for three galaxies being very metal poor, located in the centers of the subclumps, the rest of galaxies present solar metallicities or slightly above. The centers of the subclumps also contain those galaxies that reached the limiting metallicity.

The bottom panel is the most relevant one, showing the distribution of the different SFHs types. Galaxies with different SFHs clearly populate different regions in the cluster: galaxies with Pop_O are located at the center of the N-SubCl, those with Pop_M populate the whole S-SubCl and part of the N-SubCl center, and those with Pop_E are located on the outskirts of the subclumps. This indicates that galaxies formed first at the N-SubCl, followed by the S-SubCl. The outskirts have been populated more recently, probably by the infalling of new galaxies.

Moreover, there seems to be a relation between the SFH type and velocity dispersion: most massive galaxies tend to show Pop_O type, intermediate-mass galaxies tend to show Pop_M and the galaxies with the smaller velocity dispersions present Pop_E SFHs. We will extend on this issue in Section 5.6.
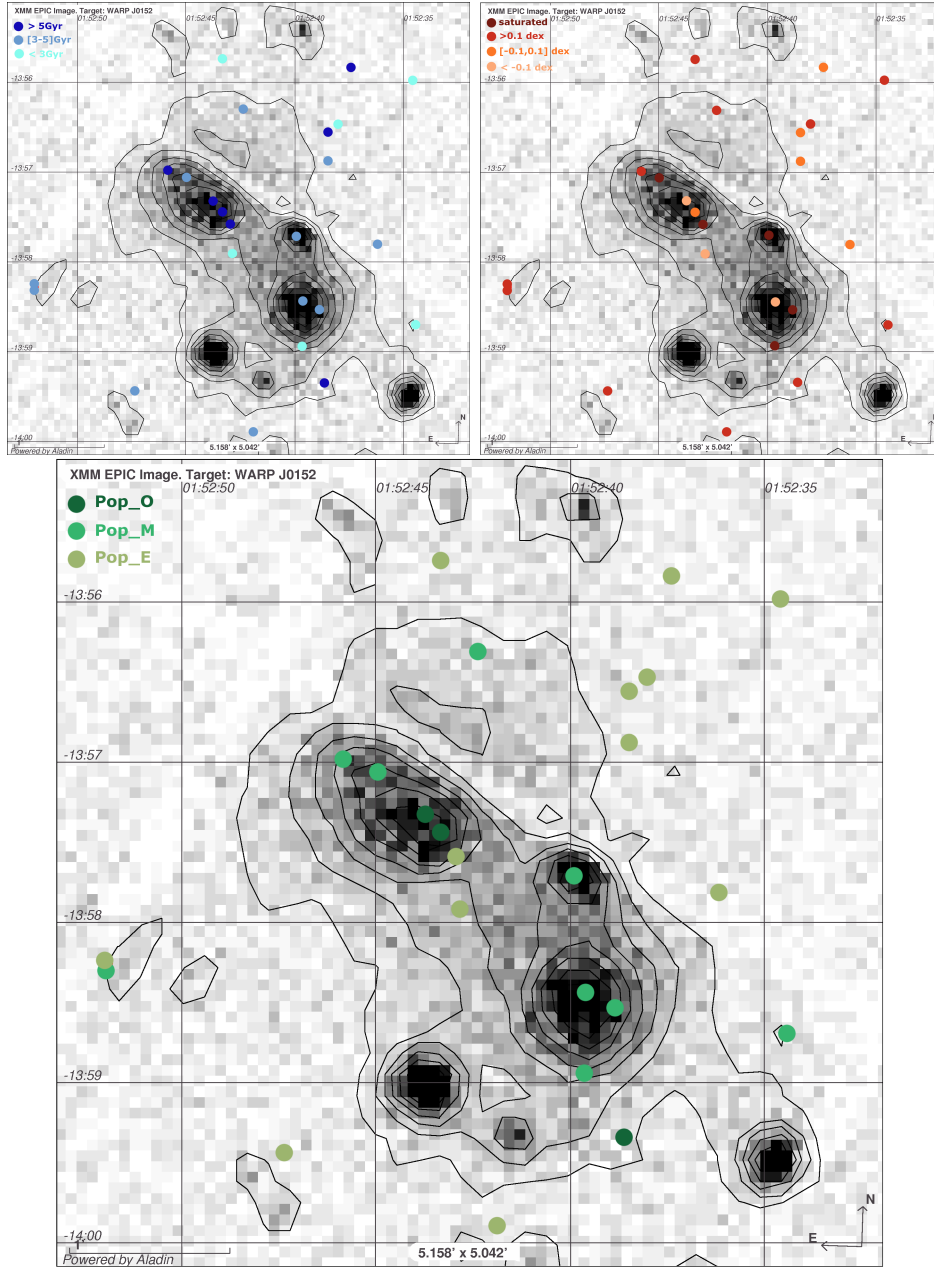
FIGURE 5.9— Galaxy location within the cluster, colour coded as specified in each panel. *Top-left panel*: mean-mass weighted age from STARLIGHT; *Top-right panel*: mass-weighted metallicity; *Bottom panel*: different SFH types as specified in Fig. 5.7.

5.5 Evolution through cosmic time

ETGs at low redshift form a very homogeneous class, following very tight relations on their global properties, such as the colour-magnitude relation, the fundamental plane and several scaling relations (e.g Visvanathan & Sandage 1977, Dressler et al. 1987 Burstein et al. 1988, Bower, Lucey & Ellis 1992, Guzman et al. 1992, Ziegler & Bender 1997, Kelson et al. 2001, Bernardi et al. 2006, Kelson et al. 2006, Sánchez-Blázquez et al. 2006a). These relations and the small scatter they present, suggest that ETGs formed at high redshifts and have evolved slowly since then. Therefore, comparing these relations for clusters with similar properties (e.g. richness, luminosities) at different redshifts allow us to constrain the formation and evolution of these galaxies (e.g. Kelson et al. 2001, J05, Sánchez-Blázquez et al. 2009, Jørgensen & Chiboucas 2013).

If ETGs are formed at $z \geq 2$, at the redshift of our cluster we should find that their stellar population parameters are compatible with a passive evolution: if galaxies were coeval and evolving passively, the slope of these relations should not vary, except for a shift in the zero-point. We use Coma as our reference cluster in the local Universe. We evolve it back in time to match the redshift of RX J0152.7-1357, assuming a passive evolution and a redshift of formation. We stress here that from now on, when we discuss the passive evolution scenario we always refer to the expected behavior for Coma.

5.5.1 Index-σ relations

Index-σ relations have shown to help at constraining the stellar content of galaxies at low-z. For example, the Mg_2-σ relation is usually interpreted as a link between the mass and the metallicity of the galaxy (e.g: Burstein et al. 1988, Guzman et al. 1992, Bender, Burstein & Faber 1993, Colless et al. 1999, Kuntschner 2000, Thomas, Maraston & Korn 2004, and references therein). Expanding the study to a larger number of indices helps to disentangle the age-metallicity degeneracy, as each index has a different sensitivity to it (e.g: J05, PSB06a, Sánchez-Blázquez et al. 2009, Harrison et al. 2011). In fact, indices sensitive to the metallicity are positively correlated, while those related to the age anticorrelate (e.g. Burstein et al. 1988, Bender, Burstein & Faber 1993, Jørgensen 1999, Kuntschner 2000, Bernardi et al. 2003, Caldwell, Rose & Concannon 2003, PSB06a).

Figure 5.10 shows the index-σ relations for the line indices of Coma (blue triangles) and our cluster at $z \sim 0.83$ (green circles, colour coded as in previous figures, parametrized by the SFH type).
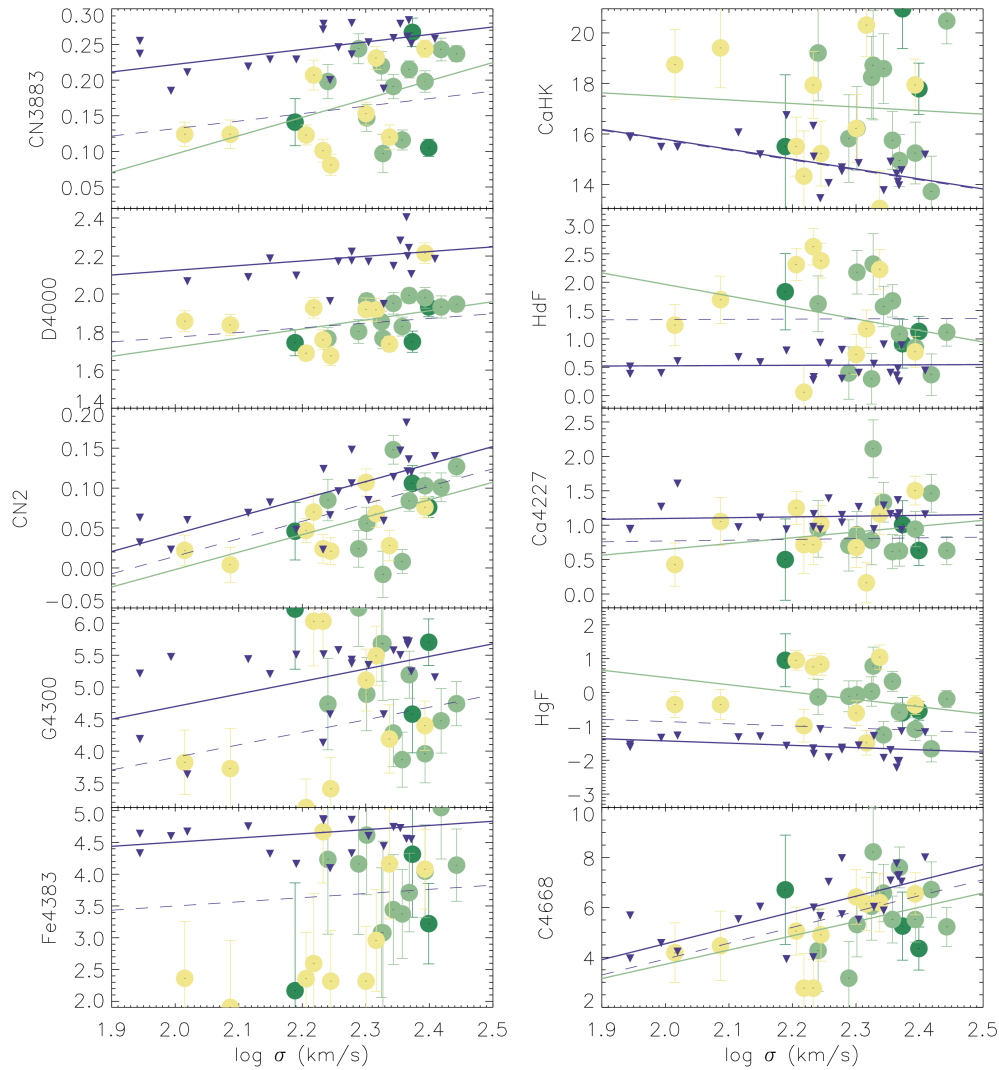
FIGURE 5.10— Relation between the measured line-strength indices and the velocity dispersion for the galaxies in the two clusters. Coma galaxies are marked as blue triangles, while the galaxies in RX J0152.7-1357 are colour-coded by their SFH type as in Fig. 5.9. The solid lines correspond to the linear fits to the data. The dashed line represents the expected relation from evolving the z=0 linear fit to the redshift of RX J0152.7-1357, assuming a $z_f = 3$. Note that the most massive galaxies are compatible with passive evolution.

The solid line shows the linear fits to the data, while the dashed line shows the expected relation for Coma at $z = 0.83$, assuming passive evolution and a $z_f = 3$. We find a positive relation for the D4000 break. The locus of this relation matches the one expected for Coma for a passive evolution (e.g. Barbaro & Poggianti 1997, Sánchez-Blázquez et al. 2009), in contrast to J05, where no correlation was found. CN2, $C_2 4668$ and Ca4227 also show relations compatible with a passive evolution of the stellar populations.

However, we find that in general the remaining indices are compatible with passive evolution only for the most massive galaxies. We see a large dispersion for CaHK, G4300, $H_\delta F$ or Fe3883. These dispersions, in particular the lower values seen for the Fe4383 index with respect to the relation corresponding to a passive evolution have been previously reported to be a real effect and not a consequence of a large data scatter for galaxies with low sigma (e.g. J05, Sánchez-Blázquez et al. 2009). The latter authors stated that while the index-σ relations for massive galaxies are compatible with a passive evolving scenario, less massive galaxies would need a more extended SFH. Indeed, we find that all those galaxies deviating from the expected relation present extended or residual SFHs. In addition, these galaxies are located preferably on the outskirts of the cluster, as we have stated before (Sect. 5.4.4).

5.5.2 Mean ages and metallicities

Figure 5.11 shows the dependence of the age and metallicity with the velocity dispersion for the galaxies both in the high-z cluster and Coma. The upper and middle panels show the estimates derived from different classical index-index diagrams (from Table 5.2), whereas the lower panels show the results obtained from the combined method (from Table 5.4). Galaxies from the high-z cluster are colour coded based on their SFH type. To guide the eye, the dashed lines correspond to the mean value obtained for each parameter.

The age-σ relation for the high-z cluster is virtually flat although a weak positive trend is seen, with a large scatter as also found by other authors (i.e. Proctor, Forbes & Beasley 2004, Thomas et al. 2005, Sánchez-Blázquez et al. 2009, Harrison et al. 2011). Galaxies in Coma show a flatter trend (as seen in Trager et al. 2000a and Sánchez-Blázquez et al. 2006b). However, the difference between both averaged ages is compatible with the difference expected for the cosmological time between the two clusters, hence compatible with a passive evolution scenario.

The large errors obtained for the [M/H] estimates from the index-index diagrams do not allow us to properly analyze them, but they present similar [M/H] values to those galaxies of similar mass in Coma.
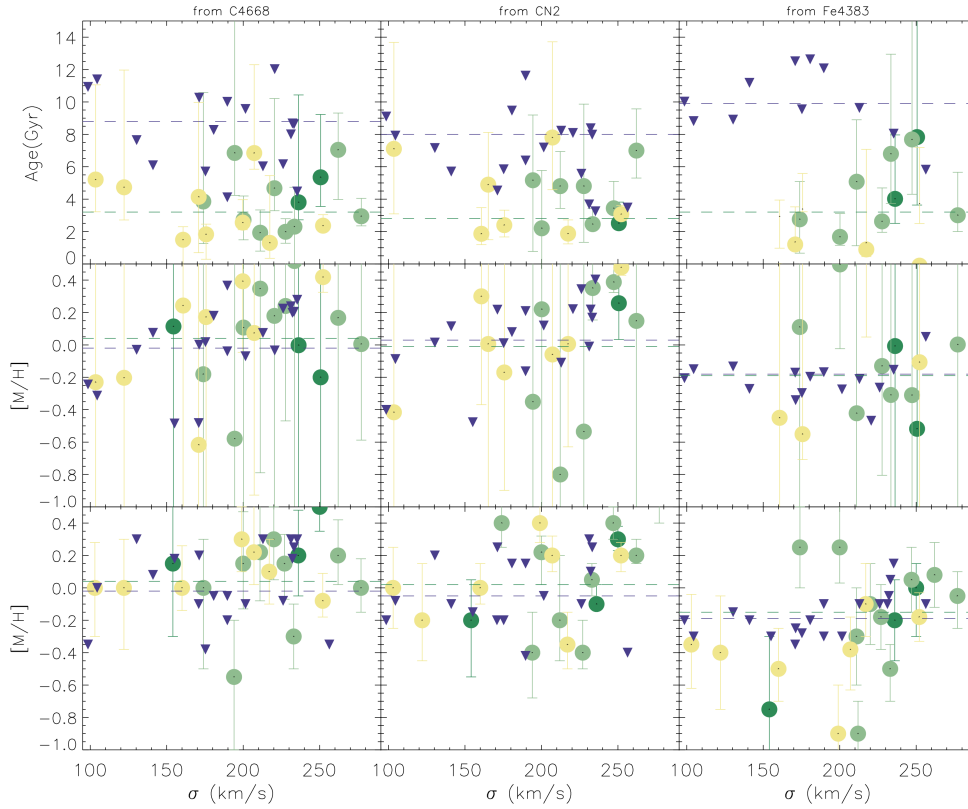
FIGURE 5.11— Relation between the mean age/metallicity and the velocity dispersion of the galaxies, where the stellar population parameters are derived from the classical index-index grids (upper and middle rows) and from the new combined method (lower row). Note that [M/H] here refers to the metallicity inferred from Figs. 5.3 and 5.8 for the index on top of each upper panel. The dashed lines are plotted to guide the eye, marking the averaged value for each cluster. Colours are as in the previous figure, with high-z galaxies colour-coded according to their SFH type. Note that the errors obtained for the metallicity are smaller for the combined method.

This shows that no variation with redshift is seen. This is confirmed in the bottom panels, where the error bars for the combined method allow us to further assess the relation of [M/H] with σ: a slight positive trend with the velocity dispersion is found.

Due to the non-orthogonality of the employed index-index grids, the information derived from the full-spectrum-fitting approach is key in this analysis. Figure 5.12 shows both the luminosity- and mass-weighted ages and metallicities for the two clusters. Note that the ages for Coma seem to decrease with velocity dispersion. This is because we are missing the most massive galaxies in

PSB06a sample (see fig. 2 in Sánchez-Blázquez et al. 2006b). In fact, the latter found a mild positive correlation between age and σ, as we do for the high-z one. We show with a dashed line the mean age derived for each cluster, whereas the solid line indicates the expected evolution from Coma. The difference in ages ($\sim 4\,\mathrm{Gyr}$ *vs* $\sim 12\,\mathrm{Gyr}$) is compatible with the lookback time corresponding to the redshift of the cluster, particularly for the most massive galaxies.

The lower panels of Figure 5.12 show the total metallicity of our galaxies. Note that this total metallicity could not be derived previously from the indices, as our spectral range did not include the appropriated indices for this purpose, such as e.g. [MgFe]. It can be seen that the total metallicity does not evolve within this redshift interval. We see a positive relation with velocity dispersion in the sense that more massive galaxies show a higher total metallicity (e.g. Greggio 1997, Thomas et al. 2005, Sánchez-Blázquez et al. 2009, Harrison et al. 2011). This could be explained with e.g. the galactic wind models (Arimoto & Yoshii, 1987), where larger galaxies with larger potential wells are able to retain the heavy elements. Galaxies for which we derive a more extended SFH show lower metallicities (except for galaxy ID 1811). These galaxies turned out to be the ones located at the outskirts of the subclumps.

All these results, from both the line indices and the full-spectrum-fitting approaches are compatible with a scenario where the most massive galaxies, located at the center of the cluster, have undergone passive evolution, while low-mass galaxies have suffered a more extended SFH or a secondary burst of star formation related to their infalling into the cluster. This is in agreement with other works that suggest that not all galaxies were fully in place at z~ 1 (e.g. De Lucia et al. 2004, De Lucia et al. 2007, Kodama et al. 2004).

5.5.3 Abundance patterns

The abundances of C and CN have been reported to be related to the environment and are interpreted as different SFHs and formation timescales for each element (e.g. Sánchez-Blázquez et al. 2003, Carretero et al. 2004, Sánchez-Blázquez et al. 2006b). C is mainly produced by the triple-alpha reaction of He and N is produced by converting C and O on the CNO cycle. But, in which evolutionary phase are they predominantly produced is still a matter of debate (to cite a few, Renzini & Voli 1981, Carigi 2000, Henry, Edmunds & Köppen 2000, Chiappini, Romano & Matteucci 2003, Akerman et al. 2004). If we assume that they are produced mainly in low- and intermediate-mass stars, the timescale for the release of these elements is around $\sim 3\,\mathrm{x}\,10^{7}$ years, while the time for the iron-peak elements such as Fe is longer ($\sim 1\,\mathrm{Gyr}$).
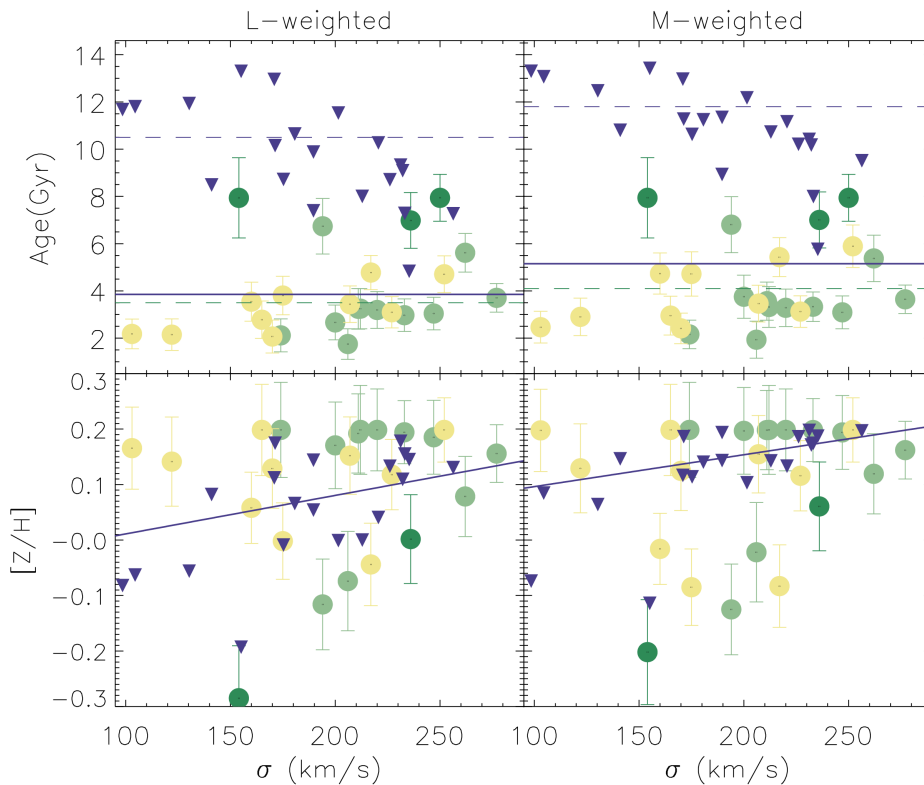
FIGURE 5.12— Same as in Fig. 5.11, but now the mean ages and metallicities are derived from the full-spectrum-fitting approach. Note that the total metallicity is similar for the two clusters, showing a mild trend with the velocity dispersion. The differences in age are compatible with a passive evolution scenario.

Even though massive galaxies are formed in short timescales, they had no time to incorporate these elements, while less massive galaxies did due to their more extended SFH. This implies, that less massive galaxies should have smaller abundance ratios, as their Fe values are larger.

Following a similar approach to Carretero et al. (2004), we have studied the CN and C abundance patterns that our galaxies present with velocity dispersion (instead of L_x), as shown in Figure 5.13. The pattern in the high-z cluster shows a larger scatter due to the lower S/N of our spectra compared to Coma. However, we find that within the errors, both clusters show similar mean values (marked by the dashed lines). As the abundance patterns are thought to be chemical clocks, this result suggests that the two clusters were settled on rather similar timescales according to Carretero et al. (2004).
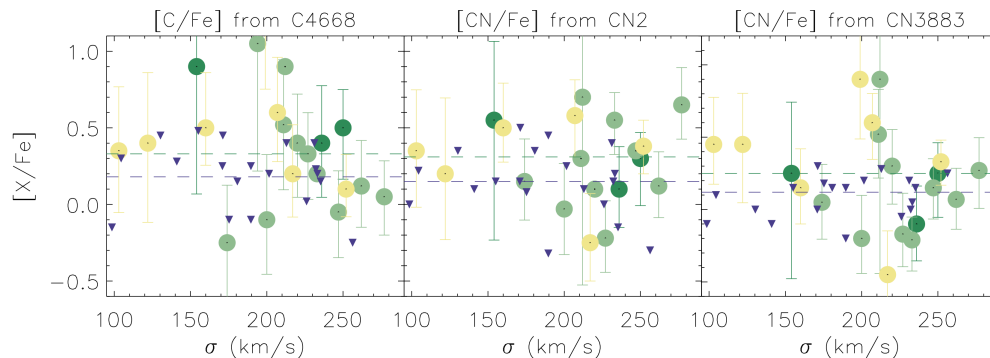
FIGURE 5.13— The abundance pattern for both clusters is plotted against the velocity dispersion, parametrized by SFH type. The dashed lines show the mean abundance ratios of each cluster. Moreover, the abundance pattern is already settled at the redshift of RX J0152.7-1357, which means that both clusters where formed on similar timescales.

This holds as long as the clusters have similar densities. Moreover, this shows that the abundance pattern of the CN and the C are already at place at z~0.8 and therefore no significant evolution of these abundance rations and the total metallicity is expected for the galaxies in this cluster.

5.6 Discussion

In this last part of the thesis, we have analyzed in detail for the first time, the stellar populations of a set of 24 ETGs in a moderately-high redshift cluster (RX J0152.7-1357, z=0.83) on an individual galaxy basis. This has allowed us to study the stellar population properties governing ETGs at high redshift and compare them to those seen in the local Universe to pose some constrains on galaxy evolution theories.

We find that the galaxies in RX J0152.7-1357 show similar relations with respect to the velocity dispersion to the Coma cluster. Our results were obtained from applying both the classical index-index and the full-spectrum-fitting approaches. A positive mild relation is found for the age and the total metallicity with σ. This implies that more massive galaxies are slightly older and with a total metallicity above solar. We also find that our proxy for the abundance ratio provides very similar values for the two clusters studied here. This suggests that the two clusters with similar richness, at intermediate redshift and in the local Universe, were settled on very similar timescales. As both the metal content and the abundance pattern seem to be already in place at intermediate redshifts, this is indicative of a formation epoch at higher redshifts than the one studied here. The index-σ as well as the age/metallicity-σ relations derived

for the galaxies in this cluster, all suggest that their stellar populations have evolved passively, always compared to Coma. This is particularly true for the most massive ones, whereas the galaxies with lower masses do not follow this trend for various relations with σ. These differences are well understood when looking at the derived SFHs: while most massive galaxies were formed in a fast single episode, low-mass galaxies tend to show extended SFHs, which permitted them to incorporate more Fe.

Summarizing, the picture that emerges for this cluster is that the center of the northern subclump was formed first in a single episode of star formation ($\sim$6-7 Gyr), populated by the most massive galaxies ($\sigma \sim 260\,\mathrm{km\,s^{-1}}$). In a similar event but slightly later in time, the southern subclump was formed ($\sim$3-4 Gyr), populated by massive galaxies ($\sigma \sim 230\,\mathrm{km\,s^{-1}}$). Eventually, both subclumps merged and afterward, new low-mass galaxies were accreted on its surroundings, presenting a more extended or residual SFH. Our results favour a picture where the most massive galaxies in the centers have evolved passively since the bulk of their stars formed at high redshift, while the less massive galaxies in the surroundings have suffered a more extended SFH due to their infalling in the cluster.

6

Conclusions and Future Work

Science never solves a problem
without creating ten more
George Bernard Shaw

Massive ETGs have shown to be the *new kids on the block* of the last decade in the field of Galaxy Evolution as they have shown to be a crucial key to constrain the classical scenarios of galaxy formation and evolution. The not-well understood evolution over cosmic time of their sizes and morphologies has lead to the creation of new scenarios to reproduce what is observed at all epochs and at all environments.

In fact, we are slowly approaching into a consensus were the true scheme seems to be a mixture of the long-standing scenarios: massive galaxies were first created in a huge episode of star formation at very early epochs (z>3), i.e. monolithic-like, and then they evolved suffering subsequent interactions with other galaxies and incorporating material as their envelopes, i.e. hierarchical-like, leaving the core untouched. This could explain both the growth in size but the passive evolution of the stellar populations and the change in the morphologies.

However, we should we cautious when studying such massive galaxies, because standard no longer means correct in terms of the initial assumptions every astronomer assumes beforehand. The fashion of the non-universality of the IMF has strongly beaten back, showing that these massive objects should be studied employing steeper IMF slopes than the standard Salpeter/Kroupa ones.

Although many evidences still prevent us to accept this as the final word, the results obtained under the framework of this Ph.D. thesis seem to be in agreement with this new tendency of thought. In this final chapter, we summarize the most relevant conclusions achieved and we present the unresolved questions and future plans.

6.1 Conclusions

Regarding the nature of the compact massive galaxies found in the nearby Universe, we conclude the following:

- They present **compact disky-shapes with no evidence of extended components**. Their stellar mass density profiles are denser in their inner regions than any massive normally-sized galaxy in the Local Universe.

- We measure **large radial velocities and high velocity dispersions** (~ 200 km s^{-1}), showing that in general, they are fast rotators.

- They have **young mean SSP-equivalent ages** (≤ 2 Gyr) and solar or slightly higher metallicities. They present scaled-solar abundance patterns.

- The SFHs derived from the full-spectrum-fitting reveal that these objects contain an **old embedded population but that they all experienced recent star formation bursts during the last 2 Gyr**. The latter contribute strongly to the total light ($\gtrsim 50\%$) and, in some galaxies, even to the total mass ($\gtrsim 30\%$).

- We have characterized this new family, showing that they are **truly unique and scarce objects in the Local Universe, sharing a large number of properties with massive compact galaxies in the distant Universe**. These galaxies represent their analogues rather their descendants. Because of their relative vicinity, they are a perfect laboratory to explore with unprecedented detail the formation mechanisms of massive galaxies at high-z.

Concerning the study of the impact of a non-universal IMF into several stellar population parameters, our conclusions are summarized as follows:

- The choice of the IMF shape (unimodal *vs* bimodal) results in different stellar population parameter estimates, in particular for the steepest slopes. **The unimodal (bimodal) IMF shape shows always stronger (milder) deviations from the derived properties with respect to the standard IMF**.

- We find a **minimum on the M/L for an IMF slope that depends slightly on the age of the SSP**. This implies that the stellar mass derived from the SFHs will be minimized in that point and then increased as we steepen the IMF (by a factor of 4 in the unimodal case, by 1.5 in the bimodal one).

- **IMF slopes steeper than Salpeter/Kroupa tend to produce SFHs with smaller contributions of old populations**. As a result, the age estimates decrease both in light and mass (by a factor of 3 in the unimodal case, by 1.5 in the bimodal one).

- **The choice of an IMF slope according to the velocity dispersion of the galaxy provides comparable SFHs for ETGs of different masses**, involving a varying amount of recent residual star formation.

- We find that the use of a **non-standard IMF delays (accelerates) the mass assembly of massive (low mass) galaxies**. Indeed, a relation between the galaxy velocity dispersion with the differences on the mass assembly timescales is seen, particularly for the unimodal case.

Finally, in relation to the detailed study of the stellar populations of 24 ETGs in a cluster at intermediate redshift (z$\sim$0.83), our most relevant results are:

- Galaxies in the centers of the subclumps are the oldest and most massive ones ($\sigma > 230 \, \mathrm{km \, s^{-1}}$). On the contrary, those located at the periphery are younger, showing lower masses ($\sigma \leq 150 \, \mathrm{km \, s^{-1}}$).

- **The SFHs of these galaxies have revealed to be a key parameter for our study**. Three different SFHs types are found, segregated by their location within the cluster. Galaxies having a virtually single episode of star formation at the oldest ages ($\sim$6-7 Gyr) are located in the center of the north subclump. Galaxies populating the south subclump are mainly described by a single episode of star formation at intermediate ages ($\sim$3-4 Gyr), while the galaxies in the outskirts of the clumps are found to present the most extended SFHs.

- We have compared the relations that the stellar populations follow with velocity dispersion at high-z and low-z, to discuss the passive evolution scenario. The evolution in time of the index-σ relations is compatible with a passive evolution scenario for the most massive ones, in contrast to low-mass galaxies with extended SFHs, which suffer more chemical

evolution. The derived ages are compatible with a passive evolution scenario, showing a mild relation with σ and both **the metallicity and the abundance pattern are already settled at z$\sim$0.8**.

- We have therefore discussed an evolutionary scenario where **passive evolution stands for the most massive galaxies**. On the contrary, low-mass galaxies seem to present a stronger evolution than expected. Most of these **low-mass galaxies show more extended SFHs and are located in the outskirts of the cluster**. Therefore, we conclude that they have been incorporated into the cluster more recently.

6.2   Plans for the future

Each one of the chapters analyzed in this PhD thesis have been devoted to shed some light into the possible scenarios for the evolution of ETGs. However, it is now time to address the unresolved and new questions that have arisen from it.

Related to the intriguing compact massive galaxies in the local Universe:

- It is now mandatory to solve the problem related to the mass estimates. As stellar masses seem to be rather constrained from several parameters (the IMF, the models and the methodology employed) we have to focus on the determination of the dynamical mass. Sizes are well determined from deep imaging, therefore other sources of uncertainties need to be considered. It seems that the problem is related to use of the proxy $M_{dyn} \propto r_e\,\sigma^2$. Due to their compactness, this gives systematically a factor of two smaller masses. In addition, the possibility that we are underestimating our velocity dispersions also needs to be considered. In both cases, this will be solved deriving dynamical models from the observations we have been recently awarded.

- The challenging SFHs derived for the compact massive galaxies, showing unprecedented fractions of young components, need to be understood in order to determine how were they formed. Due to the similarities with the high redshift massive galaxies, we expect their formation mechanism to be analog to that at high redshift. Due to their vicinity, studying this issue is easier than at high-z.

- A similar analysis of the stellar populations and SFHs is needed for massive galaxies at high redshift (z$\sim$1). This means pushing large ground-based facilities, such as GTC, to their limits.

Related to the impact of the variations on the IMF:

- We have shown that the impact that the non-universality of the IMF has on the derived stellar populations is relevant. However, our work is focused into rather peculiar objects, such as the compact massive galaxies. Therefore, a major revision of the classical works in this field should be performed with well-studied representative object.

And finally, related to the study of the stellar populations of ETGs with redshift:

- The trends and relations between the galaxy velocity dispersion, the SFH type and the location within the cluster have been derived using a single cluster. Therefore, it is now crucial to expand this study to other clusters up to z~1. We have new data for two clusters at z~0.5 and several candidates from the archive data on the *Gemini/HST Galaxy Cluster Project.*

- So far, we have only constrained the cluster evolution from the study of ETGs. A complete analysis including star-forming objects, would asess the issue about the morphological transformation.

- It is also important to expand the same analysis to galaxies in other environments, such as groups of galaxies, to assess the role of the environment.

7

Conclusiones y Trabajo Futuro

Un pueblo que no conoce su historia
no puede comprender el presente
ni construir el porvenir
Helmut Kohl

Las galaxias masivas de tipo trempano han demostrado ser las niñas bonitas de la última década en el campo de la evolución de galaxias. Se han erigido como la pieza clave para acotar los escenarios clásicos de formación y evolución. Su evolución en tamaño y en morfología a través de las distintas edades del Universo aún no se entiende completamente, y ésto ha llevado a la creación de nuevos escenarios que resproduzcan lo que se observa a cualquier época y ambiente del Universo.

De hecho, nos estamos acercando a un consenso, dónde el esquema real parece ser una mezcla de dichos escenarios clásicos: las galaxias masivas se crearon primero en épocas muy tempranas (z>3), con un episodio enorme de formación estelar, es decir, tipo monolítico, y luego evolucionaron sufriendo interacciones con otras galaxias, incorporando material formando envolturas, es decir, tipo jerárquico, mientras el centro permanecía intacto. Ésto explicaría tanto el crecimiento de los tamaños junto con el hecho de que las poblaciones estelares sean compatibles con una evolución pasiva, como el cambio en las morfologías.

No obstante, tenemos que ser cautelosos al estudiar dichas galaxias masivas, ya que algo estándar yo no significa correcto en términos de las condiciones iniciales que todo astrónomo debe asumir desde un principio. La moda de la

no universalidad de la IMF ha vuelto con fuerza, mostrando que estos objetos masivos deberían ser estudiados utilizando pendientes de la IMF mayores que las tipo Salpeter o Kroupa.

Aunque muchas evidencias aún no nos permiten aceptar sin objeciones estas consideraciones como la última palabra, los resultados obtenidos en el marco de esta tesis doctoral parecen coincidir con esta nueva tendencia. En este capítulo final resumimos las conclusiones más relevantes que se han obtenido, así como las cuestiones que quedan sin resolver y los planes para el futuro.

7.1   Conclusiones

En lo que respecta a la naturaleza de las galaxias compactas masivas del Universo local, podemos concluir lo siguiente:

- Las galaxias compactas masivas locales presentan **morfologías compactas de tipo disco y carecen de una componente extendida**. Sus perfiles de brillo superficial indican que son más densos en las regiones centrales que los correspondientes a las galaxias masivas de tamaño normal del Universo local.

- Se miden **velocidades radiales y dispersión de velocidades altas** (~ 200 km s^{-1}), mostrando que en general, estos objetos son rotadores rápidos.

- Las galaxias compactas masivas locales **presentan edades promedio jóvenes** (≤ 2 Ga) y metalicidad solar o ligeramente supersolar. Además, su patrón de abundancias relativas de elementos sigue un escalado solar.

- Las SFHs derivadas mediante el ajuste completo de sus espectros revelan que estos objetos **contienen una población vieja subyacente, pero que a la vez todas han experimentado brotes de formación estelar durante los últimos 2 Ga**. Esta componente joven contribuye fuertemente a la fracción total de luz ($\gtrsim 50\%$) y, en algunos casos, incluso a la fracción total de masa ($\gtrsim 30\%$).

- Hemos caracterizado esta nueva familia de galaxias mostrando que **se trata de unos objetos realmente únicos y muy escasos en el Universo local. Además, comparten numerosas propiedades con las galaxias masivas observadas en el Universo lejano**. De hecho, encontramos que estas galaxias constituyen sus análogos en el Universo local

en vez de sus descendientes. Debido a su relativa cercanía, son un laboratorio perfecto para explorar detalladamente los mecanismos de formación de las galaxias masivas a alto desplazamiento al rojo.

Respecto al estudio del impacto que una IMF no universal tiene en varios parámetros de las poblaciones estelares, nuestras principales conclusiones son:

- La elección de una forma de la IMF (unimodal o bimodal) da lugar a estimaciones diferentes de los parámetros de las poblaciones estelares, en particular para pendientes mayores. **Las formas unimodal (bimodal) de la IMF muestran siempre unas desviaciones mayores (más suaves) de las propiedades con respecto a una IMF estándar**.

- **Se encuentra un mínimo en la M/L para una pendiente de IMF que varía según la edad de la población**. Ésto implica que la masa estelar derivada de las SFHs resultantes también se minimiza en ese punto, para luego crecer a medida que aumentamos la pendiente de la IMF (por un factor 4 en el caso unimodal, de 1.5 para el bimodal)

- **Las pendientes de IMF mayores que Salpeter/Kroupa dan lugar a SFHs con una contribución de poblaciones viejas significativamente menor**. Como consecuencia, las edades promedio decrecen tanto al ponderarse en luz como en masa (por un factor 3 en el unimodal y 1.5 para el bimodal).

- **La elección de la pendiente en función de la dispersión de velocidades medida de la galaxia da lugar a unas SFHs comparables para ETGs de diferentes masas**. Se encuentra una cantidad variable, aunque no despreciable, de formación estelar reciente.

- Vemos que **el uso de una IMF no estándar acelera (retrasa) el proceso de formación de las estrellas en las galaxias de baja (alta) masa**. De hecho, se encuentra una relación entre la dispersión de velocidades y las diferencias entre las escalas de tiempo de formación, en particular para el caso unimodal.

Finalmente, en relación al estudio detallado de las poblaciones estelares de las 24 ETGs en un cúmulo de galaxias masivo a un desplazamiento al rojo intermedio ($z \sim 0.83$), los resultados más relevantes son:

- Las galaxias que se encuentran en los centros de los subcúmulos son las más viejas y masivas ($\sigma > 230 \, \mathrm{km \, s^{-1}}$). En cambio, las galaxias situadas en la periferia son más jóvenes y con masas menores ($\sigma \leq 150 \, \mathrm{km \, s^{-1}}$).

- **La SFH de las galaxias de este cúmulo ha resultado ser un parámetro clave en nuestro estudio**. Se encuentran tres tipos diferentes de SFHs, segregados por su localización dentro del cúmulo. Las galaxias que muestran un solo episodio de formacón estelar a edades viejas (∼6-7 Ga) se encuentran en el centro del subcúmulo situado al norte. Las galaxias del subcúmulo en el sur muestran también episodios de formación similares, pero a edades intermedias (∼3-4 Ga), mientras que las galaxias de los alrededores de los subcúmulos presentan unas SFHs más extendidas en el tiempo.

- Hemos comparado las relaciones que siguen las poblaciones estelares con la dispersión de velocidades, tanto a alto como a bajo desplazamiento al rojo, para discutir los posibles escenarios de evolución de galaxias. La evolución en el tiempo de las relaciones índice-σ es compatible con un escenario de evolución pasiva para las galaxias más masivas, mientras que no lo es para las galaxias menos masivas con SFHs extendidas. Las edades promedio obtenidas para las galaxias individuales son compatibles con un escenario de evolución pasiva, mostrando una relación suave con la dispersión de velocidades. Además, **tanto la metalicidad como el patrón de abundacias relativas están ya asentados a z∼ 0.8**

- Es decir, hemos discutido un escenario de evolución donde **la evolución pasiva sucede para las galaxias más masivas**, mientras que las menos masivas presentan una evolución mayor. Estas **galaxias menos masivas muestran unas SFHs extendidas en el tiempo y se encuentran en las afueras del cúmulo**. Esto nos permite concluir que fueron incorporadas al cúmulo más recientemente.

7.2 Trabajo Futuro

Cada uno de los capítulos de la tesis doctoral se ha centrado en aportar algo de luz en los posibles escenarios de evolución de las ETGs. No obstante, quedan pendientes cuestiones sin resolver y los nuevos problemas que hayan surgido.

En relación a las fascinantes galaxias compactas y masivas del Universo local:

- Es necesario solucionar el problema relacionado con las estimaciones de las masas. Ya que las masas estelares parecen estar acotadas por varios parámetros (la IMF, los modelos o el método empleado, entre otros), debemos centrarnos en la determinación de sus masas dinámicas. Los tamaños están bien determinados, como se ha visto con las imágenes profundas, con lo cuál debemos considerar otras fuentes de incertidumbre.

El problema parece estar en el uso de $M_{dyn} \propto r_e \sigma^2$ para la estimación. Por un lado, debido al tamaño compacto de las galaxias, ésto implica sistemáticamente unas masas menores por un factor dos. Por el otro, la posibilidad de que estemos midiendo una dispersión de velocidades menor también se tiene que tener en cuenta. En cualquier de los casos, podremos abordar este tema con la determinación de modelos dinámicos, para los cuáles nos ha concedido recientemente tiempo de observación.

- Las SFHs inusuales derivadas para las galaxias compactas masivas, las cuáles muestran unos fracciones de componente joven sin precedentes, también se tienen que entender para poder determinar cómo se formaron estos objetos. Debido a las similitudes con las galaxias masivas a alto desplazamiento al rojo, se espera que los mecanismos de formación sean los mismos. Gracias a su proximidad, este estudio es más fácil.

- Es necesario llevar a cabo un estudio similar de las poblaciones estelares y las SFHs para las galaxias a alto desplazamiento al rojo (z$\sim$1). Esto implica llevar al límite las capacidades de los telescopios de gran diámetro tipo GTC.

Relacionado con el impacto de las variaciones en la IMF:

- Hemos mostrado que el impacto que tiene una IMF no universal en las poblaciones estelares es relevante. No obstante, nuestro trabajo se ha centrado en unos objetos más bien peculiares, como las galaxias compactas masivas. Por esto, se debe llevar a cabo una revisión de los trabajos clásicos en este campo utilizando objetos representativos y bien estudiados.

Y finalmente, en relación al estudio de las poblaciones estelares de las ETGs a alto desplazamiento al rojo:

- Las tendencias y relaciones entre la dispersión de velocidades, el tipo de SFH y la localización de la galaxia dentro del cúmulo se han obtenido en un único cúmulo. Por eso, ahora es vital extender el estudio a otros cúmulos hasta al menos z$\sim$1. Para tal fin, disponemos de datos nuevos de dos cúmulos a z$\sim$0.5 y varios candidatos a z mayores con espectros del archivo del proyecto *Gemini/HST Galaxy Cluster Project*.

- Hasta el momento, solo hemos acotado la evolución del cúmulo con el estudio de las ETGs. Un análisis completo que incluya los objetos con formación estelar permitiría abordar el tema de la transformación morfológica.

- También es importante extender este tipo de análisis a galaxias en otros ambientes, como los grupos, para poder determinar la importancia del entorno.

A

More about the local compact massive galaxies

A.1 SFHs galaxy per galaxy

In this Appendix we show the SFHs recovered with the code `STARLIGHT`. For each galaxy, we have analyzed the SFH for the different apertures, to study possible gradients. In Figures A1 and A2, each row on the panel corresponds to a single galaxy, with the first column being the center (r0), the middle one the first aperture (r1), and the third one the outermost aperture (r2). Each panel contains the galaxy spectra (in black), the fitted spectra from the model templates (red) and the residuals, showing, if any, the rejected pixels and masked regions (green). The SFHs are shown on the right of each spectra, both in luminosity (up) and mass (down).

A.2 How robust is the full-spectrum-fitting approach?

We have also tested the reliability of the full-spectral-fitting techniques to estimate ages and metallicities. We have applied two different tests, explained below.

TEST 1

This test constrains the fractions of young and old populations recovered with the full-spectral-fitting technique. Given the mean SSP-equivalent age and metallicity for a galaxy, derived from the SSPs model grids, we can also recover the same mean age with a combination of two SSPs, one younger and the other older than the SSP-age. These two SSPs can be weighted by different propor-
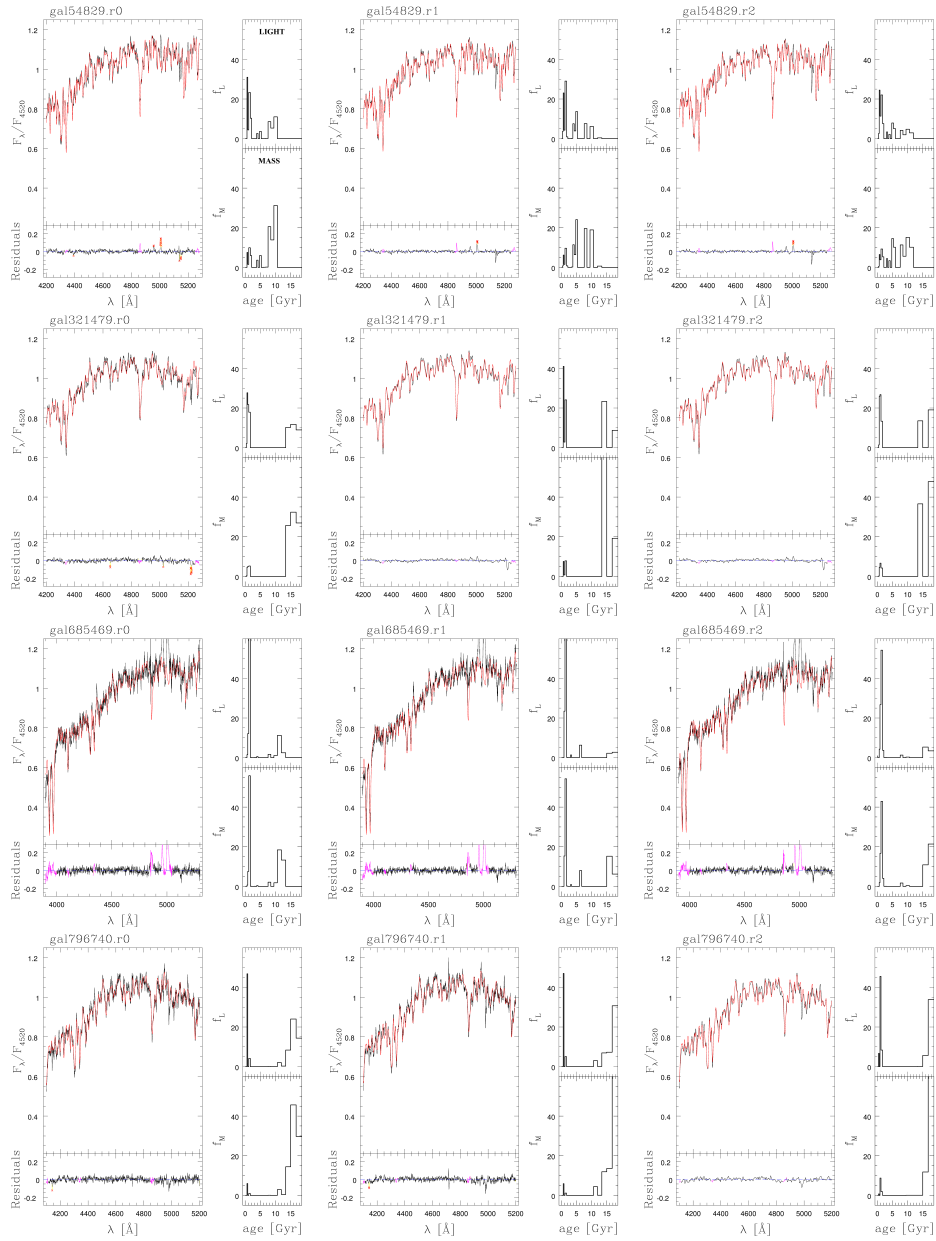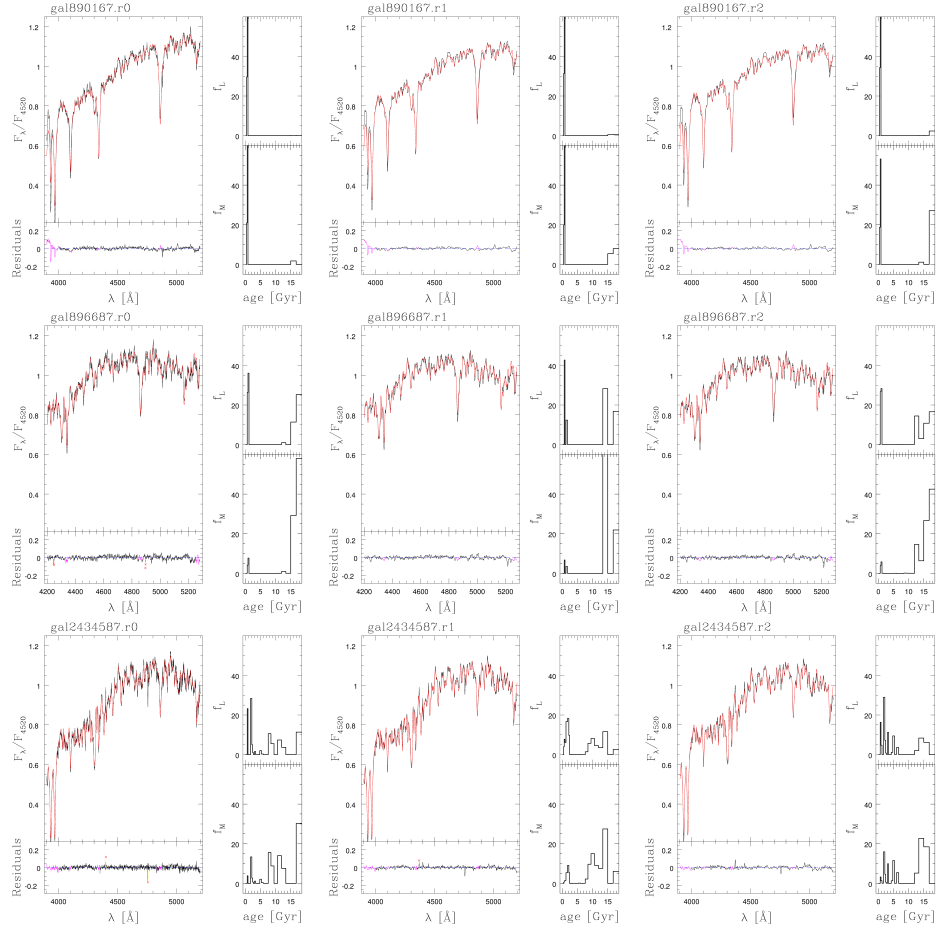
FIGURE A.1— Results from STARLIGHT for the three apertures in each galaxy (r0, r1 and r2). On the upper-left hand, the galaxy spectra (black) is fitted with the models from V10 (red). The bottom-left panel shows the fitting residuals and the masked or rejected pixels (green). The right column on each panel shows the Star Formation History recovered in light (up) and in mass (down). It can be clearly seen that all our objects show recent starbursts, some of them leading to a big contribution of young populations.

tions, either in mass or in light. We created a sample of synthetic spectra with exactly the same configuration as our galaxies, using the MILES webpage tool *"Get spectra from a given SFH"*, where our input were different SFHs, one containing a young population ($\lesssim 2\,\mathrm{Gyr}$) and the other containing an old population ($> 5\,\mathrm{Gyr}$), with varying proportions. We slightly vary the imposed limit (2.0, 1.5, 1.0 and 0.8 Gyr) to match the estimated mean luminosity-weighted age for each object in our sample.

We then measure their line-strengths in the same way we did for our galaxies and plotted them in the Hβ_o *vs* [MgFe50] diagram (Figure A3). The different combinations of ages with a fixed metallicity are plotted in different colours for [Z/H]=+0.22 and [Z/H]=0.0. Only those points (in black) that lie close to our galaxies are the possible SSP combinations that will give the galaxy mean age.

However, the dependence with the metallicity has also to be taken into account because of the known age-metallicity degeneracy (a young metal-rich system has a similar integrated energy distribution (SED) as an older metal-poor one). To illustrate this, we plot the extreme case where a young metal-rich population ([Z/H]=+0.22) is combined with an old metal-poor one ([Z/H]= = -2.43). All the gray points correspond to those possible combinations of SSPs with different ages and different metallicities that lead to our galaxy values. As we know the amount of old population for each of them, we are able to impose limits on the fractions required to achieve our galaxies values.

At a fixed age, less metal-rich components contain smaller fraction of old populations. At fixed metallicity, as the mean luminosity-weighted age increases, the fraction of old population can reach any value. For example, for the galaxy 2434587 with mean SSP-age 2.24 Gyr, the amount of old population varies from 0.05% to 95%, while for the galaxies with less than 1.0 Gyr, only SSPs with more than 60% of old population are feasible. The fractions listed in Table 3.7 are in agreement with this test, except for galaxy 54829, whose young population is higher than expected.

TEST 2

This test is a simple reanalysis of the output of the full-spectral-fitting. We measured, in exactly the same way we did for our galaxies, the absorption line-strengths of the best model fitted to each galaxy with STARLIGHT. We plotted these values in the index-index diagrams to compare them with the observed value from the galaxy spectra (for both our galaxies and for the elliptical control sample). It appears (Fig. A4) that ages are well recovered and metallicities tend to be slightly lower by -0.10 $Z_{\odot}$. For old stellar populations, the method based

on the Balmer indicator *vs.* the metallicity indicator tend to provide older ages than the full-spectral-fitting approach (Vazdekis et al. 2001a, Mendel, Proctor & Forbes 2007). This effect is seen for the control elliptical galaxies on the bottom panel of the figure. Instead, in stellar populations with strong contribution of young components, the SSP-equivalent age is strongly biased towards the age of these young components (e.g., Serra & Trager 2007).
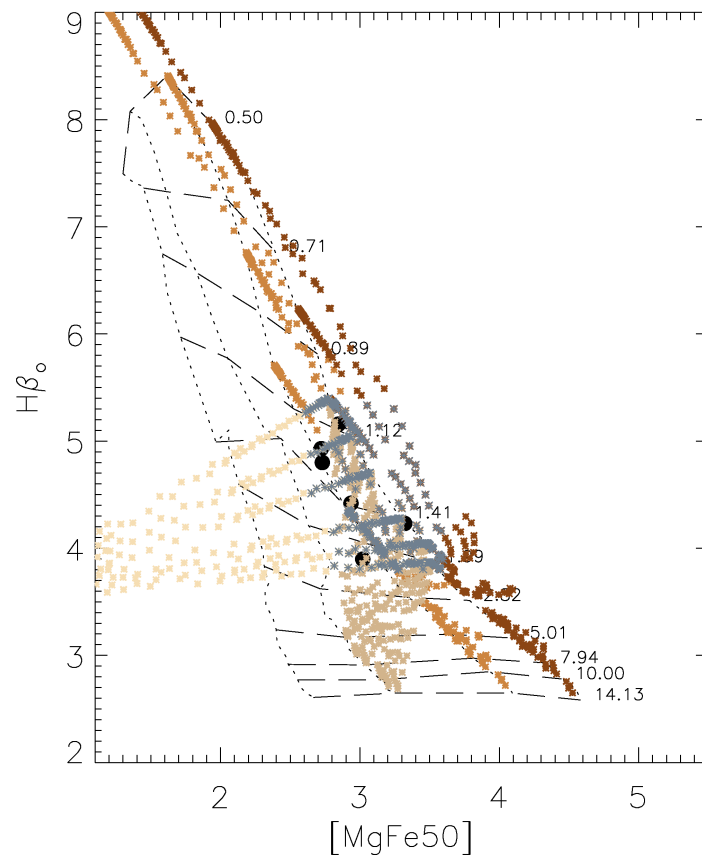
FIGURE A.2— The age-sensitive indicator Hβ_o is plotted against the composite metallicity index [MgFe50], to show the results of combining two different SSPs (young+old) with a fixed metallicity of [Z/H]= 0.0 and +0.22 (orange/brown symbols). We also show the effect of combining an old metal-poor with a young metal-rich SSP (horizontal sequence of faint points). In gray, we highlight the possible combinations that lead to the observed values.
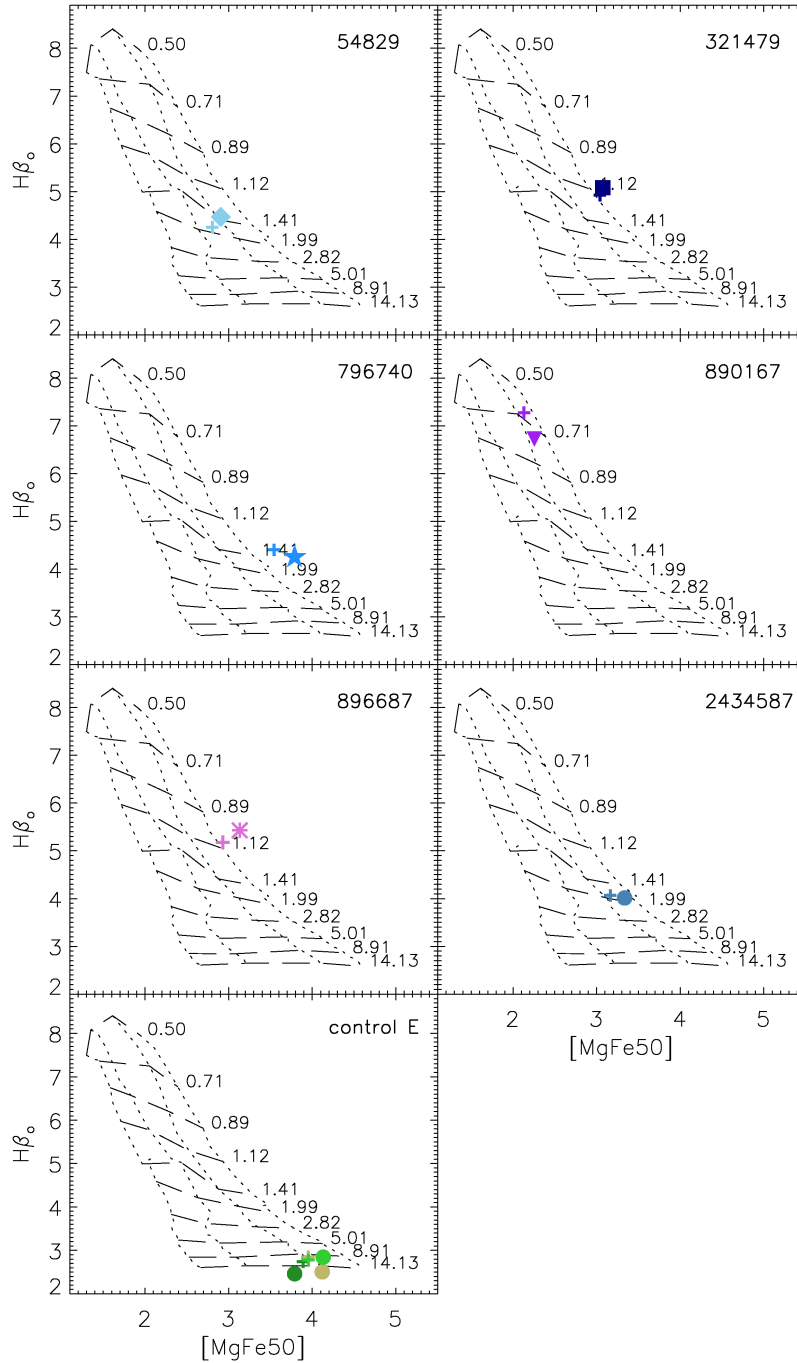
FIGURE A.3— $H\beta_o$-[MgFe50] plots for the second test. Each panel refers to each galaxy of our sample. Large filled symbols are our compact galaxies as in Fig 3.5, while the crosses refer to the values derived from the fitted spectra from STARLIGHT. For comparison we show the results for the control ellipticals in the bottom panel.

B

Is the IMF universal?

B.1 Testing our method for deriving the SFHs with `STARLIGHT`

Full-spectrum fitting codes are known to be slightly sensitive to the initial conditions, such as the spectral range (e.g. optical *vs* near-IR) or masked features (e.g. potential emission lines). We have tested the robustness of our results by varying these initial conditions, while keeping the IMF shape and slope fixed to a unimodal μ=1.3. Altogether, these tests reveal that the trends and estimates derived from the relatively short spectral range of the long-slit galaxy spectra are robust.

B.1.1 Masking test

Three masking configurations were used, involving different features on the spectra of four of our galaxies, as illustrated in the upper panel of Figure B1: (a) orange – no mask is used; (b) blue – we mask all the features in the spectra, both potential emission and Balmer-absorption lines; (c) green – we only mask the Balmer-absorption lines. The resulting mean luminosity-weighted ages can be used to provide a more quantitative estimate of the uncertainties derived from the method. We find that these mean ages, which are indicated in each panel, vary insignificantly, by less than 2%.

B.1.2 Short *vs* Long spectral range

We have compared the mean ages derived from the relatively short range ($\lambda\lambda$ 3800-5300 Å) of the high quality long-slit spectra of our sample of galaxies with those derived from the full SDSS spectral range. The latter covers bluer and redder wavelengths ($\lambda\lambda$ 3500-8500 Å), better sampling the different contributions from the various stellar populations. For this test we have selected
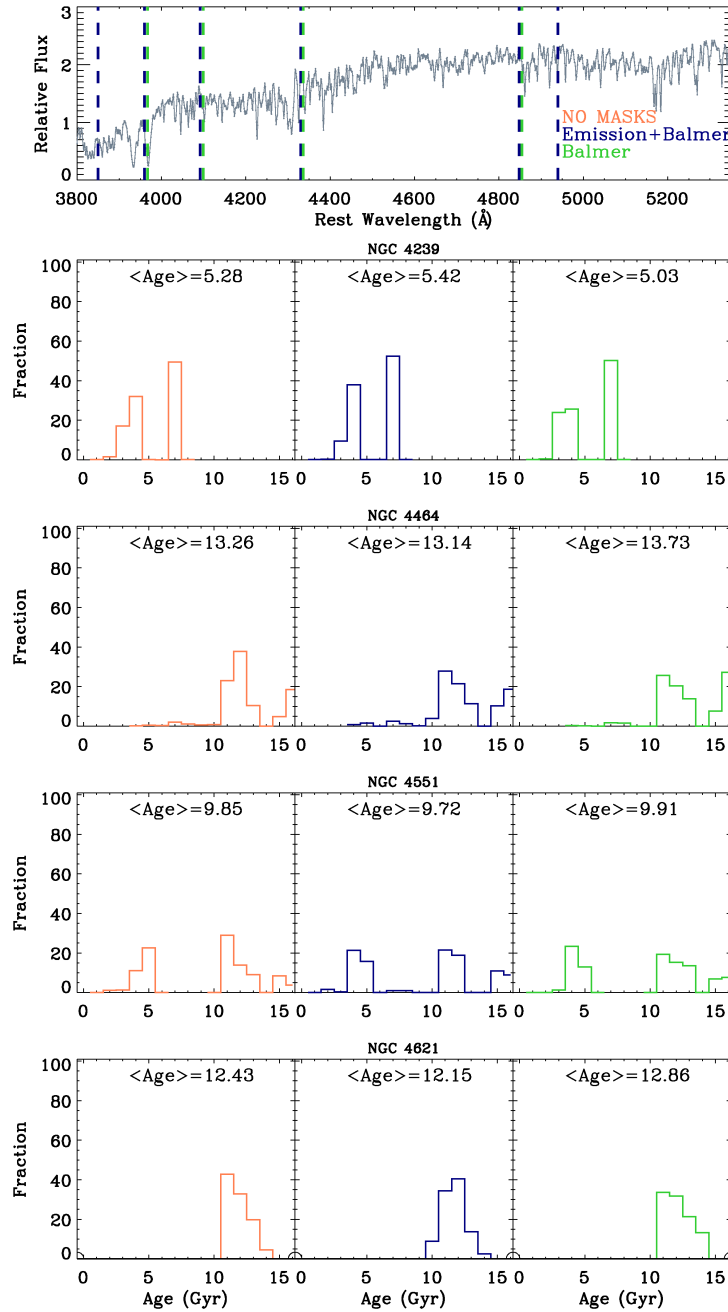
FIGURE B.1— Different masking configurations employed for the spectrum-fitting are indicated on the upper panel. The vertical blue and green dashed lines mark the masked regions for each configuration. The SFHs derived for four elliptical galaxies are shown in the following rows of panels: no masking (left), masking emission and Balmer lines (center) and only masking the Balmer lines (right). The mean mass-weighted age is shown for each SFH, giving us a quantitative estimate of the uncertainties of this method.

a set of ETGs from the sample of LB10, covering a wide range in ages. Moreover, as the compact massive galaxies were initially selected from the DR6 SDSS database (Trujillo et al., 2009), we also compared their results. The luminosity-weighted estimates show a rather good agreement in Figure B2, with deviations on the derived mean age smaller than 8%, whereas the mass-weighted estimates show deviations on the mean age of around 12%. The larger variations are found for the galaxies with the oldest ages, as expected for the errors associated to this age regime.
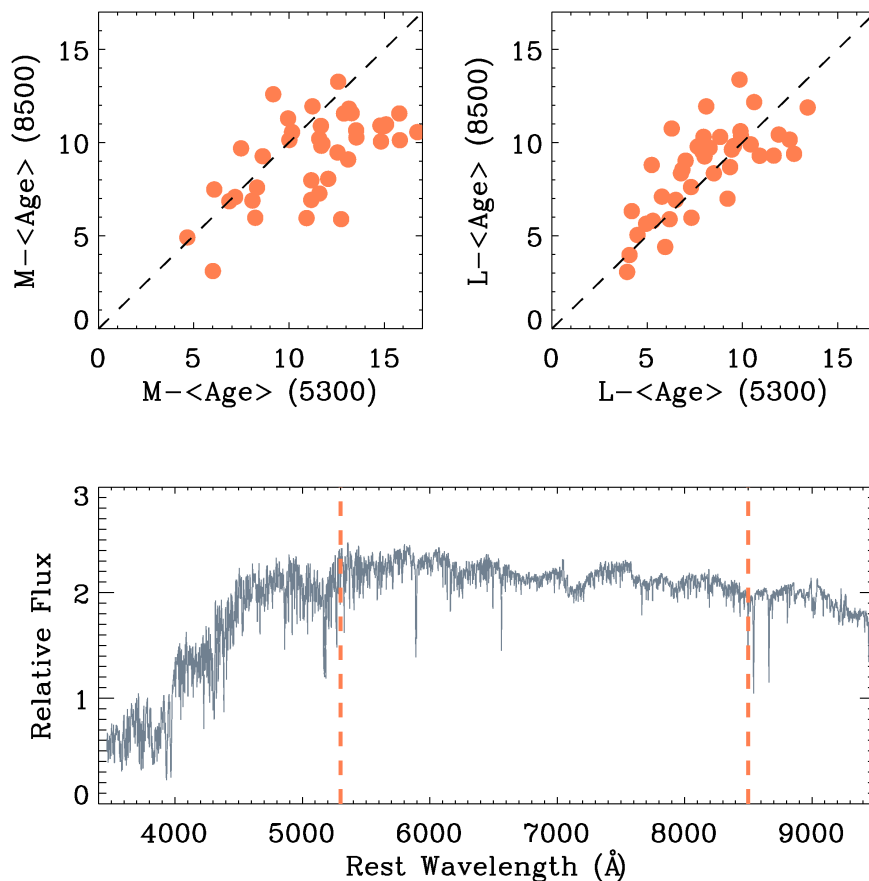
FIGURE B.2— Mean mass- and light-weighted ages (left and right, respectively) obtained from the SFHs derived using the short and large spectral ranges. The vertical lines on the spectra indicate these two spectral ranges.

B.1.3   Broadband photometry *vs* Spectrum fitting

Colour variations with the IMF slope have been already reported (e.g. Ricciardelli et al. 2012, Pforr, Maraston & Tonini 2012). However, the effect of the colours in our short spectral range is almost negligible. We compared the SDSS photometric colours with those obtained from the SFHs derived from the short spectral range of these galaxies in LB10. To obtain the synthetic colours we use the user-friendly web-tool facility dedicated for this purpose in the MILES web-page "*Get spectra from a SFH*". This facility provides us with the indices, masses and colours for our derived SFHs. Figure B3 shows that the agreement is remarkable between the derived and observed *g-r* and *r-i* colours. The web-tool does not provide us with the magnitude in the *u* band, because the MIUSCAT SEDs do not cover the whole spectral range required to measure this filter (see Ricciardelli et al. 2012).

FIGURE B.3— *g-r* and *r-i* colours derived from our SFHs on the short spectral range (open green circles) compared to those reported by the SDSS with a larger range (blue filled circles).

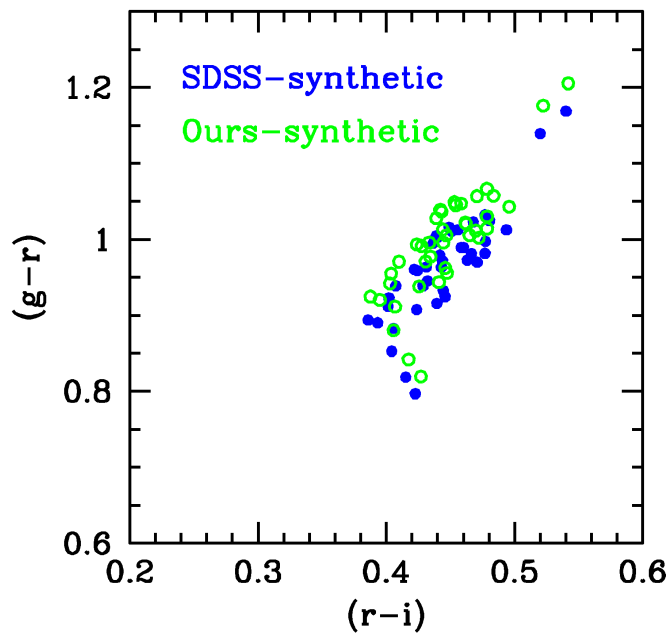| Galaxy ID	Age (Gyr) IMF Slope					%old IMF slope					Mass ($\times 10^{11} M_{sun}$) IMF slope				
	0.8	1.0	1.3	1.8	2.3	0.8	1.0	1.3	1.8	2.3	0.8	1.0	1.3	1.8	2.3
NYU 54829	6.9	6.6	5.8	4.5	3.2	68	63	45	31	15	0.91	1.13	1.31	2.34	4.80
NYU 321479	15.5	14.2	13.7	11.9	7.8	90	89	84	76	65	1.41	2.29	2.35	3.74	8.89
NYU 685469	9.7	9.8	8.6	5.6	3.4	60	55	50	30	20	1.03	0.86	1.01	1.76	3.62
NYU 796740	16.2	15.3	14.1	10.1	6.3	95	91	89	86	61	2.04	2.71	2.36	4.93	8.73
NYU 890167	9.1	10.3	10.0	6.6	3.9	62	63	55	41	18	0.31	0.43	0.42	0.86	1.84
NYU 896687	15.8	14.7	14.2	12.6	9.1	93	91	86	78	66	2.65	1.79	2.07	4.11	8.50
NYU 2434587	10.0	8.3	8.0	5.2	3.5	76	74	61	38	0	1.37	1.80	1.96	3.30	6.66
NGC 4472	11.4	11.3	11.0	10.2	8.3	99	99	97	93	86	1.08	1.01	1.10	2.33	3.02
NGC 4365	12.3	12.2	11.6	10.6	8.6	100	100	100	89	61	1.33	1.20	1.25	2.02	2.71
NGC 2329	7.9	8.4	8.0	7.7	5.8	94	96	97	88	60	1.33	1.68	1.91	3.28	5.60
NGC 4473	11.5	11.2	10.9	9.4	7.5	100	100	100	88	60	1.85	1.32	1.65	2.81	5.10
NGC 4621	11.9	11.7	11.2	11.2	9.7	100	100	100	96	95	0.33	0.38	0.44	0.56	0.99
NGC 4697	9.9	9.7	8.6	6.7	5.0	82	78	60	35	8	1.22	1.53	1.92	3.39	5.79
NGC 5812	13.1	12.8	12.2	11.5	10.	100	100	100	97	95	1.59	0.95	1.62	2.71	5.08
NGC 4239	10.7	9.2	6.1	4.3	3.1	92	94	91	22	0	0.06	0.04	0.04	0.09	0.16
NGC 4339	10.6	10.2	9.3	7.4	5.7	84	89	71	43	19	0.23	0.18	0.29	0.76	1.46
NGC 4387	13.7	12.9	11.7	9.8	7.1	100	100	100	84	35	0.04	0.04	0.04	0.06	0.09
NGC 4458	15.6	15.6	14.1	11.1	7.2	97	94	90	86	60	0.07	0.06	0.07	0.09	0.15
NGC 4464	16.8	16.2	15.3	12.7	8.8	100	100	100	98	75	0.13	0.11	0.12	0.23	0.39
NGC 4467	15.5	15.0	14.1	11.6	8.1	100	100	100	90	53	0.06	0.05	0.06	0.08	0.11
NGC 4489	8.5	6.4	4.4	3.6	3.0	65	35	5	0	0	0.09	0.07	0.08	0.15	0.33
NGC 4551	10.3	9.5	8.7	6.7	4.4	85	88	65	35	0	0.22	0.18	0.15	0.31	0.56

TABLE B.1— Mass-weighted age, fraction of old stellar populations (>5 Gyr) and stellar mass obtained from the derived SFH with a unimodal IMF shape.

Galaxy ID	Age (Gyr) IMF Slope					%old IMF slope					Mass ($\times 10^{11} M_{sun}$) IMF slope				
	0.8	1.0	1.3	1.8	2.3	0.8	1.0	1.3	1.8	2.3	0.8	1.0	1.3	1.8	2.3
NYU 54829	6.3	7.5	6.5	4.8	3.4	60	62	52	38	14	0.94	0.78	0.79	0.98	1.34
NYU 321479	12.8	13.8	13.4	11.8	10.4	85	85	84	78	71	1.78	1.61	1.62	1.90	2.52
NYU 685469	1.9	2.1	1.9	1.7	1.5	0	0	0	0	0	0.45	0.42	0.43	0.72	0.92
NYU 796740	15.9	15.9	15.3	15.0	12.7	94	93	91	89	83	1.83	2.24	2.11	2.60	2.88
NYU 890167	3.3	4.1	4.3	3.1	2.8	25	25	27	28	13	0.16	0.15	0.16	0.22	0.45
NYU 896687	14.8	14.7	13.6	12.9	12.8	80	85	77	76	71	1.62	1.82	1.51	1.99	2.78
NYU 2434587	12.4	11.1	10.5	8.1	7.3	76	68	66	61	58	1.72	1.42	1.38	1.58	2.13
NGC 4472	11.4	11.5	11.5	11.1	10.6	100	100	98	95	88	2.97	2.79	2.67	2.81	2.97
NGC 4365	13.6	13.6	13.0	12.8	12.3	100	100	100	100	100	3.38	2.73	2.40	2.64	3.25
NGC 2329	7.3	7.1	7.1	5.7	5.3	75	66	62	44	21	1.82	1.53	1.37	1.55	1.95
NGC 4473	11.7	11.5	11.1	10.6	9.8	100	100	98	93	88	4.47	3.48	2.97	3.28	4.22
NGC 4621	13.1	12.5	12.3	12.0	11.8	100	100	100	100	98	0.31	0.24	0.22	0.25	0.13
NGC 4697	9.7	9.6	9.4	8.8	8.0	80	75	73	67	54	3.45	2.81	2.65	3.04	3.06
NGC 5812	11.1	11.1	11.1	11.0	10.9	100	98	95	93	93	2.75	2.56	1.98	2.19	2.62
NGC 4239	12.3	12.6	12.2	11.6	9.9	82	82	78	74	65	0.07	0.04	0.04	0.07	0.14
NGC 4339	9.9	10.0	9.2	8.5	7.8	82	83	73	61	52	0.53	0.18	0.30	0.76	1.46
NGC 4387	13.8	13.5	12.9	11.8	10.1	96	98	95	84	61	0.03	0.03	0.03	0.05	0.08
NGC 4458	16.2	16.1	16.1	15.1	12.5	97	96	95	92	76	0.07	0.06	0.07	0.10	0.16
NGC 4464	16.0	15.6	15.7	14.6	13.3	100	100	100	99	99	0.20	0.19	0.19	0.28	0.41
NGC 4467	14.5	14.8	13.8	13.3	12.7	96	95	95	93	92	0.06	0.06	0.06	0.09	0.11
NGC 4489	9.7	10.0	8.9	7.7	5.6	72	65	65	50	32	0.09	0.08	0.08	0.15	0.33
NGC 4551	9.0	8.7	8.0	6.4	5.3	55	52	45	28	15	0.25	0.22	0.15	0.31	0.66

TABLE B.2 — Mass-weighted age, fraction of old stellar populations (>5 Gyr) and stellar mass obtained from the derived SFH with a bimodal IMF shape.

B.2 Dynamical *vs* Stellar Masses

B.2.1 Non-homology assumption

We have tested whether the non-homology assumption on the dynamical mass would change our results. Figure B4 shows the M_{star}-M_{dyn} relation as in Figure 4.11, but in this case the dynamical mass is calculated with the non-homology assumption, which takes into account the geometry of the mass distribution and the velocity projection along the line of sight of the galaxy. The factor $K(n)$ is computed as in Equation 3.4:

$$K(n) \simeq \frac{73.32}{10.465 + (n - 0.95)^2} + 0.954, \qquad (B.1)$$

where n is the Sérsic index from Table 3.4. Comparing the obtained deviations from the 1:1 relation for both assumptions (homology a non-homology) we only find a difference of the order of 0.5%. The major difference is obtained for the local compact galaxies, which under the non-homology assumption show more dispersion due to the different Sérsic index values for this type of objects.
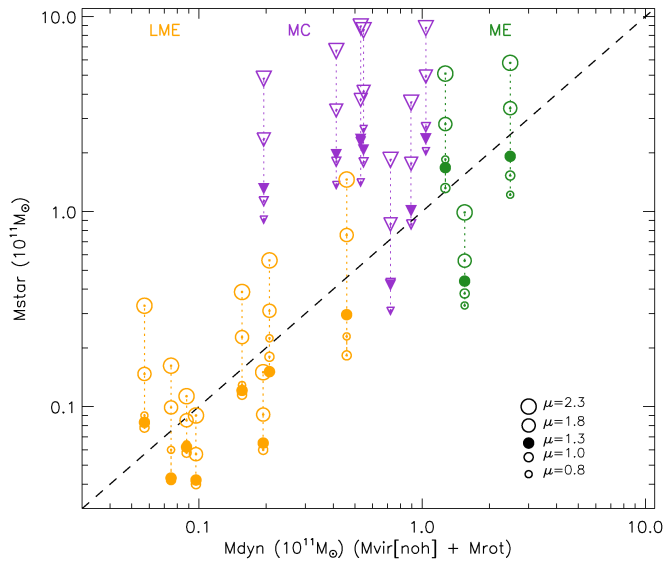

FIGURE B.4— Stellar masses obtained from the SFHs using different IMF slopes *vs* their dynamical mass. Massive compacts are plotted in purple triangles, massive ellipticals in green circles and low-mass ellipticals in yellow circles. Filled symbols correspond to the stellar mass obtained with a Salpeter IMF for each galaxy. Symbol size increases with increasing IMF slope and dynamical masses were estimated under the non-homology assumption, taking into account the Sérsic index values.

B.2.2   Deviations from the 1:1 relation

We can test how much do the parameters related to the dynamical or to the stellar mass deviate from the 1:1 relation to find any specific trend that could indicate the cause for the discrepancies. In Figure B5 we show these deviations normalized to the dynamical mass, assuming a Salpeter IMF. In the upper row we show the dynamical mass related parameters (Sérsic index, effective radii and velocity dispersion), while in the lower row we show the stellar mass parameters (mean L-weighted age and mean M-weighted age). It is shown that massive compacts always deviate from the 1:1 relation. These objects resemble to massive ellipticals in terms of velocity dispersion but to low-mass ellipticals if looking at sizes. The panel with the $< Age >_L$ is the only one showing a trend, but no correlation is found when we use the $< Age >_M$. Summarizing, we are not able to discover the parameter that leads to the controversy for the M_{dyn}-M_{star} relation, but we claim that a deeper understanding on the dynamical mass is required.
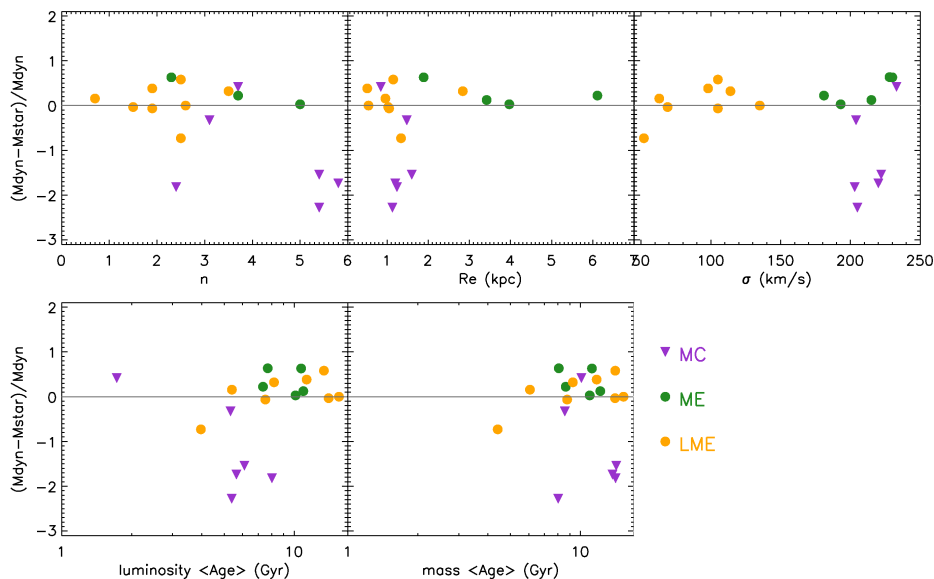

FIGURE B.5— Deviations from the 1:1 relation between M_{dyn}-M_{star} plotted against Sérsic index, effective radii, velocity dispersion and mean luminosity- and mass-weighted ages. Symbols and colors are like in Figure B.4. The gray line marks the 1:1 relation. It is clear that only the massive compacts strongly deviate from the relation, although they do it independently of the parameters.

C

Stellar populations at z∼ 0.83

C.1 Line strength measurements

We present in this section the line-strength measurements in the LIS8.4 system for the galaxies in RX J0152.7-1357 at z= 0.83, listed in Tables C1 and C2. The errors were obtained from the error spectra associated to the each galaxy final spectra. They were checked by calculating them directly from the formulas in Cardiel et al. (2003).

Figure C1 shows a comparison between some of these indices and J05. For this purpose, we transformed their indices measured in the Lick/IDS system into the LIS system using the webpage of MILES [1]. We can see that our $C_2$4668 and CN2 values are smaller, while a significant spread is found for G4300 and Fe4383 indices.

Figure C2 compares the derived ages from different pairs of index-index grids, to highlight the impact of the overabundance in the age estimates. Note that in the first panel the derived ages are in better agreement, as $C_2$4668 and CN2 present similar abundance patterns. On the contrary, the right panel shows that the ages derived with Fe4383 are systematically larger.

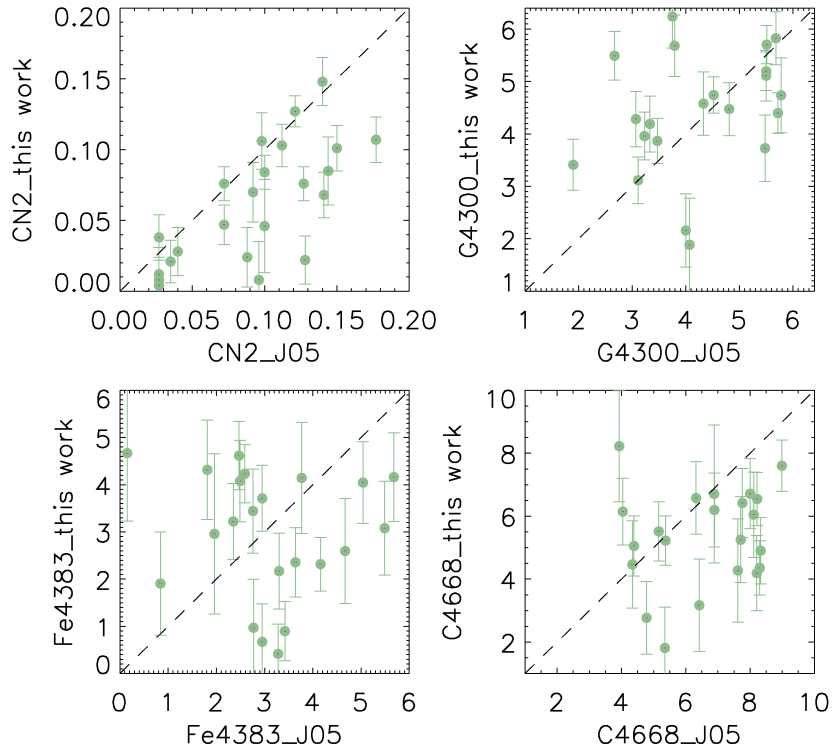[1] *http://miles.iac.es/pages/webtools/lickids-to-lis.php*

FIGURE C.1— Comparison of our index measurements with those of J05. The latter were transformed to the LIS system for a fair comparison.
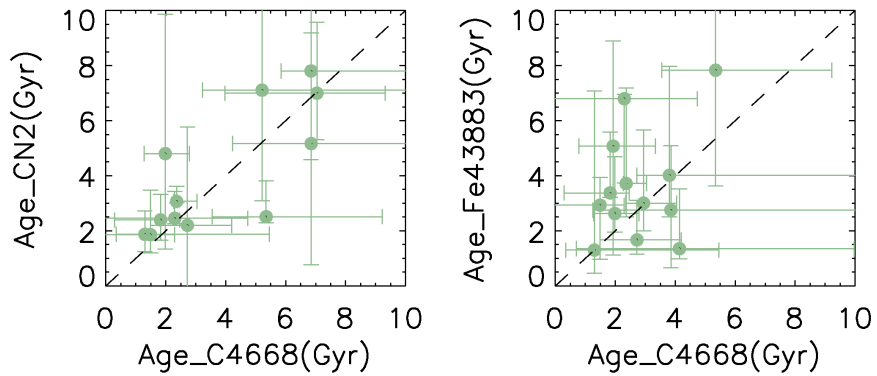

FIGURE C.2— Comparison of the derived ages from different pairs of indices, as stated on each label, to emphasize the effect of the overabundance of some elements.

ID	CN3883	D4000	CaHK	HdA	HdF	CN2
338	0.124±0.020	1.837±0.015	19.407±1.580	1.466±0.616	1.692±0.417	0.004±0.022
346	0.120±0.017	1.737±0.009	13.056±1.476	1.557±0.529	2.226±0.349	0.028±0.019
422	0.151±0.017	1.857±0.015	18.746±1.389	1.246±0.530	1.243±0.365	0.022±0.019
523	0.237±0.011	1.947±0.008	20.474±0.905	-0.683±0.369	1.117±0.243	0.127±0.012
566*	0.101±0.016	1.759±0.012	17.933±1.329	3.004±0.480	2.628±0.323	-0.038±0.018
627	0.244±0.021	1.803±0.022	15.819±1.734	0.253±0.661	0.398±0.462	0.024±0.023
766	0.243±0.016	1.932±0.018	13.723±1.399	-1.315±0.543	0.369±0.366	0.101±0.018
776	0.123±0.014	1.689±0.007	15.501±1.167	1.864±0.424	2.311±0.281	0.047±0.015
813	0.215±0.012	1.992±0.009	14.952±1.030	0.291±0.389	1.086±0.263	0.084±0.013
908	0.105±0.012	1.493±0.012	17.790±1.014	0.563±0.391	1.132±0.266	0.076±0.013
1027	0.267±0.020	1.749±0.015	20.953±1.574	-0.230±0.638	0.915±0.430	0.106±0.022
1085	0.244±0.012	2.215±0.014	17.940±1.022	-0.026±0.400	0.772±0.203	0.076±0.013
1110	0.191±0.017	1.951±0.016	18.584±1.382	-0.531±0.552	1.572±0.357	0.148±0.018
1159*	0.081±0.015	1.675±0.010	15.226±1.285	2.972±0.452	2.380±0.308	0.021±0.017
1210	0.207±0.021	1.928±0.014	14.331±1.790	-0.661±0.688	0.059±0.478	0.070±0.023
1299*	0.147±0.019	1.964±0.019	10.246±1.661	1.263±0.585	2.176±0.384	0.056±0.020
1458	0.198±0.024	1.766±0.017	19.208±1.898	0.859±0.736	1.619±0.492	0.085±0.026
1507	0.097±0.027	1.767±0.015	18.722±2.160	0.201±0.847	2.320±0.537	-0.008±0.029
1567	0.220±0.020	1.854±0.015	18.243±1.624	-2.114±0.672	0.295±0.445	0.287±0.022
1590	0.153±0.016	1.919±0.020	16.220±1.341	-0.747±0.526	0.726±0.353	0.107±0.017
1614	0.198±0.015	1.980±0.014	15.245±1.223	0.264±0.463	0.850±0.317	0.103±0.016
1682	0.116±0.014	1.829±0.010	15.750±1.145	1.232±0.425	1.672±0.286	0.008±0.015
1811	0.141±0.033	1.744±0.029	10.675±2.841	-0.570±1.054	1.832±0.672	0.046±0.036
1935	0.231±0.016	1.917±0.020	20.310±1.245	-0.692±0.508	1.178±0.333	0.068±0.017

TABLE C.1 — Measurements of the line indices of the high-z cluster treated in this study. We only show those estimates that are reliable within the wavelength coverage free of sky residuals.

ID	Ca4227	G4300	HgA	HgF	Fe4338	C_24668
338	1.054±0.348	3.726±0.714	-2.340±0.630	-0.357±0.445	1.906±1.051	4.465±1.390
346	1.163±0.296	4.190±0.534	-2.148±0.613	1.044±0.358	4.162±0.863	6.195±1.172
422	0.428±0.314	3.824±0.503	-4.644±0.642	-0.356±0.381	2.362±0.891	4.188±1.194
523	0.631±0.204	4.741±0.345	-3.858±0.418	-0.191±0.250	4.143±0.569	5.224±0.781
566*	0.716±0.291	6.030±0.474	-3.805±0.599	0.761±0.343	4.668±0.806	2.769±1.153
627	0.706±0.372	6.239±0.601	-0.028±0.769	-0.111±0.457	0.971±1.112	3.168±1.467
766	1.464±0.205	4.473±0.505	-4.835±0.618	-1.663±0.388	5.048±0.808	6.715±1.110
776	1.249±0.238	3.116±0.447	-1.232±0.486	0.952±0.291	2.356±0.725	5.053±0.961
813	0.626±0.221	5.194±0.367	-4.988±0.462	-0.582±0.205	3.711±0.619	7.603±0.818
908	0.633±0.222	5.702±0.365	-4.700±0.465	-0.537±0.208	3.222±0.633	4.355±0.862
1027	1.009±0.346	4.578±0.607	-4.169±0.736	-0.593±0.446	4.315±0.991	5.253±1.365
1085	1.503±0.209	4.397±0.385	-4.586±0.468	-0.371±0.208	4.079±0.628	6.548±0.847
1110	1.333±0.288	4.282±0.526	-4.768±0.639	-1.250±0.394	3.443±0.866	6.577±1.152
1159*	1.020±0.267	3.411±0.487	-0.702±0.527	0.836±0.322	2.317±0.797	4.904±1.058
1210	-0.509±0.418	2.159±0.699	-3.341±0.772	-0.979±0.484	2.596±1.096	8.927±1.390
1299*	0.864±0.334	4.890±0.572	-4.441±0.705	-0.069±0.415	4.615±0.938	5.315±1.299
1458	0.948±0.413	4.736±0.716	-4.200±0.874	-0.134±0.518	4.233±1.177	4.274±1.638
1507	2.110±0.420	1.886±0.887	0.225±0.898	0.781±0.561	0.417±1.441	8.226±1.765
1567	0.780±0.355	5.680±0.588	-3.661±0.732	0.030±0.435	3.079±1.022	6.048±1.358
1590	0.676±0.290	5.110±0.485	-3.713±0.593	-0.608±0.363	0.896±0.864	6.420±1.094
1614	0.943±0.256	3.958±0.455	-4.267±0.542	-1.086±0.335	4.046±0.732	13.270±0.903
1682	0.615±0.247	3.866±0.430	-3.287±0.500	0.328±0.295	3.375±0.699	5.517±0.941
1811	0.500±0.591	6.220±0.940	-4.994±1.225	-2.092±0.781	2.168±1.695	6.707±2.193
1935	0.163±0.292	5.490±0.463	-4.781±0.586	-1.486±0.365	2.959±0.801	6.144±0.428

TABLE C.2— Table C1, continued

C.2 Star Formation Histories

For internal comparison, we plot in Figure C3 the luminosity-weighted ages derived from the full-spectrum-fitting approach with `STARLIGHT` compared to those inferred from the index-index diagrams. It is known that these techniques give slightly different ages, in particular for the old stellar populations. The method based on the index-index diagrams tend to provide older ages than those from the full-spectrum-fitting approach (Vazdekis et al. 2001a, Mendel, Proctor & Forbes 2007). On the contrary, for stellar populations with a strong contribution of a young component, the SSP-equivalent age is strongly biased towards these younger ages, obtaining a better agreement (e.g. Serra & Trager 2007).

We also need to test the robustness of the results obtained with the combined method. Figure C4 shows the metallicities derived from this method compared to those inferred from the index-index diagrams. We find a good agreement, in particular in the $C_2 4668$ panel.
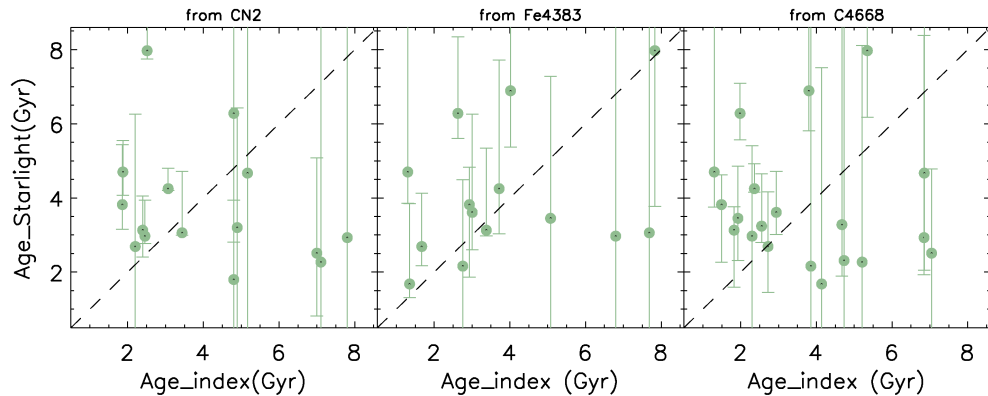

FIGURE C.3— Derived ages from different pairs of indices compared to the mean luminosity-weighted ages derived from `STARLIGHT`.
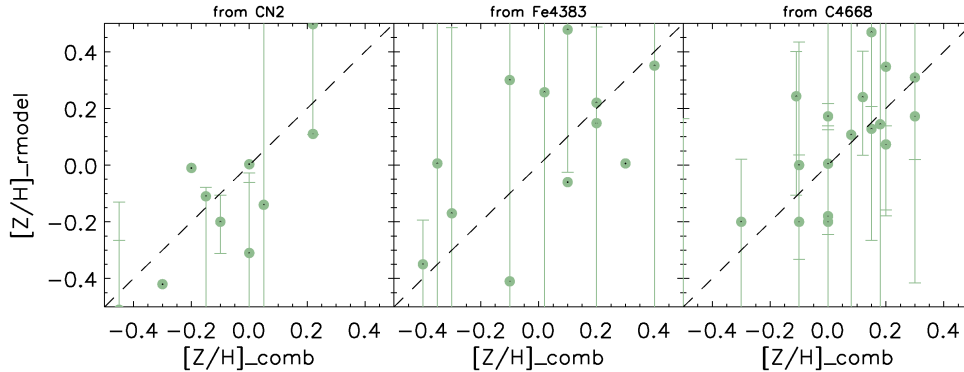
FIGURE C.4— Comparison of the derived metallicities from various index-index diagrams and from the combined approach. They are in good agreement, confirming the robustness of the combined method.

C.3 Coma as the control sample

We have selected Coma as the control cluster in the local Universe to analyze the evolution of ETGs through cosmic time because it shares similar properties to our high-redshift cluster (e.g. luminosities, densities, masses). We use for Coma the data of PSB06a, which was already reduced and analyzed by these authors. We have considered an aperture for the spectra comparable to the one employed for our cluster at high-z and then followed the same steps than for RX J0152.7-1357. We selected a set of galaxies covering the same velocity dispersion range, which encompasses a similar number of galaxies (22 galaxies).

Figures C5 and C6 present the spectra and the SFHs for each galaxy considered in our Coma sample. In this case, we have limited our models to ages below $14.12\,$Gyr, to be consistent with the methodology followed for the high-z cluster, for which we limited the age of the models to $8\,$Gyr. We have tested the impact of this choice by comparing the derived ages using the whole set of models (up to $17\,$Gyr) with the ones limited to $14\,$Gyr. We see in Figure C7 that only the oldest ones are affected, changing from $17\,$Gyr to $14\,$Gyr. On the contrary, for those that presented ages $<12\,$Gyr, their estimates remains practically unchanged. However, the derived metallicity is independent of the ages assumed, as the metallicity coverage of the models is the same for both cases.
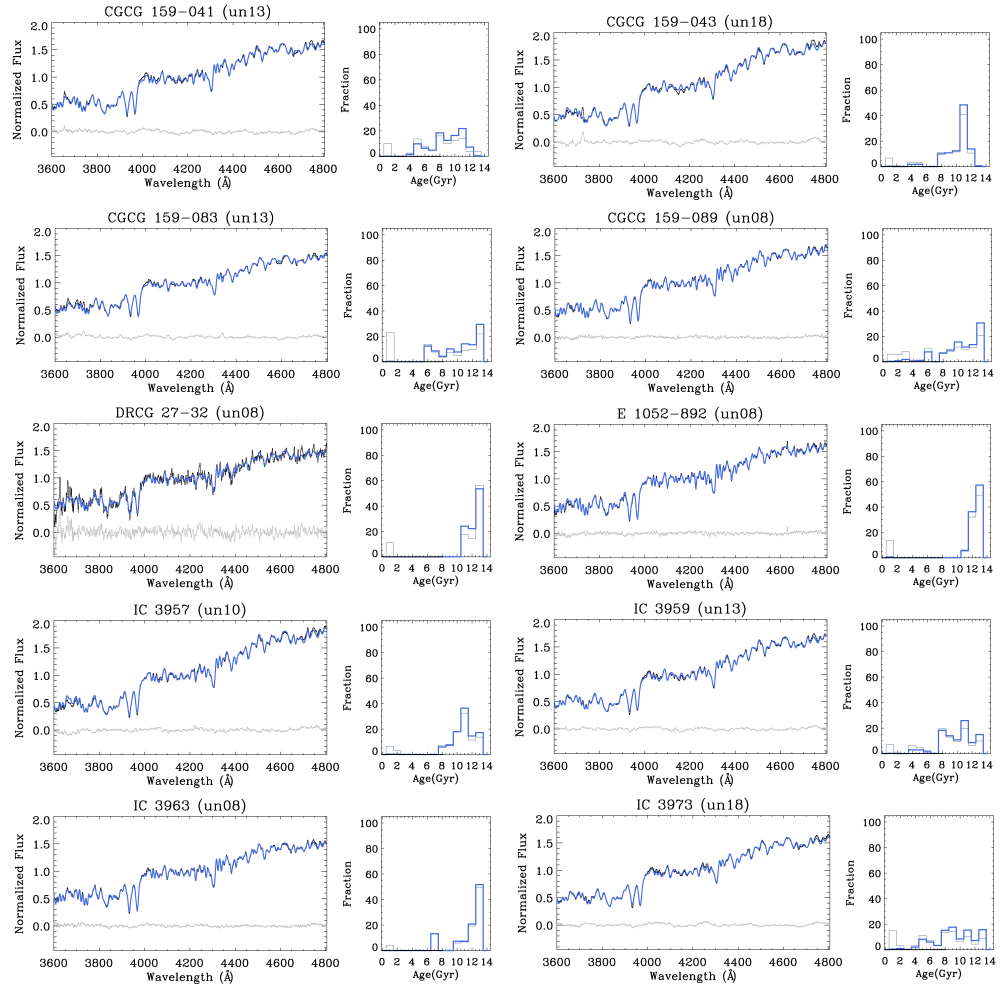
FIGURE C.5— Coma cluster galaxy spectra used as control sample are plotted, together with the best fit from STARLIGHT and the residual (left panels). The derived Star Formation Histories is shown on the right panels, where the blue histograms represent the mass-weighted derived SFH and the dashed gray line the luminosity-weighted estimate.
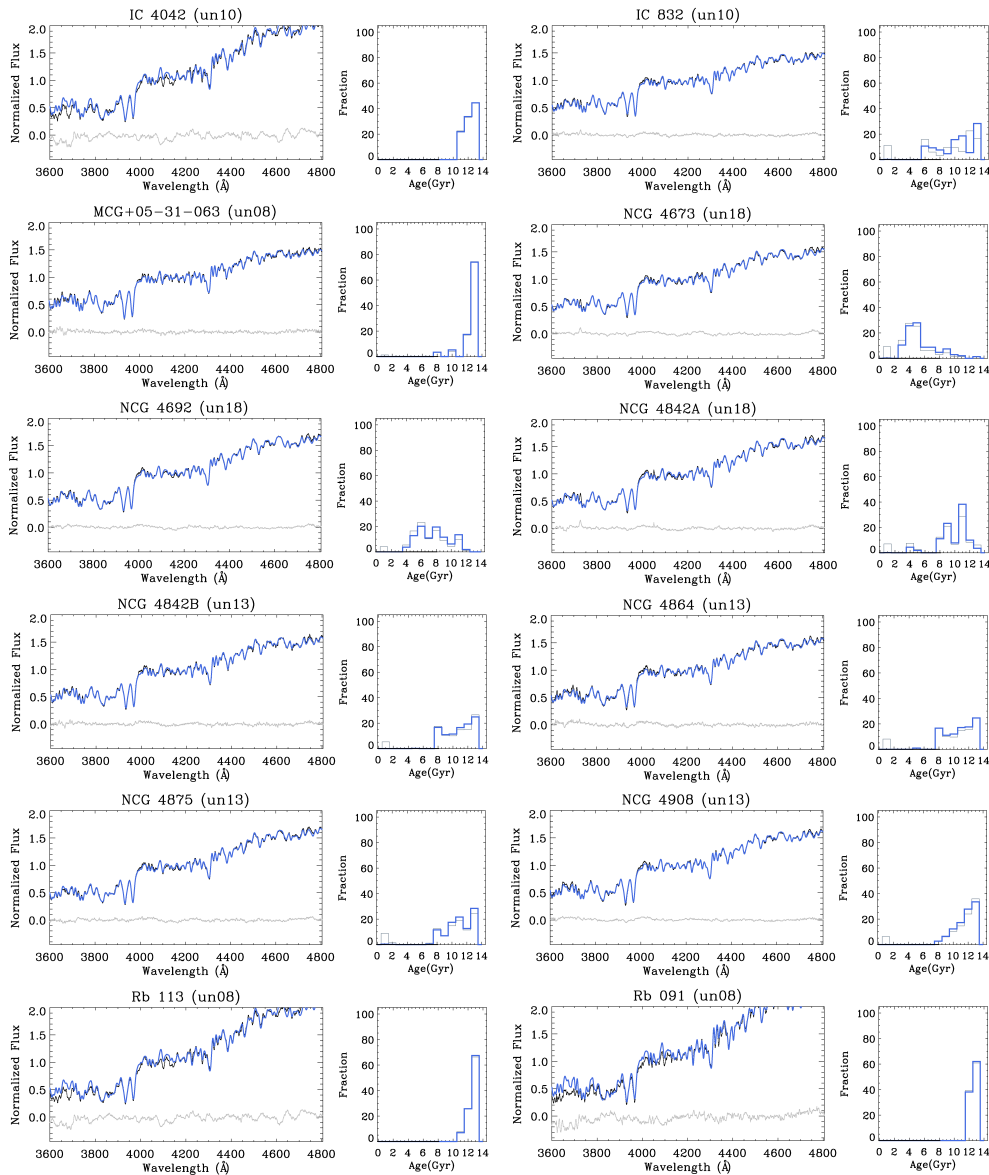
FIGURE C.6— Figure C5, continued.

Finally, we have also compared our results to the ones originally derived in Sánchez-Blázquez et al. (2006b) using a full-spectrum-fitting approach. Although the codes used were not the same, they are in good agreement, in particular for the metallicity (see Figure C8).
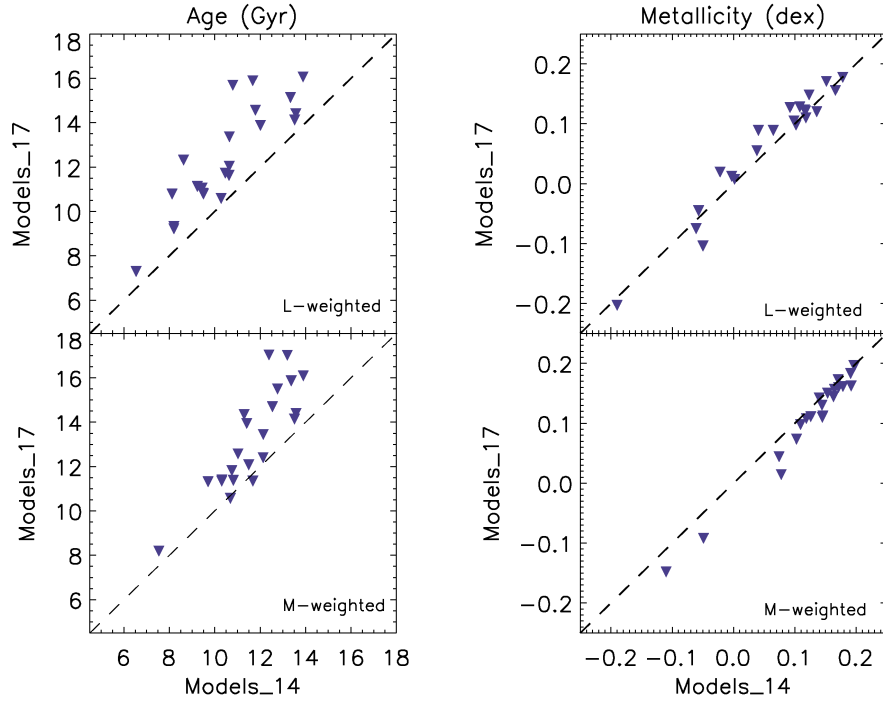
FIGURE C.7— Testing the robustness of selecting those models for the SFHs limited to the age of the Universe at the redshift of the cluster. In this case, we test the results with Coma. It is seen that only for the older ones there is a variation according to the limit imposed, while the younger ones are in good agreement.
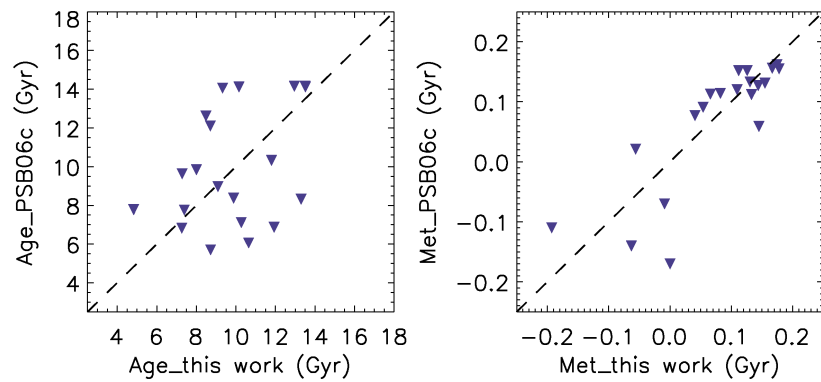

FIGURE C.8— Comparison of the ages derived from the full-spectrum-fitting in this work and in PSB06b.

C.4   IMF variations

Figure C9 shows the difference in the stellar populations derived with a non-standard IMF and with a universal Kroupa IMF. We see that the largest differences are found for the oldest galaxies in the Coma data. This occurs because the IMF effect is particularly relevant for the old populations while it does not affect that much the youngest ones (Chapter 4). Because we have removed the models corresponding approximately half the age of the Universe in the high redshift cluster, this dependence is not seen.
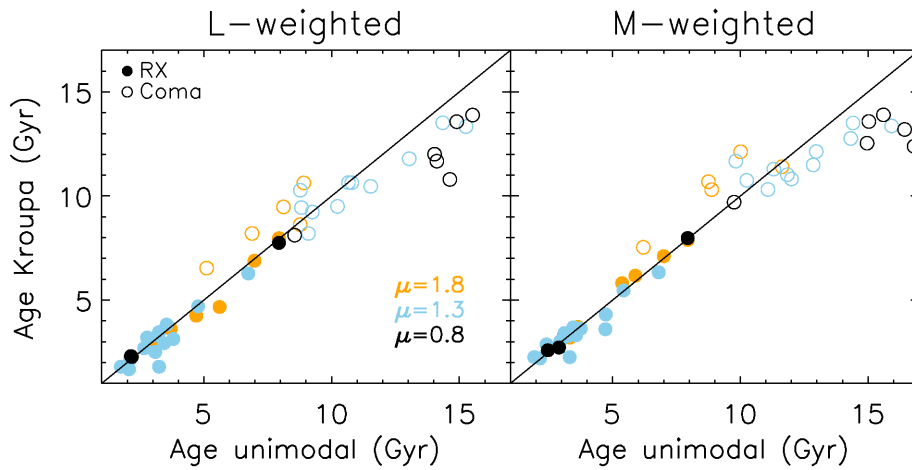

FIGURE C.9— Ages derived assuming an standard Kroupa-like IMF slope *versus* the ages assuming different IMF slopes according to the velocity-dispersion of the galaxy. Filled dots represent the high-z cluster, while open dots the galaxies in Coma. Three different IMF slopes are shown in different colors, both in the luminosity and the mass weighted panels.

Bibliography

Abadi M. G., Moore B., Bower R. G., 1999, MNRAS, 308, 947

Adams F. C., Fatuzzo M., 1996, ApJ, 464, 256

Akerman C. J., Carigi L., Nissen P. E., Pettini M., Asplund M., 2004, A&A, 414, 931

Aragon-Salamanca A., Ellis R. S., Couch W. J., Carter D., 1993, MNRAS, 262, 764

Arimoto N., Sofue Y., Tsujimoto T., 1996, PASJ, 48, 275

Arimoto N., Yoshii Y., 1987, A&A, 173, 23

Auger M. W., Treu T., Bolton A. S., Gavazzi R., Koopmans L. V. E., Marshall P. J., Moustakas L. A., Burles S., 2010a, ApJ, 724, 511

Auger M. W., Treu T., Gavazzi R., Bolton A. S., Koopmans L. V. E., Marshall P. J., 2010b, ApJ, 721, L163

Baade W., 1940, PASP, 52, 386

Balogh M. L., Navarro J. F., Morris S. L., 2000, ApJ, 540, 113

Barbaro G., Poggianti B. M., 1997, A&A, 324, 490

Barden M. et al., 2005, ApJ, 635, 959

Barnabè M., Czoske O., Koopmans L. V. E., Treu T., Bolton A. S., 2011, MNRAS, 415, 2215

Barnes J. E., 2002, MNRAS, 333, 481

Barnes J. E., Hernquist L., 1996, ApJ, 471, 115

Barr J., Davies R., Jørgensen I., Bergmann M., Crampton D., 2005, AJ, 130, 445

Barrientos L. F., Lilly S. J., 2003, ApJ, 596, 129

Bastian N., Covey K. R., Meyer M. R., 2010, ARA&A, 48, 339

Bate M. R., 2009a, MNRAS, 397, 232

—, 2009b, MNRAS, 392, 1363

Baugh C. M., Cole S., Frenk C. S., 1996, MNRAS, 283, 1361

Bekki K., 1999, ApJ, 510, L15

Bekki K., Couch W. J., Shioya Y., 2002, ApJ, 577, 651

Bell E. F., de Jong R. S., 2001, ApJ, 550, 212

Bell E. F., McIntosh D. H., Katz N., Weinberg M. D., 2003, ApJS, 149, 289

Bell E. F. et al., 2004, ApJ, 608, 752

Bender R., 1988, A&A, 193, L7

Bender R., Burstein D., Faber S. M., 1992, ApJ, 399, 462

—, 1993, ApJ, 411, 153

Bender R., Saglia R. P., Ziegler B., Belloni P., Greggio L., Hopp U., Bruzual G., 1998, ApJ, 493, 529

Bender R., Ziegler B., Bruzual G., 1996, ApJ, 463, L51

Berendzen R., Hart R., Seeley D., 1976, Man discovers the galaxies

Bernardi M., Nichol R. C., Sheth R. K., Miller C. J., Brinkmann J., 2006, AJ, 131, 1288

Bernardi M., Renzini A., da Costa L. N., Wegner G., Alonso M. V., Pellegrini P. S., Rité C., Willmer C. N. A., 1998, ApJ, 508, L143

Bernardi M. et al., 2003, AJ, 125, 1866

Bertin G., Ciotti L., Del Principe M., 2002, A&A, 386, 149

Bertola F., Capaccioli M., 1975, ApJ, 200, 439

Bezanson R., van Dokkum P. G., Tal T., Marchesini D., Kriek M., Franx M., Coppi P., 2009, ApJ, 697, 1290

Binney J., 1978, MNRAS, 183, 501

—, 1985, MNRAS, 212, 767

—, 2005, MNRAS, 363, 937

Binney J., Tremaine S., 2008, Galactic Dynamics: Second Edition, Binney, J. & Tremaine, S., ed. Princeton University Press

Bisbas T. G., Wünsch R., Whitworth A. P., Hubber D. A., Walch S., 2011, ApJ, 736, 142

Blake C. et al., 2004, MNRAS, 355, 713

Blakeslee J. P. et al., 2003, ApJ, 596, L143

—, 2006, ApJ, 644, 30

Blanton M., Cen R., Ostriker J. P., Strauss M. A., Tegmark M., 2000, ApJ, 531, 1

Blanton M. R., Eisenstein D., Hogg D. W., Schlegel D. J., Brinkmann J., 2005a, ApJ, 629, 143

Blanton M. R. et al., 2003, ApJ, 592, 819

Blanton M. R., Roweis S., 2007, AJ, 133, 734

Blanton M. R. et al., 2005b, AJ, 129, 2562

Bluck A. F. L., Conselice C. J., Bouwens R. J., Daddi E., Dickinson M., Papovich C., Yan H., 2009, MNRAS, 394, L51

Blumenthal G. R., Faber S. M., Primack J. R., Rees M. J., 1984, Nature, 311, 517

Bolton A. S., Treu T., Koopmans L. V. E., Gavazzi R., Moustakas L. A., Burles S., Schlegel D. J., Wayth R., 2008, ApJ, 684, 248

Bournaud F. et al., 2011, ApJ, 730, 4

Bower R. G., Ellis R. S., Rose J. A., Sharples R. M., 1990, AJ, 99, 530

Bower R. G., Lucey J. R., Ellis R. S., 1992, MNRAS, 254, 601

Boylan-Kolchin M., Ma C.-P., Quataert E., 2006, MNRAS, 369, 1081

Braglia F. G., Pierini D., Biviano A., Böhringer H., 2009, A&A, 500, 947

Bressan A., Tautvaisiene G., 1996, Baltic Astronomy, 5, 239

Brüggen M., De Lucia G., 2008, MNRAS, 383, 1336

Bruzual G., 1981, Spectral evolution of galaxies

Bruzual G., Charlot S., 2003, MNRAS, 344, 1000

Bruzual A. G., Charlot S., 1993, ApJ, 405, 538

Buitrago F., Trujillo I., Conselice C. J., Bouwens R. J., Dickinson M., Yan H., 2008, ApJ, 687, L61

Buitrago F., Trujillo I., Conselice C. J., Häußler B., 2013, MNRAS, 428, 1460

Bundy K. et al., 2006, ApJ, 651, 120

Bundy K., Fukugita M., Ellis R. S., Targett T. A., Belli S., Kodama T., 2009, ApJ, 697, 1369

Burstein D., Bertola F., Buson L. M., Faber S. M., Lauer T. R., 1988, ApJ, 328, 440

Burstein D., Faber S. M., Gaskell C. M., Krumm N., 1984, ApJ, 287, 586

Butcher H., Oemler, Jr. A., 1978, ApJ, 219, 18

Caldwell N., 1984, PASP, 96, 287

Caldwell N., Rose J. A., Concannon K. D., 2003, AJ, 125, 2891

Calvi R., Poggianti B. M., Vulcani B., 2011, MNRAS, 416, 727

Cameron E., Carollo C. M., Oesch P. A., Bouwens R. J., Illingworth G. D., Trenti M., Labbé I., Magee D., 2011, ApJ, 743, 146

Cappellari M., 2012, ArXiv e-prints: 1211.3998

Cappellari M. et al., 2006, MNRAS, 366, 1126

—, 2009, ApJ, 704, L34

Cappellari M., Emsellem E., 2004, PASP, 116, 138

Cappellari M. et al., 2007, MNRAS, 379, 418

—, 2011, MNRAS, 416, 1680

—, 2012a, Nature, 484, 485

—, 2012b, ArXiv e-prints: 1208.3523

Cardiel N., 1999, PhD thesis, Universidad Complutense de Madrid, Spain, (1999)

Cardiel N., Gorgas J., Sánchez-Blázquez P., Cenarro A. J., Pedraz S., Bruzual G., Klement J., 2003, A&A, 409, 511

Carigi L., 2000, XAA, 36, 171

Carlberg R. G., 1984a, ApJ, 286, 403

—, 1984b, ApJ, 286, 416

Carollo C. M. et al., 2013, ArXiv e-prints

Carrasco E. R., Conselice C. J., Trujillo I., 2010, MNRAS, 405, 2253

Carretero C., Vazdekis A., Beckman J. E., Sánchez-Blázquez P., Gorgas J., 2004, ApJ, 609, L45

Cassata P. et al., 2010, ApJ, 714, L79

—, 2011, ApJ, 743, 96

—, 2013, ArXiv e-prints

Cenarro A. J., Gorgas J., Vazdekis A., Cardiel N., Peletier R. F., 2003, MNRAS, 339, L12

Cenarro A. J., Sánchez-Blázquez P., Cardiel N., Gorgas J., 2004, ApJ, 614, L101

Cenarro A. J., Trujillo I., 2009, ApJ, 696, L43

Cervantes J. L., Vazdekis A., 2009, MNRAS, 392, 691

Chaboyer B., Sarajedini A., Demarque P., 1992, ApJ, 394, 515

Chabrier G., 2003, PASP, 115, 763

Chiappini C., Romano D., Matteucci F., 2003, MNRAS, 339, 63

Chiboucas K., Barr J., Flint K., Jørgensen I., Collobert M., Davies R., 2009, ApJS, 184, 271

Chiosi C., Carraro G., 2002, MNRAS, 335, 335

Cid Fernandes R., González Delgado R. M., 2010, MNRAS, 403, 780

Cid Fernandes R., Mateus A., Sodré L., Stasińska G., Gomes J. M., 2005, MNRAS, 358, 363

Cimatti A. et al., 2008, A&A, 482, 21

Ciotti L., van Albada T. S., 2001, ApJ, 552, L13

Coelho P., Bruzual G., Charlot S., Weiss A., Barbuy B., Ferguson J. W., 2007, MNRAS, 382, 498

Cole S., 1991, ApJ, 367, 45

Cole S., Lacey C. G., Baugh C. M., Frenk C. S., 2000, MNRAS, 319, 168

Colless M., Burstein D., Davies R. L., McMahan R. K., Saglia R. P., Wegner G., 1999, MNRAS, 303, 813

Conroy C., Gunn J. E., 2010, ApJ, 712, 833

Conroy C., Gunn J. E., White M., 2009, ApJ, 699, 486

Conroy C., van Dokkum P., 2012a, ApJ, 747, 69

Conroy C., van Dokkum P. G., 2012b, ApJ, 760, 71

Conselice C. J., Blackburne J. A., Papovich C., 2005, ApJ, 620, 564

Conselice C. J. et al., 2011, MNRAS, 413, 80

Conselice C. J., Yang C., Bluck A. F. L., 2009, MNRAS, 394, 1956

Couch W. J., Barger A. J., Smail I., Ellis R. S., Sharples R. M., 1998, ApJ, 497, 188

Couch W. J., Ellis R. S., Sharples R. M., Smail I., 1994, ApJ, 430, 121

Couch W. J., Sharples R. M., 1987, MNRAS, 229, 423

Cowie L. L., Songaila A., Hu E. M., Cohen J. G., 1996, AJ, 112, 839

Daddi E., Cimatti A., Pozzetti L., Hoekstra H., Röttgering H. J. A., Renzini A., Zamorani G., Mannucci F., 2000, A&A, 361, 535

Daddi E. et al., 2005, ApJ, 626, 680

Damjanov I. et al., 2009, ApJ, 695, 101

Davidge T. J., Clark C. C., 1994, AJ, 107, 946

Davies R. et al., 2011, ApJ, 741, 69

Davies R. L., Birkinshaw M., 1988, ApJS, 68, 409

Davies R. L., Efstathiou G., Fall S. M., Illingworth G., Schechter P. L., 1983, ApJ, 266, 41

Davies R. L., Sadler E. M., Peletier R. F., 1993, MNRAS, 262, 650

Davis M., Efstathiou G., Frenk C. S., White S. D. M., 1985, ApJ, 292, 371

de La Rosa I. G., La Barbera F., Ferreras I., de Carvalho R. R., 2011, MNRAS, 418, L74

De Lucia G., Boylan-Kolchin M., Benson A. J., Fontanot F., Monaco P., 2010, MNRAS, 406, 1533

De Lucia G., Helmi A., 2008, MNRAS, 391, 14

De Lucia G. et al., 2004, ApJ, 610, L77

—, 2007, MNRAS, 374, 809

De Lucia G., Springel V., White S. D. M., Croton D., Kauffmann G., 2006, MNRAS, 366, 499

de Propris R., Stanford S. A., Eisenhardt P. R., Dickinson M., Elston R., 1999, AJ, 118, 719

de Ravel L. et al., 2009, A&A, 498, 379

de Vaucouleurs G., 1948, Annales d'Astrophysique, 11, 247

—, 1959, Handbuch der Physik, 53, 275

Dekel A. et al., 2009, Nature, 457, 451

Della Ceca R. et al., 2004, A&A, 428, 383

Demarco R. et al., 2010, ApJ, 725, 1252

—, 2005, A&A, 432, 381

Denicoló G., Terlevich R., Terlevich E., Forbes D. A., Terlevich A., 2005, MN-RAS, 358, 813

di Serego Alighieri S., Lanzoni B., Jørgensen I., 2006, ApJ, 647, L99

Diaferio A., Kauffmann G., Balogh M. L., White S. D. M., Schade D., Ellingson E., 2001, MNRAS, 323, 999

Disney M. J., Romano J. D., Garcia-Appadoo D. A., West A. A., Dalcanton J. J., Cortese L., 2008, Nature, 455, 1082

Djorgovski S., Davis M., 1987, ApJ, 313, 59

D'Onghia E., Besla G., Cox T. J., Hernquist L., 2009, Nature, 460, 605

Dressler A., 1980, ApJ, 236, 351

Dressler A., Gunn J. E., 1983, ApJ, 270, 7

Dressler A., Lynden-Bell D., Burstein D., Davies R. L., Faber S. M., Terlevich R., Wegner G., 1987, ApJ, 313, 42

Dressler A., Oemler, Jr. A., Butcher H. R., Gunn J. E., 1994, ApJ, 430, 107

Dressler A. et al., 1997, ApJ, 490, 577

Drory N., Bender R., Hopp U., 2004, ApJ, 616, L103

Drory N., Salvato M., Gabasch A., Bender R., Hopp U., Feulner G., Pannella M., 2005, ApJ, 619, L131

Dutton A. A., Maccio' A. V., Mendel J. T., Simard L., 2012, ArXiv e-prints: 1204.2825

Dutton A. A., Mendel J. T., Simard L., 2012, MNRAS, 422, L33

Ebeling H., Edge A. C., Allen S. W., Crawford C. S., Fabian A. C., Huchra J. P., 2000, MNRAS, 318, 333

Eggen O. J., Lynden-Bell D., Sandage A. R., 1962, ApJ, 136, 748

Elbaz D., Arnaud M., Vangioni-Flam E., 1995, A&A, 303, 345

Ellis R. S., Abraham R. G., Dickinson M., 2001, ApJ, 551, 111

Ellis R. S., Smail I., Dressler A., Couch W. J., Oemler, Jr. A., Butcher H., Sharples R. M., 1997, ApJ, 483, 582

Ellis S. C., Jones L. R., 2004, MNRAS, 348, 165

Elmegreen B. G., 1995, MNRAS, 275, 944

—, 1997, ApJ, 486, 944

Emsellem E. et al., 2011, MNRAS, 414, 888

Epinat B. et al., 2009, A&A, 504, 789

Faber S. M., 1972, A&A, 20, 361

—, 1973, ApJ, 179, 731

Faber S. M., Dressler A., Davies R. L., Burstein D., Lynden-Bell D., 1987, in Nearly Normal Galaxies. From the Planck Time to the Present, Faber S. M., ed., pp. 175–183

Faber S. M., Friel E. D., Burstein D., Gaskell C. M., 1985, ApJS, 57, 711

Faber S. M., Gallagher J. S., 1976, ApJ, 204, 365

—, 1979, ARA&A, 17, 135

Faber S. M., Jackson R. E., 1976, ApJ, 204, 668

Faber S. M., Trager S. C., Gonzalez J. J., Worthey G., 1999, Ap&SS, 267, 273

Faber S. M. et al., 2007, ApJ, 665, 265

Falcón-Barroso J., Peletier R. F., Vazdekis A., Balcells M., 2003, ApJ, 588, L17

Falcón-Barroso J., Sánchez-Blázquez P., Vazdekis A., Ricciardelli E., Cardiel N., Cenarro A. J., Gorgas J., Peletier R. F., 2011a, A&A, 532, A95

Falcón-Barroso J. et al., 2011b, MNRAS, 1459

Fan L., Lapi A., Bressan A., Bernardi M., De Zotti G., Danese L., 2010, ApJ, 718, 1460

Fan L., Lapi A., De Zotti G., Danese L., 2008, ApJ, 689, L101

Fasano G. et al., 2006, A&A, 445, 805

Fasano G., Poggianti B. M., Couch W. J., Bettoni D., Kjærgaard P., Moles M., 2000, ApJ, 542, 673

Feldmann R., Carollo C. M., Mayer L., Renzini A., Lake G., Quinn T., Stinson G. S., Yepes G., 2010, ApJ, 709, 218

Ferreras I., Barbera F. L., Rosa I. G. d. l., Vazdekis A., Carvalho R. R. d., Falcón-Barroso J., Ricciardelli E., 2013, MNRAS, 429, L15

Ferreras I., Charlot S., Silk J., 1999, ApJ, 521, 81

Ferreras I., Pasquali A., de Carvalho R. R., de la Rosa I. G., Lahav O., 2006, MNRAS, 370, 828

Ferreras I., Saha P., Leier D., Courbin F., Falco E. E., 2010, MNRAS, 409, L30

Fontana A., 2005, in Multiwavelength Mapping of Galaxy Formation and Evolution, Renzini A., Bender R., eds., p. 185

Fontanot F., Pasquali A., De Lucia G., van den Bosch F. C., Somerville R. S., Kang X., 2011, MNRAS, 413, 957

Franx M., 1993, PASP, 105, 1058

—, 1995, in IAU Symposium, Vol. 164, Stellar Populations, van der Kruit P. C., Gilmore G., eds., p. 269

Franx M., Illingworth G., de Zeeuw T., 1991, ApJ, 383, 112

Frenk C. S., White S. D. M., Davis M., Efstathiou G., 1988, ApJ, 327, 507

Fukugita M., Nakamura O., Turner E. L., Helmboldt J., Nichol R. C., 2004, ApJ, 601, L127

Gallazzi A., Charlot S., Brinchmann J., White S. D. M., 2006, MNRAS, 370, 1106

Gavazzi R., Treu T., Rhodes J. D., Koopmans L. V. E., Bolton A. S., Burles S., Massey R. J., Moustakas L. A., 2007, ApJ, 667, 176

Gilmore G., 2001, in Starburst Galaxies: Near and Far, Editors: L. Tacconi & D. Lutz, Springer-Verlag, ed., p. 34

Girardi M., Demarco R., Rosati P., Borgani S., 2005, A&A, 442, 29

Gobat R., Rosati P., Strazzullo V., Rettura A., Demarco R., Nonino M., 2008, A&A, 488, 853

González J. J., 1993, PhD thesis, Thesis (PH.D.)–UNIVERSITY OF CALI-
FORNIA, SANTA CRUZ, 1993.Source: Dissertation Abstracts International,
Volume: 54-05, Section: B, page: 2551.

González Delgado R. M., Cerviño M., Martins L. P., Leitherer C., Hauschildt
P. H., 2005, MNRAS, 357, 945

Gorgas J., Faber S. M., Burstein D., Gonzalez J. J., Courteau S., Prosser C.,
1993, ApJS, 86, 153

Gorgas J., Pedraz S., Guzman R., Cardiel N., Gonzalez J. J., 1997, ApJ, 481,
L19

Goto T., 2005, MNRAS, 357, 937

—, 2007, MNRAS, 381, 187

Goudfrooij P., Hansen L., Jorgensen H. E., Norgaard-Nielsen H. U., 1994,
A&AS, 105, 341

Graham A., Colless M., 1997, MNRAS, 287, 221

Greggio L., 1997, MNRAS, 285, 151

Greggio L., Renzini A., 2012, ArXiv e-prints: 1203.1221

Grillo C., Gobat R., Lombardi M., Rosati P., 2009, A&A, 501, 461

Grogin N. A., Rajan A., Donley J. L., Kartaltepe J. S., Koekemoer A. M.,
Lucas R. A., Rosario D. J., Salvato M., 2012, in American Astronomical
Society Meeting Abstracts, Vol. 220, American Astronomical Society Meeting
Abstracts n220, p. 335.23

Guiderdoni B., Rocca-Volmerange B., 1987, A&A, 186, 1

Gunn J. E., Gott, III J. R., 1972, ApJ, 176, 1

Gunn J. E., Stryker L. L., Tinsley B. M., 1981, ApJ, 249, 48

Guzman R., Lucey J. R., Carter D., Terlevich R. J., 1992, MNRAS, 257, 187

Harrison C. D., Colless M., Kuntschner H., Couch W. J., de Propris R., Pracy
M. B., 2011, MNRAS, 413, 1036

Hausman M. A., Ostriker J. P., 1978, ApJ, 224, 320

Heavens A. F., Jimenez R., Lahav O., 2000, MNRAS, 317, 965

Hennebelle P., Chabrier G., 2008, ApJ, 684, 395

—, 2009, ApJ, 702, 1428

Henry R. B. C., Edmunds M. G., Köppen J., 2000, ApJ, 541, 660

Hocuk S., Schleicher D. R. G., Spaans M., Cazaux S., 2012, A&A, 545, A46

Hogg D. W. et al., 2003, ApJ, 585, L5

Holden B. P. et al., 2005, ApJ, 620, L83

Holmberg E., 1958, Meddelanden fran Lunds Astronomiska Observatorium Serie II, 136, 1

Homeier N. L. et al., 2005, ApJ, 621, 651

Hopkins P. F., Bundy K., Murray N., Quataert E., Lauer T. R., Ma C.-P., 2009a, MNRAS, 398, 898

Hopkins P. F., Hernquist L., Cox T. J., Keres D., Wuyts S., 2009b, ApJ, 691, 1424

Hopkins P. F., Hernquist L., Cox T. J., Kereš D., 2008, ApJS, 175, 356

Hoskin M. A., 1976, Journal for the History of Astronomy, 7, 169

Hubble E. P., 1926, ApJ, 64, 321

—, 1936, Realm of the Nebulae

Hudson M. J., Lucey J. R., Smith R. J., Schlegel D. J., Davies R. L., 2001, MNRAS, 327, 265

Huertas-Company M., Shankar F., Mei S., Bernardi M., Aguerri J. A. L., Meert A., Vikram V., 2012, ArXiv e-prints:1212.4143

Illingworth G., 1977, ApJ, 218, L43

Jackson N., Bryan S. E., Mao S., Li C., 2010, MNRAS, 403, 826

Jee M. J., White R. L., Benítez N., Ford H. C., Blakeslee J. P., Rosati P., Demarco R., Illingworth G. D., 2005, ApJ, 618, 46

Jones D. H. et al., 2004, MNRAS, 355, 747

Jørgensen I., 1999, MNRAS, 306, 607

Jørgensen I., Bergmann M., Davies R., Barr J., Takamiya M., Crampton D., 2005, AJ, 129, 1249

Jørgensen I., Chiboucas K., 2013, AJ, 145, 77

Jørgensen I., Chiboucas K., Flint K., Bergmann M., Barr J., Davies R., 2006, ApJ, 639, L9

Jørgensen I., Franx M., Hjorth J., van Dokkum P. G., 1999, MNRAS, 308, 833

Jørgensen I., Franx M., Kjaergaard P., 1996, MNRAS, 280, 167

Kaban A., Nolan L. A., Raychaudhury S., 2005, in Proceedings of the Fifth SIAM International Conference on Data Mining Editors: Hillol Kargupta, Jaideep Srivastava, Chandrika Kamath, Arnold Goodman, Publisher: Society for Industrial Mathematics, 2005. ISBN 978-0898715934, p. 183

Kauffmann G., 1996, MNRAS, 281, 487

Kauffmann G., Charlot S., 1998, MNRAS, 294, 705

Kauffmann G., Charlot S., White S. D. M., 1996, MNRAS, 283, L117

Kauffmann G., Colberg J. M., Diaferio A., White S. D. M., 1999, MNRAS, 303, 188

Kauffmann G. et al., 2003a, MNRAS, 341, 33

—, 2003b, MNRAS, 341, 54

Kauffmann G., White S. D. M., Guiderdoni B., 1993, MNRAS, 264, 201

Kaviraj S., Devriendt J. E. G., Ferreras I., Yi S. K., 2005, MNRAS, 360, 60

Kaviraj S. et al., 2008, MNRAS, 388, 67

Kaviraj S., Peirani S., Khochfar S., Silk J., Kay S., 2009, MNRAS, 394, 1713

Kaviraj S. et al., 2007, ApJS, 173, 619

Kelson D. D., Illingworth G. D., Franx M., van Dokkum P. G., 2001, ApJ, 552, L17

—, 2006, ApJ, 653, 159

Kelson D. D., Illingworth G. D., van Dokkum P. G., Franx M., 2000, ApJ, 531, 184

Kelson D. D., van Dokkum P. G., Franx M., Illingworth G. D., Fabricant D., 1997, ApJ, 478, L13

Kereš D., Katz N., Weinberg D. H., Davé R., 2005, MNRAS, 363, 2

Khochfar S., Silk J., 2006, ApJ, 648, L21

Klypin A., Kravtsov A. V., Valenzuela O., Prada F., 1999, ApJ, 522, 82

Kodama T., Arimoto N., 1997, A&A, 320, 41

Kodama T., Arimoto N., Barger A. J., Arag'on-Salamanca A., 1998, A&A, 334, 99

Kodama T., Bower R. G., 2001, MNRAS, 321, 18

Kodama T. et al., 2004, MNRAS, 350, 1005

Koekemoer A. M. et al., 2011, ApJS, 197, 36

Koleva M., Prugniel P., Bouchard A., Wu Y., 2009, A&A, 501, 1269

Koopmans L. V. E., Treu T., Bolton A. S., Burles S., Moustakas L. A., 2006, ApJ, 649, 599

Kormendy J., 1984, ApJ, 287, 577

Kormendy J., Bender R., 1996, ApJ, 464, L119+

—, 2012, ApJS, 198, 2

Korn A. J., Maraston C., Thomas D., 2005, A&A, 438, 685

Kratter K. M., Matzner C. D., Krumholz M. R., Klein R. I., 2010, ApJ, 708, 1585

Kriek M., van Dokkum P. G., Labbé I., Franx M., Illingworth G. D., Marchesini D., Quadri R. F., 2009, ApJ, 700, 221

Kroupa P., 2001, MNRAS, 322, 231

Kroupa P., Tout C. A., Gilmore G., 1993, MNRAS, 262, 545

Krumholz M. R., Klein R. I., McKee C. F., Offner S. S. R., Cunningham A. J., 2009, Science, 323, 754

Kuntschner H., 2000, MNRAS, 315, 184

Kuntschner H., Davies R. L., 1998, MNRAS, 295, L29

Kuntschner H. et al., 2006, MNRAS, 369, 497

Kuntschner H., Lucey J. R., Smith R. J., Hudson M. J., Davies R. L., 2001, MNRAS, 323, 615

Kuntschner H., Smith R. J., Colless M., Davies R. L., Kaldare R., Vazdekis A., 2002, MNRAS, 337, 172

La Barbera F., de Carvalho R. R., de La Rosa I. G., Lopes P. A. A., Kohl-Moreira J. L., Capelato H. V., 2010a, MNRAS, 408, 1313

La Barbera F., Lopes P. A. A., de Carvalho R. R., de La Rosa I. G., Berlind A. A., 2010b, MNRAS, 408, 1361

Lacey C., Cole S., 1993, MNRAS, 262, 627

Larson R. B., 1974a, MNRAS, 166, 585

—, 1974b, MNRAS, 169, 229

—, 1975, MNRAS, 173, 671

Larson R. B., Tinsley B. M., Caldwell C. N., 1980, ApJ, 237, 692

Law D. R., Steidel C. C., Shapley A. E., Nagy S. R., Reddy N. A., Erb D. K., 2012, ApJ, 745, 85

Lee H.-c., Worthey G., 2005, ApJS, 160, 176

Leggett S. K. et al., 2006, MNRAS, 373, 781

Longhetti M. et al., 2007, MNRAS, 374, 614

López-Sanjuan C., Balcells M., Pérez-González P. G., Barro G., García-Dabó C. E., Gallego J., Zamorano J., 2009, A&A, 501, 505

López-Sanjuan C. et al., 2012, A&A, 548, A7

Lubin L. M., Oke J. B., Postman M., 2002, AJ, 124, 1905

Lubin L. M., Postman M., Oke J. B., 1998, AJ, 116, 643

Maller A. H., Katz N., Kereš D., Davé R., Weinberg D. H., 2006, ApJ, 647, 763

Man A. W. S., Toft S., Zirm A. W., Wuyts S., van der Wel A., 2012, ApJ, 744, 85

Mancini C. et al., 2010, MNRAS, 401, 933

Maraston C., 2005, MNRAS, 362, 799

Maraston C., Strömbäck G., 2011, MNRAS, 418, 2785

Mármol-Queraltó E., Trujillo I., Pérez-González P. G., Varela J., Barro G., 2012, MNRAS, 422, 2187

Martinez-Manso J. et al., 2011, ApJ, 738, L22+

Massey P., 2003, ARA&A, 41, 15

Mastropietro C., Moore B., Mayer L., Debattista V. P., Piffaretti R., Stadel J., 2005, MNRAS, 364, 607

Matteucci F., 2003, Ap&SS, 284, 539

Maughan B. J., Jones L. R., Ebeling H., Perlman E., Rosati P., Frye C., Mullis C. R., 2003, ApJ, 587, 589

McCarthy I. G., Frenk C. S., Font A. S., Lacey C. G., Bower R. G., Mitchell N. L., Balogh M. L., Theuns T., 2008, MNRAS, 383, 593

McCarthy P. J. et al., 2001, ApJ, 560, L131

McIntosh D. H. et al., 2005, ApJ, 632, 191

McLure R. J. et al., 2012, ArXiv e-prints:1212.5222

Menanteau F., Ellis R. S., Abraham R. G., Barger A. J., Cowie L. L., 1999, MNRAS, 309, 208

Mendel J. T., Proctor R. N., Forbes D. A., 2007, MNRAS, 379, 1618

Miller G. E., Scalo J. M., 1979, ApJS, 41, 513

Moore B., Katz N., Lake G., Dressler A., Oemler A., 1996, Nature, 379, 613

Moore B., Lake G., Quinn T., Stadel J., 1999, MNRAS, 304, 465

Mortlock A., Conselice C. J., Bluck A. F. L., Bauer A. E., Grützbauch R., Buitrago F., Ownsworth J., 2011, MNRAS, 413, 2845

Moustakas L. A., Davis M., Graham J. R., Silk J., Peterson B. A., Yoshii Y., 1997, ApJ, 475, 445

Muzzin A., van Dokkum P., Franx M., Marchesini D., Kriek M., Labbé I., 2009, ApJ, 706, L188

Myers P. C., 2008, ApJ, 687, 340

—, 2009, ApJ, 700, 1609

Naab T., Johansson P. H., Ostriker J. P., 2009, ApJ, 699, L178

Naab T., Johansson P. H., Ostriker J. P., Efstathiou G., 2007, ApJ, 658, 710

Naab T., Khochfar S., Burkert A., 2006, ApJ, 636, L81

Napolitano N. R., Romanowsky A. J., Tortora C., 2010, MNRAS, 405, 2351

Narayanan D., Davé R., 2012, MNRAS, 423, 3601

Navarro J. F., Frenk C. S., White S. D. M., 1997, ApJ, 490, 493

Newman A. B., Ellis R. S., Bundy K., Treu T., 2012, ApJ, 746, 162

Newman A. B., Ellis R. S., Treu T., Bundy K., 2010, ApJ, 717, L103

Nichol R. C. et al., 1999, ApJ, 521, L21

Nierenberg A. M., Auger M. W., Treu T., Marshall P. J., Fassnacht C. D., 2011, ApJ, 731, 44

Nipoti C., Treu T., Leauthaud A., Bundy K., Newman A. B., Auger M. W., 2012, MNRAS, 422, 1714

Nolan L. A., Raychaudhury S., Kabán A., 2007, MNRAS, 375, 381

O'Connell R. W., 1976, ApJ, 206, 370

—, 1986, in Stellar Populations, Norman C. A., Renzini A., Tosi M., eds., pp. 167–189

Ocvirk P., Pichon C., Lançon A., Thiébaut E., 2006a, MNRAS, 365, 74

—, 2006b, MNRAS, 365, 46

Oemler, Jr. A., Dressler A., Butcher H. R., 1997, ApJ, 474, 561

Oesch P. A. et al., 2010, ApJ, 714, L47

Oey M. S., 2011, ApJ, 739, L46

Offner S. S. R., Hansen C. E., Krumholz M. R., 2009, ApJ, 704, L124

Offner S. S. R., Klein R. I., McKee C. F., Krumholz M. R., 2009, ApJ, 703, 131

Onodera M. et al., 2010, ApJ, 715, L6

Oser L., Naab T., Ostriker J. P., Johansson P. H., 2012, ApJ, 744, 63

Oser L., Ostriker J. P., Naab T., Johansson P. H., Burkert A., 2010, ApJ, 725, 2312

Padoan P., Nordlund Å., 2002, ApJ, 576, 870

Padoan P., Nordlund A., Jones B. J. T., 1997, MNRAS, 288, 145

Pahre M. A., Djorgovski S. G., De Carvalho R. R., 2001, Ap&SS, 276, 983

Panter B., Heavens A. F., Jimenez R., 2004, MNRAS, 355, 764

Patel S. G., Kelson D. D., Holden B. P., Illingworth G. D., Franx M., van der Wel A., Ford H., 2009, ApJ, 694, 1349

Peletier R. F., 1989, PhD thesis, , University of Groningen, The Netherlands, (1989)

Peng C. Y., Ho L. C., Impey C. D., Rix H., 2002, AJ, 124, 266

—, 2010, AJ, 139, 2097

Pérez-González P. G. et al., 2008, ApJ, 675, 234

Persson S. E., Murphy D. C., Krzeminski W., Roth M., Rieke M. J., 1998, AJ, 116, 2475

Peterson R. C., 1976, ApJ, 210, L123

Pforr J., Maraston C., Tonini C., 2012, MNRAS, 422, 3285

Poggianti B. M. et al., 2001, ApJ, 563, 118

—, 2013, ApJ, 762, 77

Poggianti B. M., van Gorkom J. H., 2001, in Astronomical Society of the Pacific Conference Series, Vol. 240, Gas and Galaxy Evolution, Hibbard J. E., Rupen M., van Gorkom J. H., eds., p. 599

Poggianti B. M. et al., 2006, ApJ, 642, 188

Pohlen M., Trujillo I., 2006, A&A, 454, 759

Postman M. et al., 2005, ApJ, 623, 721

Pozzetti L. et al., 2003, A&A, 402, 837

Pracy M. B., Kuntschner H., Couch W. J., Blake C., Bekki K., Briggs F., 2009, MNRAS, 396, 1349

Press W. H., Schechter P., 1974, ApJ, 187, 425

Primack J. R., Blumenthal G. R., 1984, in NATO ASIC Proc. 117: Formation and Evolution of Galaxies and Large Structures in the Universe, Audouze J., Tran Thanh Van J., eds., pp. 163–183

Proctor R. N., Forbes D. A., Beasley M. A., 2004, MNRAS, 355, 1327

Prugniel P., Simien F., 1996, A&A, 309, 749

Prugniel P., Soubiran C., 2001, A&A, 369, 1048

Puzia T. H., Saglia R. P., Kissler-Patig M., Maraston C., Greggio L., Renzini A., Ortolani S., 2002, A&A, 395, 45

Quilis V., Trujillo I., 2012, ApJ, 752, L19

Rabin D., 1982, ApJ, 261, 85

Ragone-Figueroa C., Granato G. L., 2011, MNRAS, 414, 3690

Ravindranath S. et al., 2002, in Bulletin of the American Astronomical Society, Vol. 201, American Astronomical Society Meeting Abstracts, pp. 611–+

Renzini A., 2006, ARA&A, 44, 141

Renzini A., Buzzoni A., 1986, in Astrophysics and Space Science Library, Vol. 122, Spectral Evolution of Galaxies, Chiosi C., Renzini A., eds., pp. 195–231

Renzini A., Ciotti L., 1993, ApJ, 416, L49

Renzini A., Voli M., 1981, A&A, 94, 175

Rettura A. et al., 2010, ApJ, 709, 512

Reynolds J. H., 1920, MNRAS, 80, 746

Ricciardelli E., Trujillo I., Buitrago F., Conselice C. J., 2010, MNRAS, 406, 230

Ricciardelli E., Vazdekis A., Cenarro A. J., Falcón-Barroso J., 2012, MNRAS, 424, 172

Rose J. A., 1985, AJ, 90, 1927

Rose J. A., Bower R. G., Caldwell N., Ellis R. S., Sharples R. M., Teague P., 1994, AJ, 108, 2054

Rudnick G. et al., 2008, Spitzer Proposal, 50733

—, 2003, ApJ, 599, 847

Salaris M., Chieffi A., Straniero O., 1993, ApJ, 414, 580

Salaris M., Weiss A., 1998, A&A, 335, 943

Salpeter E. E., 1955, ApJ, 121, 161

Sánchez-Blázquez P., Gorgas J., Cardiel N., Cenarro J., González J. J., 2003, ApJ, 590, L91

Sánchez-Blázquez P., Gorgas J., Cardiel N., González J. J., 2006a, A&A, 457, 787

—, 2006b, A&A, 457, 809

Sánchez-Blázquez P. et al., 2009, A&A, 499, 47

—, 2006c, MNRAS, 371, 703

Sandage A., 1961, The Hubble atlas of galaxies

Sandage A., Freeman K. C., Stokes N. R., 1970, ApJ, 160, 831

Sarzi M. et al., 2006, MNRAS, 366, 1151

Scalo J. M., 1986, Fund. Cosmic Phys., 11, 1

Schiavon R. P., 2007, ApJS, 171, 146

—, 2010, Publication of Korean Astronomical Society, 25, 83

Schiavon R. P., Faber S., 2000, in Bulletin of the American Astronomical Society, Vol. 32, American Astronomical Society Meeting Abstracts, p. 1527

Schiavon R. P. et al., 2006, ApJ, 651, L93

Schmidt M., 1963, ApJ, 137, 758

Schweizer F., 1982, ApJ, 252, 455

Schweizer F., Whitmore B. C., Rubin V. C., 1983, AJ, 88, 909

Serra P., Trager S. C., 2007, MNRAS, 374, 769

Serra P., Trager S. C., van der Hulst J. M., Oosterloo T. A., Morganti R., 2006, A&A, 453, 493

Sérsic J. L., 1968, Atlas de galaxias australes

Shapley H., Curtis H., 1921, Bull. Nat. Res. Counc., 2, 171

Shen S., Mo H. J., White S. D. M., Blanton M. R., Kauffmann G., Voges W., Brinkmann J., Csabai I., 2003, MNRAS, 343, 978

Smail I., Dressler A., Couch W. J., Ellis R. S., Oemler, Jr. A., Butcher H., Sharples R. M., 1997, ApJS, 110, 213

Smith R. W., 1982, Journal for the History of Astronomy, 13, 145

Somerville R. S., Primack J. R., 1999, MNRAS, 310, 1087

Sommer-Larsen J., Toft S., 2010, ApJ, 721, 1755

Sonnenfeld A., Treu T., Gavazzi R., Marshall P. J., Auger M. W., Suyu S. H., Koopmans L. V. E., Bolton A. S., 2012, ApJ, 752, 163

Spiniello C., Trager S. C., Koopmans L. V. E., Chen Y. P., 2012, ApJ, 753, L32

Spinrad H., Taylor B. J., 1971, ApJS, 22, 445

Spitzer, Jr. L., Baade W., 1951, ApJ, 113, 413

Stanford S. A., Eisenhardt P. R. M., Dickinson M., 1995, ApJ, 450, 512

Stockton A., Shih H.-Y., Larson K., 2010, ApJ, 709, L58

Strateva I. et al., 2001, AJ, 122, 1861

Swindle R., Gal R. R., La Barbera F., de Carvalho R. R., 2011, AJ, 142, 118

Szomoru D., Franx M., van Dokkum P. G., 2012, ApJ, 749, 121

Tanaka M., Kodama T., Arimoto N., Okamura S., Umetsu K., Shimasaku K., Tanaka I., Yamada T., 2005, MNRAS, 362, 268

Tantalo R., Chiosi C., 2004, MNRAS, 353, 405

Tantalo R., Chiosi C., Bressan A., 1998, A&A, 333, 419

Taylor E. N., Franx M., Glazebrook K., Brinchmann J., van der Wel A., van Dokkum P. G., 2010, ApJ, 720, 723

Terlevich A. I., Caldwell N., Bower R. G., 2001, MNRAS, 326, 1547

Terlevich A. I., Forbes D. A., 2002, MNRAS, 330, 547

Terlevich A. I., Kuntschner H., Bower R. G., Caldwell N., Sharples R. M., 1999, MNRAS, 310, 445

Terlevich R., Davies R. L., Faber S. M., Burstein D., 1981, MNRAS, 196, 381

Teuben P. J., 2002, in Astronomical Society of the Pacific Conference Series, Vol. 275, Disks of Galaxies: Kinematics, Dynamics and Peturbations, Athanassoula E., Bosma A., Mujica R., eds., pp. 217–228

Thomas D., Maraston C., Bender R., 2003, MNRAS, 339, 897

Thomas D., Maraston C., Bender R., Mendes de Oliveira C., 2005, ApJ, 621, 673

Thomas D., Maraston C., Korn A., 2004, MNRAS, 351, L19

Thomas D., Maraston C., Schawinski K., Sarzi M., Silk J., 2010, MNRAS, 404, 1775

Thomas J. et al., 2011, MNRAS, 415, 545

Tinsley B. M., 1978, ApJ, 222, 14

—, 1980a, Fund. Cosmic Phys., 5, 287

—, 1980b, ApJ, 241, 41

Tinsley B. M., Gunn J. E., 1976, ApJ, 203, 52

Toft S., Gallazzi A., Zirm A., Wold M., Zibetti S., Grillo C., Man A., 2012, ApJ, 754, 3

Toft S., Soucail G., Hjorth J., 2003, MNRAS, 344, 337

Toft S. et al., 2007, ApJ, 671, 285

Tojeiro R., Heavens A. F., Jimenez R., Panter B., 2007, MNRAS, 381, 1252

Toomre A., 1977, ARA&A, 15, 437

Toomre A., Toomre J., 1972, ApJ, 178, 623

Tortora C., Romanowsky A. J., Napolitano N. R., 2012, ArXiv e-prints: 1207.4475

Trager S. C., Dalcanton J., Marzke R. O., McWilliam A., Weiner B. J., 1998, in Bulletin of the American Astronomical Society, Vol. 30, Bulletin of the American Astronomical Society, pp. 1331–+

Trager S. C., Faber S. M., Worthey G., González J. J., 2000a, AJ, 120, 165

—, 2000b, AJ, 119, 1645

Tran K.-V. H., Franx M., Illingworth G. D., van Dokkum P., Kelson D. D., Blakeslee J. P., Postman M., 2007, ApJ, 661, 750

Treu T., Auger M. W., Koopmans L. V. E., Gavazzi R., Marshall P. J., Bolton A. S., 2010, ApJ, 709, 1195

Treu T. et al., 2005, ApJ, 633, 174

Treu T., Koopmans L. V., Bolton A. S., Burles S., Moustakas L. A., 2006, ApJ, 640, 662

Treu T., Koopmans L. V. E., 2004, ApJ, 611, 739

Treu T., Stiavelli M., Bertin G., Casertano S., Møller P., 2001, MNRAS, 326, 237

Treu T., Stiavelli M., Casertano S., Møller P., Bertin G., 1999, MNRAS, 308, 1037

Trimble V., 1995, PASP, 107, 1133

Tripicco M. J., Bell R. A., 1995, AJ, 110, 3035

Trujillo I., Asensio Ramos A., Rubiño-Martín J. A., Graham A. W., Aguerri J. A. L., Cepa J., Gutiérrez C. M., 2002, MNRAS, 333, 510

Trujillo I., Burkert A., Bell E. F., 2004, ApJ, 600, L39

Trujillo I., Cenarro A. J., de Lorenzo-Cáceres A., Vazdekis A., de la Rosa I. G., Cava A., 2009, ApJ, 692, L118

Trujillo I., Conselice C. J., Bundy K., Cooper M. C., Eisenhardt P., Ellis R. S., 2007, MNRAS, 382, 109

Trujillo I., Ferreras I., de La Rosa I. G., 2011, MNRAS, 415, 3903

Trujillo I. et al., 2006, MNRAS, 373, L36

Trujillo I., Graham A. W., Caon N., 2001, MNRAS, 326, 869

Valdes F., Gupta R., Rose J. A., Singh H. P., Bell D. J., 2004, ApJS, 152, 251

Valentinuzzi T. et al., 2010, ApJ, 712, 226

van Albada T. S., 1982, MNRAS, 201, 939

van de Sande J. et al., 2011, ApJ, 736, L9+

van den Bergh S., 1960a, ApJ, 131, 558

—, 1960b, ApJ, 131, 215

—, 1976, ApJ, 206, 883

van der Wel A., Franx M., van Dokkum P. G., Rix H.-W., 2004, ApJ, 601, L5

van der Wel A., Franx M., van Dokkum P. G., Rix H.-W., Illingworth G. D., Rosati P., 2005, ApJ, 631, 145

van der Wel A., Franx M., Wuyts S., van Dokkum P. G., Huang J., Rix H.-W., Illingworth G. D., 2006, ApJ, 652, 97

van der Wel A., Holden B. P., Zirm A. W., Franx M., Rettura A., Illingworth G. D., Ford H. C., 2008, ApJ, 688, 48

van der Wel A. et al., 2011, ApJ, 730, 38

van Dokkum P. G., Conroy C., 2010, Nature, 468, 940

—, 2012, ApJ, 760, 70

van Dokkum P. G., Ellis R. S., 2003, ApJ, 592, L53

van Dokkum P. G., Franx M., 1996, MNRAS, 281, 985

—, 2001, ApJ, 553, 90

van Dokkum P. G., Franx M., Fabricant D., Kelson D. D., Illingworth G. D., 1999, ApJ, 520, L95

van Dokkum P. G., Franx M., Kelson D. D., Illingworth G. D., 1998, ApJ, 504, L17

van Dokkum P. G. et al., 2008, ApJ, 677, L5

van Dokkum P. G., Stanford S. A., 2003, ApJ, 585, 78

Vazdekis A., 1999, ApJ, 513, 224

Vazdekis A., Casuso E., Peletier R. F., Beckman J. E., 1996, ApJS, 106, 307

Vazdekis A., Cenarro A. J., Gorgas J., Cardiel N., Peletier R. F., 2003, MNRAS, 340, 1317

Vazdekis A., Kuntschner H., Davies R. L., Arimoto N., Nakamura O., Peletier R., 2001a, ApJ, 551, L127

Vazdekis A., Peletier R. F., Beckman J. E., Casuso E., 1997, ApJS, 111, 203

Vazdekis A., Ricciardelli E., Cenarro A. J., Rivero-González J. G., Díaz-García L. A., Falcón-Barroso J., 2012, MNRAS, 424, 157

Vazdekis A., Salaris M., Arimoto N., Rose J. A., 2001b, ApJ, 549, 274

Vazdekis A., Sánchez-Blázquez P., Falcón-Barroso J., Cenarro A. J., Beasley M. A., Cardiel N., Gorgas J., Peletier R. F., 2010, MNRAS, 404, 1639

Visvanathan N., Sandage A., 1977, ApJ, 216, 214

Vogt N. P., Forbes D. A., Phillips A. C., Gronwall C., Faber S. M., Illingworth G. D., Koo D. C., 1996, ApJ, 465, L15

Vulcani B. et al., 2012, MNRAS, 420, 1481

Vulcani B., Poggianti B. M., Finn R. A., Rudnick G., Desai V., Bamford S., 2010, ApJ, 710, L1

Wagner S. J., Bender R., Moellenhoff C., 1988, A&A, 195, L5

White S. D. M., 1978, MNRAS, 184, 185

White S. D. M., Frenk C. S., 1991, ApJ, 379, 52

White S. D. M., Negroponte J., 1982, MNRAS, 201, 401

White S. D. M., Rees M. J., 1978, MNRAS, 183, 341

Whitworth A. P., Bhattal A. S., Chapman S. J., Disney M. J., Turner J. A., 1994, MNRAS, 268, 291

Wild V., Walcher C. J., Johansson P. H., Tresse L., Charlot S., Pollo A., Le Fèvre O., de Ravel L., 2009, MNRAS, 395, 144

Worthey G., 1994, ApJS, 95, 107

—, 1998, PASP, 110, 888

Worthey G., Faber S. M., Gonzalez J. J., 1992, ApJ, 398, 69

Worthey G., Faber S. M., Gonzalez J. J., Burstein D., 1994, ApJS, 94, 687

Worthey G., Jowett K. J., 2003, PASP, 115, 96

Worthey G., Ottaviani D. L., 1997, ApJS, 111, 377

Wuyts S., Cox T. J., Hayward C. C., Franx M., Hernquist L., Hopkins P. F., Jonsson P., van Dokkum P. G., 2010, ApJ, 722, 1666

Wuyts S., van Dokkum P. G., Kelson D. D., Franx M., Illingworth G. D., 2004, ApJ, 605, 677

Yamada Y., Arimoto N., Vazdekis A., Peletier R. F., 2006, ApJ, 637, 200

Yang Y., Zabludoff A. I., Zaritsky D., Lauer T. R., Mihos J. C., 2004, ApJ, 607, 258

Yi S. K. et al., 2005, ApJ, 619, L111

Zabludoff A. I., Zaritsky D., Lin H., Tucker D., Hashimoto Y., Shectman S. A., Oemler A., Kirshner R. P., 1996, ApJ, 466, 104

Ziegler B. L., Bender R., 1997, MNRAS, 291, 527

Ziegler B. L., Bower R. G., Smail I., Davies R. L., Lee D., 2001, MNRAS, 325, 1571

Zirm A. W. et al., 2007, ApJ, 656, 66